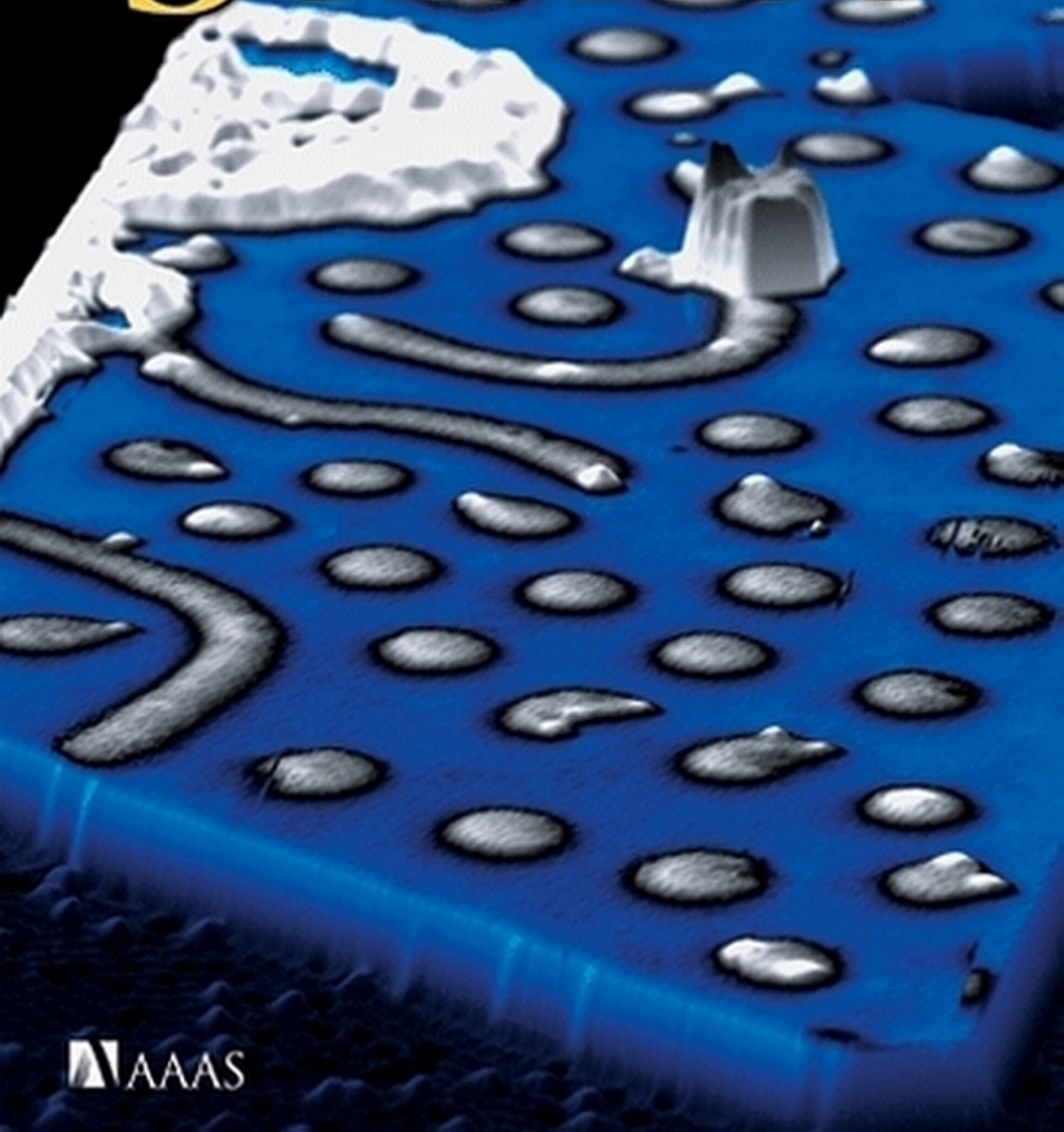


9 August 2013 | \$10

Science



EDITORIAL

- 592 Preparing for Disasters
Marcia McNutt and Alan Leshner

NEWS OF THE WEEK

- 596 A roundup of the week's top stories

NEWS & ANALYSIS

- 598 Embezzlement Casts Harsh Light on China's Grant System
- 599 How to Make a Great Ice Age, Again and Again and Again
- 600 France Córdova Brings Management Expertise to NSF
- 601 Critics Skeptical as Flu Scientists Argue for Controversial H7N9 Studies
>> *Letter by R. A. M. Fouchier et al. p. 612; Science Express Letter by H. Jaffe et al.*
- 602 Lab Burger Adds Sizzle to Bid for Research Funds
- 603 Grim Day for Turkish Science as Six Academics Get Long Prison Terms
- 604 House Subpoena Revives Battle Over Air Pollution Studies
- 605 Unconventional Vaccine Shows Promise Against Malaria
>> *Science Express Research Article by R. A. Seder et al.*

NEWS FOCUS

- 606 The Web's Faceless Judges
>> *Science Podcast*
- 609 Computing a Better Fire Forecast

LETTERS

- 612 Gain-of-Function Experiments on H7N9
R. A. M. Fouchier et al.
>> *News story p. 601; Science Express Letter by H. Jaffe et al.*
- 613 NextGenVOICES
- 613 TECHNICAL COMMENT ABSTRACTS

BOOKS ET AL.

- 614 Arming Mother Nature
J. D. Hamblin, reviewed by G. Mitman
- 615 The Lost Art of Finding Our Way
J. E. Huth, reviewed by D. Lockwood

POLICY FORUM

- 616 Who Will Pay for Public Access to Research Data?
F. Berman and V. Cerf

PERSPECTIVES

- 618 Buildings as Weapons of Mass Destruction
R. Bilham and V. Gaur
>> *Science Podcast*
- 620 Graphene for Terahertz Applications
P. Tassin et al.
- 621 Flashing a Light on the Spatial Organization of Transcription
C. Rickman and W. A. Bickmore
>> *Report p. 664*
- 622 Lymphatics Are in My Veins
M. Simons and A. Eichmann
- 624 Copper's Contribution to Amination Catalysis
S. R. Chemler
- 626 The Maturing Brain Methylome
H. W. Gabel and M. E. Greenberg
>> *Research Article p. 629*

REVIEW

- 628 Sequence-Controlled Polymers
J.-F. Lutz et al.
Review Summary; for full text:
<http://dx.doi.org/10.1126/science.1238149>

RESEARCH ARTICLE

- 629 Global Epigenomic Reconfiguration During Mammalian Brain Development
R. Lister et al.
A genome-wide map shows that DNA methylation in neurons and glial cells changes during development in humans and mice.
Research Article Summary; for full text:
<http://dx.doi.org/10.1126/science.1237905>
>> *Perspective p. 626*

CONTENTS continued >>



page 606



page 616

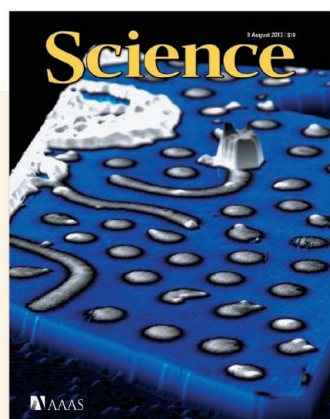
ON THE WEB THIS WEEK

>> Science Podcast

Listen to stories on dangerous buildings, a malaria vaccine, postpublication peer review, and more.

>> Find More Online

Check out Science Express, our podcast, videos, daily news, our research journals, and Science Careers at www.sciencemag.org.



COVER

Spin-resolved scanning tunneling microscopy (STM) image (width: 51.6 nanometers) of single magnetic skyrmions (gray) and a few remaining spin spiral lines in a bilayer of Pd/Fe on top of an Ir(111) surface. The magnetic STM tip is sensitive to the out-of-plane magnetization component of the sample. Skyrmions can be created and annihilated locally by injecting spin-polarized currents from the STM tip. See page 636.

Image: Group of R. Wiesendanger, University of Hamburg

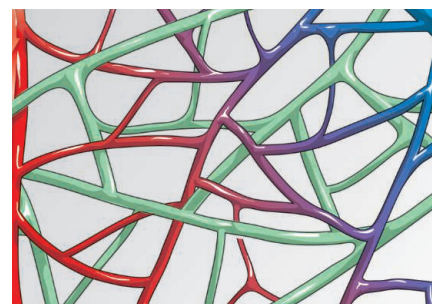
DEPARTMENTS

- 591 This Week in Science
593 Editors' Choice
594 Science Staff
678 New Products
679 Science Careers

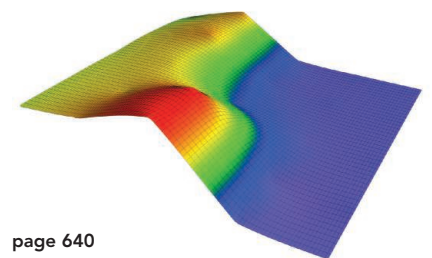
REPORTS

- 630** Imaging of the CO Snow Line in a Solar Nebula Analog
C. Qi et al.
Millimeter-wavelength observations locate the carbon monoxide condensation line within the disk around a young planet-forming star.
- 632** A Quantum Many-Body Spin System in an Optical Lattice Clock
M. J. Martin et al.
A one-dimensional lattice of pancake-shaped clouds of ^{87}Sr atoms is used to realize a strongly correlated system of spins.
- 636** Writing and Deleting Single Magnetic Skyrmions
N. Romming et al.
Spin-polarized currents delivered by a scanning tunneling microscope can be used to create and destroy spin whirlpools.
- 640** A Semi-Floating Gate Transistor for Low-Voltage Ultrafast Memory and Sensing Operation
P.-F. Wang et al.
An embedded tunneling field-effect transistor speeds switching by varying the voltage threshold of the main gate electrode.
- 643** Active Atmosphere-Ecosystem Exchange of the Vast Majority of Detected Volatile Organic Compounds
J.-H. Park et al.
Many volatile organic compounds emitted by vegetation are actively exchanged between plants and the atmosphere.
- 647** Social Influence Bias: A Randomized Experiment
L. Muchnik et al.
A social news aggregation Web site was used to test whether prior ratings influence others to create bias in rating behavior.
- 651** Pluripotent Stem Cells Induced from Mouse Somatic Cells by Small-Molecule Compounds
P. Hou et al.
A proof-of-principle study reports somatic reprogramming to the pluripotent state using small-molecule compounds.

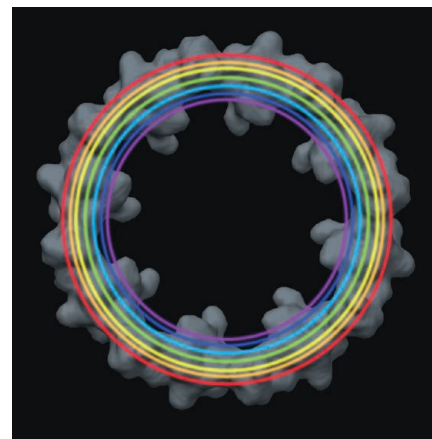
- 655** Nuclear Pore Scaffold Structure Analyzed by Super-Resolution Microscopy and Particle Averaging
A. Szymborska et al.
The localization of individual components of the nuclear pore complex was dissected using information from thousands of pores.
- 658** Polyploids Exhibit Higher Potassium Uptake and Salinity Tolerance in *Arabidopsis*
D.-Y. Chao et al.
Certain thale cress plants collected in the wild contain a duplicated genome and can cope with salty soil.
- 660** Spatial Dynamics of Chromosome Translocations in Living Cells
V. Roukos et al.
An experimental system allows the visualization of human cell chromosome translocations in real time.
- 664** Real-Time Dynamics of RNA Polymerase II Clustering in Live Human Cells
I. I. Cisse et al.
A single-cell quantitative method reveals changes in the distribution of proteins with single-molecule sensitivity.
>> *Perspective p. 621*
- 667** The Hologenomic Basis of Speciation: Gut Bacteria Cause Hybrid Lethality in the Genus *Nasonia*
R. M. Brucker and S. R. Bordenstein
Speciation may be a collective property of an organism and its microbiota.
- 670** Positive Feedback Between PU.1 and the Cell Cycle Controls Myeloid Differentiation
H. Y. Kueh et al.
Regulation of cell cycle length is a feedback mechanism that controls cell fate decisions in developing macrophages.
- 673** T Follicular Helper Cell Dynamics in Germinal Centers
Z. Shulman et al.
Tracking individual cells reveals that immunological T cell help is shared between immune B cell germinal centers.



page 622



page 640



page 655

SCIENCE (ISSN 0036-8075) is published weekly on Friday, except the last week in December, by the American Association for the Advancement of Science, 1200 New York Avenue, NW, Washington, DC 20005. Periodicals Mail postage (publication No. 484460) paid at Washington, DC, and additional mailing offices. Copyright © 2013 by the American Association for the Advancement of Science. The title SCIENCE is a registered trademark of the AAAS. Domestic individual membership and subscription (51 issues): \$149 (\$74 allocated to subscription). Domestic institutional subscription (51 issues): \$990; Foreign postage extra: Mexico, Caribbean (surface mail) \$55; other countries (air assist delivery) \$85. First class, airmail, student, and emeritus rates on request. Canadian rates with GST available upon request, GST #1254 88122. Publications Mail Agreement Number 1069624. Printed in the U.S.A.

Change of address: Allow 4 weeks, giving old and new addresses and 8-digit account number. Postmaster: Send change of address to AAAS, P.O. Box 96178, Washington, DC 20090-6178. Single-copy sales: \$10.00 current issue, \$15.00 back issue prepaid includes surface postage; bulk rates on request. Authorization to photocopy material for internal or personal use under circumstances not falling within the fair use provisions of the Copyright Act is granted by AAAS to libraries and other users registered with the Copyright Clearance Center (CCC) Transactional Reporting Service, provided that \$30.00 per article is paid directly to CCC, 222 Rosewood Drive, Danvers, MA 01923. The identification code for Science is 0036-8075. Science is indexed in the Reader's Guide to Periodical Literature and in several specialized indexes.

Epigenetic modifications and their potential changes during development are of high interest, but few studies have characterized such differences. **Lister et al.** (p. 629, published online 4 July; see the Perspective by **Gabel and Greenberg**) report whole-genome base-resolution analysis of DNA cytosine modifications and transcriptome analysis in the frontal cortex of human and mouse brains at multiple developmental stages. The high-resolution mapping of DNA cytosine methylation (5mC) and one of its oxidation derivatives (5hmC) at key developmental stages provides a comprehensive resource covering the temporal dynamics of these epigenetic modifications in neurons compared to glia. The data suggest that methylation marks are dynamic during brain development in both humans and mice.



Epigenetic Brainscape

Strongly Correlated Clocks

Optical lattice clocks with alkaline earth atoms provide one of the most stable time-keeping systems. Such clocks, in general, exhibit shifts in their transition frequencies as a consequence of interactions between atoms. Can this sensitivity be used to explore the dynamics of strongly correlated quantum systems? **Martin et al.** (p. 632) used a 1-dimensional optical lattice clock to study quantum many-body effects. Whereas the clock shift itself could be modeled within the mean field approximation, quantities such as spin noise required a full many-body treatment. This system may be useful for the quantum simulation of exotic magnetism.

Help Shared

Germinal centers are specialized structures within lymph nodes, where B cells undergo the changes required to produce high-affinity antibodies. This process relies on T follicular helper (Tfh) cells. The dynamic properties of Tfh cells and how they affect the selection of B cells, however, are not well understood. Using two-photon laser scanning microscopy of mouse lymph nodes, **Shulman et al.** (p. 673, published online 25 July) find that Tfh cells are not restricted to a single germinal center, but instead emigrate into neighboring germinal centers within the same lymph nodes. Furthermore, newly activated T cells can enter already established germinal centers and presumably influence ongoing B cell selection and

differentiation. Such active movement may ensure maximal diversification of the B cell response and promote the production of high-affinity antibodies.

Faster at the Gate

Advanced designs will be needed to continue to improve the performance of the main components of high-speed computing, metal-oxide semiconductor field-effect transistors (MOSFETs) and floating-gate (FG) MOSFETs. **Wang et al.** (p. 640) fabricated a semi-floating gate (SFG) transistor in which a tunneling field-effect transistor couples the positively doped floating gate to the negatively doped drain region. The charge stored on the SFG was used to shift the voltage threshold for switching the transistor, which in turn sped up its operation and lowered the power consumed. These devices were used for ultrahigh-speed memory and in light sensing and imaging.

Two-Way Street

Most studies of volatile organic compounds (VOCs) found in the atmosphere, which play important roles in atmospheric chemistry, have concentrated on dominant species such as isoprene. There are thousands of other classes of VOCs, and how they are exchanged between the biosphere and the atmosphere is unclear. **Park et al.** (p. 643) measured the fluxes of more than 500 types of VOCs using a highly sensitive type of mass spectrometry and an absolute value

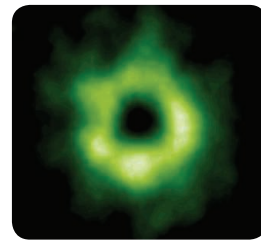
eddy covariance method. The majority of these species were actively exchanged between the atmosphere and the biosphere, with more than a quarter showing net deposition. These results should help to improve air quality and global climate models, and strengthen our understanding of atmospheric VOC chemistry.

Promoting Pluripotency

A specialized mammalian cell can be set back to the pluripotent state either by transfer of the somatic cell nucleus into an oocyte or by delivery of exogenous pluripotency-associated transcription factors. **Hou et al.** (p. 651, published online 18 July) developed an approach to induce pluripotency in somatic cells using a cocktail of small molecules. The ability to generate such chemically induced pluripotent stem cells may provide an alternate route for therapeutic cloning and for drug development in regenerative medicine.

Solar Snow Lines

Models of the formation of our solar system have suggested that condensation lines, or snow lines—the distance from a star beyond which a gas or a liquid can condense into the solid phase—are favorable locations for planet formation. Taking advantage of the increase of N_2H^+ abundance in cold regions where CO condenses out of the gas phase, **Qi et al.** (p. 630, published online 18 July) used the Atacama Large Millimeter/Submillimeter Array to image the CO snow line in the disk around TW Hya, an analog of the solar nebula from which the solar system formed. This disk's snow line corresponds to Neptune's orbit in our solar system.



Microbes → Host Speciation?

No living organism is an individual—an individual's microbiota can outnumber the host's somatic cells. Working in parasitoid wasps, **Brucker and Bordenstein** (p. 667, published online 18 July) now suggest that the gut microbiota can play a crucial role in speciation and hybrid lethality. In a clade of parasitoid wasps, interspecies hybrids survived when reared on antibiotic-treated sterile food (thus eliminating gut microbiota), but experienced high mortality when reared on conventional diet or host material.

Additional summaries

Controlled Polymers

Nature has achieved exquisite sequence control in the synthesis of polymers like DNA. In contrast, synthetic polymers rarely have the same fidelity in their chemistry or uniformity in chain-length distribution, especially when more than one monomer is involved. **Lutz et al.** (p. 628) review the progress that has been made in making sequence-controlled polymers of increasing length and complexity. These developments have come from both advances in synthetic chemistry methods and the exploitation of biological machinery.

Double Is Not Trouble

The doubling of the genome to create polyploidy is common among land plants, and most major flowering plant lineages exhibit some history of genome duplication. However, the physiological advantages of a doubled genome are not well understood. **Chao et al.** (p. 658, published online 25 July) identified accessions of the model plant *Arabidopsis thaliana* with naturally doubled genomes and found that the cytotype of the root, but not shoot, in these natural, as well as in artificially induced, polyploid plants appears to confer increased salt tolerance by regulating leaf potassium levels.

Controlling Skyrmions

Magnetic skyrmions—tiny vortex patterns of spins—hold promise for information storage because of their robustness to perturbations. Skyrmions have been observed experimentally, but manipulating them individually remains a challenge. **Romming et al.** (p. 636; see the cover) used spin-polarized electrons generated by a scanning tunneling microscope to reversibly create and destroy skyrmions in a thin iron film covered by a layer of palladium. The energy of the tunneling electrons was the decisive factor determining the probability of the process; atomic defects in the film acted as pinning sites for the skyrmions. The work demonstrates the feasibility of using spin-polarized tunnel currents for the controlled manipulation of individual skyrmions.

Follow the Leader?

The Internet has increased the likelihood that our decisions will be influenced by those being made around us. On the one hand, group decision-making can lead to better decisions, but it can also lead to “herding effects” that have

resulted in financial disasters. **Muchnik et al.** (p. 647) examined the effect of collective information via a randomized experiment, which involved collaboration with a social news aggregation Web site on which readers could vote and comment on posted comments. Data were collected and analyzed after the Web site administrators arbitrarily voted positively or negatively (or not at all) as the first comment on more than 100,000 posts. False positive entries led to inflated subsequent scores, whereas false negative initial votes had small long-term effects. Both the topic being commented upon and the relationship between the poster and commenter were important. Future efforts will be needed to sort out how to correct for such effects in polls or other collective intelligence systems in order to counter social biases.

Poring Over the Nuclear Pore

The nuclear pore is a macromolecular complex that traverses the paired membranes of the nuclear envelope through which a variety of nuclear protein and RNA cargoes must traffic. **Szymborska et al.** (p. 655, published online 11 July) combined super-resolution microscopy with single-particle averaging to localize the proteins that make up the structural scaffold of the nuclear pore complex with a precision well below one nanometer. These molecular positional constraints clarified contradictory models for the structure of the nuclear pore and demonstrate that the structural organization of protein complexes can be studied by light microscopy in situ in whole cells.

Pol II Micro Clusters

In higher eukaryotes, messenger RNA (mRNA) synthesis is thought to involve foci of clustered RNA polymerase II (Pol II) called transcription factories. However, clustered Pol II have not been resolved in living cells, raising the debate about their existence in vivo and what role, if any, they play in nuclear organization and regulation of gene expression. **Cisse et al.** (p. 664, published online 4 July; see the Perspective by **Rickman and Bickmore**) developed single-molecule in vivo analyses revealing the distribution and dynamics of Pol II clustering in living cells. Pol II clusters were smaller than the diffraction limit (<250 nm). Transient dynamics of the Pol II clusters, and correlation with changes in transcription, pointed to a role in transcription initiation rather than in elongation.

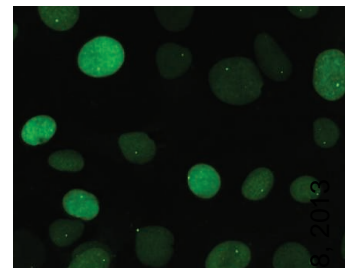
Chromosome Choreography

Chromosome translocations arise through the illegitimate pairing of broken chromosome ends and are commonly found in many cancers.

Roukos et al. (p. 660) used ultrahigh-throughput time-lapse imaging on human tissue culture cells containing marked chromosomes to capture very rare translocation events. Double-strand breaks in the DNA underwent an initial “partner

search,” with a fraction of the ends moving into spatial proximity to each other, which resulted in persistent pairing and the merging of DNA repair foci. Most paired ends arose from breaks in close

proximity, but occasionally translocations formed from more distantly positioned breaks. Proteins of the DNA repair machinery could influence the pairing and/or translocation process.



A Different Cycle for Differentiation

The regulated expression of transcription factors determines cell fate decisions during cell differentiation. The transcription factor PU.1 is an important determinant in the differentiation of hematopoietic progenitors to lymphocytes or myeloid cells, where high expression induces macrophage differentiation, whereas low expression leads to the development of B lymphocytes. How PU.1 expression levels are regulated during this cell fate choice, however, is not well understood. **Kueh et al.** (p. 670, published online 18 July) found that in mice, reduced transcription of PU.1 led to its reduced expression in developing B lymphocytes, whereas in macrophages, PU.1 was able to accumulate stably because of a lengthening of the cell cycle. Exogenous expression of PU.1 in progenitors supported cell cycle lengthening and macrophage differentiation, and mathematical modeling suggested that such a feedback loop could maintain a slow-dividing macrophage developmental state.

Preparing for Disasters

DISASTERS ARE INEVITABLE AND CAN STRIKE ANYWHERE AT ANY TIME. WHETHER IT'S A NATURAL event (such as a hurricane, flood, or earthquake), a disease pandemic, or a purposeful or accidental human action (such as an act of terrorism or fire), the consequences can be wide-ranging and devastating. Scientifically trained personnel often play vital roles in emergency response and recovery efforts. Under the right circumstances, they can mobilize research to better understand the nature of the event and how best to respond to similar events in the future. But the scientific community also needs to plan carefully for disaster preparedness and mitigation for its own infrastructure and resources.*

Disasters can produce long-term setbacks for science when they affect research facilities, as was the case when Hurricane Sandy struck the U.S. East Coast in 2012; when the 2011 earthquake, tsunami, and nuclear plant explosions happened in Japan; when the 2010 earthquake hit Haiti; or when Hurricane Katrina flooded New Orleans in 2005. In addition to damaging expensive research buildings and equipment, such disasters can wipe out experimental records, samples, voucher specimens, and unique laboratory animals that may have taken years or even decades to develop. Researchers and lab support staff may be confronted with the difficult choice of risking their own lives to save valuable experiments and equipment on which their careers depend. No amount of insurance coverage can compensate for the time lost to duplicate the interrupted work or the loss of valuable and shareable scientific resources. Furthermore, the population in the surrounding area can be placed in harm's way if toxic or dangerous chemicals or biological agents are inadvertently released or left unprotected.

One example of a scheme for disaster planning and response is the U.S. Department of the Interior's (DOI's) Strategic Sciences Group (SSG).† First deployed during the 2010 Deepwater Horizon oil spill and more recently for Hurricane Sandy, the team's methodology has been codified into DOI operations to prepare for and respond to disasters of all sorts and could be extended to include a research institution's own disaster preparedness planning. At the core of the SSG's activities is scenario development: What are the cascades of consequences that might occur as the disaster unfolds, with approximate probabilities of those chains of events? What interventions could be mobilized to prevent the most damaging effects? With this type of strategy, a lab could plan for the most likely disasters and for rare events with large impacts. This approach also facilitates deciding how to invest in disaster mitigation. Interventions that both prevent losses when frequent events happen and short-circuit the after-effects of rare but severe occurrences would clearly be prioritized over interventions that would only mitigate damages from a rare event.

A consideration in any incident response plan should be whether and how best to mobilize research efforts that can help increase understanding of both the nature of the event and its outcomes, and to determine how well crisis response efforts have worked. These analyses are essential for improving future emergency preparedness, response, and recovery. There are many reports of cases where vital data have been lost when governmental and local institutions have been poorly prepared to enable timely, well-designed, and effectively executed studies in the midst of, and after, an emergency.‡

The number of multibillion-dollar disasters is on the rise, and no part of the globe is out of the reach of one sort of disaster or another. The recent disasters and their consequences should be a signal that every research institution and its constituent laboratories should begin discussions, if they haven't already, on how to prepare for the worst, as the worst clearly can happen.

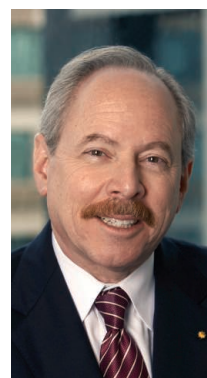
— Marcia McNutt and Alan Leshner

10.1126/science.1244097

*See the special series "Global Quake Risk" at www.sciencemag.org/extra/quakerisk. †G. E. Machlis, M. K. McNutt, *Science* **329**, 1018 (2010). ‡N. Lurie, T. Manolio, A. P. Patterson, F. Collins, T. Frieden, *N. Engl. J. Med.* **368**, 1251 (2013).



Marcia McNutt is Editor-in-Chief of *Science*.



Alan Leshner is Chief Executive Officer of AAAS and Executive Publisher of *Science*.



CHEMISTRY

Carbenes in Their Natural Habitat

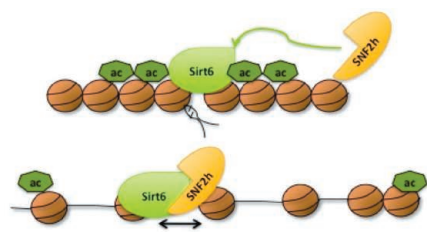
Over 50 years ago, Ronald Breslow suggested that thiamin may adopt a short-lived reactive carbene structure—with a divalent carbon center stabilized by flanking sulfur and nitrogen—during the enzymatic reaction cycle of vitamin B1. In the interim time, chemists have synthesized a huge range of stabilized cyclic carbenes, most of which are derived from imidazole (with two flanking nitrogens) rather than thiazole frameworks. These N-heterocyclic carbenes, or NHCs, are frequently stable and possible to isolate and have been applied as ligands in transition-metal catalysts. They are also versatile catalysts in their own right. Nonetheless, the question of whether thiamin itself reacts as a catalytic carbene in native context has remained open. Meyer *et al.* present a high-resolution (1.06 Å) crystal structure of pyruvate oxidase with bound phosphate (an unreactive analog of the pyruvate substrate), and the associated thiamin molecule shows clear evidence of carbene character. The carbon center in question appears to be deprotonated while lacking the excess electron density indicative of a carbanion. — JSY

Nat. Chem. Biol. **9**, 488 (2013).

MOLECULAR BIOLOGY

Open to Repair

The information stored in DNA underpins almost all life. It is therefore not surprising that there are multiple systems for rapidly sensing and repairing damage to genomic DNA within cells. The repair systems in eukaryotic cells have necessarily had to evolve to be able to correct such damage in the context of the chromatin proteins—principally histones—that compact DNA in the nucleus. Toiber *et al.* have studied the role of the SIRT6



histone deacetylase in the response of mammalian tissue culture cells to double-strand breaks in DNA. They find that SIRT6, which can bind to chromatin, interacts with the histone remodeling protein SNF2H and recruits it to sites of double-strand DNA breaks. The dual abilities of SIRT6 to deacetylate histone H3 at lysine 56 and to recruit SNF2H are necessary for DNA repair to occur and provide further evidence that remodeling chromatin to allow access by the repair machinery is critical for an effective DNA damage response. Both proteins act in the same DNA repair path-

way, and their interaction shows tissue specificity, in the pancreas and brain, possibly consistent with the role of SIRT6 in brain function. — GR

Mol. Cell **51**, 10.1016/j.molcel.2013.06.018 (2013).

MATERIALS SCIENCE

Nanoparticle Transformers

On the nanometer scale, small metal nanoparticles behave neither like atoms nor a bulk material, and hence their properties can be tuned by changing the sizes of the particles, which makes them of broad research interest. When used for catalytic purposes, they are often placed onto a supporting substrate, and both it and the presence of adsorbed atoms may further alter the nanoparticle properties. Li *et al.* studied the structure of platinum nanoparticles in the size range of 0.6 to 5 nm by using a combination of transmission electron microscopy, x-ray absorption fine-structure spectroscopy, and first-principles calculations. In studying over 3000 nanoparticles, they were able to distinguish between noncrystalline and crystalline ones. They found that there was not a single size that marked the transition between the two. Rather, the transition was a statistical one, with the potential for both ordered and disordered particles of a certain size to coexist. The coexistence size region was found to be dependent on the nature of the substrate and the amount of H₂ adsorbed. The authors believe that this effect is general for late 5d transition metals. — MSL

J. Am. Chem. Soc. 10.1021/ja405497p (2013).

IMMUNOLOGY

Reining in Responses

In response to infections, dendritic cells acquire microbial antigens and present them to T cells, and this leads to the induction of adaptive immunity. Although the dendritic–T cell interaction is essential to turn on the innate immune response, this interaction must also be turned off (or at least turned down) so as to avoid an overly aggressive response, as is observed in allergy and chronic inflammatory diseases. Carrera Silva *et al.* describe one such off switch that operates in mice and humans. Upon engagement of antigen-laden dendritic cells, T cells increased the expression of protein S (Pros1), which is a ligand for TAM-family receptor tyrosine kinases, which are expressed by dendritic cells. Conditional deletion of Pros1 in T cells in mice demonstrated that Pros1 was essential to keep dendritic cell activation in check, and the dendritic cells in these mice expressed more cytokines and activation markers. The loss of Pros1 on T cells in mice also led to worsened colitis and enhanced T cell–mediated immunity *in vivo*. Pros1 expressed on T cells did signal through TAM receptors; the deletion of TAM receptors in dendritic cells phenocopied mice with a T cell–specific deletion of Pros1. A similar expression and function of Pros1 were seen in human T cells, suggesting that this negative regulatory mechanism is evolutionarily conserved. — KLM

Immunity **39**, 160 (2013).

**1200 New York Avenue, NW
Washington, DC 20005**
Editorial: 202-326-6550, FAX 202-289-7562
News: 202-326-6591, FAX 202-371-9227
**Bateman House, 82-88 Hills Road
Cambridge, UK CB2 1LQ**
+44 (0) 1223 326500, FAX +44 (0) 1223 326501

SUBSCRIPTION SERVICES For change of address, missing issues, new orders and renewals, and payment questions: 866-434-AAAS (2227) or 202-326-6417, FAX 202-842-1065. Mailing addresses: AAAS, P.O. Box 96178, Washington, DC 20090-6178 or AAAS Member Services, 1200 New York Avenue, NW, Washington, DC 20005

INSTITUTIONAL SITE LICENSES please call 202-326-6755 for any questions or information

REPRINTS: Author Inquiries 800-635-7181
Commercial Inquiries 803-359-4578

PERMISSIONS 202-326-6765, permissions@aaas.org

MEMBER BENEFITS AAAS Travels: Bethchart Expeditions 800-252-4910; Apple Store www.store.apple.com/us/go/epstore/aaas; NASA Federal, 1-888-NASA-FCU (1-888-627-2328) or www.nasafcu.com; Cold Spring Harbor Laboratory Press Publications www.cshlpress.com/affiliates/aaas.htm; GEICO Auto Insurance www.geico.com/landingpage/go51.htm?logo=17624; Hertz 800-654-2200 CDP#343457; Office Depot <https://bsd.officedepot.com/portalLogin.do>; Seabury & Smith Life Insurance 800-424-9883; Subaru VIP Program 202-326-6417; VIP Moving Services www.vipmymover.com/domestic/index.html; Other Benefits: AAAS Member Services 202-326-6417 or www.aaasmember.org.

science_editors@aaas.org (for general editorial queries)
science_letters@aaas.org (for queries about letters)
science_reviews@aaas.org (for returning manuscript reviews)
science_bookrevs@aaas.org (for book review queries)

Published by the American Association for the Advancement of Science (AAAS), *Science* serves its readers as a forum for the presentation and discussion of important issues related to the advancement of science, including the presentation of minority or conflicting points of view, rather than by publishing only material on which a consensus has been reached. Accordingly, all articles published in *Science*—including editorials, news and comment, and book reviews—are signed and reflect the individual views of the authors and not official points of view adopted by AAAS or the institutions with which the authors are affiliated.

AAAS was founded in 1848 and incorporated in 1874. Its mission is to advance science, engineering, and innovation throughout the world for the benefit of all people. The goals of the association are to: enhance communication among scientists, engineers, and the public; promote and defend the integrity of science and its use; strengthen support for the science and technology enterprise; provide a voice for science on societal issues; promote the responsible use of science in public policy; strengthen and diversify the science and technology workforce; foster education in science and technology for everyone; increase public engagement with science and technology; and advance international cooperation in science.

INFORMATION FOR AUTHORS

See pages 716 and 717 of the 8 February 2013 issue or [access www.sciencemag.org/about/authors](http://www.sciencemag.org/about/authors)

EXECUTIVE EDITOR **Marcia McNutt**
EXECUTIVE EDITOR **Monica M. Bradford**
EXECUTIVE EDITOR **Tim Appenzeller**

MANAGING EDITOR, RESEARCH JOURNALS **Katrina L. Kelnar**
DEPUTY EDITORS **Barbara R. Jasny, Andrew M. Sugden, Valda J. Vinson**

EDITORIAL SENIOR EDITORS/COMMENTARY Lisa D. Chong, Brad Wible; **SENIOR EDITORS** Gilbert J. Chin, Pamela J. Hines, Paula A. Kiberstis (Boston), Marc S. Lavine (Toronto), Beverly A. Purnell, L. Bryan Ray, Guy Riddihough, H. Jesse Smith, Phillip D. Szuroimi (Tennessee), Jake S. Yeston, Laura M. Zahn (San Diego); **ASSOCIATE EDITORS** Melissa R. McCartney (Education Projects), Kristen L. Mueller, Jelena Stajic, Sacha Vignieri (Oregon), Nicholas S. Wigginton (Michigan); **BOOK REVIEW EDITOR** Sherman J. Suter; **ASSOCIATE LETTERS EDITOR** Jennifer Sills; **EDITORIAL MANAGER** Cara Tate; **SENIOR COPY EDITORS** Jeffrey E. Cook, Cynthia Howe, Harry Jacq, Lauren Kmeck, Barbara P. Ordway, Trista Wagoner; **COPY EDITOR** Chris Filiatreau; **SENIOR EDITORIAL COORDINATORS** Carolyn Kyle, Beverly Shields; **EDITORIAL COORDINATORS** Ramatoulaye Diop, Joi S. Granger, Lisa Johnson, Anita Wynn; **PUBLICATIONS ASSISTANTS**, Aneera Dobbins, Jeffrey Hearn, Dora Mathieu, Le-Tanya Mayne-Field, Shannon McMahon, Scott Miller, Jerry Richardson, Teresa R. Sakon, Brian White; **EDITORIAL ASSISTANT** Patricia M. Moore; **EXECUTIVE ASSISTANT** Alison Crawford; **ADMINISTRATIVE SUPPORT** Maryrose Madrid

EDITORIAL DIRECTOR, WEB AND NEW MEDIA Stewart Wills; **SENIOR WEB EDITOR** Sarah Crespi; **WEB DEVELOPMENT MANAGER** Martyn Green; **WEB DEVELOPER** Corinna Chou; **INTERNS** Kristine Hamilton, Linda Poon

NEWS DEPUTY NEWS EDITORS Robert Coontz, Elizabeth Colotta, David Grimm (Online), Eliot Marshall, Jeffrey Mervis, Leslie Roberts, Richard Stone, John Travis; **CONTRIBUTING EDITOR** Polly Shulman; **NEWS WRITERS** Yuhjiht Bhattacharjee, Adrian Cho, Jennifer Couzin-Frankel, Carolyn Gradling, Jocelyn Kaiser, Richard A. Kerr, David Malakoff, Elizabeth Pennisi, Robert F. Service (Pacific NW), Erik Stokstad, Emily Underwood; **WEB DEVELOPER** Daniel Berger; **SOCIAL MEDIA STRATEGIST** Meghna Sachdev; **INTERNS** Kelly Servick, Nisha Giridharan, Senah Yeboah-Sampong, Rachel Walther; **CONTRIBUTING CORRESPONDENTS** John Bohannon, Jon Cohen (San Diego, CA), Ann Gibbons, Sam Kean, Eli Kintisch, Andrew Lawler, Mitch Leslie, Charles C. Mann, Virginia Morell; **COPY EDITOR** Kara Estelle; **ADMINISTRATIVE SUPPORT** Scherraine Mack; **BUREAU** San Diego, CA: 760-942-3252, FAX 760-942-4979; Pacific Northwest: 503-963-1940

PRODUCTION DIRECTOR Wendy K. Shank; **ASSISTANT MANAGER** Rebecca Doshi; **SENIOR SPECIALISTS** Steve Forrester, Anthony Rosen; **PREFLIGHT DIRECTOR** David M. Tompkins; **MANAGER** Marcus Spiegler; **SPECIALISTS** Jason Hillman, Tara Kelly

ART DIRECTOR Yael Fitzpatrick; **ASSOCIATE ART DIRECTOR** Laura Creveling; **SENIOR ILLUSTRATORS** Chris Bickel, Katharine Sutcliffe; **ILLUSTRATORS** Valerie Altounian; **SENIOR ART ASSOCIATES** Holly Bishop, Preston Huey; **ART ASSOCIATES** Kay Engman, Garvin Grullón, Chrystal Smith; **PHOTO EDITOR** Leslie Blizard

SCIENCE INTERNATIONAL

EUROPE (science@science-int.co.uk) **EDITORIAL: INTERNATIONAL MANAGING EDITOR** Andrew M. Sugden; **SENIOR EDITOR/COMMENTARY** Julia Fahrenkamp-Uppenbrink; **SENIOR EDITORS** Caroline Ash, Stella M. Hurtle, Ian S. Osborne, Peter Stern; **ASSOCIATE EDITOR** Maria Cruz; **CONTRIBUTING EDITOR** Helen Pickersgill; **EDITORIAL SUPPORT** Rachel Roberts, Alice Whaley; **ADMINISTRATIVE SUPPORT** Alex Brown, Janet Clements, Joan Cuthbert; **NEWS: DEPUTY NEWS EDITOR**, U.K. Daniel Cley; **CONTRIBUTING EDITOR**, Europe Martin Enserink; **CONTRIBUTING CORRESPONDENTS** Michael Balter (Paris), Kai Kupferschmidt (Berlin), Gretchen Vogel (Berlin)

ASIA Japan Office: Asca Corporation, Tomoko Furusawa, Rustic Bldg. 7F, 77 Tenjin-cho, Shinjuku-ku, Tokyo 162-0808, Japan; +81 3 6802 4616, FAX +81 3 6802 4615, inquiry@sciencemag.jp; **CONTRIBUTING EDITOR**, ASIA Mara Hvistendahl [China: mhvisten@aaas.org]; **CONTRIBUTING CORRESPONDENTS** Dennis Normile [Japan: dnornile@gol.com]; Christina Larson [China: christina.larson@gmail.com]; Hao Xin [China: cindyhao@gmail.com]; Pallava Bagla [South Asia: pallava.bagla@gmail.com]

LATIN AMERICA CONTRIBUTING CORRESPONDENT Lizzie Wade [Mexico City: lizziewade@outlook.com]

EXECUTIVE PUBLISHER **Alan I. Leshner**
PUBLISHER **Beth Rosner**

FULFILLMENT SYSTEMS AND OPERATIONS (memberships@aaas.org); **CUSTOMER SERVICE SUPERVISOR** Pat Butler; **SPECIALISTS** LaToya Casteel, Michelle Oforidire, April Marshall; **MANAGER**, DATA ENTRY Mickie Napoleoni; **DATA ENTRY SPECIALISTS** JJ Regan, Jaimee Wise, Fiona Giblin

BUSINESS OPERATIONS AND ADMINISTRATION Director Deborah Rivera-Wienhold; **BUSINESS SYSTEMS AND FINANCIAL ANALYSIS** Director Randy Yi; **MANAGER OF FULFILLMENT SYSTEMS** Neal Hawkins; **SYSTEMS ANALYST** Nicole Mehmedovich; **MANAGER, BUSINESS ANALYSIS** Eric Knott; **MANAGER, BUSINESS OPERATIONS** Jessica Tierney; **BUSINESS ANALYSTS** Cory Lipman, Cooper Tilton, Celeste Troxler; **FINANCIAL ANALYST** Jeremy Clay; **RIGHTS AND PERMISSIONS:** **ASSISTANT DIRECTOR** Emilie David; **ASSOCIATE** Elizabeth Sandler; **MARKETING DIRECTOR** Ian King; **MARKETING MANAGERS** Alison Chandler, Julianne Wielga, Justin Sawyers; **MARKETING ASSOCIATES** Mary Ellen Crowley, Elizabeth Sattler, Rebecca Rifkin; **SENIOR MARKETING EXECUTIVE** Jennifer Reeves; **DIRECTOR, SITE LICENSING** Tom Ryan; **DIRECTOR, CORPORATE RELATIONS** Eileen Bernadette Moran; **SENIOR PUBLISHER RELATIONS SPECIALIST** Kiki Forsythe; **PUBLISHER RELATIONS MANAGER** Catherine Holland; **PUBLISHER RELATIONS, EASTERN REGION** Keith Layson; **PUBLISHER RELATIONS, WESTERN REGION** Ryan Rexroth; **CUSTOMER RELATIONS MANAGER** Iquo Edim; **CUSTOMER RELATIONS ANALYSTS** Simon Chong, Lana Guz; **ASSOCIATE DIRECTOR, MARKETING** Christina Schlecht; **MARKETING ASSOCIATES** Paulina Cotto, Mitchell Edmund; **ELECTRONIC MEDIA** Director Elizabeth Harman; **ASSISTANT MANAGER** Lisa Stanford; **PRODUCTION SPECIALISTS** Antoinette Hodal, Nichele Johnston, Lori Murphy, Kimberly Oster; **WEB AND NEW MEDIA:** **SENIOR PROJECT MANAGER** Trista Smith, **PROJECT LEADER** Luke Johnson **COMPUTER SPECIALISTS** Walter Jones, Kai Zhang, **WEB DEVELOPER** Chris Coleman; **PROGRAM DIRECTOR**, AAAS MEMBER CENTRAL Peggy Mihelich

DIRECTOR, GLOBAL COLLABORATION, CUSTOM PUBLICATIONS, ADVERTISING Bill Moran
EDITOR, CUSTOM PUBLISHING Sean Sanders: 202-326-6430

ASSISTANT EDITOR, CUSTOM PUBLISHING Tianna Hicklin 202-326-6463

SPONSORED CONTENT SPECIALIST Candice Nulsen 202-256-1528

ASSOCIATE DIRECTOR, COLLABORATION, CUSTOM PUBLICATIONS/CHINA/TAIWAN/KOREA/ SINGAPORE Ruolei Wu +86-1367-101-5294

PRODUCT (science_advertising@aaas.org); **MIDWEST** Rick Bongiovanni: 330-405-7080, FAX 330-405-7081; **EAST COAST/E. CANADA** Laurie Faraday: 508-747-9395, FAX 617-507-8189; **WEST COAST/W. CANADA** Lynne Stickrod: 415-931-7822, FAX 415-520-6940; **UK EUROPE/ASIA** Roger Gonçalves: TEL/ FAX +41 43 243 1358; **JAPAN**, Makiko Hara: +81 (0) 3 6802 4616, FAX +81 (0) 3 6802 4615; ads@sciencemag.jp; **CHINA/TAIWAN** Ruolei Wu: +86 1367 1015 294 www.aaas.org

WORLDWIDE ASSOCIATE DIRECTOR OF SCIENCE CAREERS Tracy Holmes: +44 (0) 1223 326525, FAX +44 (0) 1223 326532

CLASSIFIED (advertise@sciencereaders.org); **U.S./CANADA/SOUTH AMERICA** Tina Burks: 202-326-6577; **U.S. CORPORATE** Candice Nulsen 202-256-1528; **SALES ADMINISTRATOR** Marci Gallun; **EUROPE/ROW** sales Axel Gesatzki; **SALES ASSISTANT** Kelly Grace; **JAPAN** Yuri Kobayashi +81 (0)90-9110-1719; careers@sciencemag.jp; **CHINA/TAIWAN** Ruolei Wu: +86 1367 1015 294 www.aaas.org; **ADVERTISING SUPPORT MANAGER** Karen Foote: 202-326-6740; **ADVERTISING PRODUCTION OPERATIONS MANAGER** Deborah Tompkins; **SENIOR PRODUCTION SPECIALIST/GRAPHIC DESIGNER** Amy Hardcastle; **PRODUCTION SPECIALIST** Yuse Lajimimuh; **SENIOR TRAFFIC ASSOCIATE** Christine Hall; **SALES COORDINATOR** Shirley Young; **MARKETING MANAGER** Allison Pritchard; **MARKETING ASSOCIATE** Aimee Aponte

AAAS BOARD OF DIRECTORS RETIRING PRESIDENT, chair William H. Press; **PRESIDENT** Phillip A. Sharp; **PRESIDENT-ELECT** Gerald R. Fink; **TREASURER** David Evans Shaw; **CHIEF EXECUTIVE OFFICER** Alan I. Leshner; **BOARD** Bonnie L. Bassler, May R. Berenbaum, Claire M. Fraser, Elizabeth Loftus, Stephen L. Mayo, Raymond Orbach, Sue V. Rosser, Inder M. Verma



ADVANCING SCIENCE. SERVING SOCIETY

SENIOR EDITORIAL BOARD

A. Paul Alivisatos, Lawrence Berkeley Nat'l. Laboratory
Ernst Fehr, Univ. of Zurich
Michael S. Turner, University of Chicago

BOARD OF REVIEWING EDITORS

Adriano Aguzzi, Univ. Hospital Zürich
Takuzo Aida, Univ. of Tokyo
Leslie Aiello, Werner-Gren Foundation
Sonia Altizer, Univ. of Georgia
Virginia Armbrust, Univ. of Washington
Sebastian Amigorena, Institut Curie
Kathryn Anderson, Memorial Sloan-Kettering Cancer Center
Siv G. E. Andersson, Uppsala Univ.
Peter Andolfatto, Princeton Univ.
Meinrat O. Andreae, Max Planck Inst., Mainz
Paola Ariotta, Harvard Univ.
Johan Auwerx, EPFL
David Auschalom, Univ. of California Santa Barbara
Ben Barres, Stanford Medical School
Jordi Bascompte, Estación Biológica de Doñana, CSIC
Facundo Batista, London Research Inst.
Ray H. Baughman, Univ. of Texas, Dallas
David Baum, Univ. of Wisconsin
Mark Bear, Massachusetts Inst. of Technology
Yasmine Belkaid, NIAID, NIH
Philip Benfey, Duke Univ.
Stephen J. Benkovic, Penn State Univ.
Christopher Bernard, Aix-Marseille Univ.
Gregory C. Beroza, Stanford Univ.
Gabriele Bergers, Univ. of California, San Francisco
Peer Bork, EMBL
Bernard Bourdon, Ecole Normale Supérieure de Lyon
Chris Bowler, Ecole Normale Supérieure
Ian Boyd, Univ. of St. Andrews
Christian Büchel, Universitätsklinikum Hamburg-Eppendorf
Joseph A. Burns, Cornell Univ.
William P. Butz, Population Reference Bureau
Gyorgy Buzsáki, New York Univ., School of Medicine
Mats Carlsson, Univ. of Oslo
David Clapham, Children's Hospital, Boston
David Clary, Univ. of Oxford
Jonathan D. Cohen, Princeton Univ.
Robert Cook-Deegan, Duke Univ.
James Collins, Boston Univ.
Alan Cowman, Walter & Eliza Hall Inst.
Robert H. Crabtree, Yale Univ.
Wolfgang Crames, Mediterranean Inst. of Biodiversity and Ecology
Janet Currie, Princeton Univ.
Jeff L. Dangl, Univ. of North Carolina
Tom Daniel, Univ. of Washington
Frans de Waal, Emory Univ.
Stanislas Dehaene, Collège de France
Robert Desimone, MIT

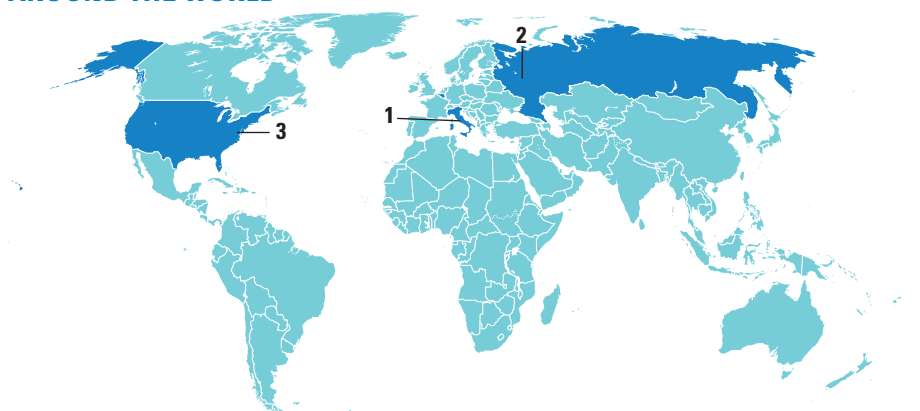
Claude Desplan, New York Univ.
Ap Dijksterhuis, Radboud Univ. of Nijmegen
Dennis Discher, Univ. of Pennsylvania
Gerald W. Dorn II, Washington Univ. School of Medicine
Jennifer A. Doudna, Univ. of California, Berkeley
Bruce Dunn, Univ. of California, Los Angeles
Christopher Dye, WHO
Todd Ehlers, University of Tuebingen
David Ehrhardt, Carnegie Inst. of Washington
Tim Elston, Univ. of North Carolina at Chapel Hill
Gerhard Ertl, Fritz-Haber-Institut, Berlin
Barry Everitt, Univ. of Cambridge
Paul G. Falkowski, Rutgers Univ.
Ernst Fehr, Univ. of Zurich
Tom Fenchel, Univ. of Copenhagen
Michael Feuer, The George Washington Univ.
Alain Fischer, INSERM
Susan Fiske, Princeton Univ.
Anne C. Ferguson-Smith, Univ. of Cambridge
Peter Fratzl, Max Planck Inst.
Elaine Fuchs, Rockefeller Univ.
Wulfram Gerstner, EPFL Lausanne
Daniel Geschwind, UCLA
Andrew Gewirth, Univ. of Illinois
Karl-Heinz Glassmeier, TU Braunschweig
Julia R. Greer, Coltech
Elizabeth Grove, Univ. of Chicago
Kip Guy, St. Jude's Children's Research Hospital
Takijika Ha, Univ. of Illinois at Urbana-Champaign
Christian Haass, Ludwig Maximilians Univ. of Munich
Steven Hahn, Fred Hutchinson Cancer Research Center
Gregory J. Hannon, Cold Spring Harbor Lab.
Martin Heimann, Max Planck Inst., Jena
Via Helariutta, Univ. of Finland
Isaac Held, NOAA
James A. Hendler, Rensselaer Polytechnic Inst.
Janet G. Hering, Swiss Fed. Inst. of Aquatic Science & Technology
Ray Hilborn, Univ. of Washington
Michael E. Himmel, National Renewable Energy Lab.
Kai-Uwe Hinrichs, Univ. of Bremen
Kei Hirose, Tokyo Inst. of Technology
David Hodell, Univ. of Cambridge
David Holden, Imperial College
Lora Hooper, UT Southwestern Medical Ctr at Dallas
Jeffrey A. Hubbell, EPFL Lausanne
Thomas Hudson, Ontario Inst. for Cancer Research
Raymond Huey, Univ. of Washington
Steven Jacobsen, Univ. of California, Los Angeles
Kai Johnsson, EPFL Lausanne
Peter Jonas, Inst. of Science & Technology (IST) Austria
Matt Kaebertlein, Univ. of Washington
William Kaelin Jr., Dana-Farber Cancer Inst.
Daniel Kahne, Harvard Univ.
Daniel Kammen, Univ. of California, Berkeley

Joel Kingsolver, Univ. of North Carolina at Chapel Hill
Robert Kingston, Harvard Medical School
Roberto Kolter, Harvard Medical School
Alberto R. Kornblith, Univ. of Buenos Aires
Leonid Kruglyak, Princeton Univ.
Thomas Lange, Univ. of Cologne
Mitchell A. Lazar, Univ. of Pennsylvania
David Lazer, Harvard Univ.
Virginia Lee, Univ. of Pennsylvania
Stanley Lemon, Univ. of North Carolina at Chapel Hill
Ottoline Leyser, Cambridge Univ.
Marcia C. Linn, Univ. of California, Berkeley
Jianguo Liu, Michigan State Univ.
Luis Liz-Marzan, CIC bioGUNE
Jonathan Losos, Harvard Univ.
Ke Lu, Chinese Acad. of Sciences
Christian Lüscher, Univ. of Geneva
Laura Machesky, CRUK Beatson Inst. for Cancer Research
Anne Magurran, Univ. of St. Andrews
Oscar Martin, CSIC & Univ. Miguel Hernández
Charles Marshall, Univ. of California, Berkeley
Chris Marshall, Inst. of Cancer Research
Martin M. Matzuk, Baylor College of Medicine
C. Robertson McClung, Dartmouth College
Graham Medley, Univ. of Warwick
Yasushi Miyashita, Univ. of Tokyo
Richard Morris, Univ. of Edinburgh
Edward Moser, Norwegian Univ. of Science and Technology
Sean Munro, MRC Lab. of Molecular Biology
Thomas Murray, The Helmholtz Center
Naoto Nagao, Univ. of Tokyo
James Nelson, Stanford Univ. School of Med.
Daniel Neumark, Univ. of California, Berkeley
Stuart Newman, New York Medical College
Timothy W. Nilsen, Case Western Reserve Univ.
Pär Nordlund, Karolinska Inst.
Helga Nowotny, European Research Advisory Board
Luke O'Neill, Trinity College, Dublin
Ben Olken, MIT
M. Plüsch, Olg. Princeton Univ.
Ole Olsen, Univ. of California, Berkeley & Lawrence Berkeley National Lab
Harry Orr, Univ. of Minnesota
Andrew Oswald, Univ. of Warwick
Steve Palumbi, Stanford Univ.
Daniel R. Paul, Univ. of Texas at Austin
David Pearson, Univ. of California, Berkeley
John H. J. Petri, Memorial Sloan-Kettering Cancer Center
Simon Philpott, Univ. of Florida
Joshua Plotkin, Univ. of Pennsylvania
Philippe Poulin, CNRS
Colin Renfrew, Univ. of Cambridge
Trevor Robbins, Univ. of Cambridge
Jim Roberts, Fred Hutchinson Cancer Research Ctr.

BOOK REVIEW BOARD

John Aldrich, Duke Univ.
David Bloom, Harvard Univ.
Angela Creager, Princeton Univ.
Richard Sweder, Univ. of Chicago
Ed Wasserman, DuPont
Lewis Wolpert, Univ. College London

AROUND THE WORLD



Rome 1

Animal Research Limits Stun Scientists

The Italian Parliament approved a bill on 31 July that puts drastic limitations on animal testing. Scientists have warned that the provisions, voted by the Senate earlier this month, will severely hurt biomedical research in their country.

The bill is Italy's implementation of a European directive adopted in September 2010, but the Italian law goes far beyond the restrictions imposed by the directive.



Off limits. Activists win a victory in Italy: The Parliament approved a bill to limit animal testing.

The law bans breeding dogs, cats, and non-human primates for research purposes, or using them for any other purpose than health research; studies without pain killers or anesthesia, if the animal may experience pain (unless these are themselves the subject of the study); and using animals in studies of addiction, xenotransplantation, and for training purposes (except in higher education for veterinarians and physicians).

Scientists, who rallied around the country earlier this summer to defend their research, haven't yet given up hope that the measures will be canceled; the Italian government has

yet to sign off on the law and may refuse to do so. Ilaria Capua, a former avian influenza researcher who is now a member of Parliament, says that the government is committed to avoiding severe restrictions on animal research. <http://scim.ag/Italyanimals>

Moscow 2

Russian Physics Institutes Merger Draws Fire

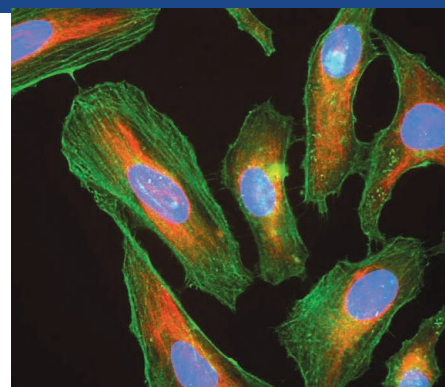
Physics research in Russia is on the cusp of a major transition. The government plans to consolidate several large scientific institutes into a single entity that proponents say will make it easier to fund major new facilities. Earlier this year, 15 institutes signed an agreement forging a partnership on megaclass research facilities. Then, just before elections to choose a new Russian Academy of Sciences (RAS) president in May, outgoing academy president Yuri Osipov and Kurchatov Institute Director Mikhail Kovalchuk wrote to Russian President Vladimir Putin asking him to transform the partnership into a separate body. Putin ordered the government to work out the legal framework for the new body by 1 September.

However, some physicists decry what they believe to be the latest government maneuver to undermine the embattled RAS, which is fighting for its identity as the government moves to strip it of control of its lucrative real estate assets. <http://scim.ag/Russiamerge>

Bethesda, Maryland 3

HeLa Genomes Back Online

Five months after it was yanked offline, the HeLa genome is again available for research. The U.S. National Institutes of Health (NIH) in Bethesda, Maryland, announced on



Famous cells. Henrietta Lacks's family is allowing HeLa genomes to be available to researchers.

7 August in *Nature* that the descendants of Henrietta—Lacks, the woman whose tissue was used—without her permission—to establish HeLa, the most widely used cancer cell line, gave the go-ahead to researchers to study its genetic sequence.

A team from the European Molecular Biology Laboratory in Heidelberg, Germany, published a HeLa genome sequence and an analysis of its content on 11 March, but took the data offline the same day in the face of harsh criticism for not getting permission from the Lacks family. NIH-funded researchers had also just sequenced a HeLa cell line, so the agency began negotiating with the family. "We have crafted a path that addresses the family's concerns, including consent and privacy," Francis Collins and Kathy Hudson, NIH director and a deputy director, respectively, write in *Nature*. Scientists must now apply for access to both teams' genomes (the second was published in *Nature* this week), and resulting papers must include an acknowledgment to Henrietta Lacks "and the continued generosity of her family." <http://scim.ag/HeLagenomes>

NEWSMAKERS

Handelsman Named to White House Post

On 31 July, Yale University microbiologist **Jo Handelsman** was nominated by President Barack Obama to be associate director for science at the White House Office of Science and Technology Policy (OSTP). If confirmed, she would succeed physicist Carl Wieman. <http://scim.ag/Handelsman>



Q: Why did you say yes?

J.H.: Because [OSTP Director] John Holdren



Setting Sail for Science

Last week, the Schmidt Ocean Institute's newly refitted *Falkor*—named for the heroic "Luck Dragon" of *The Neverending Story*—docked in San Francisco, California, for the first time. The institute, a nonprofit ocean research organization founded in 2009 by Google Chairman Eric Schmidt and wife Wendy, refitted the 32-year-old, 83-meter-long vessel to make it available to researchers to use for free for ocean exploration. Following extensive field trials, the ship began its scientific cruise program this year.

A little more than a week before the ship's appearance at the city's Exploratorium, officials from the U.S. National Oceanic and Atmospheric Administration met with scientists and technology companies such as Google and mapping software company Esri to discuss how public-private partnerships can further a national plan to map the United States' oceans, a plan in which *Falkor* will take a part.

asked me. Next to the president, he's one of my favoritest people. This is an opportunity to work at a pretty high level on a national agenda, with a team of people who are deeply committed to science.

Q: Carl focused on STEM education. Will you?

J.H.: John and the president see STEM education as a high priority. But the breadth of science not covered by the other directors at OSTP, including basic research across all fields, would certainly also be a large part of my portfolio.

Q: Will you be taking leave from Yale?

J.H.: Yep. I'll be taking 2 years' leave and planning to come back. I'm in the middle of my research career and I don't want to lose that.

Space Walker to Lead NOAA

The first American woman to walk in space has been tapped to become the head of the National Oceanic and Atmospheric Administration (NOAA). President Barack Obama on 1 August nominated **Kathryn Sullivan**,



Sullivan

now NOAA's acting administrator, to fill the post vacated in February by marine scientist Jane Lubchenco.

Outsiders like the pick. "She will enjoy respect and strong support from the academic and commercial sectors," predicts Tom Bogdan, president of the University Corporation for Atmospheric Research in Boulder, Colorado. A geologist, Sullivan, 61, is best known for being one of the first six women selected by NASA for astronaut training in 1978. She flew on three shuttle missions. This will be her second stint at NOAA; she served as the agency's chief scientist from 1993 to 1996.

FINDINGS

Just a Cup for Pregnant Moms?

Moderate caffeine consumption—one to two cups a day—doesn't promote premature births or miscarriages or harm fetal

THEY SAID IT

"Projects cannot offer genetically modified organisms as a reward."

—Crowd-funding website Kickstarter stating a policy change, effective 31 July, on the heels of a successful fundraiser to genetically engineer glowing plants for home lighting. The pitch offered the plants' seeds as rewards to online backers.

growth, according to a 2010 review. But a new study in mice suggests that at larger doses, caffeine can impair memory.

Caffeine can block the activity of adenosine, a neurotransmitter that acts as a brake on neuronal firing and makes us sleepy. Carla Silva, a neuroscientist at the



Buzzkill. A new study in mice suggests that caffeine could influence fetal brain development.

University of Coimbra in Portugal, used caffeine to study how adenosine affects fetal brain development. During mammals' development, GABA neurons, which help regulate the brain's flow of information, migrate to the hippocampus, key to memory and learning.

Silva and colleagues gave female mice caffeine-laced water—enough to mimic a human drinking three to four cups of coffee a day—prior to pregnancy, throughout pregnancy, and during nursing. Six days after birth, the drug-exposed pups had 41% fewer GABA neurons in the hippocampus, the team reports this week in *Science Translational Medicine*. The pups' GABA neuron numbers caught up a few months later, but they performed poorly on memory tests and were more susceptible to seizures. Still, the findings may not hold in humans, Silva says: "This study is not enough to give advice to pregnant women." <http://scim.ag/coffeepreg>



SCIENTIFIC COMMUNITY

Embezzlement Casts Harsh Light on China's Grant System

BEIJING—A highly decorated water researcher at one of China's leading academic institutions has been ensnared in an unfolding embezzlement scandal. Chen Yingxu, executive vice president of Zhejiang University's College of Environmental and Resource Sciences in Hangzhou, told graduate students to forge false receipts, invoices, and contracts in order to divert funds from hefty government research grants for his personal use, state media reports allege.

After a months-long investigation by China's National Audit Office and a closed-door hearing in March, a detailed report on the charges surfaced last week in *China Youth Daily*—igniting intense scrutiny in the Chinese media and blogosphere. If confirmed, the sum allegedly diverted—up to \$1.6 million, or 10% of a hefty water research grant—would make Chen's case a remarkably egregious example of grant malfeasance, says Qin Boqiang, an ecologist at the Nanjing Institute of Geography and Limnology of the Chinese Academy of Sciences (CAS). As a consequence, observers predict, the curtain will come down quickly on a laissez-faire era of grant management here. Chen's prosecution will have a “profound influence on China's research culture,” predicts Zhu Guangwei, a biochemist at the Nanjing institute.

Until the audit office took interest, Chen led a charmed career. After receiving a Ph.D.

from Zhejiang Agricultural University in 1990, he became a versatile researcher with a long list of publications on food security, environmental biochemistry, and water and soil pollution. A director of the China Society of Environmental Sciences, he received prestigious funding from the National Natural Science Foundation of China (NSFC) and from China's National Basic Research Program. His seat on the Chinese People's Political Consultative Conference, a high-powered network of political, business, and academic insiders appointed by the Communist Party to advise the central government, secured his status among the country's scientific elite.

Chen's fall from grace apparently started in 2008, after he was awarded a \$16 million grant from China's environment ministry to study water-pollution remediation and management in the Lake Tai (Taihu) watershed. In recent years, Tai, in eastern China, has become a poster child for environmental calamity, having suffered periodic pea-green algae blooms triggered by agricultural runoff and industrial effluents (*Science*, 2 September 2011, p. 1210). It's unlikely that improprieties in Chen's study hampered efforts to clean up the Tai watershed, which is slowly improving after local factories a few years ago were ordered to move their operations away from the lake, Zhu says.

Details of the case against Chen are

Skimming the green stuff. Embezzled funds were meant to probe how to clean up algae at Lake Tai.

murky. According to Chinese press reports, he steered large chunks of research money to two companies operated or owned by his graduate students, with the funds ending up in his pocket.

Chen's lawyer, Dai Menghua, has maintained to Chinese media that Chen's case emerged during a routine audit of Zhejiang University and that his client has returned the money. “From Chen Yingxu's perspective, this matter was resolved a long time ago,” Dai told *China Youth Daily*. “He doesn't know why it has turned into a criminal offense.” Reached by *Science*, Dai declined to comment. As *Science* went to press, Zhejiang University had not commented on the case, other than to confirm that Chen is the target of a probe.

Chen's alleged misdeeds have taken few Chinese researchers by surprise. The charges against him are the latest in a string of corruption stings launched in many spheres of society since Xi Jinping took over as China's president in March. And this is not the first high-profile case to roil the scientific community. Last year, Duan Zhenhao, a geophysical chemist here at CAS's Institute of Geology and Geophysics, was sentenced to 13 years in jail after a court convicted him of fraudulent use of grant money; his wife told the Chinese press he was lavishing research funds on a mistress. A rising chorus inside and outside of China's government has been calling for tighter controls on how research funds are managed.

Fiscal responsibility has become more challenging as China's R&D budget rises; the \$36 billion that the central government spent on science and technology last year was second only to the United States. Rapid budget growth has far outstripped the ability of research managers to properly oversee the money, says Cao Cong, an expert on Chinese science policy at the University of Nottingham in the United Kingdom. How grants are actually spent is a “black box,” he says. In early August, NSFC President Yang Wei publicly vowed that his agency would take greater initiative in reining in scientific misconduct in grant management and curbing “moral” hazard. The basic research agency has at least one skeleton in its closet: In 2004, NSFC accountant Bian Zhong was convicted for embezzling \$2 million.

Zhu, who did his doctorate work under Chen, notes that just a few years ago, when

Chen received the whopping \$16 million grant, supervision of how funding was spent was “not very serious” at most labs and universities. Many projects “[didn’t] use the money strictly according to the budget,” he says. It’s common for scientists to apply for funds for one purpose and then use them for a different one, though usually without criminal intent: Researchers

often fudge budget line items to pay stipends to graduate students, for instance, which would otherwise be forbidden under some grants.

Pillorying Chen could be a sign that the government is seeking to tighten the reins on research spending. Budget auditing has become more intense in the past couple of years, Zhu notes: Research institutions are

becoming “more and more strict.” But the ultimate solution to China’s woes may be a more transparent grant distribution and monitoring system, Cao says. Until then, the corruption scandal poisoning the waters around Lake Tai is unlikely to be the last mess in need of cleanup in China’s scientific community.

—CHRISTINA LARSON

With additional reporting by Ma Qionghui.

PALEOCLIMATOLOGY

How to Make a Great Ice Age, Again and Again and Again

For more than 30 years, climate researchers have been trying to figure out how slight changes in Earth’s orbit could drive the major climate events of the last million years: the great ice ages. The long-standing idea that a rhythmic stretching of Earth’s egg-shaped orbit around the sun every 100,000 years paces the growth and decay of continent-sized ice sheets has survived all challenges. But this orbital variation by itself is far too weak to actually drive the buildup and decay of the ice sheets.

Now, a group says that it has found an answer by building what many say is the best computer model of the ice ages yet. The researchers have confirmed that the 100,000-year cycle amplifies the influence of a second orbital cycle: the 23,000-year wobble of Earth’s spin axis. The new modeling also suggests that each time around, the sheer mass of the North American ice sheet doomed it to its distinctively abrupt end. “They’re getting the global [glacial] cycles pretty convincingly” in the new model, says climate researcher Shawn Marshall of the University of Calgary in Canada. “They’re getting lots of things that previous studies haven’t been able to capture before.”

As paleoclimate modeler Ayako Abe-Ouchi of the University of Tokyo and her colleagues reported in this week’s issue of *Nature*, they indirectly linked a full-blown global climate model of the sort used to forecast global warming with a reasonably complex model of the northern ice sheets. They drove the climate model with data on the changing distribution of sunlight around the globe that resulted from the orbital variations and with the swings in atmospheric carbon dioxide, a greenhouse gas, that were recorded in ice cores as the ice ages came and went. Then they fed snapshots of the changing climate into the ice sheet model.

When compared with the behavior of the

real ice sheets, the combined models performed well. The simulated ice sheets grew in the same places and at a similar pace as the real ones. Over tens of thousands of years, they slowly expanded to volumes as large as seen in the past. Then, roughly every 100,000 years, they collapsed in a matter of a few thousand years. “It’s doing it all on its own” without contrived climate forcings or grossly simplistic processes in

the model, says paleoclimatologist Maureen Raymo of the Lamont-Doherty Earth Observatory in Palisades, New York, an author on the *Nature* paper. More work needs to be done, Abe-Ouchi writes in an e-mail, but “of course I have a strong intuition and confidence that it was OK.”

The success of the model allowed Abe-Ouchi and her colleagues to point to two processes that they believe are key to a realistic glacial cycle. One is the interaction of the 23,000-year and 100,000-year cycles. For almost 100,000 years, they keep incoming solar energy low enough during the summer in northern high latitudes to let winter snows survive summer heating and pile up into ice sheets. But periodically, an increasing 100,000-year cycle combines with a rising 23,000-year cycle to give added summer warmth in high northern latitudes.

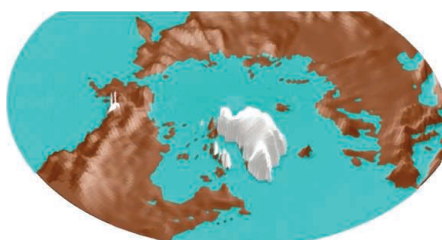
At that point the other key factor comes into play: the vast mass of the North American ice sheet, which spread from coast to coast and well south of Chicago. It reached so far south that, when the two orbital cycles conspired to warm northern summers, the ice began to melt back around its edges.

In the meantime, though, the ice sheet’s huge weight had pressed it a kilometer or more into the solid Earth. So it was melting back deeper and deeper into a hole, where the atmosphere gets warmer with depth. This warming feedback is the primary reason the model ice sheet melts away so rapidly, the authors say.

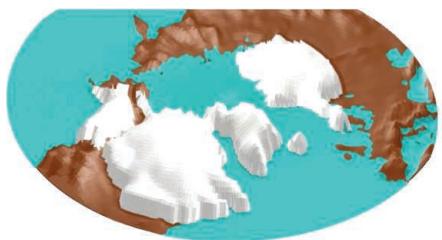
“This is the best so far, a really nice advance, because they’re using more comprehensive models,” says paleoclimate modeler David Pollard of Pennsylvania State University, University Park. The next step—a direct, interactive link between sophisticated climate and ice sheet models—must “wait for greater computer power to become available.”

—RICHARD A. KERR

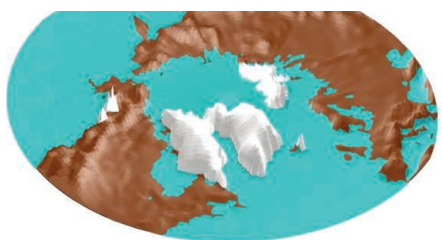
123,000 years before present



20,000 years before present



1000 years before present



About right. A model simulates slow ice-sheet growth from minimum (top) to maximum (middle) and a collapse (almost) back to minimum (bottom).

France Córdoba Brings Management Expertise to NSF

Opting for solid management skills over a soaring scientific vision, President Barack Obama last week nominated France Córdoba to succeed Subra Suresh as director of the National Science Foundation (NSF).

Córdoba, a 66-year-old astrophysicist, has led Purdue University and the University of California (UC), Riverside, and is now chair of the Board of Regents of the Smithsonian Institution. She got her start in Washington 20 years ago when NASA Administrator Dan Goldin asked her to make sure all NASA programs “were infused with science.”

The choice of Córdoba hands the job to someone much more likely to complete the NSF director’s 6-year term than a rising academic star such as Suresh. And it hints at a desire to return to a more consensual style of leadership within the \$7 billion agency and across the scientific community, which is applauding Obama’s choice. “I’m trying to think if there has ever been an NSF director with more impressive credentials,” says M. R. C. Greenwood, retiring president of the University of Hawaii and a top science official in the Clinton administration.

Suresh shook up NSF during his 29 months as director before leaving this spring to become president of Carnegie Mellon University. Arriving from the Massachusetts Institute of Technology, where he was dean of engineering, Suresh launched initiatives to foster innovative research, entrepreneurship, and international collaborations and tinkered with NSF’s organizational structure.

Those aggressive moves received mixed reviews from the scientific community, however. They also raised the hackles of Senator Barbara Mikulski (D-MD), chair of the Senate Appropriations Committee, who wants them scaled back in favor of bread-and-butter research programs.

Córdoba, who is expected to sail through Senate confirmation, says that she is prepared to deal with a daunting fiscal environment. “Every time I’ve had a leadership position there have been big budget concerns,” she told *Science* in an exclusive interview from her home in Santa Fe. “At Riverside, we had huge cuts from the state. At Purdue, we had to regroup after the global recession and do all

sorts of restructuring. Would I like to see the federal investment in research grow? Absolutely. ... But I’m not worried about navigating budget constraints. It’s part of every job.”

Córdoba will also be called upon to mend fences with Congress. This spring, Representative Lamar Smith (R-TX), who chairs the science committee of the House of Representatives, launched a surprise attack on NSF’s vaunted peer-review system. NSF also faces a congressional mandate to restrict funding for political science, part of an ongoing campaign by some congressional Republicans to halt NSF’s support for social science research.

Córdoba will be the second woman to lead NSF in its 63-year history, following micro-

oldest of 12 children], or as a Hispanic, then I think that’s a wonderful thing. Still, I’d also like to be a role model for anyone who wants to pursue a career in science.”

Colleagues say that Córdoba has been successful over the years by laying out a clear strategy and then getting others to buy into her plans. “France excels at setting a tone in which people feel appreciated, and not tolerating bad behavior,” says Anne Petersen, a developmental psychologist at the University of Michigan, Ann Arbor, who has known Córdoba since the two were at Pennsylvania State University, University Park, where Córdoba was chair of the astronomy department. Although several years removed from the bench, Córdoba designed an experiment

for the European Space Agency’s X-ray Multi-Mirror Mission that is still generating data 14 years after it was launched.

“She has an I-beam as a spine,” says Goldin, now CEO of The Intellisys Corp. in southern California, about Córdoba’s 3 years as chief scientist. “But she is able to lead by convincing people, not bullying them.”

Those qualities may help quiet some of the grumbling within NSF stemming from what was seen as Suresh’s top-down management style, including his decision to reassign several offices that reported directly to him. “She’s familiar with the bottom-up approach of a university, and I think she’ll listen to staff,” says Arden Bement, who preceded Suresh as NSF director and

who returned to Purdue as a faculty member in 2010. Bement, who recently retired, says that Córdoba earned the respect of students by addressing their concerns and won over faculty members by attracting top talent and raising the university’s international ranking.

Asked why she took a job that several prominent scientists had declined, Córdoba admits that she had some “qualms” before saying yes. “One has qualms when you get up in the morning or when you get into your car and there’s a storm brewing,” she laughs. “But this is a good time for me. I’ve had the chance to lead a couple of wonderful universities. I’ve had a chance to do some exciting research, and I’m at a point in my life where I can say yes to this opportunity.”

—JEFFREY MERVIS



NSF-bound. France Córdoba speaks at Purdue University in 2007 after being named its first female president.

biologist Rita Colwell, who was director from 1998 to 2004. And it will be the first time women have held both of NSF’s top jobs, as Córdoba teams with longtime NSF administrator Cora Marrett, now deputy director.

Breaking gender and ethnic barriers was never one of Córdoba’s goals. “It’s not something I think about,” she says. Nevertheless, Córdoba made a splash in 2007 when she became the first woman to lead Purdue, and also when she was chosen as UC Riverside’s first Latina chancellor in 2002. And she admits that her perspective has changed as she has gotten older.

“I’ve become more aware of myself as a role model,” she says. “And to the extent that people can see themselves in me—as a woman, as part of a large family [she’s the



AVIAN INFLUENZA

Critics Skeptical as Flu Scientists Argue for Controversial H7N9 Studies

Flu scientists are hoping to vaccinate themselves against another outbreak of a crippling controversy.

In a letter published this week by *Nature* and *Science* (see p. 612), 22 researchers make their case for launching potentially risky experiments with the H7N9 avian influenza virus, which emerged earlier this year in China and which some scientists fear could spark a deadly human pandemic. The scientists, who mostly work in U.S.-funded labs, also detail the safety and security precautions that they would take to prevent the possibly dangerous viruses they create from escaping from the lab—or falling into the hands of terrorists. In an accompanying online letter (<http://scim.ag/fluHHS>), officials from the U.S. Department of Health and Human Services (HHS) write that they will require extra review of especially problematic studies.

The communiqué, the authors say, is intended to head off the kind of global controversy that in 2011 engulfed researchers conducting experiments with another avian flu virus, H5N1, halting certain studies for more than a year (*Science*, 22 June 2012, p. 1494). Critics charged that those studies—which involved engineering new H5N1 strains able to move between mammals, and not just birds—carried risks that outweighed any benefits and had too little public oversight.

“With H5N1, we were criticized for not being transparent,” says virologist Ron Fouchier of Erasmus MC in Rotterdam, the Netherlands, one of the scientists at the center of the H5N1 storm and a lead author of the 7 August letter. “So this time we want to be sure the public understands what we want to do before we do it, why we need to do it, and how we are going to do it safely.”

The openness offensive isn’t quieting critics. “The scientific justification presented for doing this work is very flimsy, to put it mildly, and the claims that it will lead to anything useful are lightweight,” says Adel A. F. Mahmoud, an infectious disease specialist at Princeton University and the former president of Merck Vaccines. And the security precautions are “insufficient and amazingly lame,” says molecular biologist Richard Ebright of Rutgers University in Piscataway, New Jersey.

At issue are gain-of-function studies, in which researchers use several techniques to give viruses characteristics that they don’t have in nature, such as the ability to infect new species or transmit more easily through the air. Such studies are critical to understanding the sometimes subtle changes that can make a bird virus a pandemic threat, some scientists argue, and to developing better vaccines and surveillance. But others are skeptical and say that just because scientists can do the experiments doesn’t mean they should.

The dispute went public in late 2011, after Fouchier and virologist Yoshihiro Kawaoka of the University of Wisconsin, Madison, submitted papers on their mammal-transmissible H5N1 viruses to *Science* and *Nature*, respectively. A U.S. government panel, the National Science Advisory Board for Biosecurity (NSABB), recommended against publishing complete versions, for fear the details might provide a bioweapon blueprint. Ultimately, a divided NSABB supported full publication, but only after H5N1 researchers had declared a voluntary moratorium on gain-of-function studies and the U.S. government imposed new regulations.

The world can’t afford to repeat that

No gain? Critics say gain-of-function studies with the H7N9 bird flu virus wouldn’t help guide defense measures, such as culling chickens at markets in China.

uproar, the letter’s authors suggest. “[E]xperiments that may result in GOF [gain-of-function] are critical” to gauging H7N9 risks and preparing defenses, they write, and there is little time to lose. Although no new human H7N9 cases have appeared recently, the virus has killed 43 of the 134 people it is known to have infected; some researchers fear that it will reemerge this fall. There is no reliable vaccine. And this week, researchers reported in *BMJ* the first probable case of person-to-person transmission, between a father and his adult daughter; both died.

To attack these problems, researchers need to get moving on five lines of research, the authors write, including transmissibility and drug resistance studies. To reduce risks, they pledge to work only in “enhanced” biosafety level 3 (BSL 3+) labs and not to create superbugs by adding capabilities to viruses already able to resist drugs or evade immune defenses. To bolster their case, they suggest that the controversial H5N1 research has already paid off, because it helped identify worrisome mutations that “factored into” Chinese and global risk assessments of H7N9.

That last claim incenses some critics. Knowledge of those mutations was not necessary to recognize H7N9’s risk, Mahmoud argues. Nor was it “essential to containing the virus in China by closing poultry markets,” says virologist Simon Wain-Hobson of the Institut Pasteur in Paris. “The mutations guided nothing.” Moreover, gain-of-function studies are unlikely to predict whether H7N9—or any other virus—will actually become a pandemic virus, critics argue. “It’s laughable to claim that,” Mahmoud says. And Ebright argues that all such studies should be confined to more secure BSL-4 labs.

The debate will get specific as researchers submit proposals to the U.S. government, the most likely funder. (Other nations have shown less interest.) HHS says that a special panel will review proposals involving transmissibility. The process could be long; Fouchier says that U.S. officials are still reviewing requests he and Kawaoka made early this year to resume gain-of-function studies with H5N1. In the meantime, some prominent H7N9 researchers, including Chen Hualan, director of China’s National Avian Influenza Reference Laboratory in Harbin, say they have no plans to pursue such studies.

—DAVID MALAKOFF

FOOD SCIENCE

Lab Burger Adds Sizzle to Bid for Research Funds

LONDON—It looked like a cooking show, but a slightly surreal one; Martha Stewart with a twist of Mary Shelley. In what was billed as a “historic” event, Dutch stem cell researcher Mark Post presented his lab-grown hamburger to the world here on Monday—a beef patty assembled from thousands of small shreds of meat grown from bovine stem cells. British chef Richard McGeown fried the revolutionary burger with generous amounts of butter and oil, and two volunteers then tried it. “Close to meat, not that juicy,” was the verdict of one of them, Austrian food trend researcher Hanni Rützler.

The tightly orchestrated event, organized by PR company Ogilvy, aimed to convince the public and potential funders

have a paper to present. “It was not a science event; it was more something you would see during the introduction of a new product by a company,” says Henk Haagsman, a veterinary researcher at Utrecht University in the Netherlands who has collaborated with Post. Details need to be published so other scientists can repeat the work, Haagsman says.

Post’s method could greatly reduce animal suffering and shrink meat’s environmental footprint. Already, almost a third of the Earth’s land surface is dedicated to pasturing or raising feed for livestock, according to the U.N. Food and Agriculture Organization. Global meat consumption is only expected to rise, from 228 million tons in 2002 to almost

Van Eelen saw a piece of animal tissue that a cell biology professor was keeping alive. “As someone who had suffered starvation, I didn’t think about science but about food,” he says. Van Eelen dropped out of college but relentlessly lobbied the Dutch government to fund in vitro meat research. It paid off in 2004 with a €2 million grant for three projects, including Post’s.

When the money had run out 4 years later, Post tried to lure new donors by floating the idea of a proof of concept: a pork sausage made entirely in the lab. Google co-founder Sergey Brin bit, agreeing to sponsor the project under two conditions: The product

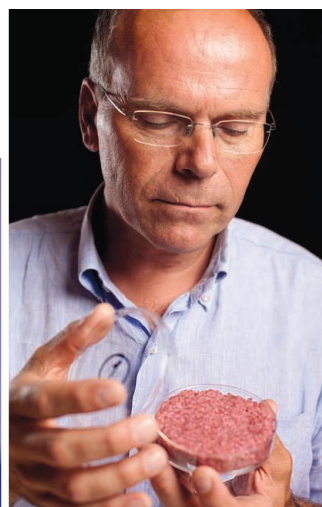
had to be beef, and it had to be a burger. (Post had said he had a wealthy benefactor, but Brin’s involvement remained a secret until Monday.)

Post hopes that his petri patty will attract the next round of funding. To make it, he used tissue taken from the shoulders of two cow carcasses at a slaughterhouse. He cut the tissue into small pieces and treated these with collagenase, an enzyme that helps break down connective tissue, to release the cells. When

he cultured the cell mixture, muscle cells soon died, but so-called satellite cells—stem cells that replenish dead muscle cells in the animal—started dividing. Satellite cells cannot replicate indefinitely, but Post says they can go through some 50 divisions—enough, on paper, to produce 20,000 tons of beef from one biopsy. Previous in vitro meat projects had great difficulty coaxing the cells to become muscle cells, but a mix of growth factors helped Post achieve a 70% to 80% success rate.

There are still plenty of obstacles. Because the muscle cells lack blood vessels to provide them with nutrients and oxygen, the shreds of meat begin to die if they grow more than 1 millimeter thick. The cell culture thrives only in fetal bovine serum, a growth medium made from the blood of slaughtered calves. Serum-free alternatives exist, but the ones that Post tried were disappointing. “Nine were not good, one was okay,” he says. Antibiotics were needed to keep bacteria from colonizing

What’s for lunch? British chef Richard McGeown cooked a beef patty grown by Mark Post (inset) in front of an audience of journalists.



that lab-grown meat is possible, if far from economically viable. (Producing the 140-gram burger had cost about €250,000.) It represented “a paradigm shift in the way animal protein can be produced,” says Nicholas Genovese of the University of Missouri, Columbia, who is studying in vitro meat with support from People for the Ethical Treatment of Animals.

For those hungry for scientific details, the show, attended by reporters from around the world, had little to offer. Post, a researcher at Maastricht University in the Netherlands, discussed a few technical advances, but didn’t

have a paper to present. “It was not a science event; it was more something you would see during the introduction of a new product by a company,” says Henk Haagsman, a veterinary researcher at Utrecht University in the Netherlands who has collaborated with Post. Details need to be published so other scientists can repeat the work, Haagsman says.

Post’s method could greatly reduce animal suffering and shrink meat’s environmental footprint. Already, almost a third of the Earth’s land surface is dedicated to pasturing or raising feed for livestock, according to the U.N. Food and Agriculture Organization. Global meat consumption is only expected to rise, from 228 million tons in 2002 to almost

SCIENTIFIC COMMUNITY

Grim Day for Turkish Science as Six Academics Get Long Prison Terms

the muscle tissue; growing the meat in a sterile environment and replacing humans with robots could solve that problem, Post says.

Then there is the problem of exercise. Muscles get bulky when they are used, but shreds of muscle in a dish don't exercise. Initially, Post tried stimulating the tissue mechanically or with electric shocks. Later, he found that placing two Velcro anchor points in the petri dish did the trick: The muscle cells spontaneously formed small fibers that stretch between the two points. But sometimes they pulled away from the Velcro, and at the press event, Post said that he now places a column of agarose gel in the middle of the dish and pipettes the cells around it. The muscle cells attach to each other, forming a doughnut-shaped piece of beef that contracts and thickens in a kind of *in vitro* training regimen.

For the patty, tens of thousands of these beef circles were turned over to Peter Verstrate, a self-employed food technologist in the Netherlands, who cut the rings to produce shreds of meat about a centimeter long, which he ground up. He added breadcrumbs and some binder to improve the texture, but color was a problem: Because of a lack of myoglobin—the oxygen-carrying molecule that makes muscle tissue red—the meat looked white. A mix of beetroot juice, saffron, and a little bit of caramel made the raw burger look a pinkish red and helped it turn brown while cooking.

The end result won't win any gastronomy awards. "The surface was surprisingly crunchy," Rützler says, but the inside did not have the meaty taste she was expecting. The other taster, Chicago, Illinois-based journalist Josh Schonwald, noted that the meat had a "familiar mouthfeel," but said the taste wasn't quite like a real burger, in part because of the absence of fat. Post said that adding fat-producing cells is one of the many challenges that this field is still facing.

Supporters of "cultured meat"—as Post prefers to call his creation—say such issues can be solved later. "Post's demonstration is a proof of concept. The message is that it is doable," says Gabor Forgacs, who is trying to build bigger pieces of meat from muscle cells using 3D printing technology at the University of Missouri, Columbia. "This is no longer a strange idea," adds Cor van der Wee, a biophilosopher at Wageningen University in the Netherlands who studies public attitudes toward cultured meat. The lack of science at Monday's event did not bother her. "Mark Post is not making a secret of the fact that he is not doing science here," she says. "The science will come once the money comes in." —KAI KUPFERSCHMIDT

The rift between Turkey's government and many of its scientists became a chasm this week when half a dozen academics were among hundreds of defendants convicted of crimes ranging from terrorism and treason to "insulting Turkishness." The trial, which has dragged on for 5 years, ended on 5 August in a courtroom in Silivri, west of Istanbul, when all the accused academics were sentenced to between 10 and 23 years in prison.

Outside Silivri, riot police used tear gas to disperse thousands of protestors. The verdicts are also drawing condemnation from human rights organizations and academics elsewhere. "I am greatly disappointed," says Peter Diamond, an economist at the Massachusetts Institute of Technology in Cambridge who visited some of the accused in prison. "Their detention is a violation of human rights."

According to the Turkish government, the 275 people rounded up since 2008 are connected to an alleged secret organization of secular elites known as "Ergenekon" that have been plotting to overthrow Turkey's democratically elected government, controlled since 2002 by the religiously conservative Justice and Development (AK) Party. Critics contend that the AK government is using the trial to punish critics and political opponents, including secular, liberal academics.

One professor who has become a cause célèbre in the scientific community is Kemal Gürüz, a chemical engineer sentenced to 13 years and 11 months in prison. "No credible evidence [against him] was ever produced," says Carol Corillon, executive director of the International Human Rights Network of Academies and Scholarly Societies (IHRN) in Washington, D.C. Gürüz has spent the past year in jail during the court proceedings, during which time his health has deteriorated due to a blocked artery. According to family members, Gürüz has grown despondent and attempted suicide by cutting his wrists in his prison cell in June. He faces another trial, on similar charges, slated to start in September.

Some of Gürüz's colleagues insist that the true motivation behind his conviction is political revenge. Gürüz chaired Turkey's

Council of Higher Education during the previous administration. One of the most controversial policies during his tenure was a ban on female university students wearing headscarves, a Muslim practice. The ban had been passed by Turkey's parliament, but religious conservatives blame Gürüz for enforcing the ban on campuses, says Aslı Tolun, a molecular biologist at Boğaziçi University in Istanbul. Once it came to power, the AK Party



Hard time. Kemal Gürüz grew so despondent in prison that he attempted suicide in June. On 5 August he was sentenced to nearly 14 years in prison.

reversed that policy, as well as many others intended to counteract religion in Turkish higher education.

The other jailed academics, all accused of involvement in the conspiracy to overthrow the government, are medical professors and presidents of Turkish universities during the previous administration. They received lengthy terms. The sole glimmer of good news was that at least three of the academics, including Mehmet Haberal, will be released from prison for the time being. Haberal is one of Turkey's most accomplished doctors, a transplant surgeon with an active research laboratory. Although he was sentenced to 12 years and 6 months of prison time, he was freed pending an appeal. He is suffering from liver disease and was reportedly ill after receiving no medical treatment in prison.

All the academics found guilty this week plan to appeal their convictions. IHRN, which issued a report last week that found no convincing evidence that any of them committed a crime, is helping the families of the accused

academics contact other international rights organizations. “We will not give up until justice is done in these sad cases,” Corillon says.

The persecution of academics who don’t see eye to eye with the government is likely to continue. “Currently there are hundreds of academics in similar situations,” who may face reprisals for holding views at odds with the government, says Çiğdem Atakuman, an archaeologist at Middle East Technical University in Ankara. Turkish academics who study “dangerous topics” such as the Kurdish or Armenian minorities, evolution, or secular

democracy are at risk of being “excommunicated from academia,” she says. Atakuman says she is disappointed that “despite all the outcry of Turkish academics,” the European Union and United States haven’t brought any pressure to bear on the Turkish government.

Discouraged Turkish scientists may take heart from Atakuman’s own story. She was chief editor of a popular science journal published by the government until she ran an issue in 2009 celebrating Charles Darwin, whose theory of evolution does not sit well with many supporters of the AK-led govern-

ment. After losing her position over the publication, Atakuman sued the government for lost wages and damage to her reputation. Last week, she won the first of two cases.

Gürüz and his five colleagues facing more than a decade in prison can only hope for a similar vindication when their appeal is heard. “Throughout my life, I have pursued academic excellence and upheld human intellect above all,” Gürüz penned in an essay in prison last year. “Where I should get rewarded, I now get punished.”

—JOHN BOHANNON

ENVIRONMENTAL POLICY

House Subpoena Revives Battle Over Air Pollution Studies

Republicans in the U.S. House of Representatives have taken an old battle over the health data that underlie Clean Air Act regulations to a new level. For the first time in 21 years, the House science committee has issued a subpoena, demanding confidential data from the Environmental Protection Agency (EPA). Committee Chair Lamar Smith (R–TX) has said that if EPA does not oblige, he may go after the institutions that conducted the groundbreaking studies decades ago.

Since 2011, Smith has made repeated requests to EPA for what he calls the “secret science” used to justify regulations that the agency promulgates under the Clean Air Act. Smith argues that the public should have a chance to scrutinize the data from two federally funded studies: the so-called Harvard Six Cities Study and a body of related data gathered by the American Cancer Society (ACS). Yet critics say the move is designed to allow industry to attack what is widely considered to be seminal work on the health impacts of air pollution. The latest move is “déjà vu all over again,” says economist C. Arden Pope of Brigham Young University in Provo, Utah, an author of both studies.

In the 1993 Six Cities study, published in *The New England Journal of Medicine*, Harvard researchers followed more than 8000 participants for 14 to 16 years and found an association between the risk of death from lung cancer and cardiopulmonary disease and exposure to particulate matter, or soot, in the air. Two years later, some of those same researchers used ACS’s much larger patient database to support the

connection between air pollution and mortality in Cancer Prevention Study II. Both studies were cited in EPA’s tightening of soot standards last December.

The battle over Six Cities is almost as old as the study itself. In 1997, EPA issued new air quality standards based on the Six Cities findings, placing the first limits on fine parti-



Mounting evidence. Chair Lamar Smith is apparently unpersuaded by the stacks of research, handed to him by Democrats, in support of air pollution regulations.

cles (2.5 micrometers across or less), whose sources include vehicle exhaust and industrial smokestacks.

Industry representatives demanded that the raw data be made public so the findings could be checked for errors (*Science*, 25 July 1997, p. 467). Harvard refused, citing confidentiality agreements with the study participants. The researchers had collected birth and death dates, smoking habits, diet, and health information including the presence of cancer and lung disease. In a compromise, Harvard shared the data with the Health Effects Institute (HEI), a nonprofit research organization partially funded by the auto

industry. HEI convened a team of independent scientists, which confirmed the findings in a study published in 2000.

At a contentious committee meeting last week, ranking member Eddie Bernice Johnson (D–TX) placed that HEI study in front of Smith, along with thousands of pages of other peer-reviewed research supporting the studies. She asked that the stacks be inserted into the committee record “since the Majority has claimed they don’t have enough science to review.” House Democrats also argued that most of the information requested was already available to legitimate researchers. ACS has a procedure for sharing its data with other institutions.

“I have to assume you will be passing this data to—excuse my language—industry hacks,” Johnson said in her opening statement Thursday. Smith asserted the data would be shared with “various reputable entities and organizations” and would be “de-identified” so that no names would be made public. But because the six cities were small, it would be easy to quickly figure out who the participants were, according to Pope.

The resolution was passed on 1 August in a vote strictly along party lines. It authorizes subpoenas for EPA as well as “other custodians of research data,” which could include both Harvard University and ACS, Smith said. Only EPA has received a subpoena so far, directing EPA Administrator Gina McCarthy to produce the data by 19 August. The agency has not indicated what it intends to do.

—KELLY SERVICEK



Exacting work. A Sanaria researcher extracts malaria parasites from a mosquito.

INFECTIOUS DISEASES

Unconventional Vaccine Shows Promise Against Malaria

For the past decade, tropical disease researcher Stephen Hoffman has been obsessed with a quixotic scheme for making a malaria vaccine: by bottling weakened malaria parasites. Two years ago, the first test of this vaccine in people failed. Now he has come back with evidence that his idea might just work. Online this week in *Science* (<http://scim.ag/SederVac>), Hoffman's company and federal researchers report that when given in a new way, their experimental vaccine protected 12 of 15 volunteers from malaria infection, including all six receiving the most doses.

Those numbers are tiny, and the vaccine will need to overcome a host of hurdles to be of practical use. But 100% protection is the best result yet in the long and frustrating effort to develop a malaria vaccine. "The results are extremely encouraging," says Pedro Alonso of the Barcelona Institute for Global Health in Spain, who has co-led studies of the most advanced malaria vaccine in clinical trials, called RTS,S. "This is a really important, really exciting proof of concept."

Even if the early success holds up, Hoffman's company, Sanaria Inc. of Rockville, Maryland, has a long way to go to show that its vaccine, which is complicated to produce and administer, could be used in poor, malaria-plagued regions such as sub-Saharan Africa. But Hoffman is undaunted: "Our goal was to demonstrate full protection," he says. "Working out the practical aspects is something many people can do."

Caused by *Plasmodium* parasites transmitted by mosquitoes, malaria infected an estimated 220 million people in 2010 and killed 660,000, most of them children, according to

the World Health Organization. The current leading vaccine candidate, RTS,S, contains a single surface protein from the *Plasmodium falciparum* sporozoite, an immature form of the parasite. In recent phase III trials, RTS,S protected only 31% of young infants and 56% of older babies and toddlers (*Science*, 16 November 2012, p. 871).

Hoffman, who worked on RTS,S as a U.S. Navy researcher, concluded years ago that a single-protein vaccine would "never do the job" of achieving full protection against the complex, 5000-gene malaria parasite and that only a vaccine containing whole sporozoites would work. He seized on studies in the 1970s that showed that more than 90% of volunteers were protected against malaria infection after they received more than 1000 bites from *P. falciparum*-infected mosquitoes that had been irradiated to weaken the parasite. Hoffman launched Sanaria in 2002 to develop a vaccine that could mimic the effect of those bites.

It was an ambitious goal: Technicians must dissect mosquito salivary glands to obtain the sporozoites, which have been weakened with radiation, and getting a safe, pure formulation through regulatory approval was tough. When Sanaria tested the vaccine in a small phase I trial, the results were disappointing—only two of 44 volunteers were protected. In that trial, the vaccine was administered into the skin, the standard delivery method for vaccines. However, animal studies by Robert Seder at the National Institute of Allergy and Infectious Diseases had suggested that the sporozoites might work much better if injected intravenously (*Science*, 28 October 2011, p. 475).

So Sanaria teamed up with Seder to test the vaccine on 40 adult volunteers. After receiving the vaccine intravenously, they were exposed to malaria-carrying mosquitoes. (They were promptly treated with antimalarial drugs if they became infected.) After four shots of the highest dose—135,000 sporozoites per injection—given a month apart each, six of nine volunteers were protected. Another six who received five doses on a slightly different schedule were all protected, with minimal side effects.

Seder calls the results "very promising" but cautions that the study was small. "We need to repeat it in a larger number of people." He points out that in a trial of RTS,S published in 1997, the vaccine protected six of seven adults in one group. That level of protection was not seen in subsequent studies.

Another next step is to explore whether the vaccine can protect against multiple *P. falciparum* strains. Researchers will also look at durability—ideally the vaccine will protect longer than RTS,S, which fades over a year. The team will soon launch several small trials in Africa, Germany, and the United States. They will also test different vaccination schedules in the hope that they can achieve 100% protection with fewer than five doses.

To move on to large-scale production and reduce costs, Sanaria will need to speed up the dissection process, which now employs about 12 to 15 "dissectors" who can each tease apart about 150 mosquitoes an hour. Hoffman is collaborating with Harvard's engineering school to automate the process.

The challenges don't end there. The vaccine must be stored in liquid nitrogen, unlike traditional vaccines in developing countries. And administering several intravenous doses to very young children whose veins aren't easy to find could be tricky.

Beyond vaccinating soldiers and travelers to malaria-endemic areas, Hoffman and others think the vaccine could play a valuable role in countries where malaria is still a huge killer, or in those close to eliminating the disease. Stefan Kappe of the Seattle Biomedical Research Institute in Washington, who is working on a similar vaccine that contains genetically engineered sporozoites, says the approach is worth supporting: "If we were talking about an HIV vaccine, there would be no question about investing in this type of success."

—JOCELYN KAISER



The Web's Faceless Judges

PubPeer is the latest forum for free-ranging discussion of published papers. It can only succeed, say its anonymous founders, if participants are able to keep their identities hidden

■ ■ ■ ■ ■

"I think it's going to be very hard to stay anonymous forever."

—PUBPEER FOUNDER

WHAT DOES IT TAKE TO RUN A WEBSITE WHERE SCIENTISTS CAN chat freely about published papers?

Anonymous e-mail addresses. Temporary phone numbers. Undisclosed locales. Jitters that one day, your cover will be blown, your career destroyed, and your family's finances depleted. It sounds like a John le Carré novel. But no, the protagonists here are a handful of biologists who last fall unveiled PubPeer, which bills itself as "an online community that uses the publication of scientific results as an opening for fruitful discussion." The goal is something of a free-for-all journal club, welcoming comments from readers and authors across disciplines.

PubPeer is one of several recent ventures to encourage scrutiny of published work, seeking to fill what many consider a gap in scientific publishing. "I myself have kind of longed for a place where I can see discussion of work after publication," says Ferric Fang, a microbiologist at the University of Washington, Seattle, and editor-in-chief of *Infection and Immunity*. Journals are one obvious place to leave comments about a paper, says Fang, who has written extensively about scientific publishing and misconduct (*Science*, 25 January, p. 386). But he says that most "haven't been very good" at nurturing such discussion. Some don't allow comments at all, and others require commenters to be named or remove those that may imply wrongdoing.

When questions about published research bleed into misconduct accusations, journals and institutions have their protocols, but many researchers grouse that the process can take years and its outcome is often unsatisfying.

"Universities charged with investigation [have a] huge conflict of interest," says Jennifer Nyborg, a biochemist at Colorado State University, Fort Collins, who's been frustrated by her efforts to report potential misconduct through the proper channels.

Given these shortcomings, many agree there's a place for sites that engage in postpublication peer review. They can clarify experiments and catch errors, something several, including PubPeer, have done. They can challenge how studies are interpreted and suggest avenues for follow-up work.

But many who participate in these discussions sit at a tense nexus: They long for more unfettered conversation about science, yet insist on doing so anonymously, fearful that their words will come back to haunt them. One of PubPeer's founders, who describes himself as a tenured professor, says that even a senior scientist "very rarely, myself included, wants to take the risk" of criticizing fellow scientists under their own names. The professor and his shadowy brethren—another founder tells *Science* that he is finishing up his Ph.D. somewhere in the United States—have gone to great lengths to protect their identities. "I don't want it to impact my scientific life or my personal life," says the professor of his site, adding that the phone number from which he was calling "probably won't work after a few days."

While anonymity can spur discussion, it does not always elevate it.

When PubPeer launched in October 2012, the founders' goal was genteel dialogue. "I enjoyed this paper greatly," an anonymous commenter wrote early this year, about a study in *Science* on empathy in rats. The commenter politely queried about comparisons between littermates and nonlittermates and sought more information about how the animals behaved.

Posts like this one, though, were interspersed with those of a different nature. "The paper was VERY effective for getting his lab a lot of publicity (and money?)," one commenter wrote about an article in *Scientific Reports*, a *Nature* journal. "Was it just sensationalism or did it tell us something new about the brain?"

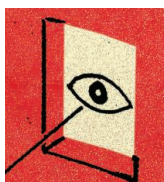
In May, PubPeer underwent a tectonic shift after a tip exposed errors in a high-profile paper. The anonymous post flagged apparent image duplications in a manuscript describing how human embryonic stem cells could be produced by cloning, published in *Cell* by a group based in Oregon (*Science*, 31 May, p. 1026). *Cell* subsequently printed an erratum. Suddenly, PubPeer was in the news, and whistleblowers began flooding it with tips suggesting problematic images in dozens of papers. It now receives between 10 and 50 comments a day. "They're getting a little bit out of control, in my opinion," the professor founder says.

"The volume of material they're dealing with, I think, is far, far greater than anyone anticipated," agrees Paul Brookes, a biologist at the University of Rochester in New York. Brookes knows well what it takes, and what it's like, to play scientific watchdog. Last year he launched www.science-fraud.org, which

unlike PubPeer sought from the start to expose problematic images in published papers. Brookes, too, was anonymous—until January, when a still-unidentified individual outed him (*Science*, 11 January, p. 132). Amid threats of lawsuits, science-fraud.org imploded. Brookes quickly pulled accusations of wrongdoing from the site. Although many criticized him for questioning the integrity of authors, the site had an impact: More than 40 of the papers that appeared on science-fraud.org have since been corrected or retracted, Brookes says.

So far PubPeer's record is slimmer, but the site appears to be gaining traction. In July, it posted 89 comments, up from just 26 in June. In May, when the Oregon stem cell case broke and science-fraud.org posted an endorsement of PubPeer, comments on the site topped 360. Some challenge the integrity of images; others question whether a paper's conclusions are backed by its data. Scientists who are first or last authors on a paper can register as anonymous "peers" and leave comments, which are posted automatically but can be removed if deemed inappropriate. Anyone can send unregistered submissions to PubPeer's e-mail address, and the founders often vet their claims against the paper in question. (In June and July, more than 500 comments were submitted but not posted due to problematic tone or content.) There's also the option of commenting under one's name, but few take that route.

"If it's a verifiable fact, ... it just shouldn't matter" if the person is named, says Ivan Oransky, a journalist who 3 years ago started



"When I saw that it was not signed by anybody, I felt uncomfortable—it was an instinctive reaction."

—SHAUL HESTRIN, NEUROSCIENTIST
AT STANFORD UNIVERSITY

the popular blog Retraction Watch with fellow reporter Adam Marcus. But he says that in some intangible way, “it does. People like to know where people are coming from.” Many of the tips about retracted papers that he and Marcus investigate arrive under pseudonyms, from anonymous e-mail addresses. Even though Oransky supports anonymity, he admits that he can’t help but be curious himself, especially about those who attack Retraction Watch and accuse it of having “an agenda.” “I would very much like to know who all these people are,” he says.

A big reason for staying hidden, many scientists suggest, is that despite all the talk of honest discussion in their community, there’s little reward for engaging in it. “If the system was much more open and much more tolerant of dissent then this would not be needed,” says Raphael Levy, who studies cell imaging at the University of Liverpool in the United Kingdom. He has left both anonymous and named comments on PubPeer.

Another occasional commenter, neuroscientist Boris Barbour at the Institute of Biology at École Normale Supérieure in Paris, concedes that his writing changes when it’s backed by his name. “It’s very easy to say, ‘That paper’s crap and how did it ever get accepted,’” Barbour says. “To be sure you have a watertight case isn’t trivial.” Although he tries to be equally rigorous whether posting anonymously or not, he says the pressure to “make extra certain” the text is accurate is heightened when he goes public. Fang, who has left comments on Retraction Watch, agrees. “When I have to sign my name to it, it makes me just a little bit more thoughtful before I hit ‘send,’” he says.

When a paper is flagged on PubPeer, the site immediately notifies the corresponding author. Peter Klein, a physician and developmental biologist at the University of Pennsylvania, received an automated e-mail from PubPeer in late May. A poster listed 18 questions and comments about his 2012 report in *Nature Medicine*, including what this person described as “contradictions between text and figures” and “incomplete or inconsistent description of methods and figures.”

Klein had never heard of the site. “Because there were so many small details, my first response was, do we have to respond? We’ve already gone through peer review,” he says. “But then as I went through it ... it occurred to me that this person probably found the omissions frustrating. ... I felt like, we can answer them, we can help them out.” He and his postdoc crafted a nearly 900-word rejoinder.

Few authors were as relaxed about anonymity as Klein. “When I saw that it was not signed by anybody, I felt uncomfortable—it was an instinctive reaction,” says Shaul Hestrin, a neuroscientist at Stanford University in Palo Alto, California, whose paper in *The Journal of Neuroscience* was questioned. Hestrin sensed an imbalance, because only one person was named. (That would be him.) “Either you want to stand by what you’re saying, or you don’t say it.” Hestrin e-mailed the site to say he’d be happy to respond if he knew who was asking the questions, but was told that wasn’t an

option. “I just disengaged,” he says, and didn’t reply, although he acknowledges the points raised—essentially, whether the data had been overinterpreted—weren’t unreasonable.

Ironically, some of those who decry anonymity most vigorously insisted that their names not appear in this story. “Anonymity’s a great cover for people who want to take other people down,” says one author whose work was cited on PubPeer. Another scientist argued that PubPeer “becomes basically a gossip site” lacking “credibility or accountability.” (“I’ve never done anything anonymously,” this person emphasized, while stipulating that their name not be publicized.)

Brookes, who is facing several threatened lawsuits, has thought a great deal about anonymity. His views are still evolving. “Previously I think I was very much like the owners of PubPeer—very scared, very wary,” he says. “And I’m sort of coming around to the idea that doing this stuff using your real name is the way to go.”

Brookes cites a couple of reasons for the swing of his internal compass. For one, he was frustrated when he tried to contact a journal anonymously about potential image manipulations in five papers by a single author. After dozens of e-mails generated not a single reply, he became convinced that the reason was that no one knew who he was.

Brookes also notes an important change in his own scientific fortunes: Last year, while running science-fraud.org, he was applying for a grant from the National Institutes of Health. In February, he learned that his application would be approved. “It’s really down to what career state you’re at and what you’re comfortable with,” he says. Brookes is contemplating a new site for postpublication peer review. He’s still considering

the place anonymity might have on that site.

PubPeer’s founders watched science-fraud.org’s collapse warily. “We learned from that, we’re not accusing anybody of fraud,” says the professor founder. The site’s administrators, whom he says number about eight spread across different institutions, have consulted with some family friends who are attorneys “but we are mostly winging it.”

At the same time, PubPeer is doing what it can to raise its profile. It’s planning to offer its users browser plug-ins that can link PubPeer comments to PubMed, which thousands of researchers rely on to sift through biomedical papers. Its administrators are also developing citation software plug-ins that would alert users to comments on papers when those papers are referenced in manuscripts or grants. “Our dream,” he says, “is that this becomes an important side piece to the scientific literature.”

The professor has already had occasion to be grateful for his double life. A visitor grading his lab for funding had a paper flagged on the site; a department colleague had research discussed there. “If he knew I was involved, it would change our interactions,” he says, referring to the colleague. Still, he’s resigned to a day when he’s unmasked. “I think it’s going to be very hard,” he says, “to stay anonymous forever.”

—JENNIFER COUZIN-FRANKEL



“If it’s a verifiable fact, ... it just shouldn’t matter” if the person is named. But “people like to know where people are coming from.”

—IVAN ORANSKY,
CO-FOUNDER OF RETRACTION WATCH



Firestorm. The 2006 Esperanza wildfire burned 16,000 hectares of chaparral and killed five firefighters in southern California.

Forty years later, Rothermel's formulas are the foundation for two varieties of operational fire models. Strategic modeling tools allow managers to forecast, well beforehand, how fires might spread or visualize where future fires might break out; tactical tools allow modeling of specific fires on shorter time-scales, sometimes

with an eye toward figuring out whether to confront them or let them burn. Perhaps the most widely used model is a tactical model called FARSITE, which uses terrain, fuel, and weather data to project a fire's path over a 2D map.

Fire analysts use it tens of thousands of times a year in their work, says FARSITE developer Mark Finney of the Missoula lab. And in the hands of an analyst who understands its limitations, FARSITE can be a valuable tool. In 1994, for example, officials in Glacier National Park were confronted with a pair of wildfires. They faced "a lot of tense decision-making," Finney says, over whether the flames might harm settlements, and whether they should put firefighters in harm's way. But FARSITE predicted that the fire would stay within a safe area, Finney says, and it did. In other instances, it has given planners a reliable 3- to 5-day forecast of a fire's spread, enabling them to more efficiently—and safely—deploy crews.

Still, Rothermel-based tools like FARSITE have some glaring weaknesses. They assume that fuel is evenly distributed, for instance, and that it burns uniformly. They don't simulate the movement of particles and gases that can affect a fire's path, or the complex relationships with the atmosphere that can enable some blazes to create their own wind and weather, even generating so-called pyrocumulus clouds. The models also have a hard time with complex phenomena like rotating air masses known as fire whirls, fires spread by embers, or explosive blasts of flame that can shoot out from a fire's

WILDFIRE SCIENCE

Computing a Better Fire Forecast

Scientists and firefighters ponder new ways to predict the spread of wildfire as the U.S. West faces ever more potent blazes

Firefighters who were there that deadly morning would later describe trees with glowing orange bark and flames that leapt hundreds of meters in moments. An arsonist in the southern California town of Cabazon started the October 2006 blaze, known as the Esperanza fire. Havoc reigned at dawn as residents evacuated and fire trucks snaked up smoky mountain roads.

At about 6:30 a.m., a five-man crew from Engine 57 set up a water pump above one edge of the fire, hoping to save an octagon-shaped house. But the blaze swept up an adjacent gully and over the structure in less than 10 seconds. None of the crew escaped.

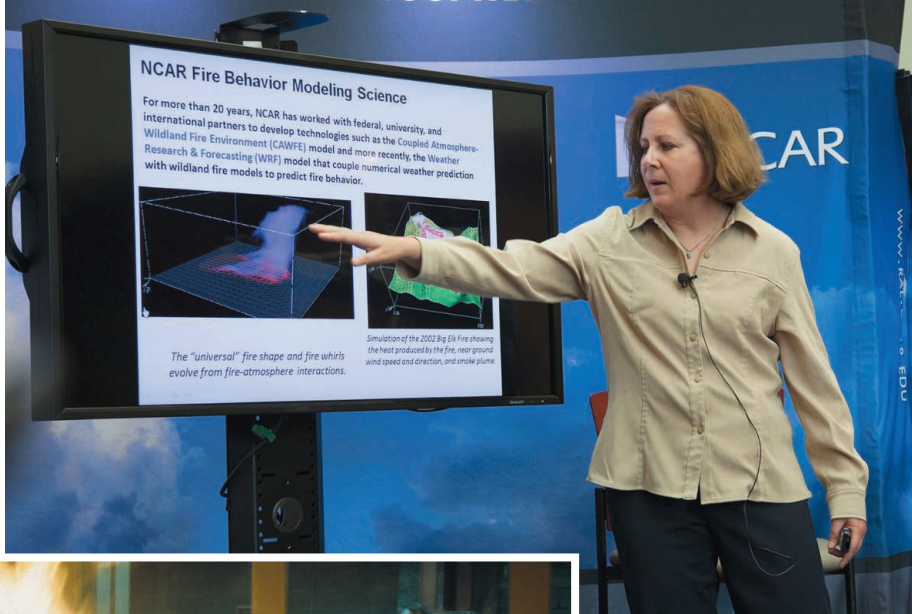
Now, 7 years after the Esperanza tragedy, U.S. wildfire specialists are still debating exactly what happened—and whether improved computer models might help scientists, firefighters, and disaster planners avert such deadly surprises. Relatively crude existing simulations already help the U.S. Forest Service and other agencies predict the course of hundreds of fires each year, mostly in the western United States. But researchers agree that these models do a poor job of simulating extreme events like Esperanza, when wildfire can seemingly act capriciously and erratically.

"The current models have been stretched

to their limits," says Kelly Close, a fire behavior analyst in Fort Collins, Colorado. They will be stretched further if a warming climate makes extreme fires more common, raising the odds of additional Esperanza-like calamities, such as the Yarnell, Arizona, blaze that killed 19 elite firefighters in June. More sophisticated models that can simulate both the extreme behavior of individual fires and the risk of fire across entire landscapes are on the horizon. But a variety of factors, including limited funds, technical disagreements, and the sometimes clashing cultures of academic scientists and wildland firefighters, is complicating the search for alternatives.

Model behavior

Wildfire modeling is a relatively young endeavor. In the early 1970s, when the U.S. Forest Service sought to analyze fire risk over large landscapes, it turned to its research laboratory in Missoula, Montana. There, fire scientist Richard Rothermel led a team that observed fires in field tests and the laboratory. They went on to write a set of equations, which for the first time related the speed and direction of a model fire's spread to terrain, the vegetation available for fuel, and nearby wind patterns.



Enlightenment. These days, meteorologist Janice Coen (above) is working to develop fire-atmosphere simulations that improve pioneering models devised by Richard Rothermel (left, behind window) in the 1970s.

flanks. A Rothermel-based model “describes very well a fire burning in a field of wheat,” one of the researcher’s colleagues once told *Fire Science Digest*. “As you get further away from that uniformity, the less accurate it becomes.”

Such limitations became clear to FAR-SITE analysts studying a 2002 fire in northwestern Colorado. The model suggested that it could be stopped in its tracks by using time-tested methods such as lighting controlled “backfires” to deny it fuel. But the backfires wouldn’t ignite even though the blaze went on marching across the landscape. The reason: The fire was spreading treetop to treetop via a flammable lichen known as “old man’s beard,” instead of creeping along the ground as the model assumed. (In such cases, Colorado’s Close says, wildfire specialists “just have to turn off the computer” and rely on experience and intuition.)

Flare up

One scientist working to bring fire models into the 21st century is Janice Coen, a meteorologist at the National Center for Atmospheric Research (NCAR) in Boulder, Colorado. Unlike most wildfire experts, Coen’s career path began not in the forest, but in

the laconic researcher. In graduate school, Coen studied airflow over complex surfaces, which led her in 1992 to join NCAR, where a team was working to connect a high-resolution regional weather model to the Rothermel equations.

Since then, Coen has become a leading advocate for the idea that robust simulations must reflect a coupling between the fire and the atmosphere. Each affects the other, she says, creating feedback loops that are critical to predicting fire behavior, including the seemingly whimsical way extreme fires move. She has drawn on aspects of fluid dynamics, for instance, to show why fires don’t move through a landscape in a straight line, but with a front edge curved in the direction of prevailing winds. That’s because rising parcels of air ahead of the fire front pull the fire into that shape.

In 2005, Coen turned heads with a simulation of the Big Elk fire, a medium-sized blaze that had struck Colorado 3 years before. By modeling how the fire and the

atmosphere interacted, Coen built what Close called a “surprisingly accurate” recreation of the Big Elk blaze in silico. The model showed, for example, how the blaze affected winds some 5 kilometers away—one of the first times such coupling had been quantified.

Coen has also drawn attention for her more recent simulations of the 2006 Esperanza fire. Although fire modelers often don’t have the real-world data necessary to test their models against real events, Esperanza was different: The Forest Service’s Pacific Southwest Research Station mapped its heat by airplane, in real time. That has allowed Coen to see if her models could accurately recreate its spread and intensity.

The answer is a qualified yes, she and ecologist Philip Riggan of the Forest Service lab have reported at meetings and in a paper under review at the *International Journal of Wildland Fire*. Despite incorporating atmospheric coupling, the model didn’t do a good job of mimicking some aspects of local warm winds, called Santa Anas. But it faithfully recreated how the fire raced through canyons, split into two flanks, and engulfed the firefighters at the octagon house. Such results suggest that “this is a really promising approach,” says Max Moritz, a fire scientist at the University of California (UC), Berkeley.

Could it have prevented the tragedy at the octagon house? Coen emphasizes that her work isn’t designed to tell firefighters where—and where not—to go. “I’m not one who says that fire modeling saves lives,” she says. But she does believe that more sophisticated models would give crews a better idea of how an extreme blaze might behave, perhaps enabling them to build in bigger margins of safety.

Her Esperanza work, for example, suggests that responders need to keep in mind that fires can create their own winds that can pull flames uphill. A California state review concluded that a combination of factors explained the “erratically”

behaving fire, including Santa Ana winds trapped near the ground by a layer of cool air, which made them move faster. But Coen thinks that the fire’s behavior at the octagon house wasn’t so unpredictable. In her simulation, fire-generated winds largely explain “how the fire dragged itself up the gully so quickly,” she says. Adding to the speed of

A warmer climate will lead to a “higher probability of extreme fire behavior, not in every fire of course, but more often than in the past.”

—STEVEN RUNNING, UNIVERSITY OF MONTANA

those winds was a fire whirl, which developed in her model in the heat of the blaze.

Jeff Zimmerman, a retired local fire chief who investigated the fire, isn't fully convinced. But he says Coen's model does show that "a computer model is a good tool to help predict future fire behavior."

Her approach hasn't caught on among the modelers at the Missoula lab, however, who aren't convinced that they need to add fire-atmosphere coupling to the Rothermel equations. Given "the complication of adding such interactions" to current models, says the Missoula lab's Finney, wider tests are required. More important, he says, is establishing new, fundamental physics on combustion, convection, and other aspects of fire to eventually replace the Rothermel equations. "We don't understand how fire spreads," he says.

Bringing the heat

A warmer climate will lead to a "higher probability of extreme fire behavior, not in every fire of course, but more often than in the past," predicts forest scientist Steven Running of the University of Montana in Missoula. This new regime will not only tax tactical simulators like FARSITE, but strategic models as well.

Such tools use historic weather data on previous fires to map the probability of fire spread. But existing databases of previous fires are increasingly not representative of the changing climate regime in the western United States, says Krista Gollnick-Waid, a fire analyst with the Bureau of Land Management in Boise. That should raise doubts about results produced by one oft-used strategic modeling tool, called FSPro, she warns: "Analysts need to be aware of the potential for FSPro to underpredict fire spread [and] probability." During her work analyzing a recent fire in southwest Colorado, for example, she found that the blaze traveled farther in 1 day than "what the model said it would go in 5 days." Says Close: "If that's the new normal, we better be ready."

UC Berkeley's Moritz is already grappling with the changing climate of the West. In a 2010 paper published in *Geophysical Research Letters*, he used roughly a decade

of wind and weather information to map the Santa Ana winds across coastal southern California, which dry out landscapes and stoke brushfires into conflagrations. The results were fairly broad but disturbing, highlighting areas that were potentially vulnerable to major fires. "I had fire departments calling me asking whether they could have even finer resolution maps to understand their local risks better," Moritz recalls. Unfortunately, those are still largely unavailable. But he says that the experience highlights the growing demand for better, and more detailed, strategic fire models.

million-a-year program managed by the Forest Service. "Our focus is primarily fuels management," or ways to reduce the amount of tinder-dry vegetation on the landscape, says spokesperson Tim Swedberg. None of the program's 50 research awards this year focus on wind, climate, or weather. That's typical, says Moritz, adding that he is routinely disappointed when he reads the program's annual description of research questions it wants to answer. "You look at it and you say wow, these research questions are really narrow," says Moritz, whose funders include the National Science Foundation.

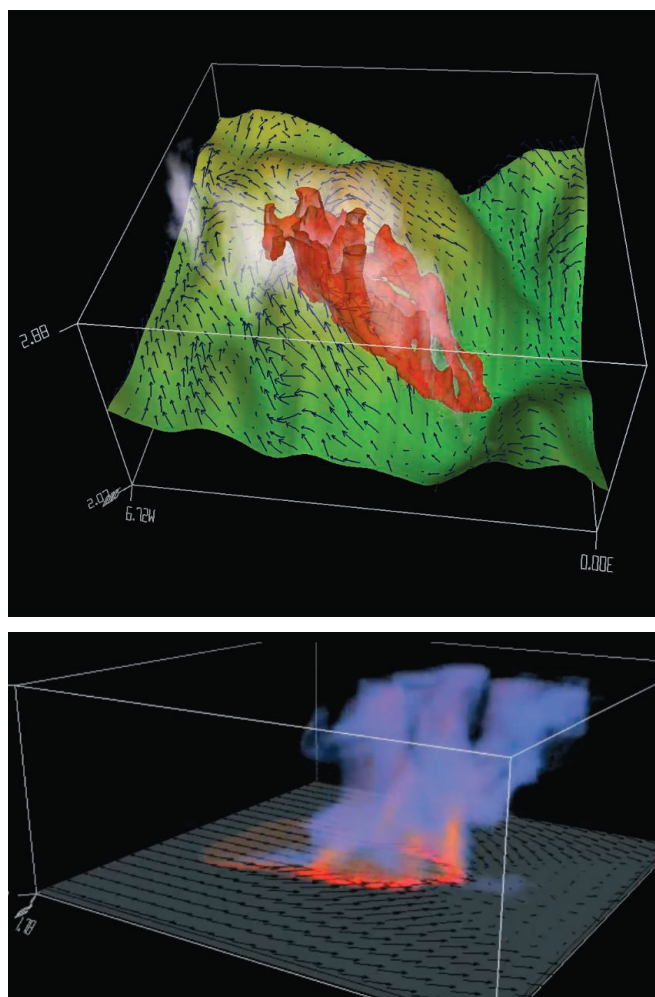
Cultural barriers to trying new ideas can also loom large. Wildfire officials who literally undergo trials by fire aren't necessarily inclined to put much value on knowledge gained from "a peer-reviewed study by a Ph.D.," says Matthew Desmond, who fought wildfires in Arizona before becoming a sociologist at Harvard University. And Coen is matter-of-fact about the challenges that she's faced in collaborations. She's from Pittsburgh, not the West; she's an academic, not "a forest person" and, well, she's a woman in a largely male professional world. "I've become much better at finding where people are coming from and finding ways to bridge that gap," she says diplomatically.

She's tramped out to field command posts, for instance, to learn about what managers need—and would be willing to try out. "The procedures in place to manage wildfires make it very hard to try new things," she says. "You can't just say 'Try this model' to someone with no experience using it, who is engaged in responding to the incident."

In 2007, she visited the octagon house destroyed by the Esperanza fire, at the invitation of Zimmerman, the retired fire

chief. Zimmerman has visited the site repeatedly; each time, he says, "it's a very difficult experience." But Coen reveals little emotion. "I am freakishly analytical and Spock-like" sometimes, she says. And Zimmerman thinks more of that kind of thinking may be just what fire science needs.

—ELI KINTISCH



Ignition. Computers simulate how fire may affect nearby winds (*above*) and how flows of air shape fire naturally into an oval (*below*).

A unified front

Improving all varieties of fire modeling, however, may require some shifts in funding priorities—and perhaps in attitudes toward collaboration among scientists and firefighters.

Consider the priorities of the federal Joint Fire Science Program, a \$13-



LETTERS

edited by Jennifer Sills

Gain-of-Function Experiments on H7N9

SINCE THE END OF MARCH 2013, AVIAN A INFLUENZA VIRUSES OF THE H7N9 SUBTYPE HAVE caused more than 130 human cases of infection in China, many of which were severe, resulting in 43 fatalities. Although this A(H7N9) virus outbreak is now under control, the virus (or one with similar properties) could reemerge as winter approaches. To better assess the pandemic threat posed by A(H7N9) viruses, NIAID/NIH Centers of Excellence in Influenza Research and Surveillance (CEIRS) investigators and other expert laboratories in China and elsewhere have characterized the wild-type avian A(H7N9) viruses in terms of host range, virulence, and transmission, and are evaluating the effectiveness of antiviral drugs and vaccine candidates. However, to fully assess the potential risk associated with these novel viruses, there is a need for additional research including experiments that may be classified as “gain-of-function” (GOF). Here, we outline the aspects of the current situation that most urgently require additional research, our proposed studies, and risk-mitigation strategies.

The A(H7N9) virus hemagglutinin protein has several motifs that are characteristic of mammalian-adapted and human influenza viruses, including mutations that confer human-type receptor-binding and enhanced virus replication in mammals. The pandemic risk rises exponentially should these viruses acquire the ability to transmit readily among humans.

Reports indicate that several A(H7N9) viruses from patients who were undergoing antiviral treatment acquired resistance to the primary medical countermeasure—neuraminidase inhibitors (such as oseltamivir, peramivir, and zanamivir). Acquisition of resistance to these inhibitors by A(H7N9) viruses could increase the risk of serious outcomes of A(H7N9) virus infections.

The hemagglutinin proteins of A(H7N9) viruses have a cleavage site consistent with a low-pathogenic phenotype in birds; in the past, highly pathogenic H7 variants (with basic amino acid insertions at the cleavage site that enable the spread of the virus to internal organs) have emerged from populations of low pathogenic strains circulating in domestic gallinaceous poultry.

Normally, epidemiological studies and characterization of viruses from field isolates are used to inform policy decisions regarding public health responses to a potential pandemic. However, classical epidemiological tracking does not give public health authorities the time they need to mount an effective response to mitigate the effects of a pandemic virus. To provide information that can assist surveillance activities—thus enabling appropriate public health preparations to be initiated before a pandemic—experiments that may result in GOF are critical.

Therefore, after review and approval, we propose to perform the following experiments that may result in GOF:

(i) **Immunogenicity.** To develop more effective vaccines and determine whether genetic changes that confer altered virulence, host range, or transmissibility also change antigenicity.

(ii) **Adaptation.** To assist with risk assessment of the pandemic potential of field strains and evaluate the potential of A(H7N9) viruses to become better adapted to mammals, including determining the ability of these viruses to reassort with other circulating influenza strains.

(iii) **Drug resistance.** To assess the potential for drug resistance to emerge in circulating viruses, evaluate the genetic stability of the mutations conferring drug resistance, evaluate the efficacy of combination therapy with antiviral therapeutics, determine whether the A(H7N9) viruses could become resistant to available antiviral drugs, and identify potential resistance mutations that should be monitored during antiviral treatment.

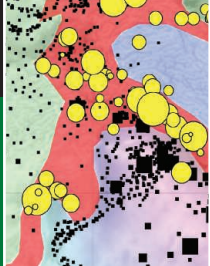
(iv) **Transmission.** To assess the pandemic potential of circulating strains and perform transmission studies to identify mutations and gene combinations that confer enhanced transmissibility in mammalian model systems (such as ferrets and/or guinea pigs).

(v) **Pathogenicity.** To aid risk assessment and identify mechanisms, including reassortment and changes to the hemagglutinin cleavage site, that would enable circulating A(H7N9) viruses to become more pathogenic.

All experiments proposed by influenza investigators are subject to review by institutional biosafety committees. The committees include experts in the fields of infectious disease, immunology, biosafety, molecular biology, and public health; also, members of the lay public represent views from outside the research community. Risk-mitigation plans for working with potentially dangerous influenza viruses, including 1918 virus and highly pathogenic avian H5N1 viruses, will be applied to conduct GOF experiments with A(H7N9) viruses (see supplementary text). Additional reviews may be required by the funding agencies for proposed studies of A(H7N9) viruses (see scim.ag/13BK5Hs).

The recent H5N1 virus transmission con-





Quake risk
in Asia

618



Methylation and
maturation in the brain

626

NextGenVOICES

Work-Life Balance: Last Call

You have one more week to respond to the NextGen VOICES survey! Share your thoughts about this question:

What one change would most improve work-life balance for scientists?

To submit, go to http://scim.ag/NextGen_8

Deadline for submissions is 16 August. A selection of the best responses will be published in the 4 October issue of *Science*. Submissions should be 250 words or less. Anonymous submissions will not be considered. Please submit only once.

troverly focused on the balance of risks and benefits of conducting research that proved the ability of the H5N1 virus to become transmissible in mammals (see www.sciencemag.org/special/h5n1). These findings demonstrated the pandemic potential of H5N1 viruses and reinforced the need for continued optimization of pandemic preparedness measures. Key mutations associated

with adaptation to mammals, included in an annotated inventory for mutations in H5N1 viruses developed by the U.S. Centers for Disease Prevention and Control, were identified in human isolates of A(H7N9) viruses. Scientific evidence of the pandemic threat posed by A(H7N9) viruses, based on H5N1 GOF studies, factored into risk assessments by the public health officials in China, the United States, and other countries.

Since the H5N1 transmission papers were published, follow-up scientific studies have contributed to our understanding of host adaptation by influenza viruses, the development of vaccines and therapeutics, and improved surveillance.

Finally, a benefit of the H5N1 virus research controversy has been the increased dialogue regarding laboratory biosafety and dual-use research. The World Health Organization issued laboratory biosafety guidelines for conducting research on H5N1 transmission and, in the United States, additional oversight policies and risk-mitigation practices have been put in place or proposed. Some journals now encourage authors to include biosafety and biosecurity descriptions in their manuscripts, thereby raising the

awareness of researchers intending to replicate experiments.

The risk of a pandemic caused by an avian influenza virus exists in nature. As members of the influenza research community, we believe that the avian A(H7N9) virus outbreak requires focused fundamental and applied research conducted by responsible investigators with appropriate facilities and risk-mitigation plans in place. To answer key questions important to public health, research that may result in GOF is necessary and should be done.

RON A. M. FOUCHIER,^{1*} YOSHIHIRO KAWAOKA,^{2*} CAROL CARDONA,³ RICHARD W. COMPANS,⁴ ADOLFO GARCÍA-SASTRE,⁵ ELENA A. GOVORKOVA,⁶ YI GUAN,⁷ SANDER HERFST,¹ WALTER A. ORENSTEIN,⁸ J. S. MALIK PEIRIS,⁹ DANIEL R. PEREZ,¹⁰ JUERGEN A. RICHT,¹¹ CHARLES RUSSELL,⁶ STACEY L. SCHULTZ-CHERRY,⁶ DEREK J. SMITH,¹² JOHN STEEL,⁴ S. MARK TOMPKINS,¹³ DAVID J. TOPHAM,¹⁴ JOHN J. TREANOR,¹⁵ RALPH A. TRIPP,¹³ RICHARD J. WEBBY,⁶ ROBERT G. WEBSTER⁶

¹Department of Viroscience, Erasmus Medical Center, 3015GE, Rotterdam, Netherlands. ²Department of Pathobiological Sciences, School of Veterinary Medicine, University of Wisconsin-Madison, Madison, WI 53711, USA. ³Veterinary and Biomedical Sciences, University of Minnesota, St. Paul, MN 55108, USA. ⁴Department of Microbiology and Immunology, Emory University School of Medicine, Atlanta, GA 30322, USA. ⁵Department of Microbiology, Icahn School of Medicine at Mount Sinai, New York, NY 10029, USA. ⁶Department of Infectious Diseases, St. Jude Children's Research Hospital, Memphis, TN 38105, USA. ⁷State Key Laboratory of Emerging Infectious Diseases, School of Public Health, The University of Hong Kong, Hong Kong SAR. ⁸Department of Medicine, Emory University School of Medicine, Atlanta, GA 30322, USA. ⁹Centre of Influenza Research, School of Public Health, The University of Hong Kong, Hong Kong SAR. ¹⁰Department of Veterinary Medicine, University of Maryland, College Park, College Park, MD 20742, USA. ¹¹College of Veterinary Medicine, Kansas State University, Manhattan, KS 66506, USA. ¹²Department of Zoology, University of Cambridge, Cambridge, CB2 3EJ, UK. ¹³Department of Infectious Diseases, College of Veterinary Medicine, University of Georgia, Athens, GA 30602, USA. ¹⁴Department of Microbiology and Immunology, Center for Vaccine Biology and Immunology, University of Rochester Medical Center, Rochester, NY 14642, USA. ¹⁵Infectious Diseases Division, University of Rochester Medical Center, Rochester, NY 14642, USA.

*Corresponding author. E-mail: r.fouchier@erasmusmc.nl (R.A.M.F.); kawaokay@svm.vetmed.wisc.edu (Y.K.)

Supplementary Materials

www.sciencemag.org/cgi/content/full/science.1243325/DC1
Supplementary Text

Published online 7 August 2013; 10.1126/science.1243325

TECHNICAL COMMENT ABSTRACTS

Comment on "The Placental Mammal Ancestor and the Post-K-Pg Radiation of Placentals"

Mark S. Springer, Robert W. Meredith, Emma C. Teeling, William J. Murphy

O'Leary *et al.* (Research Article, 8 February 2013, p. 662) examined mammalian relationships and divergence times and concluded that a single placental ancestor crossed the Cretaceous-Paleogene (K-Pg) boundary. This conclusion relies on phylogenetic analyses that fail to discriminate between homology and homoplasy and further implies virus-like rates of nucleotide substitution in early Paleocene placentals.

Full text at <http://dx.doi.org/10.1126/science.1238025>

Response to Comment on "The Placental Mammal Ancestor and the Post-K-Pg Radiation of Placentals"

Maureen A. O'Leary, Jonathan I. Bloch, John J. Flynn, Timothy J. Gaudin, Andres Giallombardo, Norberto P. Giannini, Suzann L. Goldberg, Brian P. Kraatz, Zhe-Xi Luo, Jin Meng, Xijun Ni, Michael J. Novacek, Fernando A. Perini, Zachary S. Randall, Guillermo W. Rougier, Eric J. Sargis, Mary T. Silcox, Nancy B. Simmons, Michelle Spaulding, Paúl M. Velazco, Marcelo Weksler, John R. Wible, Andrea L. Cirranello

Tree-building with diverse data maximizes explanatory power. Application of molecular clock models to ancient speciation events risks a bias against detection of fast radiations subsequent to the Cretaceous-Paleogene (K-Pg) event. Contrary to Springer *et al.*, post-K-Pg placental diversification does not require "virus-like" substitution rates. Even constraining clade ages to their model, the explosive model best explains placental evolution.

Full text at <http://dx.doi.org/10.1126/science.1238162>

Letters to the Editor

Letters (~300 words) discuss material published in *Science* in the past 3 months or matters of general interest. Letters are not acknowledged upon receipt. Whether published in full or in part, Letters are subject to editing for clarity and space. Letters submitted, published, or posted elsewhere, in print or online, will be disqualified. To submit a Letter, go to www.submit2science.org.

HISTORY OF SCIENCE

The End Times of Cold War Ecology

Gregg Mitman

The recognition that humans could modify the entire planet did not originate with concerns about global warming. In *Arming Mother Nature*, Jacob Hamblin offers a far-reaching and provocative account of just how dependent narratives of global climate change are upon the military support, apocalyptic scenarios, and political ideology that shaped the growth of the modern environmental sciences during the Cold War.

The triumph of physics during the Second World War, and the nuclear arms race that followed, long overshadowed historical attention to the national defense roles other scientific disciplines played in the battles between communism and the West. But the past decade has brought increasing recognition of the importance of geology, atmospheric science, oceanography, and ecosystem ecology, among other disciplines, to Cold War geopolitical concerns. Hamblin (a historian at Oregon State University) offers a much-needed synthesis that reveals “how fully the experience of the Cold War transformed thinking about humanity, the vulnerabilities of the earth, and the poisoned fruits of human labor.” As he compellingly shows, the prospect of a third world war has been integral to the scientific study, monitoring, and diplomacy of global environmental change since the dawning of the nuclear age.

As the Iron Curtain closed, and U.S. troops landed in Korea, the Joint Chiefs of Staff saw the next war as a total war, one that would be a clash not just of armies but of civilizations. Even without the use of atomic bombs, the military arsenal of biological, chemical, and radiological weapons to come could transform vast areas into uninhabitable wastelands. Hamblin finds little evidence that the United States actually deployed biological weapons in the Korean War, despite accusations by China and endorsements by the French physicist Frédéric Joliot-Curie and the British microbiologist Joseph Needham. The claim’s real significance, Hamblin argues, is that no one questioned the United

States was capable of doing so. Such capability underscored the vulnerability of life—human and nonhuman alike—to the newly acquired, godlike powers of man.

The lessons of ecology for war were readily apparent to military, intelligence, agricultural, and public health agencies in both the East and the West. The disruption of commodities and foodstuffs during World War II made visible the interdependencies of food chains across the world. Taking advantage of vulnerable economies of nature and nations through the design of

biological agents that could destroy crops and livestock was but a first step in the full-scale attempt at ecocide the U.S. military would eventually adopt during the Vietnam War. In one of the most intriguing chapters, Hamblin connects the pioneering work of British ecologist Charles Elton on invasion ecology to issues of agriculture, national security, and defense being discussed within military circles. Elton argued that ecological diversity was the best defense against biological invasion. How fortunate, experts in the United States and Britain believed, that the free market would, unlike centralized communist regimes, ensure the greatest variety of commodities during times of peace, protecting the health of biological populations in the event of war.

The military strategists’ scorched-earth policies held the seeds of a growing global environmental awareness. Harnessing the forces of nature in the interest of defense required knowledge about Earth’s physical environment: its atmosphere, oceans, and lithosphere. Keeping a pulse on the planet arose as a result of both American and Soviet interest in monitoring the bombs going off in each other’s territories and the accompanying spread of radiation around the globe. Programs such as the International Geophysical Year and agencies such as the Atomic Energy Commission and Office of Naval Research channeled funding into meteorology, oceanography, the geological sciences, and ecology to detect radioactivity, monitor fallout,

and understand the operational environment of the next war. With each nuclear test, the environment became a different place. With each thermonuclear explosion came data and the growing recognition—as President John Kennedy observed in 1963—that “science today has the power for the first time in history to undertake experiments with premeditation which can irreversibly alter our biological and physical environment on a global scale.”

In the final section, Hamblin elucidates how much the scenarios emerging at military think tanks like RAND and the doomsday predictions of environmentalists, popularized in best-selling books like *The Population Bomb* and *Limits to Growth* (1, 2), had in common. Both relied upon the same tools, data, and, often, scientists to imagine a future in which overpopulation, disease, resource scarcity, and atmospheric changes threatened human survival. The rhetoric of catastrophic environmentalism proved particularly useful, especially to President Richard Nixon in his pursuit of détente with the Sovi-

Arming Mother Nature
The Birth of Catastrophic Environmentalism

by Jacob Darwin Hamblin
Oxford University Press,
Oxford, 2013. 308 pp. \$29.95,
£18.99. ISBN 9780199740055.



ets. The behind-the-scenes maneuvering of the United States to take control of the 1972 United Nations Conference on the Human Environment and to bankroll the U.N. Environment Programme was, in Hamblin’s view, a strategic move. The Nixon administration sought to neutralize criticism of its environmental warfare in Vietnam and to ensure the United States maintained a leadership role vis-à-vis the Soviet Union as public cries for global environmental action grew louder.

When President Jimmy Carter convened a National Academy of Sciences panel in 1980 to conduct the first comprehensive review of carbon dioxide and climate change, its findings (3) were informed by the previous three decades of research and strategic thinking on environmental futures. Most important, two of the most conservative members of the panel—physicist William Nierenberg

The reviewer is at the Department of Medical History and Bioethics, University of Wisconsin, Madison, WI 53706–1532, USA. E-mail: gmitman@med.wisc.edu

Downloaded from www.sciencemag.org on August 8, 2013

CREDIT: JIM BRANDENBURG/MINDEN PICTURES/GETTY IMAGES

and economist Thomas Schelling—did not deny global warming. Instead, they took issue with the tendency of doomsday environmentalists to regard statist approaches to regulation as the only viable means to avert catastrophe and were confident that the market would help drive adaptation. The Central Intelligence Agency also took seriously the National Academy's report, an indication that the military and intelligence communities have consistently been out ahead of the American public and Congress in imagining and planning for a future in which climate change is real. But they continued to frame it within a Cold War ideology that saw Western market economies as more able to adapt to environmental change than the sluggish, complacent "Communist centralized economies." In the clash of civilizations, the West conveniently "appeared more capable of avoiding extinction."

A telling history, *Arming Mother Nature* illuminates the multiple ways in which our Cold War past continues to shape our environmental future.

References

1. P. R. Ehrlich, *The Population Bomb* (Ballantine, New York, 1968).
2. D. H. Meadows et al., *Limits to Growth: A Report for the Club of Rome's Project on the Predicament of Mankind* (Universe Books, New York, 1972).
3. *Changing Climate: Report of the Carbon Dioxide Assessment Committee* (National Academy of Sciences, Washington, DC, 1983).

10.1126/science.1241257

NAVIGATION

Wayfinding in the Information Age

Deirdre Lockwood

In October 2003, John Edward Huth was kayaking in Nantucket Sound when fog set in. Two months earlier, he had lost his bearings in fog while kayaking in Maine, so this time he had noted the direction of the wind and the sound of a harbor buoy as he set out. He used these signs to steer himself back to land. Unbeknownst to him, two young women were paddling nearby, but they never made it back. Only one of their bodies was recovered, after days of searching. Huth concludes they may have mistakenly headed out to sea.

The reviewer, a 2010 AAAS Mass Media Fellow, is a freelance science writer in Seattle. E-mail: delockwood@gmail.com



Navigational aid. Marshall Islands stick chart from the Peabody Museum, Harvard University.

The incident deeply affected Huth, a Harvard particle physicist who has spent time in pursuit of the Higgs boson. It prompted him to delve into the science and history of human navigation without the aid of our current embarrassment of satellites. He turned his investigations into a freshman seminar, "Primitive Navigation." Now he has synthesized what he's learned into *The Lost Art of Finding Our Way*.

The book offers a clear, comprehensive, and entertaining short course in navigation that draws on Earth science, history, anthropology, neuroscience, archaeology, and linguistics. It provides both a primer on navigational techniques and a tour through "the historical evolution of way finding." Huth punctuates instruction on celestial navigation and reading wind, weather, and currents with engaging stories and images. These are derived from sources as varied as the oral histories of Pacific Islanders and Inuit hunters, Homer's *Odyssey*, Icelandic sagas, navigational tables from the medieval Islamic world, and contemporary news reports and sailing accounts. Huth jumps around nimbly in time and space. For example, he shifts from a mention of stellar navigation in the Book of Job to the story of the "French James Bond," Marc Aubriere. (Kidnapped in 2009 by a radical Islamist group in Mogadishu, Somalia, Aubriere escaped at night and used the stars to find his way to safety.)

In some of the most fascinating parts of

the book, Huth explains the kit of navigational tools traditionally used by Pacific Islanders to find their way over large stretches of ocean between tiny atolls. Mariners created a mental "star compass" by dividing the sky into sections and memorizing which stars rise and set in them depending on progress along a journey and time of year. On the Marshall Islands, navigators have used wave patterns created by winds and refraction and reflection off islands to pilot their way between them. To illustrate and teach these patterns, they constructed complex stick charts by lashing together the midribs of coconut palms and pandanus roots.

Chronicles of human wayfinding are also stories of getting lost, as all navigation is prone to error. Huth describes exercises with his undergraduate students to estimate the uncertainty of different navigational techniques as well as statistical models that predict how far a lost person will stray from his or her origin over time. (The answer: not far. Most, driven by the anxiety of "woods shock," tend to take an approximately "random walk," going in circles.

The author also tells the story of Crocker Land, a gleaming vista in the Canadian Arctic spotted by explorer Robert Peary in 1906. The discovery prompted a 1913 expedition to find it. When the expedition's leader, Donald MacMillan, and a U.S. Navy ensign thought they had sighted the land Peary had described, their Inuit companions saw it for what it was: a mirage caused by light refracting near the horizon. As night fell, Crocker Land had disappeared. MacMillan wondered, "Could Peary with all his experience have been mistaken?" and soon concluded he had been tricked by a *fata morgana*.

Huth is at his best when recounting stories like these. The sections covering the basics of celestial navigation and ocean currents, though clearly written, resemble a textbook in some places. While reading *The Lost Art*, however, I found myself noticing the prevailing winds and watching the skies to predict advancing weather. These things tend to drop away from us in our "bubble," as Huth calls it—whether it is the familiar grid system of a city or the compass of a smartphone in our pockets. As he stresses, to acquire the skills of wayfinding we "absolutely must leave the bubble and look at the stars, the clouds, and the Sun." For those who want to take that journey, he provides an excellent start.

The Lost Art of Finding Our Way

by John Edward Huth
Harvard University Press,
Cambridge, MA, 2013.
538 pp. \$35, £25.00, €31.50.
ISBN 9780674072824.

10.1126/science.1240678

Who Will Pay for Public Access to Research Data?

Francine Berman¹ and Vint Cerf²

On 22 February, the U.S. Office of Science and Technology Policy (OSTP) released a memo calling for public access for publications and data resulting from federally sponsored research grants (1). The memo directed federal agencies with more than \$100 million R&D expenditures to “develop a plan to support increased public access to the results of research funded by the Federal Government.” Perhaps even more succinctly, a subsequent *New York Times* opinion page sported the headline “We Paid for the Research, So Let’s See It” (2). So who pays for data infrastructure?

The OSTP memo requested agencies to provide plans by September 2013 that describe their strategies for providing public access to both research publications and research data. Plans are expected to be implemented using “resources within the existing agency budget,” i.e., no new money should be expected. Currently, federal R&D agencies are working hard to foster approaches to public access, to assess needs for supporting partnerships and enabling infrastructure, and to develop timetables and approaches for implementation. We focus here on the research data portion of the OSTP memo, rather than on publications.

Digital data are ephemeral, and access to data involves infrastructure and economic support. In order to support the downloading of data from federally funded chemistry experiments, astronomy sky surveys, social science studies, biomedical analyses, and other research efforts, the data may need to be collected, documented, organized in a database, curated, and/or made available by a computer that needs maintenance, power, and administrative resources. Access to data requires that the data be hosted somewhere and managed by someone. Technological and human infrastructure supporting data stewardship is a precondition to meaningful access and reuse, as “homeless” data quickly become no data at all.

¹Rensselaer Polytechnic Institute, Troy, NY 12180, USA.

²Google, Reston, VA 20190, USA.

*Corresponding author. E-mail: bermaf@rpi.edu



Research data of community value are supported today in a variety of ways. Some of them, like those in the Protein Data Bank (PDB) (3)—a database of protein structure information used heavily by the life sciences community—are supported by the public sector. (In particular, U.S. funding from the National Science Foundation (NSF), the National Institutes of Health (NIH), and the U.S. Department of Energy for the Research Collaboratory for Structural Bioinformatics (RCSB) PDB is \$6.3 million annually.) Other data, as from the Longitudinal Study of American Youth (LSAY) (4)—a longitudinal study of student attitudes about science and careers—are available through subscription from the Inter-university Consortium for Political and Social Research (ICPSR) at the University of Michigan. (ICPSR membership ranges from \$15,750 for doctoral research—extensive academic institutions to \$1680 for community colleges and provides access to 7500 data collections.) Some data live on researchers’ hard drives, some are stored by the commercial sector, and some are hosted in academic libraries, private or public repositories, or archives. Much of our federally funded research data are “at risk,” with no long-term viable economic model in place to ensure continuing access and preservation for the community. An in-depth study of the economics of digital preservation (5, 6) explored the complex issues of supporting valued data for the public good, but ultimately there is no economic “magic bullet” that does not require someone, somewhere, to pay.

When economic models and infrastructure are not in place to ensure access and preservation, federally funded research data are “at risk.”

What happens to valuable data when project funding ends? Consider, for example, a 3-year research project in which valuable sensor data are collected from an environmentally sensitive area. Those data may be useful not just for the duration of the project but for the next decade or more to collaborators and a broader community of researchers. For the first 3 years, the costs of stewardship (including development of a database that supports analysis, access to the data for the community through

a portal, adequate storage and management of the data collection, and so on) may be paid for by the grant. But who pays for subsequent support? In such cases, research data may become more valuable just as the economics of stewardship become less viable.

Up to this point, no one sector has stepped up to take on the problem alone, and it is unrealistic to expect as much. In the public sector, federal R&D agencies are unlikely to allocate enough resources to support all federally funded research data. The costs of infrastructure would absorb too great a portion of a budget that must support both innovation and the infrastructure needed to drive innovation. The private sector, especially in information technology, has tremendous capacity and expertise to support the stewardship of public-access research data; however, there are few explicit incentives to take this on. In early 2008, Google announced that it would begin to support open-source scientific data sets. By the end of the year, the project was shut down for business reasons (7). Without explicit incentives and credits, it is challenging for companies to step forward and partner productively to support the common good. In the academic sector, university libraries are natural foci for the stewardship of digital research data. But they need financial support to evolve in this direction at a time when many budgets are being cut.

The key is not to look to a particular sector alone but to develop much stronger

partnerships among sectors. Such a division of labor can provide a framework of options that distribute the burdens and benefits of stewardship and economic support. This is a growing trend internationally, where initiatives such as the Vector Ecology and Control Network (VEcNet) (8) are combining private funding (The Gates Foundation and others), public funding (the Australian National Data Service and others), and academic sponsorship (Oxford, the University of Pittsburgh, James Cook University, and others) with the goal of building tools to analyze malaria transmission and reduce its spread by vector control interventions.

... research data may become more valuable just as the economics of stewardship become less viable.

The recent emergence of the community-driven Research Data Alliance (RDA) (9) is also capitalizing on cross-sector and transnational opportunities to build the social, organizational, and technical infrastructure needed to accelerate open-access research data sharing and exchange.

Within the United States, the public access for research data stewardship problem could begin to be addressed through four coordinated approaches:

Facilitate private-sector stewardship of public access to research data. With sufficient public incentives, including tax credits and other means, federal and state governments could make it attractive for the private sector to host, preserve, and serve up public-access research data. Support for the public good is not new to the private sector. Private companies frequently sponsor the arts and social causes, often leveraging advantageous economic models that promote support for the public good. Why not utilize the same approaches to provide stewardship for public-access research data, itself a quasi-public good? Note that it will be important for federal and state incentives to incorporate a commitment to smooth the transition for research data collections when companies choose to move their investments elsewhere. Moreover, adequate safeguards need to be in place to avoid private-sector control of access and use (10, 11).

Use public-sector investment to jump-start sustainable stewardship solutions in other sectors. The success of the Alzheimer's Disease Neuroimaging Initiative (ADNI) (12) demonstrates that public-private partnerships can accelerate research

discovery through data sharing and collaboration. Public partnership with the academic sector can help provide access and stewardship options as well. At present, many progressive university libraries, such as the Johns Hopkins Sheridan Libraries (13), are proactively seeking to address community needs for digital research data stewardship. With an initial public or private short-term "ramp-up" investment in library capacity and workforce (perhaps through something analogous to the federal government's Small Business Innovation Research and Small Business Technology Transfer programs), as well as with the expectation that univer-

sities will work with their libraries to create sustainable economic models when such initial funding has ended, libraries can begin to curate and provide access to some of the data that researchers are generating.

Create and clarify public-sector stewardship commitments for public access to research data. There is ample precedent for the government to support certain data collections of great community value, such as the PDB. However, with thousands of grants per year and data sets ranging from megabytes or less to terabytes or more, not all federally funded data can be realistically hosted within a public repository. In light of this, clarification about which collections would be supported by the public sector, for how long, and under what circumstances would be tremendously helpful to the research community. Knowing what will not be hosted within public repositories could help drive new stewardship efforts in other sectors as well.

Encourage research culture change to take advantage of what works in the private sector. Finally, researchers, like the general public, subscribe to digital versions of newspapers, donate to Wikipedia, pay for and download iTunes, buy data services online, and so forth. In other words, researchers pay for many kinds of digital data. Yet there is widespread expectation that access to research data should be supported by the government or academic institutions and be free to the research community. As community infrastructure becomes increasingly fundamental for data-driven research, the research community could begin to use economic models that are effective else-

where. Imagine supporting the National Virtual Observatory (astronomy data) from telescope advertisements or paying a small download fee for data from digital marine collections in the same way we download music from the Internet. Such economic models will not solve the whole problem but could help provide some infrastructure support necessary for access and preservation of research data. [The possibility of charging for the commercial use of databases as data tools under the take-and-pay rule has been suggested (10).]

Public access presupposes that the research data supported by public funding will be available when they are sought. Such availability is dependent on the existence of effective data infrastructure, i.e., to access data, they must be hosted somewhere, and someone must fund the human and technological infrastructure that hosts the data. Without viable economic models for this infrastructure, valuable research data may disappear, making it accessible to no one and deterring us from making the most of our research investments.

References and Notes

1. J. P. Holdren, Public access memorandum from the Office of Science and Technology Policy; www.whitehouse.gov/sites/default/files/microsites/ostp/ostp_public_access_memo_2013.pdf.
2. Editors, "We Paid for the Research, So Let's See It," *New York Times*, 25 February 2013, p. A24; www.nytimes.com/2013/02/26/opinion/we-paid-for-the-scientific-research-so-lets-see-it.html?_r=0.
3. Biological Macromolecular Resource, RCSB PDB. www.rcsb.org/pdb/home/home.do.
4. Longitudinal Study of American Youth, www.isr.umich.edu/cps/project_lsay.html.
5. Blue Ribbon Task Force on Sustainable Digital Preservation and Access, *Sustaining the Digital Investment: Issues and Challenges of Economically Sustainable Digital Preservation: Interim Report* (BRTF-SDPA, La Jolla, CA, 2008); <http://brtf.sdsc.edu/publications.html>.
6. BRTF-SDPA, *Sustainable Economics for a Digital Planet: Final Report* (BRTF-SDPA, La Jolla, CA, 2010); <http://brtf.sdsc.edu/publications.html>.
7. P. Lenssen, "Google stops research datasets program," Google Blogoscooped; <http://blogoscooped.com/archive/2008-12-23-n33.html>.
8. The Vector Ecology and Control Network, www.vecnet.org/.
9. The Research Data Alliance, <http://rd-alliance.org/node>.
10. J. H. Reichman, R. L. Okediji, *U. Minn. Law Rev.* **96**, 1362 (2012).
11. J. H. Reichman, P. F. Uhlir, *Law Contemp. Probl.* **66**, 315 (2003).
12. Alzheimer's Disease Neuroimaging Initiative, ADNI Overview; <http://www.adni-info.org/Scientists/ADNIOverview.aspx>.
13. R. Monastersky, *Nature* **495**, 430–432 (2013).

Acknowledgments: We thank G. Alter, H. Berman, P. Bourne, B. Plale, S. Choudhury, J. Bicarregui, R. Wilkinson, and the reviewers for their help with specific information for, and comments on, this piece.

10.1126/science.1241625

Buildings as Weapons of Mass Destruction

Roger Bilham¹ and Vinod Gaur²

A quarter of the world's population inhabits the nations of Iran, Afghanistan, Pakistan, India, Nepal, Bhutan, Bangladesh, Sri Lanka, and Myanmar. These countries lie on or near the northern edge of the Arabian and Indian Plates that are colliding with the southern margin of the Eurasian Plate (see the figure, panel A). The collision occurs mid-continent and, as a result, earthquakes have historically destroyed many settlements, especially in Iran (*1*). Deaths from earthquakes since 1900 have exceeded those in all previous centuries, and earthquake deaths to the east of Iran have far outnumbered those in Iran (see the figure, panel B). We ascribe this to the recently increased population at risk in Pakistan and India and to the fragility of construction methods introduced there in the past century.

Construction Without Oversight

After each damaging earthquake, engineers tasked with reconstruction confront two questions: Why did so many structures collapse? And to what potential future accelerations will new construction be exposed?

Postseismic investigations reveal that structural collapse is typically attributable to shoddy construction resulting from poverty and ignorance, or to covert avoidance of building codes by contractors (*2, 3*). Moreover, earthquake-resistant design codes, where they exist, are generally applied to civic structures only, and not to the dwellings where most of the people of South Asia live (*3*). Pervasive building fragility is all too frequently highlighted by the spontaneous collapse of multistory structures in the major cities of south Asia. During strong earthquakes, widespread building collapse is not only expected but also statistically quantifiable within minutes of the mainshock and is used to aid search and rescue (*4, 5*).

The second question addresses the adequacy of prevailing seismic building codes.

After an earthquake, the default engineering fix has been to rebuild with a code anticipating an earthquake of similar severity. Revisions to seismic risk maps of India and Pakistan soon follow major earthquakes, endorsing a perception of increased seismic risk in the region of a recent earthquake. A moment's reflection will reveal a flaw in this reasoning. Once an earthquake has drained local strain energy, the next damaging earthquake will most likely occur elsewhere in the region. Improved hazard maps are desirable, and where the historical record is long compared to the recurrence interval of earthquakes, a map of seismic risk may indeed resemble that of historical earthquakes. Unfortunately, the seismic history of most of the region is short compared to the recurrence interval between its earthquakes.

Toward Estimates of Seismic Risk

The region of highest seismic productivity in south central Asia is the Himalaya collision itself, where several major earthquakes in the past 200 years have resulted in tens of thousands of fatalities (see the figure, panel A). Geological evidence for slip on the Himalayan frontal thrust caused by two great historical earthquakes in 1255 and 1505 has also been reported (*6, 7*). Furthermore, the tectonic setting of recent and anticipated earthquakes has been elucidated from Global Positioning System (GPS) geodesy (measurements of surface strain rates) and background seismicity measurements (*8*). The recurrence interval of earthquakes remains elusive for most of the Himalayan arc, but there is good reason to suppose (*7*) that a sequence of great Himalayan earthquakes in the past 10,000 years will eventually be assembled that will guide quantitative estimates of Himalayan seismic risk.

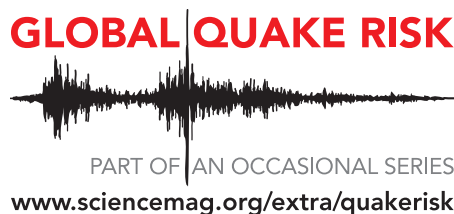
Although populations near the Himalaya face a clear risk from future great earthquakes, moderate earthquakes throughout the continental collision zone threaten a far

The enforcement of sound building practices would substantially reduce future fatalities from earthquakes in south central Asia.

greater population. The characterization of seismic risk in Iran benefits from a well-documented seismic history and numerous seismogenic surface faults that permit this history to be extended, in some cases by many tens of thousands of years (*9*). The faults that host earthquakes far from India's plate boundaries are less easy to characterize. GPS geodesy reveals negligible deformation (below 2 mm per year) within the Indian Plate, even near the fatal June 1819 and January 2001 magnitude 7 earthquakes in Bhuj. The historical record of mid-plate earthquakes offers little quantitative guidance (*10*), and the paleoseismic history of mid-plate earthquakes is difficult to capture, because the faults on which they occur rarely rupture the surface. The secondary effects of strong shaking recorded by disturbed soils and marine sediments, however, hold promise for complementing the meager written record.

Another approach to supplement the historical record in the Indian Plate has been to investigate physical models of continental collision. The front edge of India is bent downward by about 4 km by the weight of Tibet. This flexural loading stretches the surface and compresses the base of the Indian Plate in northern India and does the reverse in southern India, with a stress intensity that diminishes with distance from the Himalaya. Local extremes in compression or tension result in earthquakes throughout the subcontinent. Additional stresses arise from sedimentary loads along India's rifted shorelines (*11*). These stresses and their slow variation with time are the reason that much of the continental Indian Plate is close to seismic failure; their spatial distribution provides a foundation for maps of future seismic risk.

There remains the disquieting possibility that India's historical record—even if it were known precisely—may not be a reliable key to its seismic future. Reservoirs have triggered earthquakes in Koyna,



¹Cooperative Institute for Research in Environmental Sciences and Department of Geological Sciences, University of Colorado, Boulder, CO 80309, USA. ²CSIR Centre for Mathematical Modelling and Computer Simulation, Bangalore, and Indian Institute of Astrophysics, Bangalore 560 034, India. E-mail: bilham@colorado.edu; vgaur@iiap.res.in

Warna, and, debatably, Latur (12). On a continental scale, the unloading of the flexural depression in the north by depletion of subsurface reservoirs in the Punjab and Ganges plains and the corresponding increase in loading from new reservoirs in the south (13) have adversely perturbed the preindustrial flexural loading of the Indian Plate. Although these stresses are small, they could prove fatal because they act on a system close to failure.

Seismic Risk Versus Progress

Earthquake hazard maps characterizing potentially active faults (in India, few active faults are exposed at Earth's surface) are in

their infancy, and there are almost no data on the attenuation of strong shaking with distance in large earthquakes or the local amplification of seismic waves in cities. The establishment and implementation of credible earthquake-resistant building codes thus remains a data-gathering challenge for scientists, engineers, and planners of South Asia.

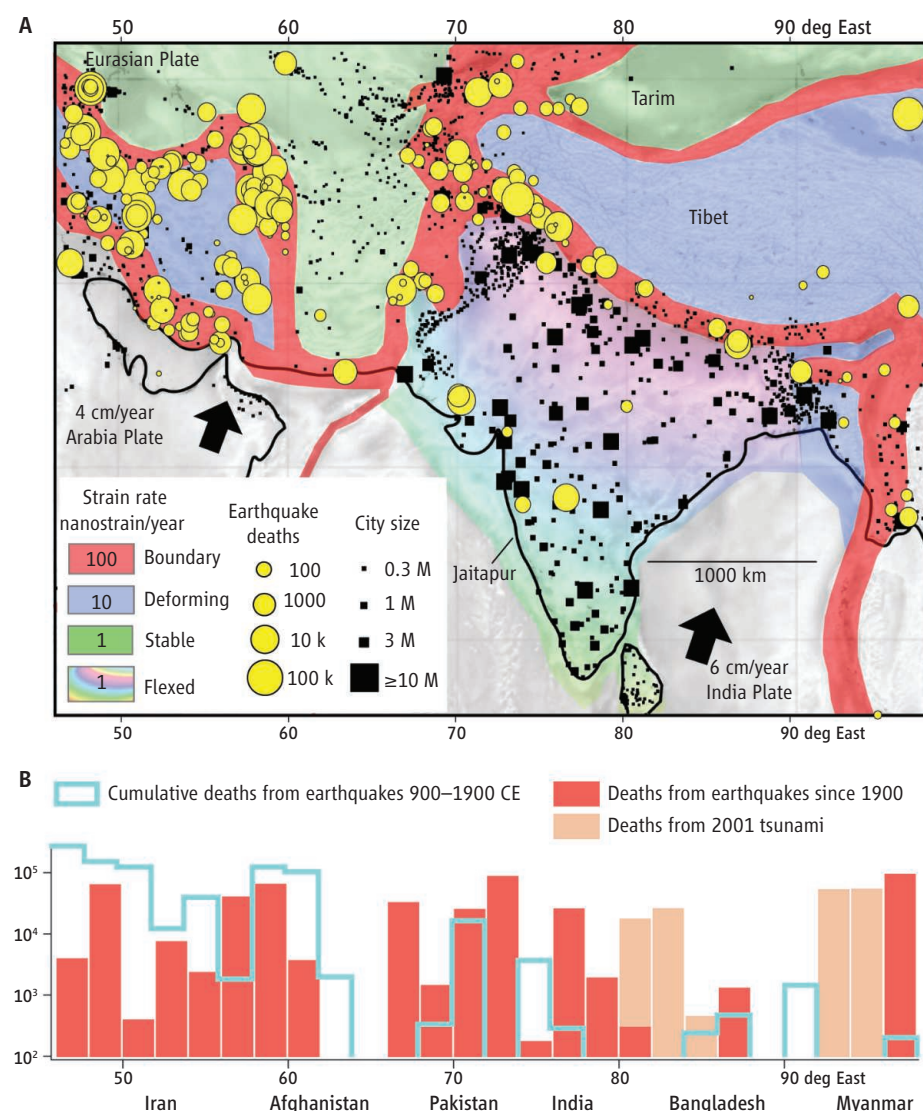
These studies will take many decades to complete, yet immediate and crucial decisions must also be made by those responsible for the safety of critical facilities. Nuclear power plants can be constructed to withstand the largest of earthquakes, but engineers need trustworthy estimates

of potential future accelerations. India has adopted a routine approach to calculating these accelerations (14) but unsubstantiated claims for low seismic hazards at a planned nuclear power plant at Jaitapur south of Mumbai have left many uneasy (15). The plant will be constructed on a coastal plain crossed by a fault that since 50,000 years ago may have lowered (11) the planned plant site by more than 20 m. The timing of earthquakes that permitted the fault to slip, and therefore its earthquake hazard, is unknown (11, 15).

However, by far the greatest risk from earthquakes in South Asia is currently not from its nuclear facilities but from its fragile dwellings that will collapse in quite modest future shaking. Deaths from future earthquakes could be vastly reduced, with no additional scientific input, were governments to enforce existing construction codes. Conversely, the development of improved estimates of seismic risk will be futile if governments permit unauthorized and unsound construction practices to continue (3, 4).

References and Notes

1. P. England, J. Jackson, *Nat. Geosci.* **4**, 348 (2011).
2. S. K. Jain, *Curr. Sci.* **89**, 1464 (2005).
3. R. Bilham, *Tectonophysics* **584**, 166 (2013).
4. M. Wyss, in *Disasters and Society: From Hazard Assessment to Risk Reduction*, D. Malzahn, T. Plapp, Eds. (Logos, Karlsruhe, 2004), pp. 165–173.
5. K. Jaiswal, D. Wald, D. D'Ayala, *Earthq. Spectra* **27**, 775 (2011).
6. S. Kumar, S. G. Wesnousky, R. Jayagondaperumal, T. Nakata, Y. Kumahara, V. Singh, *J. Geophys. Res.* **115**, B12422 (2010).
7. S. N. Sapkota, L. Bollinger, Y. Klinger, P. Tappinier, Y. Gaudemer, D. Tiwari, *Nat. Geosci.* **6**, 152 (2013).
8. J. P. Avouac, *Adv. Geophys.* **46**, 1 (2003).
9. R. Walker, J. Jackson, *Tectonics* **23**, TC5010 (2004).
10. R. N. Iyengar, D. Sharma, J. M. Siddiqui, *Indian J. Hist. Sci.* **34**, 181 (1999).
11. V. K. Gaur, R. Bilham, *Curr. Sci.* **103**, 1273 (2012).
12. P. Talwani, *Pure Appl. Geophys.* **150**, 511 (1997).
13. V. M. Tiwari, J. Wahr, S. Swenson, *Geophys. Res. Lett.* **36**, L18401 (2009).
14. A. C. Roshan, P. C. Basu, *Nucl. Eng. Des.* **240**, 3443 (2010).
15. Recent seismic quiescence near a planned coastal nuclear power plant at Jaitapur is interpreted in an unpublished government report to signify a zero to low future seismic risk (16, 17), but recent damaging earthquakes at Koyna and Latur suggest the potential for a strong earthquake at Jaitapur if a capable fault exists near the site (11). The scientific discussion of seismic hazards in southern India has triggered unexpected government intervention (18).
16. Press release issued by the Nuclear Power Corporation of India on 17 January 2012; see www.npcil.nic.in/pdf/Seismicity_Considerations_for_Jaitapur_NPP.pdf (last accessed 18 June 2013).
17. B. K. Rastogi, *Curr. Sci.* **103**, 130 (2011).
18. P. Bagla, *Science* **338**, 1275 (2012).
19. R. Bilham, *Bull. Earthquake Eng.* **2009**, pp. 1–49.



Zones of death. (A) High strain rates at plate boundaries result in more frequent earthquakes, but infrequent mid-continent earthquakes far from plate boundaries and near urban populations are responsible for most earthquake fatalities (11). M, million; k, thousand. (B) Most fatalities from earthquakes before 1900 occurred in Iran. Earthquakes since 1900 have killed as many again as in the 900 preceding years and have been more evenly distributed across the region. Data from (19).

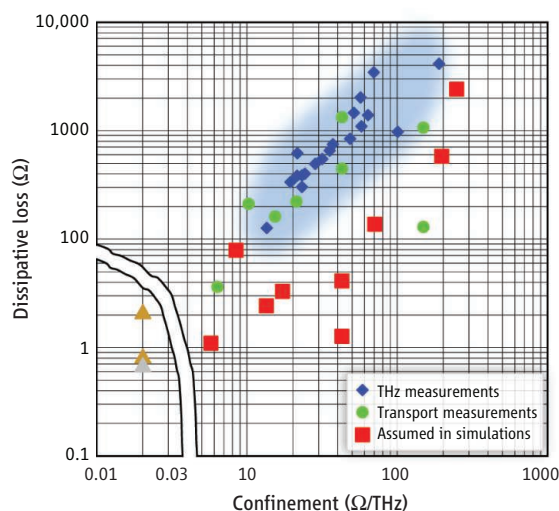
Graphene for Terahertz Applications

Philippe Tassin¹, Thomas Koschny¹, Costas M. Soukoulis^{1,2}

Graphene is a one-atom-thick sheet of carbon atoms arranged in a honeycomb lattice. First obtained by exfoliation of graphite in 2004 (1), graphene has since evolved into a thriving research topic because of its attractive mechanical, thermal, and electrical properties (2–4), particularly the exceptionally high electron mobility. Such properties promise to revolutionize many applications (2–4), ranging from solar cells and light-emitting devices to touch screens, photodetectors (4), microwave transistors (5), and ultrafast lasers (6). We discuss here a number of special qualities of graphene that also make it desirable for devices manipulating terahertz waves.

The single layer of carbon atoms enables device miniaturization down to the atomic length scale. The tunable electrical properties, realized by raising or lowering the Fermi level, allow for unprecedented tunability of electromagnetic structures made of this material. The electric response of a graphene sheet is highly reactive, resulting in the existence of strongly localized, deeply subwavelength plasmons (collective electronic excitations), as well as the reduction of the resonance frequency of resonant structures made of patterned graphene that allows these resonators to be made much smaller than their resonance wavelengths. Also, with optical excitation, it is possible to create an inversion of the whole conical electronic band around the Dirac point up to the pump frequency, which should afford sizable broadband gain from terahertz to optical frequencies.

Although there are abundant estimates from simplified theoretical models and experimental data for the DC properties of graphene from transport measurements, experimental data on the terahertz properties, especially the complex optical sheet conductivity, have become available only in the past few years. These data are essential to assess the potential performance of graphene in its various envisioned applications (7). The sheet resistivity (the real part of the inverse com-



How graphene measures up. Overview of the sheet conductivity of graphene classified according to the dissipative loss and the confinement as found in current literature [detailed data are provided in the supplementary materials (15)].

plex sheet conductivity) determines the loss, which relates to the dissipative quality factor of graphene-based metamaterials, as well as the propagation length of surface plasmons. The sheet inductivity (the imaginary part of the inverse complex sheet conductivity divided by the angular frequency) determines the confinement or kinetic inductance, which translates to the saturation frequency—or maximum resonance frequency—of small-scale metamaterial resonators, as well as to the “subwavelengthness” and lateral confinement of the surface plasmons.

We surveyed direct experimental measurements of the terahertz sheet conductivity of graphene found in the literature (see the figure, blue diamonds) (8–11). Select experimental data from transport measurements (green circles) are shown for comparison. Theoretical investigations of potential graphene applications have chosen different, mostly very optimistic, assumptions (red squares) for the sheet conductivity. Notably, the theoretical loss estimates are generally about one order of magnitude below the experimental data. For reasonable carrier densities, these theoretical studies obtain interesting device behavior if the sheet resistivity is roughly 100 ohms or smaller (12, 13). Much

The optoelectronic properties of graphene are being explored for possible use in plasmonics and metamaterials at terahertz frequencies.

effort has been directed to producing pristine samples and, indeed, suspended graphene (minimizing disorder and phonons originating from the substrate), cleaned in situ by heating, has shown impressive mobilities exceeding $10^5 \text{ cm}^2/\text{V}\cdot\text{s}$, but at the expense of very limited carrier concentrations. On the other hand, large doping levels have been demonstrated by electrolytic gating, but this has led to much higher scattering.

Interestingly, the experimental data line up within a rather narrow corridor (shaded blue), indicating that the variance in carrier concentration roughly trades higher confinement for higher loss in existing graphene samples. However, this observation should not be considered to indicate a particular dependence of the momen-

tum relaxation time on carrier concentration, as the available samples differ substantially from one another. Nevertheless, it illustrates the current discrepancy between the experimentally realizable and the theoretically desired performance.

For metamaterial applications, graphene has to compete with metals. A 30-nm film of gold (7) has an experimentally measured sheet resistivity on the order of 1 ohm [yellow (Au) and gray (Ag) triangles in the figure], two orders of magnitude smaller than the theoretical lower limit of 30 ohms for free-standing graphene at room temperature (14). The miniaturization advantage of graphene is marginal at terahertz frequencies, because the gold film is still much thinner than the free-space wavelength, and other constraints (e.g., minimum area to maintain a useful magnetic moment) require larger unit cells. However, a major drawback of metals is their lack of control over carrier density. Graphene offers a substantial advantage as its properties can be readily tuned by applying a gate voltage.

For plasmonics, the main challenge is the short propagation length in graphene that is on the order of a few surface plasmon wavelengths at best in state-of-the-art experiments. However, tunability and confinement,

¹Ames Laboratory—U.S. Department of Energy and Department of Physics and Astronomy, Iowa State University, Ames, IA 50011, USA. ²Institute of Electronic Structure and Lasers (IESL), FORTH, 71110 Heraklion, Crete, Greece. E-mail: soukoulis@ameslab.gov

in particular, may outweigh this limitation in the terahertz region as there are few alternatives (plasmon confinement on metals is very poor below optical frequencies).

Graphene is a fascinating material for terahertz applications with its strengths in atomic thickness, easy tunability, and high kinetic inductance. The major challenge for these resonant high-frequency applications remains to overcome the dissipative loss, which might be less of a disadvantage for surface plasmonics on graphene than for graphene as a substitute for metals in metamaterials.

References and Notes

1. K. S. Novoselov *et al.*, *Science* **306**, 666 (2004).
2. F. Bonaccorso, Z. Sun, T. Hasan, A. C. Ferrari, *Nat. Photon.* **4**, 611 (2010).
3. K. S. Novoselov *et al.*, *Nature* **490**, 192 (2012).
4. A. N. Grigorenko, M. Polini, K. S. Novoselov, *Nat. Photon.* **6**, 749 (2012).
5. Y. M. Lin *et al.*, *Science* **327**, 662 (2010).
6. T. Li *et al.*, *Phys. Rev. Lett.* **108**, 167401 (2012).
7. P. Tassin, T. Koschny, M. Kafesaki, C. M. Soukoulis, *Nat. Photon.* **6**, 259 (2012).
8. H. Yan *et al.*, *Nat. Nanotechnol.* **7**, 330 (2012).
9. J. Chen *et al.*, *Nature* **487**, 77 (2012).
10. Z. Fei *et al.*, *Nature* **487**, 82 (2012).
11. Z. Q. Li *et al.*, *Nat. Phys.* **4**, 532 (2008).
12. A. Vakil, N. Engheta, *Science* **332**, 1291 (2011).
13. F. H. L. Koppens, D. E. Chang, F. J. García de Abajo, *Nano Lett.* **11**, 3370 (2011).

14. J.-H. Chen, C. Jang, S. Xiao, M. Ishigami, M. S. Fuhrer, *Nat. Nanotechnol.* **3**, 206 (2008).
15. See supplementary materials on Science Online.

Acknowledgments: Supported by Ames Laboratory, U.S. Department of Energy (Basic Energy Sciences, Division of Materials Sciences and Engineering), under contract DE-AC02-07CH1358; by European Research Council grant no. 320081 (PHOTOMETA); and by Office of Naval Research, award no. N00014-10-1-0925.

Supplementary Materials

www.sciencemag.org/cgi/content/full/341/6146/620/DC1
Table S1
References

10.1126/science.1242253

TRANSCRIPTION

Flashing a Light on the Spatial Organization of Transcription

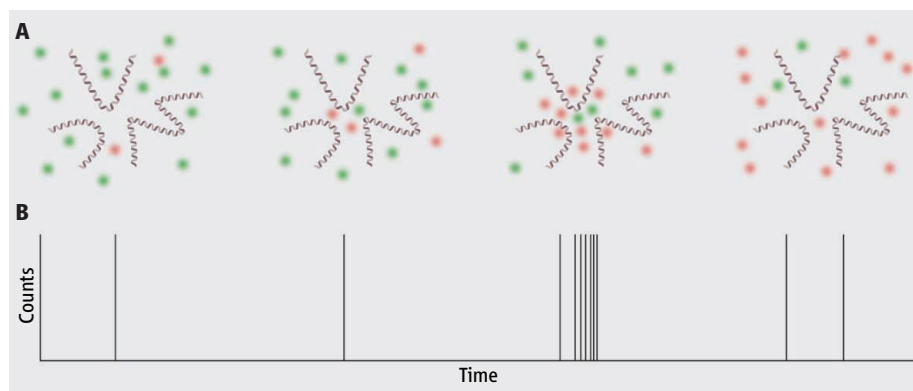
Colin Rickman^{1,2} and Wendy A. Bickmore^{2,3}

It is surprising that the question of how transcription occurs in the eukaryotic cell nucleus is still a matter of controversy, given that it is such a basic cellular process. Conventional imaging of transcription sites, RNA polymerase II (Pol II), and active genes suggests that transcription occurs at discrete places in the nucleus, termed transcription factories. What has not been clear is whether these sites are pre-assembled structures that prefigure function and to which genes must then move to be transcribed, or whether they are self-organizing zones that form at active gene loci during the process of gene expression (1). One problem in resolving these issues has been the lack of information about the formation and stability of transcription factories in living cells—which could not be detected by conventional light microscopy with green fluorescent protein (GFP)-tagged Pol II (2). On page 664 of this issue, Cisse *et al.* (3) surmount this problem by using single-molecule light microscopy to determine the spatiotemporal organization of Pol II in the nucleus. Their observations of the formation of short-lived Pol II clusters that respond to transcriptional stimuli provide compelling

evidence against the idea of preassembled stable transcription factories.

Cisse and colleagues expressed an α -amanitin-resistant form of the Pol II catalytic subunit (RPB1), fused to the photo-switchable fluorescent protein Dendra2, in a human cell line in which endogenous Pol II was destroyed with α -amanitin (4). Photo-activation localization microscopy (PALM) (5) was then used to examine Pol II at single-molecule resolution. By photoswitching a small subset of the Dendra2–Pol II molecules (see the figure, panel A), their emitted light can be spatially resolved and their

molecular position determined with high precision (on the order of tens of nanometers). However, a major limitation of PALM is that all depth (axial) information is lost in the final data set, commonly limiting its application to the study of events at the cell surface. Cisse *et al.* circumvented this problem by performing PALM in live cells and analyzing both the size and the dynamics of cluster formation. Pair correlation was used to determine the probability of molecules residing at given distances from each other. This demonstrated the presence of Pol II clusters with an estimated size of ~100 nm,



Clustering to transcribe. (A) Cartoon showing four frames taken from a time series of images of Dendra2–Pol II molecules (small circles) in a small genomic region before (green) and after (red) photoswitching. In the third frame from the left, the sudden appearance of a large number of photoswitched molecules in the imaged area indicates the formation of a Pol II cluster. That this does not continue into the fourth frame, even though photoswitching continues generally, indicates cluster dispersal. (B) Graph showing the detection (vertical lines) of Dendra2–Pol II photoswitching events per frame that might be seen from the images in (A); the temporally correlated high detection counts in the third frame indicate cluster formation.

¹Institute of Biological Chemistry, Biophysics and Bioengineering, Heriot-Watt University, Edinburgh EH14 4AS, UK. ²Edinburgh Super-Resolution Imaging Consortium, www.esric.org. ³MRC Human Genetics Unit, Institute of Genetics and Molecular Medicine, University of Edinburgh, Edinburgh EH4 2XU, UK. E-mail: wendy.bickmore@igmm.ed.ac.uk

in good agreement with electron microscopy studies of transcription factories (6).

Normally in PALM data sets, the time of localization during the experiment is discarded. However, by using this information in a technique called tcPALM (time-correlated detection counting PALM), the authors detected molecules that were clustered not only in space but in time. Clusters formed rapidly (average lifetime ~5 s), followed by a sharp decrease in the number of molecules detected in the cluster (see the figure, panel B). This can be interpreted as the dynamic assembly and disassembly of Pol II foci, compatible with previous observations of GFP-tagged Pol II on an artificial gene array (7) but not consistent with the idea of preformed stable transcription factories. Furthermore, both the size and lifetime of clusters increase (the latter by almost an order of magnitude) when transcription is stimulated by serum addition. Together, these data strongly suggest that Pol II clusters form as a consequence of events linked to transcription.

Transcription initiates when Pol II is bound to a promoter and opens the double-stranded DNA to form a transcription bubble. However, for most genes Pol II then pauses and subsequent elongation requires the removal of negative elongation factors by the P-TEFb kinase (4). Because Pol II clusters were still detected when transcription elongation was blocked with the P-TEFb inhibitor flavopiridol, Cisse *et al.* conclude that cluster formation is not a consequence of transcription elongation but is likely linked to transcription initiation, or preinitiation. However, the clusters that formed in the presence of flavopiridol appeared much more stable, implying that cluster dissolution is linked to the transition from transcription initiation into elongation. Disassembly could not be directly reported by the technique described in their study, because molecules that have already been used to report cluster formation cannot be imaged again (the fluorophores are photodestroyed during the acquisition) and the inverse of a burst would simply be an uninterpretable absence of signal. To measure disassembly directly will require an entirely new experimental approach, potentially using dynamic fluorescence resonance energy transfer (FRET) measurements to report loss of clustering.

The data provided by the creative imaging approach reported by Cisse *et al.* are consistent with the transient accumulation of Pol II at genes as they are activated, as has been seen during the activation of Hsp70 genes

on *Drosophila* polytene chromosomes (8). Although RNA fluorescence in situ hybridization was used to show the coincidence of messenger RNA (mRNA) for an active gene (β -actin) with a Pol II cluster, the current study cannot address whether Pol II clusters form over the gene, or whether the gene is recruited to a Pol II cluster—although the latter would have to occur very rapidly, given the observed kinetics. Also unresolved is whether any one cluster is associated with just one gene or with several.

What might be the function—if any—of the rapid formation of transient Pol II clusters? Transcription involves a complex series of protein-protein and protein-DNA interactions, and requires the assembly of very large complexes at promoters. The efficiency of transcription initiation may therefore be enhanced if transient molecular crowding of key components helps to drive rate-limiting steps. For most genes, transcription is discontinuous, with bursts of mRNA production interspersed with periods of inactivity (9). By coupling the dynamic analysis of Pol II with live-cell imaging of transcription from a specific gene, it may be possible to determine whether the Pol II cluster lifetime corresponds directly to the burst size of transcription.

PHYSIOLOGY

Lymphatics Are in My Veins

Michael Simons^{1,2} and Anne Eichmann^{1,3,4}

Molecular mechanisms regulating lymphangiogenesis may be exploited as potential treatments for disorders of lymphatic circulation.

The lymphatic system is generally underappreciated until something goes wrong. It controls fluid balance, dietary lipid absorption, and immune surveillance (1). When disrupted in adults, the consequences can be lethal, arising from inflammation, infection, and fibrosis. Impaired lymphatic vessel development causes fluid and protein accumulation in tissues, resulting in lymphedema, a disfiguring and disabling swelling of the extremities and

The elegant study of Cisse *et al.* serves to illustrate how super-resolution and fast live-cell imaging, when coupled to carefully considered data analysis and the ability to inhibit specific processes, can provide insights into long-standing biological questions. A goal must now be to integrate this new information into the biochemistry of transcription initiation and into studies of three-dimensional genome organization.

References and Notes

1. H. Sutherland, W. A. Bickmore, *Nat. Rev. Genet.* **10**, 457 (2009).
2. H. Kimura, K. Sugaya, P. R. Cook, *J. Cell Biol.* **159**, 777 (2002).
3. I. I. Cisse *et al.*, *Science* **341**, 664 (2013); 10.1126/science.1239053.
4. O. Bensaude, *Transcription* **2**, 103 (2011).
5. A. L. McEvoy, D. Greenfield, M. Bates, J. Liphardt, *BMC Biol.* **8**, 106 (2010).
6. F. J. Iborra, A. Pombo, D. A. Jackson, P. R. Cook, *J. Cell Sci.* **109**, 1427 (1996).
7. X. Darzacq *et al.*, *Nat. Struct. Mol. Biol.* **14**, 796 (2007).
8. J. Yao, M. B. Ardehali, C. J. Fecko, W. W. Webb, J. T. Lis, *Mol. Cell* **28**, 978 (2007).
9. J. R. Chubb, T. Trcek, S. M. Shenoy, R. H. Singer, *Curr. Biol.* **16**, 1018 (2006).

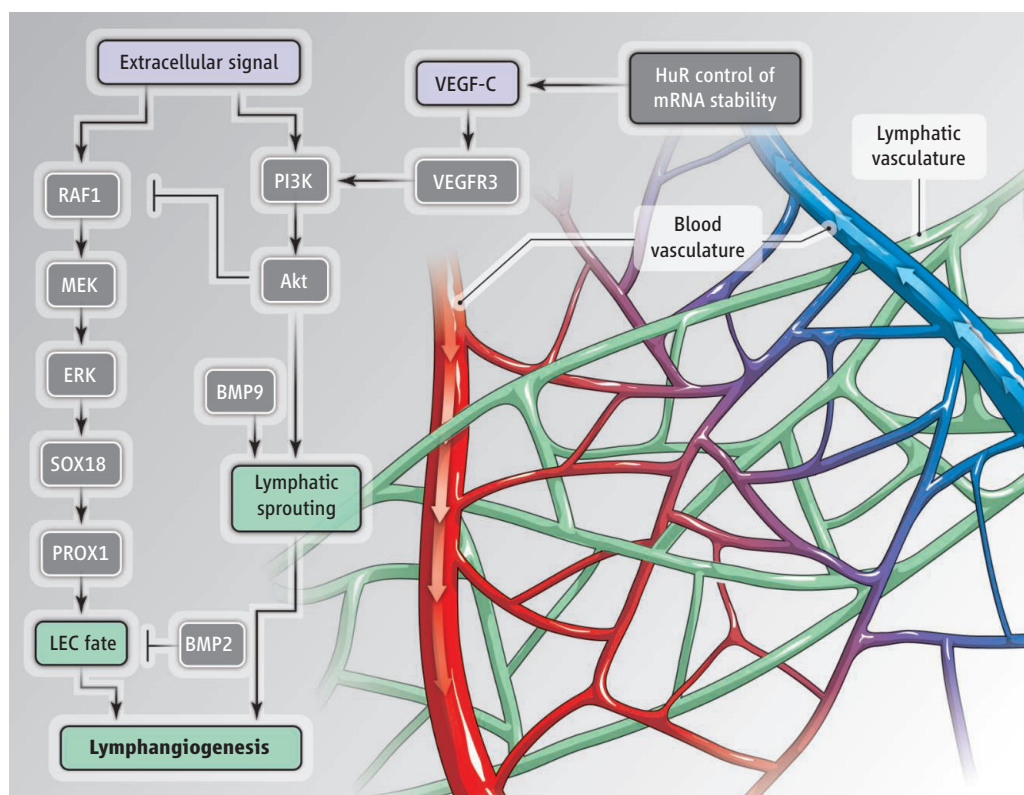
Acknowledgments: Supported by the Wellcome Trust (C.R.), European Research Council advanced grant 249956 (W.A.B.), and the UK Medical Research Council.

10.1126/science.1242889

other parts of the body. Moreover, lymphedema and chronic inflammation are aggravating factors in cardiovascular disease. Therapeutic agents that can promote lymphatic vessel formation (lymphangiogenesis) should prevent lymphedema and benefit individuals with cardiovascular pathologies. Both blood-vascular and lymphatic circulatory systems are closely intermingled and share many molecular signaling mechanisms for their development (2). At a recent meeting (3), advances in our understanding of these mechanisms indicate that selectively targeting lymphatic vessels without affecting blood vessels remains a challenge.

The major growth factors that regulate angiogenesis (new blood vessel formation from existing vessels) and lymphangiogenesis include vascular endothelial growth fac-

¹Yale Cardiovascular Research Center, Yale University School of Medicine, New Haven, CT 06510, USA. ²Department of Cell Biology, Yale University School of Medicine, New Haven, CT 06510, USA. ³Department of Cellular and Molecular Physiology, Yale University School of Medicine, New Haven, CT 06510, USA. ⁴Center for Interdisciplinary Research in Biology, Collège de France, Inserm 1050, Paris cedex 05, France. E-mail: michael.simons@yale.edu



Lymphatic vessels. The blood-vascular system and lymphatic system are closely intertwined in tissues. The growth factor VEGF-C promotes both angiogenesis and lymphangiogenesis. The signaling pathways that promote lymphangiogenesis are shown. MEK, mitogen-activated protein kinase kinase; RAF1, rapidly accelerated fibrosarcoma 1.

tor A and C (VEGF-A and -C). A deficiency in VEGF-A is lethal in early embryonic mice due to nearly complete failure of blood vessel development. Mice lacking VEGF-C die later in embryogenesis from the absence of lymphatic vessel sprouting. Thus, there are critical, nonoverlapping functions for VEGF-A and -C in the development of both circulatory systems. However, VEGF-C also affects angiogenesis (4), and although it is currently the most promising avenue to treat lymphedema (5), it may also induce blood vessel growth and unwanted side effects in patients. Developing selective therapies to promote lymphangiogenesis requires better knowledge about the context-dependent signaling of VEGF-C in blood and lymphatic vessels.

During embryonic life, lymphatics develop from veins after the onset of circulation. This requires a subset of blood-vascular endothelial cells (BECs) in the jugular vein to acquire lymphatic identity. These lymphatic endothelial cells (LECs) must then migrate out of the cardinal vein and form the jugular lymphatic sacs, which through expansion and sprouting give rise to the entire lymphatic vasculature.

The cellular signaling events determining lymphatic fate specification involve

sequential activation of two transcription factors, SOX18 and PROX1, in the cardinal vein. In the absence of Sox18 or Prox1 function in the mouse, venous endothelial cells fail to express LEC-specific “identity” markers, leading to failure of lymphatic programming (6, 7). Prox1 is required throughout life to maintain LEC identity; deletion of the *Prox1* gene at any stage of mouse development reverses LEC to BEC identity, and leads to the fusion of LECs with blood vessels (8). How Sox18 expression is limited to a subset of cells in the cardinal vein is unknown. Sox18 and Prox1 are expressed in vein endothelial cells for a defined developmental period, but how this determines the total number of LECs generated is also unknown.

Two key findings provide new insight into how LEC specification is controlled. Signaling by bone morphogenetic protein 2 (BMP2) is required for venous sprouting angiogenesis, without affecting arteries (9). This increase in venous cells may occur at the expense of LEC formation; BMP2 blocks Prox1 expression, which suppresses LEC specification (3). Factors turning off BMP2 signaling may hence represent the elusive inducers of LEC differentiation. Another finding is that increased signaling

by extracellular signal-regulated kinase (ERK) enhances Sox18 expression and LEC differentiation, leading to sustained LEC specification and outmigration from the cardinal vein. The result is pathologically smaller veins, enlarged lymphatic vessels, and lymphangiectasia (dilation of lymph vessels) (10). Together, these findings suggest that the BEC decision to become lymphatic or remain venous is determined by a balance between different signaling inputs, and reveal at least two variables that control LEC specification—BMP2 and ERK signaling. Thus, the simultaneous suppression of BMP2 and activation of ERK should markedly increase this specification (see the figure).

The process of LEC sprouting is also mysterious. VEGF-C and its cognate receptor VEGFR3 constitute the only signaling system thus far implicated in this process (1, 2). In the absence of functional VEGFR3, LECs become properly specified but cannot sprout from the cardinal

vein. However, VEGFR3 also affects angiogenesis (4). It is expressed on both BECs and LECs during early mouse embryonic development, and its expression decreases in BECs after LEC specification while remaining high in LECs. How VEGFR3 signaling acts in several distinct contexts during both blood-vascular and lymphatic development is unknown. In BECs, VEGFR3 regulates sprouting angiogenesis through crosstalk with the signaling pathway controlled by Notch protein, but the role of Notch in LECs is not fully understood (3, 11).

VEGF-C binding induces VEGFR3 dimerization and subsequent receptor autophosphorylation of tyrosine residues within its cytoplasmic domain. VEGFR3 activates two signaling pathways—phosphatidylinositol 3-kinase (PI3K)—Akt and ERK—through different phosphorylated tyrosines, which suggests that each output may lead to distinct cellular responses at the different developmental steps (3, 12). However, little is known about the *in vivo* requirement for either signaling branch. Mice lacking *pik3r1*, which encodes the regulatory subunit of PI3K, display defects in lymphatic remodeling and maturation, whereas lymphatic vessels show an increased expression of BEC markers such as endoglin (13). It may be that

down-regulation of ERK activity (by the enzyme Akt) could serve as a critical control point in LEC sprouting and also contribute to LEC differentiation and the maintenance of lymphatic identity (3).

It is likely that VEGFR3 signaling outputs are further modulated by other signaling molecules expressed at the same time. The receptors for BMPs and transforming growth factor- β (TGF β) emerge as interesting candidates in this context. Inducible, endothelial-specific deletion of TGF β receptors (TGF β R2 and Alk5) suppresses LEC sprouting at the expense of LEC proliferation by altering the expression of VEGFR3 and another VEGF-C receptor called neuropilin-2 (3). BMP9, which binds with high affinity to a receptor complex composed of BMPR2 and Alk1, also affects lymphangiogenesis (14, 15). Alk1 inhibition using a “ligand trap” blocked sprouting angiogenesis and decreased lymphangiogenesis (15, 16), which suggests that BMP9 may be a potential target for promoting lymphangiogenesis without stimulating growth of blood vessels. Further studies are required

to determine how BMPs and TGF β affect lymphangiogenesis.

Other important recent discoveries in the field include the RNA binding protein called human antigen R (HuR) in maintaining the stability of mRNA encoding VEGF-C and -A. Depending on the cell type in which HuR is deleted, this results in impairment of lymphangiogenesis or angiogenesis (3). LEC mechanosensing is also emerging as a critical regulator of lymphangiogenesis and lymphatic valve formation, although many details are yet to be filled in (17, 18). And exciting results suggest that cutaneous lymph capillaries are important for systemic blood pressure control by locally modulating skin electrolyte composition (19).

Unlike the blood system, much about the lymphatic system remains elusive. As our understanding of its development and pathology grows, we should begin to finally develop treatments for lymphedema and other disorders of lymphatic circulation—progressive, lifelong conditions that affect millions of people, for whom curative treatments are currently not available.

References and Notes

1. K. Alitalo, *Nat. Med.* **17**, 1371 (2011).
2. K. Koltowska, K. L. Betterman, N. L. Harvey, B. M. Hogan, *Development* **140**, 1857 (2013).
3. Yale-North American Vascular Biology Organization (NAVBO) Lymphatic Circulation in Health and Disease meeting, New Haven, CT, 3 to 4 May 2013.
4. T. Tammela *et al.*, *Nat. Cell Biol.* **13**, 1202 (2011).
5. T. Tammela *et al.*, *Nat. Med.* **13**, 1458 (2007).
6. J. T. Wigle, G. Oliver, *Cell* **98**, 769 (1999).
7. M. François *et al.*, *Nature* **456**, 643 (2008).
8. N. C. Johnson *et al.*, *Genes Dev.* **22**, 3282 (2008).
9. D. M. Wiley *et al.*, *Nat. Cell Biol.* **13**, 686 (2011).
10. Y. Deng *et al.*, *J. Clin. Invest.* **123**, 1202 (2013).
11. A. Murtomaki *et al.*, *Development* **140**, 2365 (2013).
12. L. D. Covassin, J. A. Villefranc, M. C. Kacergis, B. M. Weinstein, N. D. Lawson, *Proc. Natl. Acad. Sci. U.S.A.* **103**, 6554 (2006).
13. C. Mouta-Bellum *et al.*, *Dev. Dyn.* **238**, 2670 (2009).
14. S. Levet *et al.*, *Blood*. 10.1182/blood-2012-12-472142 (2013)
15. K. Niessen *et al.*, *Blood* **115**, 1654 (2010).
16. B. Larrivée *et al.*, *Dev. Cell* **22**, 489 (2012).
17. C.-Y. Chen *et al.*, *J. Clin. Invest.* **122**, 2006 (2012).
18. A. Sabine *et al.*, *Dev. Cell* **22**, 430 (2012).
19. H. Wiig *et al.*, *J. Clin. Invest.* **123**, 2803 (2013).

Acknowledgments: We thank J. Bender, T. Hla, Y. Mukoyama, S.-W. Jin, and W. Sessa for permission to cite findings that were presented at the conference (3).

10.1126/science.1243452

CHEMISTRY

Copper's Contribution to Amination Catalysis

Sherry R. Chemler

Copper complexes are used as catalysts in modern synthetic chemistry because of their low cost, versatile reactivity, and broad tolerance for functional groups on substrates. Oxidation states in copper complexes can range from Cu⁰ to Cu^{IV}, and the metal center can participate in either two-electron or single-electron processes, sometimes both in the same catalytic cycle (1–6). This perspective highlights copper's contribution to amination catalysis, specifically the formation of carbon-nitrogen (C–N) bonds by coupling amines or amides with aryl halides (ArX) and alkyl halides (Ullmann-Goldberg reaction), arenes and alkanes [carbon-hydrogen (C–H) bond amination], or alkenes (oxidative amination, aminooxygenation, carbamination, and diamination).

Formation of C–N bonds is one of the most common transformations in pharma-

ceutical synthesis. The Ullmann-Goldberg reaction, which couples aryl halides with anilines and amides (see the figure, panel A), has undergone extensive development since its initial discovery in 1906 (4, 7). Initially, this reaction was performed with limited substrates at high temperatures (~210°C) with elemental copper (>13 mol %). Subsequent work showed that certain ligands and solvents (that can serve as ligands) substantially increase copper's catalytic activity and opened up a much broader substrate range. The reaction can be run at moderate temperatures (23° to 130°C) and in most cases with lower catalyst loading (1 to 20 mol %).

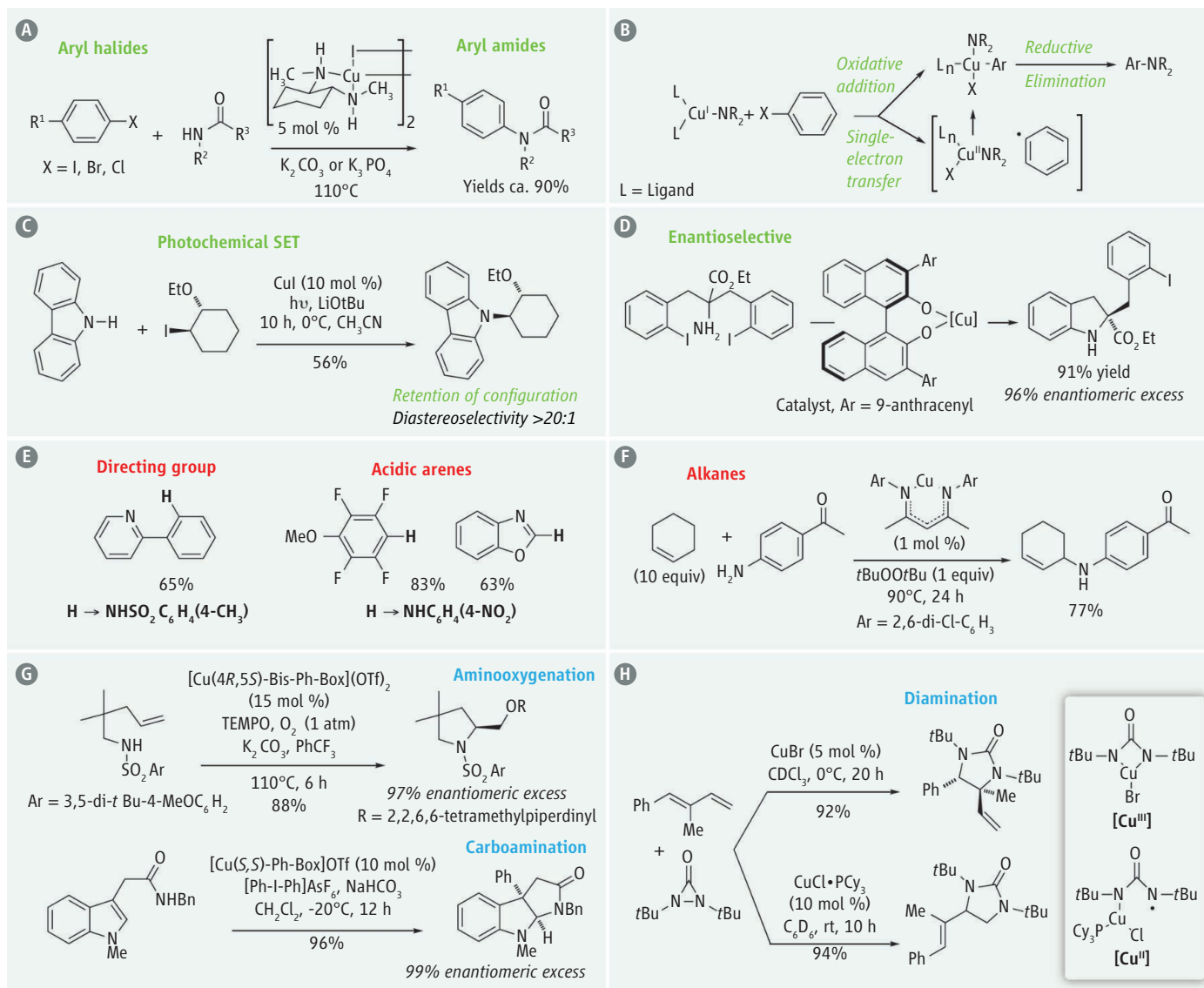
The mechanism of the Ullmann-Goldberg reaction is thought to initiate with the formation of an amido-copper(I) intermediate (see the figure, panel B) (8, 9) that reacts with aryl halides. The resulting organocopper(III) intermediate undergoes reductive elimination to form the C–N bond and regenerate the [Cu^I] catalyst (10). Mech-

Copper complexes catalyze a remarkably broad range of organic reactions that form carbon-nitrogen bonds.

anisms involving oxidative addition into the Ar–X bond or single-electron transfer (SET), possibly via atom transfer, have been proposed for this step. The former creates the organocopper(III) intermediate directly, whereas the latter forms an aryl radical that can add to the resulting [Cu^{II}].

The SET mechanism can be favored if the reaction is promoted by light at temperatures where the thermal reaction is not observed (11). Ultraviolet light excites an electron on the copper(I) amide to a higher-energy state, which in turn reduces the aryl halide to an aryl radical that combines with the resulting copper(II) amide to form a copper(III) intermediate. This strategy was also used to couple amines and alkyl halides (12). Reaction temperatures can be reduced with these photoreactions, and the stereochemical outcome could be altered, such as net retention of configuration at carbon instead of the usual inversion of configuration (see the figure, panel C) (12). In this reaction, the

Department of Chemistry, The State University of New York, Buffalo, NY 14260, USA. E-mail: schemler@buffalo.edu



Copper catalysis of carbon-nitrogen bond formation. Examples and mechanistic details are shown for reactions that form amides from (A to D) aryl and alkyl halides, and (E and F) activated C-H bonds. In (G), nucleophilic addition of amine nucleophiles to alkenes is shown for aminooxygenation and carboamination. In (H), an example of diamination is shown. Conditions in (D) were 10 mol %

CuI, 20 mol % chiral ligand, Cs₂CO₃, dioxane, room temperature (rt) for 10 hours (h). Conditions in (E) were 20 mol % copper(II) acetate, 1 atm O₂. For the first example, *p*-toluenesulfonamide, dimethylsulfoxide, 48 hours, 160°C were used, and for the other examples 4-NOC₆H₄NH₂, dimethylformamide, potassium *tert*-butoxide, TEMPO, 40° or 80°C, 24 hours were used.

stereochemistry of the alkyl amine product is controlled by the chirality of the carbon adjacent to the halogenated carbon.

A chiral copper catalyst can be used to control the absolute stereochemistry in the thermal Ullmann-Goldberg reaction manifold (see the figure, panel D) (13). The desymmetrization of an achiral substrate that contains both amine and aryl halide components was achieved, forming a chiral indoline. The researchers proposed that the enantioselectivity was determined in the oxidative addition step (13).

Direct amination of a C-H bond bypasses the need for adding a halide to an existing molecule. Oxygen gas is frequently used as

an environmentally benign stoichiometric oxidant in these reactions. At present, copper-catalyzed C-H aminations are limited to acidic arenes (those functionalized with electron-withdrawing groups) and those functionalized with directing groups usually adjacent (ortho) to the C-H bond (see the figure, panel E) (6, 10). Copper-catalyzed C-H aminations can occur either via two-electron or SET mechanisms, depending largely upon the substrate's structure and the oxidants and ligands used. Copper-catalyzed intra- and intermolecular net C-H aminations of activated alkenes (vinyl arenes) that involve nitrogen radical intermediates have also been reported (14).

The C-H amination of alkanes under oxidizing conditions (15) can occur and proceed either as concerted, C-H insertion of copper nitrenes ([Cu]=NR), or cascades in which C-H atom abstraction is followed by radical rebound processes. In both cases, weaker C-H bonds, such as those adjacent to phenyl rings and alkenes, can be targeted (see the figure, panel F). Asymmetric catalysis has been achieved in a few allylic amination cases; yields and enantioselectivities are promising but moderate (yields up to 44%; enantioselectivities up to 70%) (16).

Copper catalysts enable the addition of amine nucleophiles to alkenes by acting as an electrophile to accept π -bond electrons.

Copper(II)-2,2'-isopropylidenebis[(4*R*,5*S*)-4,5-diphenyl-2-oxazoline]ditriflate {[Cu(4*R*,5*S*)-bis-Ph-box](OTf)₂} catalyzes intramolecular additions of sulfonamides to terminal alkenes with concomitant addition of the stable oxygen radical (2,2,6,6-tetramethylpiperidine-1-yl)oxyl (TEMPO) (see the figure, panel G) (17). The mechanism involves concerted intramolecular addition of R₂N-[Cu^{II}] across the alkene followed by C-[Cu^{II}] homolysis and subsequent carbon radical coupling with TEMPO. A different ring-forming alkene amino-functionalization strategy involves electrophilic addition of a chiral organocopper(III) complex (formed in situ by oxidation of a chiral Cu^I complex with [Ph-I-Ph]AsF₆) (where Ph is phenyl) to the electron-rich alkene of an indole (see the figure, panel G) (18). Amine addition to the resulting iminium ion forms a new C–N bond, and reductive elimination provides the chiral C–C bond.

Finally, diamination is one of the more sought-after alkene difunctionalization

reactions, and it can occur as an intermolecular copper-catalyzed reaction of dienes with diaziridinones with complementary regioselectivity by either a two-electron or single-electron mechanism, depending upon the ligands used (see the figure, panel H) (19). Oxidative addition of [Cu^I] into the diaziridinone gives a new [Cu^{III}] species that can be in equilibrium with a [Cu^{II}] species by Cu–N homolysis. Electrophilic addition of the copper(III) species to the alkene occurs at the more electron-rich, internal alkene, generating the internal diamine. This preference can be changed by addition of the bulky PCy₃ (tricyclohexylphosphine) ligand, which shifts the equilibrium to the copper(II)-aminyl radical species that favors addition to the terminal alkene carbon.

References

1. J. S. Johnson, D. A. Evans, *Acc. Chem. Res.* **33**, 325 (2000).
2. S. R. Harutyunyan, T. den Hartog, K. Geurts, A. J. Minnaard, B. L. Feringa, *Chem. Rev.* **108**, 2824 (2008).
3. M. Meldal, C. W. Tornøe, *Chem. Rev.* **108**, 2952 (2008).

4. K. Kunz, U. Scholz, D. Ganzer, *Synlett* **2003**, 2428 (2003).
5. A. Casitas, X. Ribas, *Chem. Sci.* **4**, 2301 (2013).
6. C. Zhang, C. Tang, N. Jiao, *Chem. Soc. Rev.* **41**, 3464 (2012).
7. A. Klapars, X. Huang, S. L. Buchwald, *J. Am. Chem. Soc.* **124**, 7421 (2002).
8. G. O. Jones, P. Liu, K. N. Houk, S. L. Buchwald, *J. Am. Chem. Soc.* **132**, 6205 (2010).
9. E. Sperotto, G. P. M. van Klink, G. van Koten, J. G. de Vries, *Dalton Trans.* **39**, 10338 (2010).
10. A. E. Wendlandt, A. M. Suess, S. S. Stahl, *Angew. Chem. Int. Ed.* **50**, 11062 (2011).
11. S. E. Creutz, K. J. Lotito, G. C. Fu, J. C. Peters, *Science* **338**, 647 (2012).
12. A. C. Bissemer, R. J. Lundgren, S. E. Creutz, J. C. Peters, G. C. Fu, *Angew. Chem. Int. Ed.* **52**, 5129 (2013).
13. F. Zhou *et al.*, *J. Am. Chem. Soc.* **134**, 14326 (2012).
14. T. W. Liwosz, S. R. Chemler, *Chem. Eur. J.* **10**, 1002/chem.201301800 (2013).
15. R. T. Gephart III, T. H. Warren, *Organometallics* **31**, 7728 (2012).
16. J. S. Clark, C. Roche, *Chem. Commun.* **2005**, 5175 (2005).
17. M. C. Paderes, J. B. Keister, S. R. Chemler, *J. Org. Chem.* **78**, 506 (2013).
18. S. Zhu, D. W. C. MacMillan, *J. Am. Chem. Soc.* **134**, 10815 (2012).
19. B. Zhao *et al.*, *J. Am. Chem. Soc.* **133**, 20890 (2011).

10.1126/science.1237175

GENETICS

The Maturing Brain Methylome

Harrison W. Gabel and Michael E. Greenberg

The methylation of DNA in mammalian genomes regulates gene expression, guiding differentiation and maintaining cellular identity within tissues. However, it may have a distinct function in the brain. On page 629 of this issue, Lister *et al.* (1) present a comprehensive analysis of DNA methylation and hydroxymethylation at single-base resolution in the mammalian frontal cortex. The authors chart out striking postnatal alterations in neuronal methylation profiles that occur as synapses develop and are refined, from the fetal to adult stage. The patterns suggest that DNA methylation is important in the maturation of neurons in the developing brain.

DNA methylation represses gene expression in all mammalian cells. The methylation of cytosines in the context of cytosine-guanine dinucleotides (mCG) is a stable repressive mark on DNA. However, the Tet family of enzymes converts methylcytosine to hydroxymethylcytosine (hmC), an oxidized form that can be demethylated (2, 3). hmC is enriched in stem cells and neurons, suggest-

ing that they might be particularly susceptible to changes in DNA methylation state (2, 4). Intriguingly, stem cells and brain tissue also contain substantial cytosine methylation outside of the CG context [mCH, where H is adenine (A), thymine (T), or cytosine (C)], which is rare in most somatic cells (5, 6). Although the role of hmC and mCH in stem cells has been extensively investigated at base-pair resolution (5, 7), there has been limited examination of DNA methylation at high resolution in the brain.

Using high-throughput sequencing to profile the mouse and human cortex from the fetal to adult stage, Lister *et al.* revealed a conserved, genome-wide increase in mCH amounts in the brain after birth. Although the period during which mCH accumulates differs between mice and humans (several weeks versus several years, respectively), the increase coincides with the peak of synaptogenesis and synaptic pruning in the brain for each organism (see the figure). Thus, the acquisition of mCH may be linked to neuronal maturation. High amounts of mCH were found in neurons compared to low amounts in nonneuronal (glial) cells. Although the average percentage methylation detected in neu-

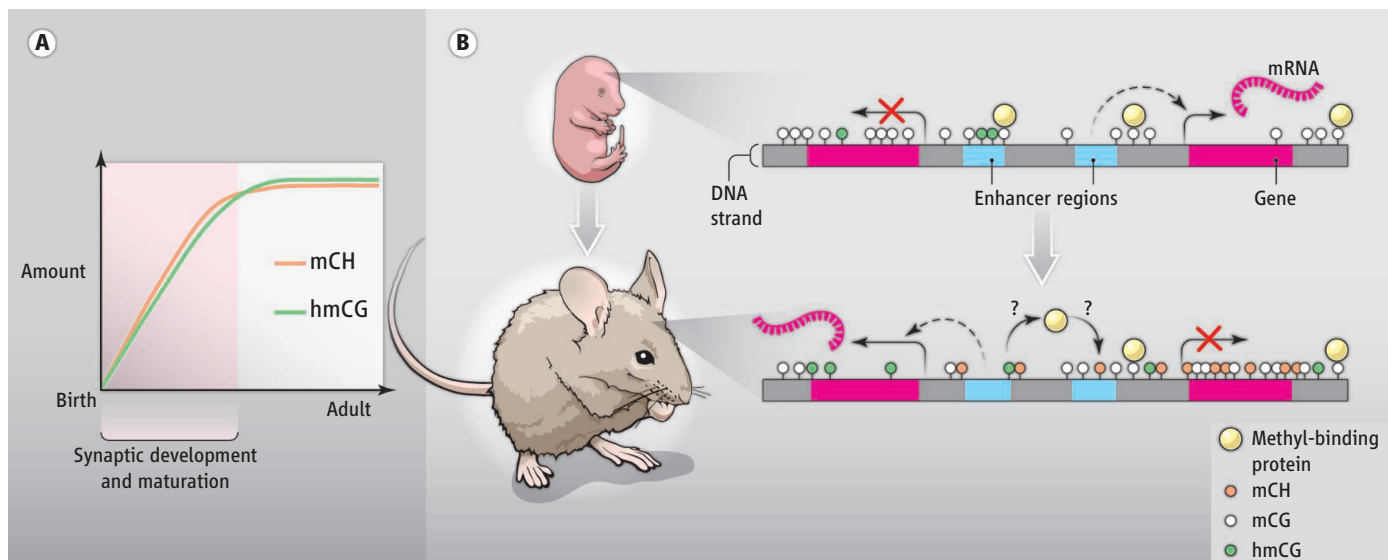
DNA methylation patterns in the developing and adult mammalian brain point to a role in synaptic development and maturation.

rons at CH is quite low (~2 to 6%) and quite high at CG (~80%), because CG is rare in mammalian genomes relative to CH, a similar number of total mCH and mCG events occur in neurons. Indeed, in adult human neurons, the total number of mCH sites surpasses that of mCG sites. Rather than a minor addition to the methylation modifications in the genome ("methylome"), mCH is likely a major substrate for gene regulation in the maturing brain.

hmC builds up in neurons with a timing similar to that of mCH (8), raising the possibility that, in addition to occurring at CG, hydroxymethylation also takes place at CH in the brain. Lister *et al.* used another high-throughput sequencing method (9) to profile hmC at single-base resolution in mouse fetal and adult frontal cortex. Surprisingly, even though hmC and mCH both accumulate as the brain matures, hydroxymethylation occurs almost exclusively in the hmCG context. If mCH is converted to hmCH at all, it must be extraordinarily short-lived, as it is essentially undetectable at steady-state amounts.

To better understand how methylation contributes to transcriptional regulation, Lister *et al.* performed integrated analysis

Department of Neurobiology, Harvard Medical School, Boston, MA 02115, USA. E-mail: michael.greenberg@hms.harvard.edu



A distinct neuronal methylome. (A) High mCH and hmCG accumulate in mammalian neurons postnatally, coinciding with the period of active synapse development and maturation. (B) mCH builds up in adult neurons and is enriched at repressed genes and enhancers. hmCG associates with active genes and can premark enhancers in the fetal brain that will become demethylated and active in the adult. Differential affinity to hmCG and mCH may alter the binding profile of methyl-DNA-binding proteins and thereby control distinct neuronal transcription.

of hmC, mCG, and mCH profiles, mRNA expression, and epigenomic data sets from the brain. The authors observed an expected enrichment of mCG and mCH at genes and distal regulatory elements correlating with transcriptional repression, whereas hmC is deposited across active genes (6, 8). Previously undescribed patterns of methylation in the brain also were uncovered, such as enrichment of mCH at genes that escape X-chromosome inactivation in females. Lister *et al.* also noted that, while glial genomes contain low global amounts of mCH, mCH is enriched at genes that are repressed in either neurons or glia, indicating that mCH may enforce cell-type-specific transcription in both of these related cell lineages. Further, the authors detected thousands of developmental-stage- and cell-type-specific methylation sites at putative enhancers. Thus, some inactive enhancers in the fetal brain are marked with hydroxymethylation, which likely leads to subsequent demethylation and activation in the adult.

The findings of Lister *et al.* pave the way for examining how the brain-specific methylome is established. For example, the enzymes that generate high amounts of hmC and mCH in neurons have not yet been described. A strong candidate is Dnmt3a, a

methyltransferase that peaks in expression in neurons during the period of mCH deposition and displays methylation activity on CH dinucleotides (10). Likewise, it has not been fully determined which Tet enzyme(s) drive the buildup and patterning of neuronal hmC. Because hmC and mCH profiles display a high degree of conservation and reproducibility across individuals, they likely result from regulated processes. However, it is unclear to what extent the patterns of hmC and mCH in neurons result from sequence-directed targeting mechanisms or if they occur secondarily, guided by accessible chromatin structure or transcriptional activity.

Although the profiles point to regulatory roles for mC and hmC in the brain, the mechanisms by which these marks are read out to affect gene expression await elucidation. It will be essential to understand which DNA binding factors are recruited to mCG, mCH, and hmCG to mediate their regulatory functions. Multiple proteins differentially bind to unmethylated, methylated, and hydroxymethylated DNA (11, 12). In neurons, high hmCG amounts at some CG sites could block proteins from binding, whereas mCH may provide an array of new binding sites in the genome. Notably, the methyl-DNA-binding protein MeCP2 accumulates in the brain with a timing similar to that of the increase in mCH and hmC (13). It is possible that in neurons, MeCP2 binds to the additional sites afforded by mCH to repress genes. Because disruption of MeCP2 leads to the neurodevelopmental disorder Rett syndrome (14), it will be important to determine how mCH affects the function of this protein.

Could the epigenomic rearrangements uncovered by Lister *et al.* participate in the development and maturation of synaptic con-

nections? Because the frontal cortex develops postnatally in concert with input from the environment, it is possible that neuronal-specific DNA methylation contributes to sensory input-dependent changes in gene expression and synaptic development. Alternatively, high amounts of mCH and hmC may facilitate the generation of diverse neuronal subtypes; acquisition of the neuronal-specific methylome coincides with the final stages of neuronal differentiation that give rise to the many neuronal subtypes of the brain. The propensity of mCH to mark cell-type-specific genes and the differential methylation of enhancers suggest that the methylation profile of a neuron may dictate its specific gene expression profile and functions within the context of a neural circuit. Future studies should determine whether epigenomic rearrangements affect neuronal cell-type diversity and/or sensory-dependent synapse maturation and circuit formation in the developing brain.

References

1. R. Lister *et al.*, *Science* **341**, 1237905 (2013); 10.1126/science.1237905.
2. M. Tahiliani *et al.*, *Science* **324**, 930 (2009).
3. J. U. Guo, Y. Su, C. Zhong, G. L. Ming, H. Song, *Cell Cycle* **10**, 2662 (2011).
4. S. Kriaucionis, N. Heintz, *Science* **324**, 929 (2009).
5. R. Lister *et al.*, *Nature* **462**, 315 (2009).
6. W. Xie *et al.*, *Cell* **148**, 816 (2012).
7. M. J. Ziller *et al.*, *PLoS Genet.* **7**, e1002389 (2011).
8. K. E. Szulwach *et al.*, *Nat. Neurosci.* **14**, 1607 (2011).
9. M. Yu *et al.*, *Cell* **149**, 1368 (2012).
10. B. H. Ramsahoye *et al.*, *Proc. Natl. Acad. Sci. U.S.A.* **97**, 5237 (2000).
11. M. Mellén, P. Ayata, S. Dewell, S. Kriaucionis, N. Heintz, *Cell* **151**, 1417 (2012).
12. C. G. Spruijt *et al.*, *Cell* **152**, 1146 (2013).
13. P. J. Skene *et al.*, *Mol. Cell* **37**, 457 (2010).
14. R. E. Amir *et al.*, *Nat. Genet.* **23**, 185 (1999).

10.1126/science.1242671

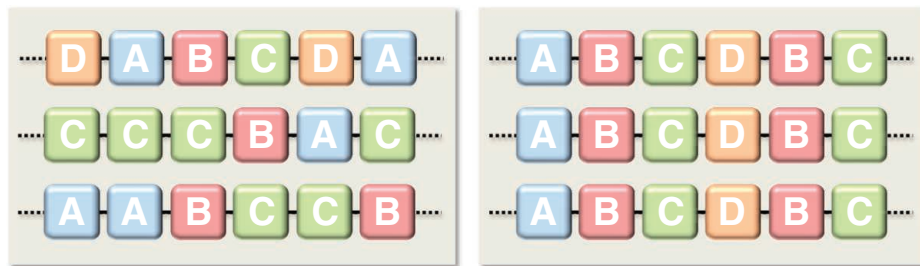
Sequence-Controlled Polymers

Jean-François Lutz,* Makoto Ouchi, David R. Liu, Mitsuo Sawamoto

Background: During the last few decades, progress has been made in manipulating the architecture of synthetic polymer materials. However, the primary structure—that is, the sequential arrangement of monomer units in a polymer chain—is generally poorly controlled in synthetic macromolecules. Common synthetic polymers are usually homopolymers, made of the same monomer unit, or copolymers with simple chain microstructures, such as random or block copolymers. These polymers are used in many areas but do not have the structural and functional complexity of sequence-defined biopolymers, such as nucleic acids or proteins. Indeed, monomer sequence regulation plays a key role in biology and is a prerequisite for crucial features of life, such as heredity, self-replication, complex self-assembly, and molecular recognition. In this context, developing synthetic polymers containing controlled monomer sequences is an important area for research.

Advances: Various synthetic methods for controlling monomer sequences in polymers have been identified, and two major trends in the field of sequence-controlled polymers have emerged. Some approaches use biological concepts that have been optimized by nature for sequence regulation. For instance, DNA templates, enzymes, or even living organisms can be used to prepare sequence-defined polymers. These natural mechanisms can be adapted to tolerate nonnatural monomers. The other trend is the preparation of sequence-controlled polymers by synthetic chemistry. In the most popular approach, monomer units are attached one by one to a support, which is an efficient method but demanding in practice. Recently, some strategies have been proposed for controlling sequences in chain-growth and step-growth polymerizations. These mechanisms usually allow fast and large-scale synthesis of polymers. Specific kinetics and particular catalytic or template conditions allow sequence regulation in these processes.

Outlook: The possibility of controlling monomer sequences in synthetic macromolecules has many scientific and technological implications. Information can be controlled at the molecular level in synthetic polymer chains. This opens up interesting perspectives for the field of data storage. In addition, having power over monomer sequences could mean structural control of the resulting polymer, as it strongly influences macromolecular folding and self-assembly. For instance, functional synthetic assemblies that mimic the properties of globular proteins, such as enzymes and transporters, can be foreseen. Moreover, monomer sequence control influences some macroscopic properties. For example, bulk properties such as conductivity, rigidity, elasticity, or biodegradability can be finely tuned in sequence-controlled polymers. The behavior of polymers in solution, particularly in water, is also strongly dependent on monomer sequences. Thus, sequence regulation may enable a more effective control of structure-property relations in tomorrow's polymer materials.



Precise molecular encoding of synthetic polymer chains. In most synthetic copolymers, monomer units (represented here as colored square boxes A, B, C, and D) are distributed randomly along the polymer chains (left). In sequence-controlled polymers, they are arranged in a specific order in all of the chains (right). Monomer sequence regularity strongly influences the molecular, supramolecular, and macroscopic properties of polymer materials.

READ THE FULL ARTICLE ONLINE

<http://dx.doi.org/10.1126/science.1238149>



Cite this article as J.-F. Lutz *et al.*, *Science* **341**, 1238149 (2013). DOI: 10.1126/science.1238149

ARTICLE OUTLINE

Sequence-Controlled Biological Polymerization Processes

Sequence-Controlled Polymerizations Based on Chemical Approaches

Properties and Promises of Sequence-Controlled Polymers

Outlook

RELATED ITEMS IN SCIENCE

K. Matyjaszewski, Architecturally complex polymers with controlled heterogeneity. *Science* **333**, 1104–1105 (2011). doi:10.1126/science.1209660

V. B. Pinheiro *et al.*, Synthetic genetic polymers capable of heredity and evolution. *Science* **336**, 341–344 (2012). doi:10.1126/science.1217622

F. S. Bates *et al.*, Multiblock polymers: Panacea or Pandora's box? *Science* **336**, 434–440 (2012). doi:10.1126/science.1215368

G. M. Church *et al.*, Next-generation digital information storage in DNA. *Science* **337**, 1628 (2012). doi:10.1126/science.1226355

B. Lewandowski *et al.*, Sequence-specific peptide synthesis by an artificial small-molecule machine. *Science* **339**, 189–193 (2013). doi:10.1126/science.1229753

BACKGROUND READING

R. B. Merrifield, Solid phase synthesis (Nobel lecture). *Angew. Chem. Int. Ed. Engl.* **24**, 799–810 (1985). doi:10.1002/anie.198507993

D. M. Rosenbaum, D. R. Liu, Efficient and sequence-specific DNA-templated polymerization of peptide nucleic acid aldehydes. *J. Am. Chem. Soc.* **125**, 13924–13925 (2003). doi:10.1021/ja038058b Medline

S. Pfeifer, J.-F. Lutz, A facile procedure for controlling monomer sequence distribution in radical chain polymerizations. *J. Am. Chem. Soc.* **129**, 9542–9543 (2007). doi:10.1021/ja0717616 Medline

J. Li, R. M. Stayshich, T. Y. Meyer, Exploiting sequence to control the hydrolysis behavior of biodegradable PLGA copolymers. *J. Am. Chem. Soc.* **133**, 6910–6913 (2011). doi:10.1021/ja200895s Medline

The list of author affiliations is available in the full article online.

*Corresponding author. E-mail: jflutz@unistra.fr

Sequence-Controlled Polymers

Jean-François Lutz,^{1*} Makoto Ouchi,² David R. Liu,³ Mitsuo Sawamoto²

Sequence-controlled polymers are macromolecules in which monomer units of different chemical nature are arranged in an ordered fashion. The most prominent examples are biological and have been studied and used primarily by molecular biologists and biochemists. However, recent progress in protein- and DNA-based nanotechnologies has shown the relevance of sequence-controlled polymers to nonbiological applications, including data storage, nanoelectronics, and catalysis. In addition, synthetic polymer chemistry has provided interesting routes for preparing nonnatural sequence-controlled polymers. Although these synthetic macromolecules do not yet compare in functional scope with their natural counterparts, they open up opportunities for controlling the structure, self-assembly, and macroscopic properties of polymer materials.

Copolymers are long macromolecular chains composed of at least two monomers of different chemical natures (1). In many copolymers, the distribution of the monomers along the chains is uncontrolled and, therefore, varies from chain to chain. In sequence-controlled polymers, however, the monomer units are arranged in the same precise order in all chains rather than randomly distributed. Alternating, periodic, or block copolymers composed of two monomers, A and B, for example, represent the simplest level of sequence-controlled polymers (2). Beyond that, there are more complex monomer sequence patterns. For instance, two or more monomer units can constitute a precise molecular “code” in a polymer chain. Prime examples are found in biology. Nucleic acids, such as DNA and RNA, exhibit ordered sequences based on four-nucleotide monomer units. In proteins, 20 amino acids are used to form precisely regulated monomer sequences. Such precise positioning of monomer units (or functionalities) has an important influence on polymer structure and creates unique properties, such as molecular recognition, biocatalysis, and molecular encoding of information.

Similar to the role DNA plays in genes, well-defined sequences in synthetic polymers may serve as molecular-level information storage devices in which each functional side-group may be regarded as an information “bit.” Therefore, sequence-defined oligomers and polymers have gained importance in both fundamental polymer science and numerous technological applications. For instance, the application of DNA goes well beyond biotechnology to areas of nanotechnology and materials science (3). However, DNA is not unique in its suitability as a manipulable sequence-controlled polymer. Chemistry and bi-

ology offer many interesting alternatives for the preparation of sequence-defined macromolecules. The most serious challenge may be that no general and versatile strategy has been found for synthesizing sequence-controlled polymers. In principle, polymers with regulated sequences of monomers can be prepared using either chemical or biological methods. The latter strategy is especially efficient, as it relies on highly evolved biological mechanisms. For example, the enzymes—or even the complete systems for replication, transcription, and translation—of living organisms can be reprogrammed for the synthesis of sequence-defined macromolecules. The polymerase chain reaction (PCR) (4) and protein engineering (5) are two successful examples of such strategies. Although these methods remain limited to natural biopolymer backbones, they can be extended to the synthesis of nonnatural biopolymers using noncanonical monomers. The pros and cons of these approaches are discussed in the first section of this review.

Synthetic chemistry can be used to prepare sequence-controlled macromolecules with diverse chemical structures. Moreover, in comparison with DNA technologies, chemical procedures may enable larger-scale production of simpler and cheaper sequence-defined materials. However, fully synthetic sequence-controlled protocols are more challenging than biotechnological pathways and are often limited to short oligomer synthesis. The most obvious method for preparing sequence-defined segments is to connect monomer units one by one by using iterative chemical steps (see Box 1). This strategy was studied as early as the late 1940s for the synthesis of oligopeptides. The introduction of solid-phase chemistry (6) and automated synthesizers has greatly simplified this approach; however, it remains a tedious process requiring very high reaction yields and repeated purification steps. Therefore, other mechanisms for monomer sequence control in polymerizations have been investigated. For instance, the development of living polymerization methods—such as ionic polymerizations (7), controlled radical polymerizations (8, 9), and ring-opening metathesis polymerization (10)—has

aided progress in the field of polymer science, and it is now possible to form multiblock copolymers with complex microstructures in ways that were unimaginable a few decades ago (11). Synthetic sequence regulation constitutes the obvious next step in the field. Current progress in macromolecular chemistry points to a new era for polymers (12), in which the development of molecularly encoded synthetic polymer chains may open up opportunities in materials science and nanotechnology.

Sequence-Controlled Biological Polymerization Processes

Three sequence-controlled polymerization processes are dominant in living organisms: DNA replication, DNA→RNA transcription, and RNA→protein translation, in which the molecular information carried by nucleic acids is converted into sequence-defined protein chains. During DNA replication and transcription, nucleic acid-templated polymerization takes place by the action of DNA and RNA polymerases. The mechanism of translation is even more complex and relies on ribosomes, large catalytic particles composed of both RNA and proteins. All three of these polymerizations are more tightly controlled than any known synthetic polymerization processes. Thus, there are obvious advantages in using biological methods for polymer synthesis and materials science.

The principles that mediate biological polymerization can be adopted at different levels of complexity (Fig. 1). The most basic adaptation of a biological mechanism uses DNA templates to direct the coupling of nucleic acids and their analogs (Fig. 1A). In such approaches, activated nucleotides are associated to an oligonucleotide template via Watson-Crick base pairing and polymerized by chemical means (i.e., in the absence of enzyme). This field of research has been pioneered and chiefly developed by Orgel and co-workers, who optimized the nonenzymatic replication of nucleic acids (13). Such protein-free replicating systems often suffer from lack of efficiency and replication fidelity. Another drawback is the strong binding of the newly formed oligomers to the template, which hinders repetition of the process. Nevertheless, convincing proof of the concept has been reported (14–16). It has also been shown that nonenzymatic replication can be extended to nonnatural nucleic acids. For instance, artificial backbones based on nonribose sugars were efficiently used as templates for RNA synthesis (16). Perhaps even more remarkably, complementarity between RNA and peptide nucleic acids (PNA) was described (17). Although constructed from polyamide backbones, PNA oligomers can act as templates for sequence-defined RNA synthesis and vice versa. This behavior was further developed by Liu and colleagues, who reported the synthesis of long sequence-defined PNA oligomers on DNA templates (18, 19). Recently, the Liu group used DNA-templated polymerization to synthesize sequence-defined

¹Precision Macromolecular Chemistry Group, Institut Charles Sadron, UPR22-CNRS, 23 rue du Loess, Boîte Postale 84047, 67034 Strasbourg Cedex 2, France. ²Department of Polymer Chemistry, Graduate School of Engineering, Kyoto University, Katsura, Nishikyō-ku, Kyoto 615-8510, Japan. ³Department of Chemistry and Chemical Biology and the Howard Hughes Medical Institute, Harvard University, Cambridge, MA 02138, USA.

*Corresponding author. E-mail: jflutz@unistra.fr

polymers with no necessary structural similarity to nucleic acids by using macrocyclic PNA adapters, analogous to transfer RNAs (tRNAs), that serve as an intermediate layer between DNA templates and corresponding synthetic monomers (20). With this approach, a variety of synthetic polymers have been translated from DNA templates, including β -peptides of up to 26 kD containing 16 consecutively coupled building blocks comprising 90 densely functionalized β -amino acid residues. Without relying on a polymerase enzyme or on direct polymer-template hybridization, this approach enables a wide variety of potential polymer structures. Limitations include lower polymerization yields than with enzyme-catalyzed polymerizations, correspondingly lower numbers of consecutive coupled building blocks, and the need to synthesize complex substrates.

The next level of complexity in biologically based polymerization strategies is using enzymes for performing *in vitro* replication (Fig. 1B). The most important example of such processes is PCR, which allows copying and amplification of sequence-encoded DNA strands. Such approaches were initially performed using the Klenow fragment of DNA polymerase I. However, the high temperatures required for strand dissociation in PCR strongly limited the use of this enzyme. The utilization of the thermostable *Taq* polymerase allowed the successful development and commercialization of PCR (4). Today, this approach is certainly the most widespread *in vitro* sequence-regulated polymerization technique. However, PCR is routinely used only for natural nucleic acids. Polymerase-based approaches can be applied to nonnatural monomers, which expands the natural alphabet. For instance, the groups of Benner (21) and Kool (22) reported the use of nonnatural base pairs in enzyme-catalyzed polymerizations. Still, PCR amplification of enzymatic processes involving noncanonical monomers remains very challenging. Indeed, the fidelity of certain combinations of nonnatural (versus natural) nucleotide incorporation during PCR can be modest. Nevertheless, progress has been reported (23), opening new opportunities for the enzymatic synthesis of nonnatural sequence-defined polymers.

Ultimately, the whole ribosomal machinery of a living organism can be used to produce sequence-controlled polymers (Fig. 1C). Genetic engineering has been used for several decades for the synthesis of therapeutic proteins, structural proteins, and enzymes. In this approach, an artificial gene, encoding the protein of interest, is incorporated into plasmid DNA, which is introduced into a bacterial host (usually *Escherichia coli*) (24). Bacterial expression of the artificial gene produces the desired protein, which is ultimately extracted from the host and purified. This strategy is not restricted to natural amino acids but also tolerates noncanonical monomers (25). For incorporating nonnatural amino acids into proteins, the simplest approach is replacing natural amino acids with noncanonical residues in a competitive process (26). Alternatively, Schultz

and others have described a set of related approaches for adding nonnatural monomers to the common 20-amino acid alphabet (27). This strategy creates an “expanded” genetic code, in which nonsense or four-base codons encode nonnatural amino acids. All these features make protein engineering a robust technique for materials science (5, 24). In comparison with the other biological concepts described earlier, protein engineering is the most accepted approach in the field of polymer science. Limitations to this approach of coopting the ribosomal machinery to generate non-natural polymers include modest yields of polymers, in which multiple nonnatural monomers are successively incorporated, and the considerable structural constraints imposed by the ribosome that limit the functional diversity of the resulting polymeric products.

Sequence-Controlled Polymerizations Based on Chemical Approaches

Biological polymerization approaches can offer outstanding sequence control but are limited in terms of structural diversity. In comparison, synthetic chemical processes give access to a much broader range of chemical structures. As described in Box 1, iterative synthesis onto insoluble supports (e.g., cross-linked resins) is one of the best pathways for monomer sequence regulation. Monomers can be sequentially connected one by one, stepwise, with washing of unreacted reagents

and/or catalyst and deprotection of the reactive site, followed by cleavage of product from the support. The solid-phase methodology has been primarily developed for peptide synthesis using amino acids as monomers, but many other types of building blocks can be used (see Box 1). One drawback of solid-phase synthesis is the restricted accessibility of the reaction sites in the resin, which influences coupling efficiency. An interesting alternative to this problem is the use of individual soluble polymer chains as supports. For example, polystyrene, which is soluble in common organic solvents but insoluble in methanol, is an efficient liquid-phase support. Linear polystyrene soluble supports can be prepared by living polymerization techniques and carry optimized end-groups for iterative synthesis (Fig. 2A) (28). This efficient approach can be used to prepare new types of nonnatural sequence-controlled oligomers. However, conceptually, the use of soluble supports is only an optimization of the solid-phase methodology.

A more important challenge in the field is the control of monomer sequences in “traditional” polymerization processes, such as chain growth or step growth. For instance, if single-monomer addition could be controlled in living chain-growth polymerization, a stepwise addition of equimolar amounts of monomer and initiator would allow sequence regulation. However, even when living polymerization mechanisms that are highly

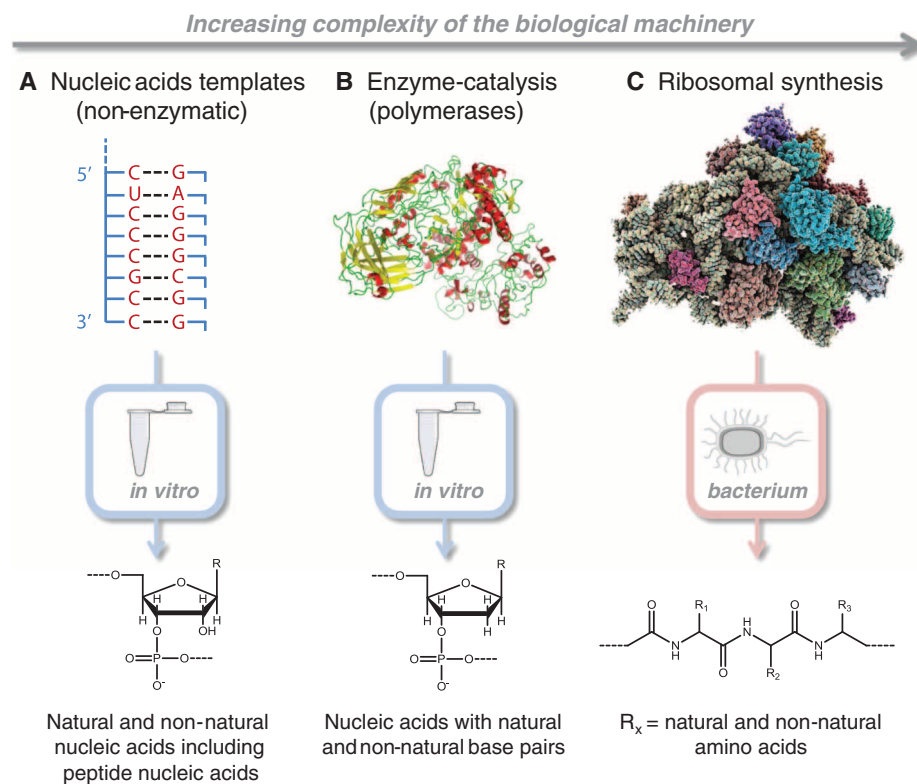


Fig. 1. (A to C) Synthesis of sequence-defined artificial macromolecules with evolutionarily optimized biological mechanisms. Note that the diagram is not to scale; a bacterial ribosome is about 50 times the size of a polymerase. [Sources of polymerase image (B) Wikimedia Commons and bacterial ribosome image (C) Laguna Design/Science Photo Library]

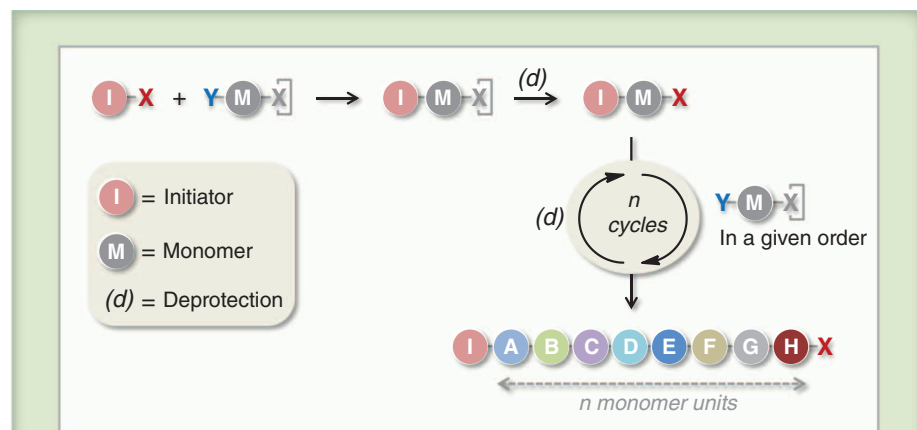
controlled and involve dormant species are used, such “single-monomer addition” strategies are difficult because of the inherent tendency of the monomers to react with themselves (i.e., in the propagation step). One way to overcome this problem is to decrease gradually the reactivity of the added monomers. This idea was verified in living cationic polymerization of vinyl ether monomers using ZnI_2 as a catalyst, although absolute control was not reached and, therefore, chromatographic purification was required at each step (29). Moad and co-workers have investigated single-monomer addition in the RAFT process, which is a controlled radical polymerization method (30). However, the measured yields of monomer insertion were low and, therefore, unsuitable for a reliable stepwise process.

Tong and colleagues have described single-monomer addition by atom-transfer radical polymerization (ATRP), which is another type of

controlled radical polymerization (Fig. 2B) (31). Allyl alcohol, a nonconjugated vinyl monomer that cannot radically propagate into polymers can, nevertheless, undergo atom-transfer radical addition (i.e., single-monomer addition) because the resulting halogen terminal is inactive for radical generation or further propagation, even in the presence of a metal catalyst. However, once the hydroxyl methyl side chain is subsequently oxidized into a carboxylic acid, the terminal bond becomes active for another allyl alcohol single addition. The acid side chain can become functional by means of esterification, and thus, an iterative cycle of single-monomer addition, pendant-transformation, and functionalization allows monomer sequence control regulation as shown in Fig. 2. Similarly, in olefin cross-metathesis (CM), 4-vinylbenzaldehyde becomes a monomer potentiating single-monomer addition and further coupling via transformation into active

form thereafter. The aldehyde unit can be converted into a vinyl group via Wittig olefination after CM reaction (32). Thus, an iterative cycle of CM and olefination gives a sequence of well-defined conjugated oligomers [i.e., oligo(phenylene-vinylene)s]. Recently, a series of sequence-defined oligomers (from dimer to hexamer) were synthesized with “electron-poor” unsubstituted monomers and “electron-rich” dialkoxy-substituted counterparts. Such an approach could facilitate sequence-oriented functions for conjugated materials (33).

Sequence regulation can also be attained in chain-growth polymerizations by using specific comonomer pairs. For example, some combinations of an electron-donor monomer (e.g., styrene or vinyl ether) and an acceptor one (e.g., maleic anhydride or maleimide) can be copolymerized in an alternating manner to give an AB repeat sequence (34), because, in these specific combinations of monomers, cross-propagation is favored over homopropagation. Note that such an alternating behavior can be tuned through specific interactions. For instance, when a bulky fluoroalcohol is used as solvent for copolymerization of limonene (donor) with a maleimide derivative (acceptor), AAB repetitive sequences (A: maleimide, B: limonene) are obtained instead of the conventional AB pattern (35). This particular sequence is most probably due to the interaction of the fluoroalcohol with the carbonyl of the maleimide and to the bulkiness of the limonene monomer. Conventional alternating behaviors can also be tuned using time-controlled additions of monomers in conjunction with living polymerization mechanisms. Lutz and co-workers have used such a concept to achieve the local functionalization of polymer chains (Fig. 2C) (36, 37). In this strategy, a donor monomer, such as styrene, is polymerized in excess by controlled radical polymerization (e.g., ATRP), and small amounts of functional acceptor comonomers are added during the course of the reaction. Because of the favored donor-acceptor cross-propagation, the acceptor monomers are incorporated into narrow regions of the growing polymer chains. Thus, by controlling addition time, the positions of the acceptor monomer units can be precisely controlled in the polymer backbone. However, this approach to chain growth leads to chain-to-chain deviations in length, composition, and sequence. These defects can be considerably minimized by using optimized polymerization protocols (38) but cannot be fully suppressed. However, this strategy is applicable to a wide variety of functional N-substituted maleimides (39) and was shown to be efficient for the preparation of periodic polymers (40), encoded chain microstructures (41), and complex macromolecular topologies (42). Such appealing concepts are not restricted to radical polymerization. In anionic polymerization, 1,1-diphenylethylene derivatives are suited for such local modification in growing polymer chain, because they are not polymerizable but are reactive for growing anion species (43).



Box 1. Going the long way: Attaching monomers one by one.

An evident chemical strategy to attain sequence-defined polymers consists in covalently attaching monomers one by one in a given order. Such a concept implies that polymer chain growth has to be regulated in order to avoid repeated incorporation of the same monomer in a given chain. Although different mechanisms of regulation may be considered, the most common approach is using a self-reacting bifunctional monomer XY, in which one of the reactive functions is temporarily protected (i.e., deactivated) as depicted above.

The self-reacting bifunctional monomer XY strategy was developed and optimized for the solution synthesis of oligopeptides (91). However, solution approaches are limited and time-consuming because they require purification after each monomer coupling. The field was revolutionized by the development of solid-phase supports by Merrifield (6). In this simple approach, the growing oligomers are covalently bound to filterable polymer beads, which greatly improve and facilitate purification protocols. Moreover, the automation of this chemical process has substantially reduced reaction times. The concept was applied for the synthesis of many natural and nonnatural sequence-defined oligomers, including oligopeptides and oligonucleotides (92). Such iterative approaches still exhibit some drawbacks. First, in order to avoid substantial sequence defects, the yields of monomer coupling should be very high, particularly if a long polymer chain is targeted. Another limitation is the use of main-chain protecting groups, which imply time-consuming deprotection steps. Protecting groups are currently mandatory in bio-oligomer synthesis, e.g., peptide solid-phase chemistry. However, some nonnatural sequence-defined oligomers can be synthesized in the absence of main-chain protecting groups, for example, if two successive building blocks are used instead of a single XY monomer (28, 93, 94). An elegant example of that type is the synthesis of peptoids (i.e., oligomers of N-substituted glycines) described by Zuckermann and co-workers (95). This approach relies on a “submonomer” strategy. Each N-substituted glycine unit is formed by successive coupling of two submonomer synthons. The backbone chemistry is chemoselective and, therefore, does not require main-chain protecting groups.

Step-growth polymerizations also allow synthesis of sequence-regulated macromolecules and are highly suited to the preparation of periodic microstructures. Indeed, sequence-defined oligomers containing reactive chain ends can be polymerized by step growth. A variety of efficient reactions can be used, for example, the azide-alkyne click reaction (44). Satoh, Kamigaito, and co-workers have described the preparation of sequence-controlled vinyl polymers by a step-growth process. (Fig. 2D) (45, 46). Their approach involves a metal-catalyzed radical addition reaction between nonconjugated olefin and a carbon-chlorine bond (active under a one-electron redox catalyst) to give a unit of vinyl chloride as the junction linkage. They thus used a sequence of well-defined vinyl oligomer blocks carrying olefin and chlorine at the terminals to construct vinyl polymers of periodic sequence. As pioneered by Wagener (47), an acyclic diene metathesis polymerization of symmetric α,ω -dienes can form sequence-regulated vinyl polymers, in conjunction with subsequent hydrogenation. Various alkyl chains can be substituted at the center in the symmetric α,ω -diene $[R \cdot \text{in } \text{CH}_2=\text{CH}-(\text{CH}_2)_n-\text{CH}(\text{R})-(\text{CH}_2)_n-\text{CH}=\text{CH}_2]$, which leads to unique polyethylene of precisely branched structures (48). This versatile design also allows the introduction of amino acids and drugs at well-defined positions in polyethylene

for biological applications (49). Hillmyer proposed making sequence-specific vinyl copolymers by regioselective ring-opening metathesis polymerizations (ROMP) of asymmetric substituted cyclooctenes and subsequent hydrogenation (Fig. 2E) (50). Both metathesis systems are expected to generate polyolefins displaying sequence-oriented functions.

In nature, template systems are crucial to regulating monomer sequences in biopolymers, such as RNA and proteins. Thus, template effects have also been extensively studied in synthetic polymerizations. In the late 1970s, sequence control by free radical polymerization was attempted with vinyl monomers carrying a set of nucleobases on the side chains (51). A few interesting results demonstrating template effects with the complementary interactions in polymerizations have been reported (52–54). However, these approaches did not reach sequence regulation, and the template effects were restricted to rate enhancement or molecular weight transcription. The limitations of enzyme-free templating approaches are also relevant to these synthetic approaches. O'Reilly and Turberfield have demonstrated another type of DNA-templated synthesis to prepare sequence-regulated oligomers (55). They used the end groups of stranded DNA molecules as adjacent and dissociative reaction

scaffolds for the Wittig reaction between triphenylphosphonium (ylide) and aldehyde that gives a C=C bond and phosphine oxide. The molecules are sophisticatedly designed for sequential transfer reaction of the embedded building block from one DNA terminal to another, which allows construction of sequence-regulated molecules. Eventually, they achieved sequence control for a decamer with this methodology (56). Lynn and co-workers have described the DNA-catalyzed step-growth polymerization of monomers containing primary amine and aldehyde reactive functions (57). Although limited to short oligomers, this approach allows the synthetic translation of information encoded in DNA chains. Schuster and colleagues have also taken advantage of the complementarity of DNA strands to synthesize sequence-defined linear and cyclic oligomers based on bis(2-thienyl)pyrrole and aniline (58). To achieve sequence control with synthetic templates, a positional regulation of an initiator or active species generator is first important, and thus, a combination with living polymerization should be promising. Ouchi and Sawamoto designed template molecules to embed an initiator site (i.e., radical generator) close to a recognition site for vinyl monomer and, thus, demonstrated a way to control selectivity of radical species for “recognized” monomer

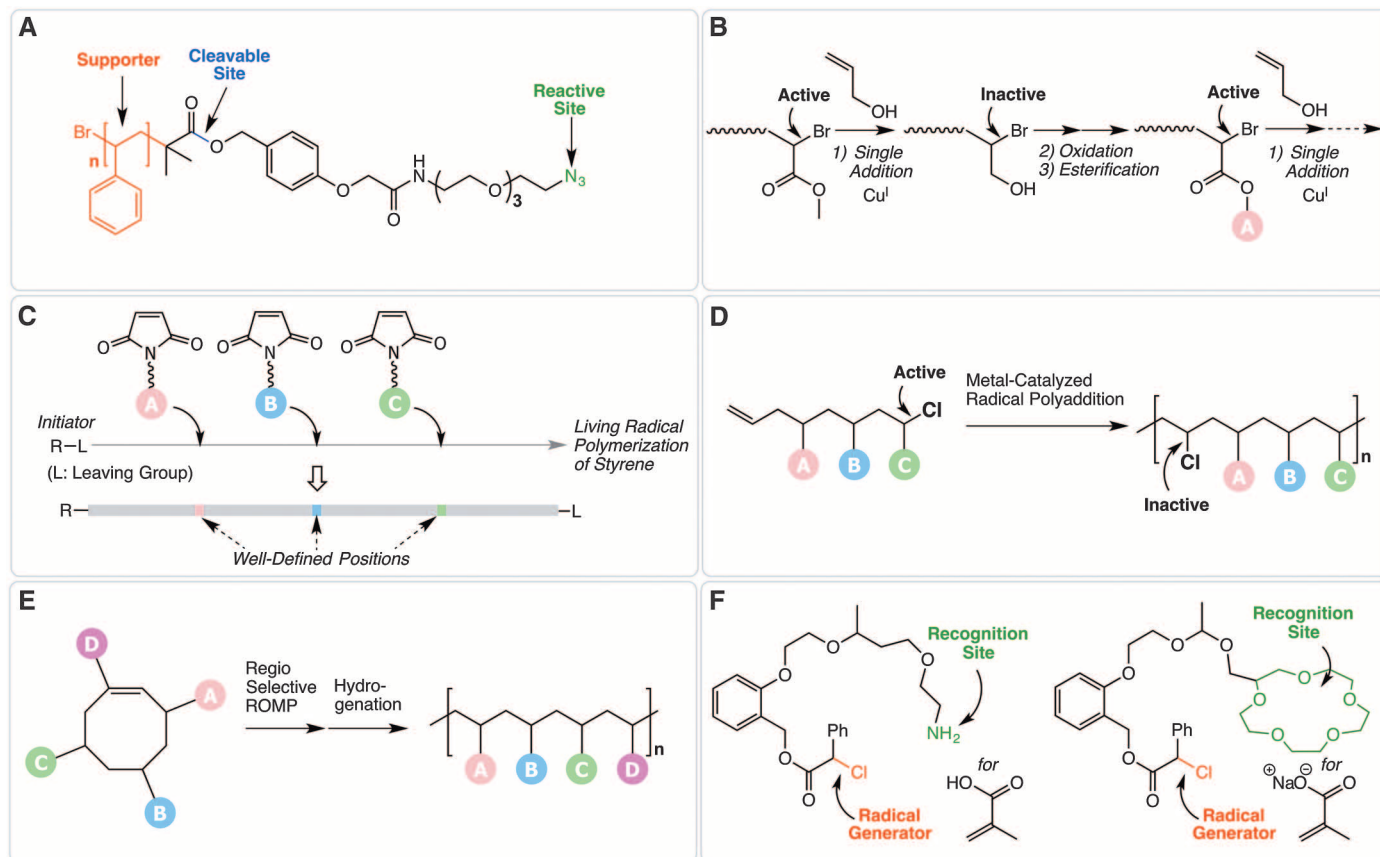


Fig. 2. Representative chemical approaches to sequence control. (A) Soluble polymer supporter for azide-alkyne click reaction, (B) iterative single-monomer addition with allyl alcohol in living radical polymerization, (C) posi-

tioning control in living radical polymerization of styrene, (D) metal-catalyzed radical polyaddition, (E) region-selective ROMP of asymmetric substituted cyclooctene, and (F) template initiators for living radical polymerization.

over “not recognized,” but similar, reactive counterpart (Fig. 2F) (59, 60). Such selectivity was just achieved in a single monomer-addition process, but the control was noteworthy. However, this strategy presumably falls into difficulty, as the chain is longer, because multiple recognition sites need to be arranged on template. A more feasible way to use a template is chain-growth polymerization of multivinyl monomers on a cleavable template, although the sequence pattern is limited to being periodic. In this strategy, immobilization of the vinyl groups on a template during polymerization is important to avoid both cross-linking reaction and unfavorable jumping propagation. AB and ABA patterns were achieved via radical polymerizations (61, 62).

Another strategy for sequence-regulation in synthetic processes is catalysis. This approach is currently underexplored. Thomas, Coates, and co-workers demonstrated catalyst-driven sequence control (63), and they achieved alternating sequence control in a polyester from a set of enantiomerically pure, but different, substituted monomers (i.e., β -lactones) by using yttrium catalysts for stereospecific polymerization. Ultimately, the development of artificial catalytic nano-machines resembling ribosomes would be a key to controlling sequences in chemical processes. Although this dream is far off, promising concepts have been described. For instance, Leigh's group has reported a rotaxane-based molecular machine that allows synthesis of sequence-specific peptides (64). In this approach, a molecular

ring bearing a thiolate initiator moves on a molecular axle on which are attached amino acids. The directional progression of the ring on the axle allows sequence-controlled polymerization to occur (Fig. 3). Such an advanced chemical design, combining macromolecular and supramolecular concepts, is at the forefront of the field and opens up interesting avenues for the future.

Properties and Promises of Sequence-Controlled Polymers

In comparison with conventional synthetic macromolecules, such as homopolymers and block copolymers, sequence-controlled polymers allow a higher level of control over structural and physicochemical properties. The most remarkable features of sequence-controlled biological polymers and their degree of utilization and mimicry in synthetic materials are listed in Table 1. The first and last entries of this table are not directly discussed in this section. Using encoded primary structures for data storage is presented in more detail in Box 2, whereas self-replication is described partly in the first section of this review, but can be explored in (65, 66).

The self-assembly of sequence-controlled oligomers, such as oligopeptides and oligonucleotides, has been investigated (3, 67). Many of these studies have shown the relevance of such oligomers in materials science. For instance, sequence-defined oligopeptides self-organize into a variety of nanostructures, including fibers, tapes, ribbons, vesicles, and tubes. This broad range of self-assembly behaviors has been used to guide the organization of other types of materials, such as biocompatible polymers (68), conducting polymers (69), and inorganic matter (70). Beyond oligopeptide self-assembly, protein engineering allows the design of artificial materials with highly optimized properties. For example, Tirrell and co-workers have described the preparation of stimuli-responsive hydrogels based on triblock proteins (71). The monomer sequences of these macromolecules were engineered in order to obtain charged water-soluble middle blocks flanked by two self-associating leucine zippers. Such optimized primary structures exhibited pH and thermo-reversible gelling in aqueous medium. Sequence-defined nucleic acids have also opened up avenues for materials design. As demonstrated by Seeman (72) and many others, the self-recognition of complementary DNA strands is currently an unrivaled feature for organizing and sorting building-blocks such as polymers, nanoparticles, or nanocrystals (3, 73).

Aside from biopolymers, the nonnatural sequence-controlled polymers discussed in the previous sections and Box 1 also open up technological opportunities. In terms of folding and self-assembly, some basic features of proteins can be mimicked using synthetic sequence-defined foldamers (74). However, many of these approaches rely on synthetic chemical concepts, which are very close to natural design (e.g., peptidomimetics). Yet, proteinlike materials can also be prepared

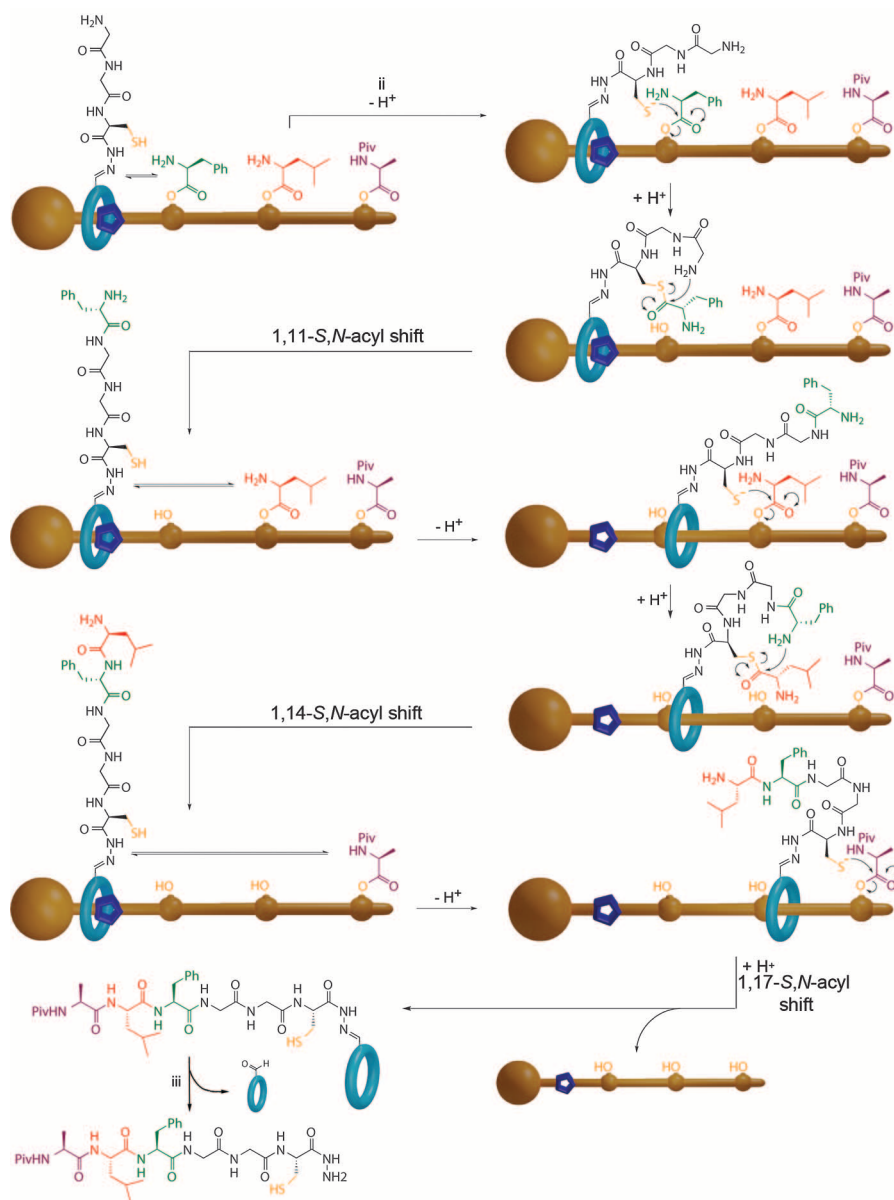


Fig. 3. Proposed mechanism for the synthesis of sequence-defined oligopeptides on a molecular machine. The molecular structure of the rotaxane machine and the detailed experimental conditions can be found in (64). [Adapted with permission from (64), copyright AAAS 2013]

Table 1. Known properties of sequence-controlled polymers and their utilization in materials science.

Sequence-dependent property	Some important implications in biology	Degree of realization in synthetic materials
Molecular storage of information	Heredity	Proof of principle
Spatial organization of functional elements	Cell signaling Photosynthesis	Proof of principle
Folding and self-assembly	Complex globular objects Mechanical properties of tissues Molecular motors	Multiple examples
Molecular recognition	Biocatalysis Molecular transport Signal transduction	Multiple examples
Self-replication	Cell signaling Reproduction Evolution Living matter	Limited success

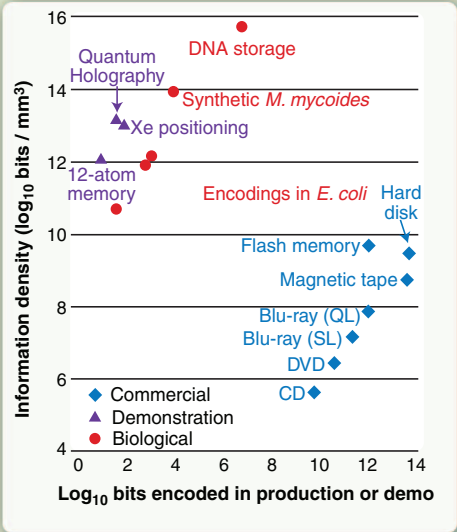
using very different chemistries (75). For example, Meijer and co-workers described the preparation and catalytic properties of enzyme like globular particles (76). These objects were obtained by the folding of individual polymer chains in aqueous medium. The monomer sequence distribution of these polymers was regulated with a controlled radical polymerization process, and their folding in water was driven by the helical assembly of nonnatural side-chain supramolecular motifs. Despite being based on fully nonnatural chemical design, these single-chain particles exhibited promising enzymelike behaviors. As listed in Table 1, another advantage of sequence-controlled polymers is the possibility of controlling the chain positioning of functional elements. For instance, it was demonstrated that the sequence-controlled copolymerization of styrene and N-substituted maleimides allows preparation of single-chain sugar arrays (77). Such sequence-controlled glycopolymers interact with complementary lectins and are, therefore, interesting glycoprotein mimics.

Sequence-regulation also strongly influences the macroscopic properties of synthetic polymer materials. For instance, the solution and solid-state behaviors of polymers closely depend on their primary structure. Solubility and phase transitions in water and organic solvents can be tuned by using subtle monomer sequence modifications (78–80). Some properties of polyelectrolytes, such as charge density (81) and persistence length (82), can also be precisely adjusted by sequence regulation. It was also reported that the solution self-assembly behavior of triblock copolymers containing nucleobases is strongly influenced by the block sequences (83, 84). In the solid state, it was reported that both block copolymer mesophases and semicrystalline phases are strongly dependent on monomer sequences (85, 86). For example, Zuckermann and co-workers have studied the influence of sequence-controlled segments on the phase behavior of polystyrene-based block copolymers (86). Their results indicate that order-disorder transition can be finely controlled using composition and sequence variations. Other im-

Box 2. Data-storage on sequence-controlled polymers.

In living organisms, all heredity information is encoded by the four-monomer units of DNA chains. Such monomer encoding offers a huge storage capacity. Moreover, as genetic archeology has shown, the message of DNA chains can be preserved for thousands of years if nucleic acid degradation is prevented. Thus, DNA and, perhaps, other sequence-controlled polymers appear to be valid options for storing data in man-made technologies. For instance, the storage mechanism of DNA can be used in a nonbiological context, as for artificial DNA encryption (96). Short messages, sentences, and poems have been written in DNA chains (97). However, in most of the reported examples, the number of encoded bits of information remained relatively limited.

A breakthrough was described by Church and co-workers (96). These authors have demonstrated that a full textbook containing about 50,000 words could be written on DNA and read. In particular, two interesting innovations were reported in that work. First of all, a single bit of information was encoded on each base, i.e., both adenine and cytosine encoded a 0, whereas guanine and thymine encoded a 1. This simplification allows more flexibility in terms of synthetic chemistry. The authors did not attempt to synthesize very long macromolecules but developed instead a library of oligonucleotides, in which each element can be tracked by a short molecular barcode. Each oligomer contained 159 monomer units: 96 for information storage, 19 for the barcode, and 44 for PCR amplification. These fragments were synthesized on DNA microchips and, after amplification, were read using next-generation sequencing technology. Although technological applications are not yet in sight, this scientific breakthrough reduces the limits of artificial DNA storage. As shown in the displayed graphic, this system combines a huge information density with a relatively large storage capacity. Moreover, recent innovations in rewritable nucleic acid storage indicate that this technological field is rapidly progressing (98). [Image adapted with permission from (96), copyright AAAS 2012.]



portant macromolecular properties have been found to be strongly sequence-dependent. For instance, Meyer and colleagues have shown that the degradation kinetics of biodegradable aliphatic polyesters is influenced by comonomer sequences (87, 88). Nearly linear release profiles were found for poly(lactide-co-glycolide) (common name PLGA), which is one the most used polymers for biomedical applications. Sequence-

controlled nonnatural polymers can also be tailored to create optimal interactions with specific materials. Börner and co-workers have highlighted the relevance of sequence-defined poly(amidoamine)s in nonviral gene-delivery (89). Indeed, the primary structure of these synthetic gene carriers can be tailored for optimal DNA complexation. Similarly, nonnatural macromolecules with optimized monomer sequences can

be used to control the mineralization of inorganic materials (90).

Outlook

Sequence-controlled polymers should provide major improvements for atom economy, molecular precision, adjustment of physicochemical properties, and device miniaturization. However, as described above, this emerging field consists of two converging trends: (i) exploitation and engineering of readily available sequence-defined biopolymers (26); and (ii) development of synthetic sequence-regulated polymerization processes. The former option is more promising on a short-term basis because it uses already existing structures. Nucleic acids and proteins are in a sense “perfect” sequence-defined macromolecules, and their properties and functions are now well-understood. However, these macromolecules were optimized by nature for use in a given environment (i.e., biological conditions) and are, therefore, not always suitable or practical in other contexts. The recent progress in the synthesis of nonnatural nucleic acids and proteins has broadened the scope of use of these polymers. However, their widespread utilization in nonbiological applications remains limited by economical, technical, and scalability issues.

In that regard, synthetic sequence-controlled polymers, prepared using traditional high-scale polymerization processes, such as chain-growth and step-growth polymerizations, represent an interesting alternative to natural polymers. Primary progress has come from controlled radical chain-growth polymerizations. The degree of sequence regulation in such approaches still remains low in comparison with DNA. Nevertheless, synthetic sequence-controlled polymers bring additional benefits in terms of chemical diversity and scalability. As the fields of natural and synthetic sequence-regulated polymers start to converge, we can expect the selection of practical, scalable, and versatile systems. It is tempting to speculate that protein engineering is simply the first example of a discipline bridging the gap between biological sciences and polymer science and that many new analogous fields will emerge as our ability to create and manipulate sequence-controlled polymers comes of age.

References and Notes

1. K. Matyjaszewski, Architecturally complex polymers with controlled heterogeneity. *Science* **333**, 1104–1105 (2011). doi: [10.1126/science.1209660](#)
2. J.-F. Lutz, Sequence-controlled polymerizations: The next Holy Grail in polymer science? *Polym. Chem.* **1**, 55–62 (2010). doi: [10.1039/b9py00329k](#)
3. F. A. Aldaye, A. L. Palmer, H. F. Sleiman, Assembling materials with DNA as the guide. *Science* **321**, 1795–1799 (2008). doi: [10.1126/science.1154533](#)
4. R. K. Saiki *et al.*, Primer-directed enzymatic amplification of DNA with a thermostable DNA polymerase. *Science* **239**, 487–491 (1988). doi: [10.1126/science.2448875](#)
5. K. P. McGrath, M. J. Fournier, T. L. Mason, D. A. Tirrell, Genetically directed syntheses of new polymeric materials. Expression of artificial genes encoding proteins with repeating -(AlaGly)3ProGluGly- elements. *J. Am. Chem. Soc.* **114**, 727–733 (1992). doi: [10.1021/ja00028a048](#)
6. R. B. Merrifield, Solid phase peptide synthesis. I. The synthesis of a tetrapeptide. *J. Am. Chem. Soc.* **85**, 2149–2154 (1963). doi: [10.1021/ja00897a025](#)
7. M. Szwarc, ‘Living’ polymers. *Nature* **178**, 1168–1169 (1956). doi: [10.1038/1781168a0](#)
8. T. E. Patten, J. Xia, T. Abernathy, K. Matyjaszewski, Polymers with very low polydispersities from atom transfer radical polymerization. *Science* **272**, 866–868 (1996). doi: [10.1126/science.272.5263.866](#)
9. M. Ouchi, T. Terashima, M. Sawamoto, Transition metal-catalyzed living radical polymerization: Toward perfection in catalysis and precision polymer synthesis. *Chem. Rev.* **109**, 4963–5050 (2009). doi: [10.1021/cr900234b](#); pmid: [19788190](#)
10. C. W. Bielawski, R. H. Grubbs, Living ring-opening metathesis polymerization. *Prog. Polym. Sci.* **32**, 1–29 (2007). doi: [10.1016/j.proppolymsci.2006.08.006](#)
11. F. S. Bates *et al.*, Multiblock polymers: Panacea or Pandora’s box? *Science* **336**, 434–440 (2012). doi: [10.1126/science.1215368](#)
12. F. A. Leibfarth, K. M. Mattson, B. P. Fors, H. A. Collins, C. J. Hawker, External regulation of controlled polymerizations. *Angew. Chem. Int. Ed.* **52**, 199–210 (2013). doi: [10.1002/anie.201206476](#); pmid: [23166046](#)
13. L. E. Orgel, Molecular replication. *Nature* **358**, 203–209 (1992). doi: [10.1038/358203a0](#); pmid: [1630488](#)
14. T. Li, K. C. Nicolau, Chemical self-replication of palindromic duplex DNA. *Nature* **369**, 218–221 (1994). doi: [10.1038/369218a0](#); pmid: [8183341](#)
15. D. Sievers, G. von Kiedrowski, Self-replication of complementary nucleotide-based oligomers. *Nature* **369**, 221–224 (1994). doi: [10.1038/369221a0](#); pmid: [8183342](#)
16. Y. Budino, D. R. Liu, Recent progress toward the templated synthesis and directed evolution of sequence-defined synthetic polymers. *Chem. Biol.* **16**, 265–276 (2009). doi: [10.1016/j.chembiol.2009.02.004](#); pmid: [19318208](#)
17. C. Böhrer, P. E. Nielsen, L. E. Orgel, Template switching between PNA and RNA oligonucleotides. *Nature* **376**, 578–581 (1995). doi: [10.1038/376578a0](#); pmid: [7543656](#)
18. D. M. Rosenbaum, D. R. Liu, Efficient and sequence-specific DNA-templated polymerization of peptide nucleic acid aldehydes. *J. Am. Chem. Soc.* **125**, 13924–13925 (2003). doi: [10.1021/ja038058b](#); pmid: [14611205](#)
19. R. E. Kleiner, Y. Budino, M. E. Birnbaum, D. R. Liu, DNA-templated polymerization of side-chain-functionalized peptide nucleic acid aldehydes. *J. Am. Chem. Soc.* **130**, 4646–4659 (2008). doi: [10.1021/ja0753997](#); pmid: [18341334](#)
20. J. Niu, R. Hill, D. R. Liu, Enzyme-free translation of DNA into sequence-defined synthetic polymers structurally unrelated to nucleic acids. *Nat. Chem.* **5**, 282–292 (2013). doi: [10.1038/nchem.1577](#); pmid: [23511416](#)
21. J. A. Piccirilli, T. Krauch, S. E. Moroney, S. A. Benner, Enzymatic incorporation of a new base pair into DNA and RNA extends the genetic alphabet. *Nature* **343**, 33–37 (1990). doi: [10.1038/343033a0](#); pmid: [1688644](#)
22. E. T. Kool, Replacing the nucleobases in DNA with designer molecules. *Acc. Chem. Res.* **35**, 936–943 (2002). doi: [10.1021/ar000183u](#); pmid: [12437318](#)
23. D. A. Malyshev *et al.*, Efficient and sequence-independent replication of DNA containing a third base pair establishes a functional six-letter genetic alphabet. *Proc. Natl. Acad. Sci. U.S.A.* **109**, 12005–12010 (2012). doi: [10.1073/pnas.1205176109](#); pmid: [22773812](#)
24. J. C. M. van Hest, D. A. Tirrell, Protein-based materials, toward a new level of structural control. *Chem. Commun. (Cambridge)* **19**, 1897–1904 (2001). doi: [10.1039/b105185g](#); pmid: [12240211](#)
25. L. Wang, P. G. Schultz, Expanding the genetic code. *Angew. Chem. Int. Ed.* **44**, 34–66 (2004). doi: [10.1002/anie.200460627](#); pmid: [15599909](#)
26. K. L. Kiick, J. C. van Hest, D. A. Tirrell, Expanding the scope of protein biosynthesis by altering the methionyl-tRNA synthetase activity of a bacterial expression host. *Angew. Chem. Int. Ed.* **39**, 2148–2152 (2000). doi: [10.1002/1521-3773\(20000616\)39:12<2148::AID-ANIE2148>3.0.CO;2-7](#); pmid: [10941044](#)
27. K. J. Noren, S. J. Anthony-Cahill, M. C. Griffith, P. G. Schultz, A general method for site-specific incorporation of unnatural amino acids into proteins. *Science* **244**, 182–188 (1989). doi: [10.1126/science.2649980](#)
28. S. Pfeifer, Z. Zarafshani, N. Badi, J.-F. Lutz, Liquid-phase synthesis of block copolymers containing sequence-ordered segments. *J. Am. Chem. Soc.* **131**, 9195–9197 (2009). doi: [10.1021/ja903635y](#); pmid: [19522508](#)
29. M. Minoda, M. Sawamoto, T. Higashimura, Sequence-regulated oligomers and polymers by living cationic polymerization. 2. Principle of sequence regulation and synthesis of sequence-regulated oligomers of functional vinyl ethers and styrene derivatives. *Macromolecules* **23**, 4889–4895 (1990). doi: [10.1021/ma00225a001](#)
30. S. Houshyar *et al.*, The scope for synthesis of macro-RAFT agents by sequential insertion of single monomer units. *Polym. Chem.* **3**, 1879–1889 (2012). doi: [10.1039/c2py00529h](#)
31. X. M. Tong, B. H. Guo, Y. B. Huang, Toward the synthesis of sequence-controlled vinyl copolymers. *Chem. Commun. (Cambridge)* **47**, 1455–1457 (2011). doi: [10.1039/c0cc04807k](#); pmid: [21125120](#)
32. B. N. Norris, T. Q. Pan, T. Y. Meyer, Iterative synthesis of heterotelechelic oligo(phenylene-vinylene)s by olefin cross-metathesis. *Org. Lett.* **12**, 5514–5517 (2010). doi: [10.1021/ol102398y](#); pmid: [21069981](#)
33. B. N. Norris *et al.*, Sequence matters: Modulating electronic and optical properties of conjugated oligomers via tailored sequence. *Macromolecules* **46**, 1384–1392 (2013). doi: [10.1021/ma400123r](#)
34. Z. M. O. Rzaev, Complex-radical alternating copolymerization. *Prog. Polym. Sci.* **25**, 163–217 (2000). doi: [10.1016/S0079-6700\(99\)00027-1](#)
35. K. Satoh, M. Matsuda, K. Nagai, M. Kamigaito, AAB-sequence living radical chain copolymerization of naturally occurring limonene with maleimide: An end-to-end sequence-regulated copolymer. *J. Am. Chem. Soc.* **132**, 10003–10005 (2010). doi: [10.1021/ja1042353](#); pmid: [20586492](#)
36. S. Pfeifer, J.-F. Lutz, A facile procedure for controlling monomer sequence distribution in radical chain polymerizations. *J. Am. Chem. Soc.* **129**, 9542–9543 (2007). doi: [10.1021/ja0717616](#); pmid: [17636902](#)
37. J.-F. Lutz, B. V. K. J. Schmidt, S. Pfeifer, Tailored polymer microstructures prepared by atom transfer radical copolymerization of styrene and N-substituted maleimides. *Macromol. Rapid Commun.* **32**, 127–135 (2011). doi: [10.1002/marc.201000664](#); pmid: [21433134](#)
38. M. Zamfir, J.-F. Lutz, Ultra-precise insertion of functional monomers in chain-growth polymerizations. *Nat. Commun.* **3**, 1138 (2012). doi: [10.1038/ncomms2151](#)
39. S. Pfeifer, J.-F. Lutz, Development of a library of N-substituted maleimides for the local functionalization of linear polymer chains. *Chem.-Eur. J.* **14**, 10949–10957 (2008). doi: [10.1002/chem.200801237](#); pmid: [18942700](#)
40. M.-A. Berthet, Z. Zarafshani, S. Pfeifer, J.-F. Lutz, Facile synthesis of functional periodic copolymers: A step toward polymer-based molecular arrays. *Macromolecules* **43**, 44–50 (2010). doi: [10.1021/ma902075q](#)
41. D. Chan-Seng, M. Zamfir, J.-F. Lutz, Polymer-chain encoding: Synthesis of highly complex monomer sequence patterns by using automated protocols. *Angew. Chem. Int. Ed.* **51**, 12254–12257 (2012). doi: [10.1002/anie.201206371](#); pmid: [23109042](#)
42. B. V. K. J. Schmidt, N. Fechner, J. Falkenhagen, J.-F. Lutz, Controlled folding of synthetic polymer chains through the formation of positionable covalent bridges. *Nat. Chem.* **3**, 234–238 (2011). doi: [10.1038/nchem.964](#); pmid: [21336330](#)
43. A. Natalello, J. N. Hall, E. A. L. Eccles, S. M. Kimani, L. R. Hutchings, Kinetic control of monomer sequence distribution in living anionic copolymerisation. *Macromol. Rapid Commun.* **32**, 233–237 (2011). doi: [10.1002/marc.201000482](#); pmid: [21433146](#)
44. T.-B. Yu, J. Z. Bai, Z. Guan, Cycloaddition-promoted self-assembly of a polymer into well-defined beta sheets and hierarchical nanofibrils. *Angew. Chem. Int. Ed.* **48**, 1097–1101 (2009). doi: [10.1002/anie.200805009](#); pmid: [19115358](#)
45. K. Satoh, M. Mizutani, M. Kamigaito, Metal-catalyzed radical polyaddition as a novel polymer synthetic route. *Chem. Commun. (Cambridge)* (12): 1260–1262 (2007). doi: [10.1039/b616598b](#); pmid: [17356776](#)

46. K. Satoh, S. Ozawa, M. Mizutani, K. Nagai, M. Kamigaito, Sequence-regulated vinyl copolymers by metal-catalysed step-growth radical polymerization. *Nat. Commun.* **1**, 6 (2010). doi: [10.1038/ncomms1004](#); pmid: [20975670](#)
47. E. B. Berda, K. B. Wagener, in *Polymer Science: A Comprehensive Reference*, K. Matyjaszewski, M. Möller, Eds. (Elsevier, Amsterdam, 2012), pp. 195–216.
48. G. Rojas, B. Inci, Y. Wei, K. B. Wagener, Precision polyethylene: Changes in morphology as a function of alkyl branch size. *J. Am. Chem. Soc.* **131**, 17376–17386 (2009). doi: [10.1021/ja907521p](#); pmid: [19891434](#)
49. P. Atallah, K. B. Wagener, M. D. Schulz, ADMET: The future revealed. *Macromolecules* **46**, 4735–4741 (2013). doi: [10.1021/ma400067b](#)
50. J. Zhang, M. E. Matta, M. A. Hillmyer, Synthesis of sequence-specific vinyl copolymers by regioselective ROMP of multiply substituted cyclooctenes. *ACS Macro Lett.* **1**, 1383–1387 (2012). doi: [10.1021/mz300535r](#)
51. Y. Inaki, K. Ebisutani, K. Takemoto, Functional monomers and polymers. 132. Template polymerization of methacrylamide derivatives containing nucleic-acid bases. *J. Polym. Sci. A Polym. Chem.* **24**, 3249–3262 (1986). doi: [10.1002/pola.1986.080241209](#)
52. H. J. Spijker, F. L. van Delft, J. C. M. van Hest, Atom transfer radical polymerization of adenine, thymine, cytosine, and guanine nucleobase monomers. *Macromolecules* **40**, 12–18 (2007). doi: [10.1021/ma061808s](#)
53. P. K. Lo, H. F. Sleiman, Nucleobase-templated polymerization: Copying the chain length and polydispersity of living polymers into conjugated polymers. *J. Am. Chem. Soc.* **131**, 4182–4183 (2009). doi: [10.1021/ja809613n](#); pmid: [19275231](#)
54. R. McHale, J. P. Patterson, P. B. Zetterlund, R. K. O'Reilly, Biomimetic radical polymerization via cooperative assembly of segregating templates. *Nat. Chem.* **4**, 491–497 (2012). doi: [10.1038/nchem.1331](#); pmid: [22614385](#)
55. M. L. McKee *et al.*, Multistep DNA-templated reactions for the synthesis of functional sequence controlled oligomers. *Angew. Chem. Int. Ed.* **49**, 7948–7951 (2010). doi: [10.1002/anie.201002721](#); pmid: [20836102](#)
56. P. J. Milnes *et al.*, Sequence-specific synthesis of macromolecules using DNA-templated chemistry. *Chem. Commun. (Cambridge)* **48**, 5614–5616 (2012). doi: [10.1039/c2cc31975f](#); pmid: [22549725](#)
57. X. Li, Z.-Y. J. Zhan, R. Knipe, D. G. Lynn, DNA-catalyzed polymerization. *J. Am. Chem. Soc.* **124**, 746–747 (2002). doi: [10.1021/ja017319j](#); pmid: [11817938](#)
58. W. Chen, G. B. Schuster, Precise sequence control in linear and cyclic copolymers of 2,5-bis(2-thienyl)pyrrole and aniline by DNA-programmed assembly. *J. Am. Chem. Soc.* **135**, 4438–4449 (2013). doi: [10.1021/ja312507z](#); pmid: [23448549](#)
59. S. Ida, T. Terashima, M. Ouchi, M. Sawamoto, Selective radical addition with a designed heterobifunctional halide: A primary study toward sequence-controlled polymerization upon template effect. *J. Am. Chem. Soc.* **131**, 10808–10809 (2009). doi: [10.1021/ja903131a](#); pmid: [19603819](#)
60. S. Ida, M. Ouchi, M. Sawamoto, Template-assisted selective radical addition toward sequence-regulated polymerization: Lariat capture of target monomer by template initiator. *J. Am. Chem. Soc.* **132**, 14748–14750 (2010). doi: [10.1021/ja1070575](#); pmid: [20886904](#)
61. Y. Hibi, M. Ouchi, M. Sawamoto, Sequence-regulated radical polymerization with a metal-templated monomer: Repetitive ABA sequence by double cyclopolymerization. *Angew. Chem. Int. Ed.* **50**, 7434–7437 (2011). doi: [10.1002/anie.201103007](#); pmid: [21717555](#)
62. Y. Hibi, S. Tokutaka, T. Terashima, M. Ouchi, M. Sawamoto, Design of AB divinyl "template monomers" toward alternating sequence control in metal-catalyzed living radical polymerization. *Polym. Chem.* **2**, 341–347 (2011). doi: [10.1039/c0py00252f](#)
63. J. W. Kramer *et al.*, Polymerization of enantiopure monomers using syndiospecific catalysts: A new approach to sequence control in polymer synthesis. *J. Am. Chem. Soc.* **131**, 16042–16044 (2009). doi: [10.1021/ja9075327](#); pmid: [19835375](#)
64. B. Lewandowski *et al.*, Sequence-specific peptide synthesis by an artificial small-molecule machine. *Science* **339**, 189–193 (2013). doi: [10.1126/science.1229753](#)
65. D. H. Lee, J. R. Granja, J. A. Martinez, K. Severin, M. R. Ghadiri, A self-replicating peptide. *Nature* **382**, 525–528 (1996). doi: [10.1038/382525a0](#); pmid: [8700225](#)
66. V. B. Pinheiro *et al.*, Synthetic genetic polymers capable of heredity and evolution. *Science* **336**, 341–344 (2012). doi: [10.1126/science.1217622](#)
67. H. G. Börner, Strategies exploiting functions and self-assembly properties of bioconjugates for polymer and materials sciences. *Prog. Polym. Sci.* **34**, 811–851 (2009). doi: [10.1016/j.proppolymsci.2009.05.001](#)
68. D. Eckhardt, M. Groenewolt, E. Krause, H. G. Börner, Rational design of oligopeptide organizers for the formation of poly(ethylene oxide) nanofibers. *Chem. Commun. (Cambridge)* (22): 2814–2816 (2005). doi: [10.1039/b503275j](#); pmid: [15928767](#)
69. H. Frauenrath, E. Jahnke, A general concept for the preparation of hierarchically structured pi-conjugated polymers. *Chem.-Eur. J.* **14**, 2942–2955 (2008). doi: [10.1002/chem.200701325](#); pmid: [18228550](#)
70. J. D. Hartgerink, E. Beniash, S. I. Stupp, Self-assembly and mineralization of peptide-amphiphile nanofibers. *Science* **294**, 1684–1688 (2001). doi: [10.1126/science.1063187](#)
71. W. A. Petka, J. L. Harden, K. P. McGrath, D. Wirtz, D. A. Tirrell, Reversible hydrogels from self-assembling artificial proteins. *Science* **281**, 389–392 (1998). doi: [10.1126/science.281.5375.389](#)
72. N. C. Seeman, Nucleic acid nanostructures and topology. *Angew. Chem. Int. Ed.* **37**, 3220–3238 (1998). doi: [10.1002/\(SICI\)1521-3773\(19981217\)37:23<3220::AID-ANGE3220>3.0.CO;2-C](#)
73. T. Schnitzler, A. Herrmann, DNA block copolymers: Functional materials for nanoscience and biomedicine. *Acc. Chem. Res.* **45**, 1419–1430 (2012). doi: [10.1021/ar200211a](#); pmid: [22726237](#)
74. D. J. Hill, M. J. Mio, R. B. Prince, T. S. Hughes, J. S. Moore, A field guide to foldamers. *Chem. Rev.* **101**, 3893–4012 (2001). doi: [10.1021/cr990120t](#); pmid: [11740924](#)
75. M. Ouchi, N. Badi, J.-F. Lutz, M. Sawamoto, Single-chain technology using discrete synthetic macromolecules. *Nat. Chem.* **3**, 917–924 (2011). doi: [10.1038/nchem.1175](#); pmid: [22109270](#)
76. T. Terashima *et al.*, Single-chain folding of polymers for catalytic systems in water. *J. Am. Chem. Soc.* **133**, 4742–4745 (2011). doi: [10.1021/ja2004494](#); pmid: [21405022](#)
77. N. Baradel, S. Fort, S. Halila, N. Badi, J.-F. Lutz, Synthesis of single-chain sugar arrays. *Angew. Chem. Int. Ed.* **52**, 2335–2339 (2013). doi: [10.1002/anie.201209052](#); pmid: [23345258](#)
78. H. K. Murnen, A. R. Khokhlov, P. G. Khalatur, R. A. Segalman, R. N. Zuckermann, Impact of hydrophobic sequence patterning on the coil-to-globule transition of protein-like polymers. *Macromolecules* **45**, 5229–5236 (2012). doi: [10.1021/ma300707t](#)
79. J. Weiss, A. Li, E. Wischerhoff, A. Laschewsky, Water-soluble random and alternating copolymers of styrene monomers with adjustable lower critical solution temperature. *Polym. Chem.* **3**, 352–361 (2012). doi: [10.1039/c1py00422k](#)
80. Z. Hao, G. Li, K. Yang, Y. Cai, Thermoresponsive synergistic hydrogen bonding switched by several guest units in a water-soluble polymer. *Macromol. Rapid Commun.* **34**, 411–416 (2013). doi: [10.1002/marc.201200685](#); pmid: [23288579](#)
81. B. S. Aitken *et al.*, Precision ionomers: Synthesis and thermal/mechanical characterization. *Macromolecules* **45**, 681–687 (2012). doi: [10.1021/ma202304s](#)
82. H. K. Murnen, A. M. Rosales, A. V. Dobrynin, R. N. Zuckermann, R. A. Segalman, Persistence length of polyelectrolytes with precisely located charges. *Soft Matter* **9**, 90–98 (2013). doi: [10.1039/c2sm26849c](#)
83. H. S. Bazzi, J. Bouffard, H. F. Sleiman, Self-complementary ABC triblock copolymers via ring-opening metathesis polymerization. *Macromolecules* **36**, 7899–7902 (2003). doi: [10.1021/ma034683p](#)
84. Y. Ishihara, H. S. Bazzi, V. Toader, F. Godin, H. F. Sleiman, Molecule-responsive block copolymer micelles. *Chemistry* **13**, 4560–4570 (2007). doi: [10.1002/chem.200601423](#); pmid: [17343289](#)
85. J. A. Smith, K. R. Brzezinska, D. J. Valenti, K. B. Wagener, Precisely controlled methyl branching in polyethylene via acyclic diene metathesis (ADMET) polymerization. *Macromolecules* **33**, 3781–3794 (2000). doi: [10.1021/ma9920792](#)
86. A. M. Rosales, B. L. McCulloch, R. N. Zuckermann, R. A. Segalman, Tunable phase behavior of polystyrene-polypeptide block copolymers. *Macromolecules* **45**, 6027–6035 (2012). doi: [10.1021/ma300625b](#)
87. J. Li, R. M. Stayschich, T. Y. Meyer, Exploiting sequence to control the hydrolysis behavior of biodegradable PLGA copolymers. *J. Am. Chem. Soc.* **133**, 6910–6913 (2011). doi: [10.1021/ja200895s](#); pmid: [21488683](#)
88. J. Li, S. N. Rothstein, S. R. Little, H. M. Edenborn, T. Y. Meyer, The effect of monomer order on the hydrolysis of biodegradable poly(lactic-co-glycolic acid) repeating sequence copolymers. *J. Am. Chem. Soc.* **134**, 16352–16359 (2012). doi: [10.1021/ja306866w](#); pmid: [22950719](#)
89. L. Hartmann, S. Häfele, R. Peschka-Süss, M. Antonietti, H. G. Börner, Tailor-made poly(amidoamine)s for controlled complexation and condensation of DNA. *Chem.-Eur. J.* **14**, 2025–2033 (2008). doi: [10.1002/chem.200701223](#); pmid: [18260067](#)
90. C. L. Chen, J. H. Qi, R. N. Zuckermann, J. J. DeYoreo, Engineered biomimetic polymers as tunable agents for controlling CaCO₃ mineralization. *J. Am. Chem. Soc.* **133**, 5214–5217 (2011). doi: [10.1021/ja200595f](#); pmid: [21417474](#)
91. V. du Vigneaud, C. Ressler, J. M. Swan, C. W. Roberts, P. G. Katsoyannis, The synthesis of oxytocin. *J. Am. Chem. Soc.* **76**, 3115–3121 (1954). doi: [10.1021/ja01641a004](#)
92. N. Badi, J.-F. Lutz, Sequence control in polymer synthesis. *Chem. Soc. Rev.* **38**, 3383–3390 (2009). doi: [10.1039/b806413j](#); pmid: [20449057](#)
93. L. Hartmann, H. G. Börner, Precision polymers: Monodisperse, monomer-sequence-defined segments to target future demands of polymers in medicine. *Adv. Mater.* **21**, 3425–3431 (2009). doi: [10.1002/adma.200801884](#); pmid: [20882508](#)
94. L. Hartmann, Polymers for control freaks: Sequence-defined poly(amidoamine)s and their biomedical applications. *Macromol. Chem. Phys.* **212**, 8–13 (2011). doi: [10.1002/macp.201000479](#)
95. R. N. Zuckermann, J. M. Kerr, S. B. H. Kent, W. H. Moos, Efficient method for the preparation of peptoids [oligo(N-substituted glycines)] by submonomer solid-phase synthesis. *J. Am. Chem. Soc.* **114**, 10646–10647 (1992). doi: [10.1021/ja00052a076](#)
96. G. M. Church, Y. Gao, S. Kosuri, Next-generation digital information storage in DNA. *Science* **337**, 1628 (2012). doi: [10.1126/science.1226355](#)
97. C. Bancroft, T. Bowler, B. Bloom, C. T. Clelland, Long-term storage of information in DNA. *Science* **293**, 1763c–1765c (2001). doi: [10.1126/science.293.5536.1763c](#)
98. J. Bonnet, P. Subsoontorn, D. Endy, Rewritable digital data storage in live cells via engineered control of recombination directionality. *Proc. Natl. Acad. Sci. U.S.A.* **109**, 8884–8889 (2012). doi: [10.1073/pnas.1202344109](#); pmid: [22615351](#)

Acknowledgments: The authors thank D. A. Tirrell for his helpful comments and suggestion. J.F.L. thanks the European Research Council (Project SEQUENCES, grant agreement no. 258593), the CNRS, the University of Strasbourg, the International Center for Frontier Research in Chemistry (FRC, Strasbourg), and the excellence network Chimie des Systèmes Complexes (LabEx CSC) for financial support. M.S. and M.O. thank the Ministry of Education, Science, Sports, and Culture (MEXT) through a grant-in-aid for financial support [Creative Science Research (18GS0209), Grant-in-Aid for Scientific Research (A 24245026), and Grant-in-Aid for Young Scientists (A 23685024)]. D.R.L. is grateful for support from the Howard Hughes Medical Institute and National Institute of General Medical Sciences, NIH, R01GM065865.

10.1126/science.1238149

Global Epigenomic Reconfiguration During Mammalian Brain Development

Ryan Lister,* Eran A. Mukamel, Joseph R. Nery, Mark Urich, Clare A. Puddifoot, Nicholas D. Johnson, Jacinta Lucero, Yun Huang, Andrew J. Dwork, Matthew D. Schultz, Miao Yu, Julian Tonti-Filippini, Holger Heyn, Shijun Hu, Joseph C. Wu, Anjana Rao, Manel Esteller, Chuan He, Fatemeh G. Haghighi, Terrence J. Sejnowski, M. Margarita Behrens,* Joseph R. Ecker*

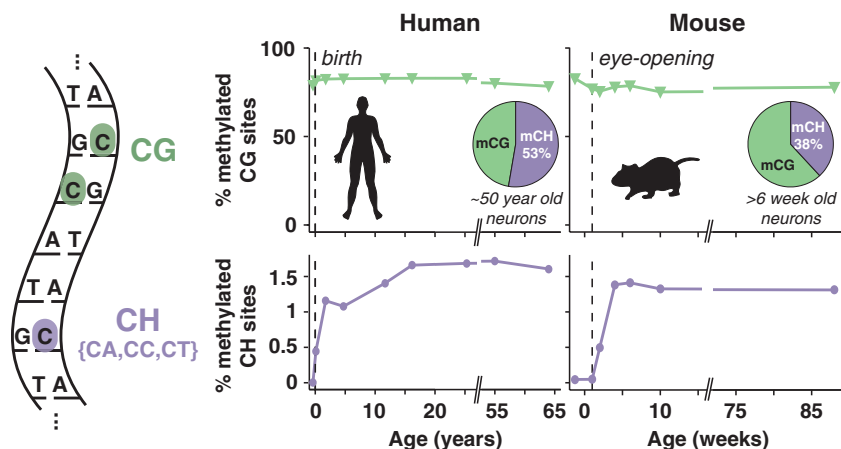
Introduction: Several lines of evidence point to a key role for dynamic epigenetic changes during brain development, maturation, and learning. DNA methylation (mC) is a stable covalent modification that persists in post-mitotic cells throughout their lifetime, defining their cellular identity. However, the methylation status at each of the ~1 billion cytosines in the genome is potentially an information-rich and flexible substrate for epigenetic modification that can be altered by cellular activity. Indeed, changes in DNA methylation have been implicated in learning and memory, as well as in age-related cognitive decline. However, little is known about the cell type-specific patterning of DNA methylation and its dynamics during mammalian brain development.

Methods: We performed genome-wide single-base resolution profiling of the composition, patterning, cell specificity, and dynamics of DNA methylation in the frontal cortex of humans and mice throughout their lifespan (MethylC-Seq). Furthermore, we generated base-resolution maps of 5-hydroxymethylcytosine (hmC) in mammalian brains by TAB-Seq at key developmental stages, accompanied by RNA-Seq transcriptional profiling.

Results: Extensive methylome reconfiguration occurs during development from fetal to young adult. In this period, coincident with synaptogenesis, highly conserved non-CG methylation (mCH) accumulates in neurons, but not glia, to become the dominant form of methylation in the human neuronal genome. We uncovered surprisingly complex features of brain cell DNA methylation at multiple scales, first by identifying intragenic methylation patterns in neurons and glia that distinguish genes with cell type-specific activity. Second, we report a novel mCH signature that identifies genes escaping X-chromosome inactivation in neurons. Third, we find >100,000 developmentally dynamic and cell type-specific differentially CG-methylated regions that are enriched at putative regulatory regions of the genome. Finally, whole-genome detection of 5-hydroxymethylcytosine (hmC) at single-base resolution revealed that this mark is present in fetal brain cells at locations that lose CG methylation and become activated during development. CG-demethylation at these hmC-poised loci depends on Tet2 activity.

Discussion: Whole-genome single-base resolution methylcytosine and hydroxymethylcytosine maps revealed profound changes during frontal cortex development in humans and mice. These results extend our knowledge of the unique role of DNA methylation in brain development and function, and offer a new framework for testing the role of the epigenome in healthy function and in pathological disruptions of neural circuits. Overall, brain cell DNA methylation has unique features that are precisely conserved, yet dynamic and cell-type specific.

The DNA methylation landscape of human and mouse neurons is dynamically reconfigured through development. Base-resolution analysis allowed identification of methylation in the CG and CH context (H = A, C, or T). Unlike other differentiated cell types, neurons accumulate substantial mCH during the early years of life, coinciding with the period of synaptogenesis and brain maturation.



READ THE FULL ARTICLE ONLINE

<http://dx.doi.org/10.1126/science.1237905>



Cite this article as R. Lister *et al.*, *Science* 341, 1237905 (2013). DOI: 10.1126/science.1237905

FIGURES IN THE FULL ARTICLE

Fig. 1. Methylcytosine in mammalian frontal cortex is developmentally dynamic and abundant in CG and CH contexts.

Fig. 2. mCH is positionally conserved and is the dominant form of DNA methylation in human neurons.

Fig. 3. mCH is enriched in genes that escape X inactivation.

Fig. 4. Cell type-specific and developmental differences in mC between mouse neurons and glia.

Fig. 5. hmCG is enriched within active genomic regions in fetal and adult mouse brain.

Fig. 6. Developmental and cell type-specific differential mCG.

SUPPLEMENTARY MATERIALS

Materials and Methods

Figs. S1 to S12

Tables S1 to S5

References (63–78)

The list of author affiliations is available in the full article online.

*Corresponding author. E-mail: ryan.lister@uwa.edu.au (R.L.); mbehrens@salk.edu (M.M.B.); ecker@salk.edu (J.R.E.)

Global Epigenomic Reconfiguration During Mammalian Brain Development

Ryan Lister,^{1,2*†} Eran A. Mukamel,^{3*} Joseph R. Nery,¹ Mark Urich,¹ Clare A. Puddifoot,³ Nicholas D. Johnson,³ Jacinta Lucero,³ Yun Huang,⁴ Andrew J. Dwork,^{5,6} Matthew D. Schultz,^{1,7} Miao Yu,⁸ Julian Tonti-Filippini,² Holger Heyn,⁹ Shijun Hu,¹⁰ Joseph C. Wu,¹⁰ Anjana Rao,⁴ Manel Esteller,^{9,11} Chuan He,⁸ Fatemeh G. Haghighi,⁵ Terrence J. Sejnowski,^{3,12,13} M. Margarita Behrens,^{3†} Joseph R. Ecker^{1,13†}

DNA methylation is implicated in mammalian brain development and plasticity underlying learning and memory. We report the genome-wide composition, patterning, cell specificity, and dynamics of DNA methylation at single-base resolution in human and mouse frontal cortex throughout their lifespan. Widespread methylome reconfiguration occurs during fetal to young adult development, coincident with synaptogenesis. During this period, highly conserved non-CG methylation (mCH) accumulates in neurons, but not glia, to become the dominant form of methylation in the human neuronal genome. Moreover, we found an mCH signature that identifies genes escaping X-chromosome inactivation. Last, whole-genome single-base resolution 5-hydroxymethylcytosine (hmC) maps revealed that hmC marks fetal brain cell genomes at putative regulatory regions that are CG-demethylated and activated in the adult brain and that CG demethylation at these hmC-poised loci depends on Tet2 activity.

Dynamic epigenetic changes have been observed during brain development, maturation, and learning (1–6). DNA methylation (mC) is a stable covalent modification that persists in postmitotic cells throughout their lifetime, defining their cellular identity. However, the methylation status at each of the ~1 billion cytosines in the genome is potentially an information-rich and flexible substrate for epigenetic modification that can be altered by cellular activity (7, 8). Changes in DNA methylation were implicated in learning and memory (9, 10), as well as in age-related

cognitive decline (11). Mice with a postnatal deletion of DNA methyltransferases Dnmt1 and Dnmt3a in forebrain excitatory neurons, or with a global deletion of methyl-CpG-binding protein 2 (MeCP2), show abnormal long-term neural plasticity and cognitive deficits (2, 12).

DNA methylation composition and dynamics in the mammalian brain are highly distinct. A modification of mC catalyzed by the Tet family of mC hydroxylase proteins, 5-hydroxymethylcytosine (hmC), accumulates in the adult brain (13–15) along with its more highly oxidized derivatives 5-formylcytosine and 5-carboxylcytosine. These modifications of mC were implicated as intermediates in an active DNA demethylation pathway (16–19). In addition, methylation in the non-CG context (mCH, where H = A, C, or T) is also present in the adult mouse and human brains (20, 21) but is rare or absent in other differentiated cell types (22, 23). Little is known about cell type-specific patterning of DNA methylation and its dynamics during mammalian brain development. Here, we provide integrated empirical data and analysis of DNA methylation at single-base resolution, across entire genomes, with cell-type and developmental specificity. These results extend our knowledge of the unique role of DNA methylation in brain development and function and offer a new framework for testing the role of the epigenome in healthy function and in pathological disruptions of neural circuits.

Accumulation of Non-CG DNA Methylation During Brain Development

To identify the composition and dynamics of transcription and methylation during mammalian brain development, we performed transcriptome profiling (mRNA-Seq) and whole-genome bi-

sulfite sequencing [MethylC-Seq (24)] to comprehensively identify sites of cytosine DNA methylation (mC and hmC) and mRNA abundance at single-base resolution throughout the genomes of mouse and human frontal cortex (table S1). DNA methylation in embryonic stem (ES) cells occurs in both the CG (mCG) and non-CG (mCH) contexts, but mCH is largely lost upon cell differentiation (22, 23, 25, 26). We found that although mCH levels are negligible in fetal cortex, abundant mCH occurs in adult frontal cortex (Fig. 1A). mCH has previously been identified throughout the genome of the adult mouse brain (20) and at several hundred genomic positions in the human adult brain (21). Supporting previous studies, we found that mammalian brain mCH is typically depleted in expressed genes, with genic mCH level inversely proportional to the abundance of the associated transcript (Fig. 1, A and B) (20). This pattern is the opposite of that observed in ES cells (22) and suggests that genic mCH in the brain may inhibit transcription. The absence of mCH in fetal brain suggests that this signature for gene repression is added to the genome at a later developmental stage.

We performed MethylC-Seq on mouse and human frontal cortex during early postnatal, juvenile, adolescent, and adult stages (Fig. 1C). CH methylation level, defined as the fraction of all base calls at CH genome reference positions that were methylated (denoted mCH/CH), accumulates in mouse and human brain during early postnatal development to a maximum of 1.3 to 1.5% genome-wide at the end of adolescence before diminishing slightly during aging. mCH increases most rapidly during the primary phase of synaptogenesis in the developing postnatal brain, from 2 to 4 weeks in mouse (27) and in the first 2 years in humans (28), followed by slower accumulation of mCH during later adolescence. mCH accumulation initially parallels the increase in synapse density within human middle frontal gyrus (synaptogenesis lasts from birth to 5 years), but it subsequently continues to increase during the period of adolescent synaptic pruning, which in humans occurs between 5 and 16 years of age (Fig. 1C). Notably, the accumulation of mCH in mice from 1 to 4 weeks after birth coincides with a transient increase in abundance of the *de novo* methyltransferase Dnmt3a mRNA and protein (Fig. 1D). Analysis of the context of mCH sites showed that it is mainly present in the CA context (fig. S1, A to F), as previously reported for mCH (20, 22, 23, 26).

Overall, genomes in the frontal cortex are highly methylated. Whereas CG partially methylated domains (PMDs) account for about a third of the genome of various differentiated human cells (22, 25), human brain genomes have negligible CG PMDs, resembling pluripotent cell methylomes (25) (fig. S1, G and H). Given the high spatial concordance of CG PMDs and nuclear lamina-associated domains reported previously (29), the

¹Genomic Analysis Laboratory, The Salk Institute for Biological Studies, La Jolla, CA 92037, USA. ²Plant Energy Biology [Australian Research Council Center of Excellence (CoE)] and Computational Systems Biology (Western Australia CoE), School of Chemistry and Biochemistry, The University of Western Australia, Perth, WA 6009, Australia. ³Computational Neurobiology Laboratory, The Salk Institute for Biological Studies, La Jolla, CA 92037, USA. ⁴La Jolla Institute for Allergy and Immunology and Sanford Consortium for Regenerative Medicine, La Jolla, CA 92037, USA. ⁵Department of Psychiatry, Columbia University and The New York State Psychiatric Institute, New York, NY 10032, USA. ⁶Department of Pathology and Cell Biology, Columbia University, New York, NY 10032, USA. ⁷Bioinformatics Program, University of California at San Diego, La Jolla, CA 92093, USA. ⁸Department of Chemistry and Institute for Biophysical Dynamics, The University of Chicago, Chicago, IL 60637, USA. ⁹Cancer Epigenetics Group, Cancer Epigenetics and Biology Program (PEBC), Bellvitge Biomedical Research Institute (IDIBELL), L'Hospitalet de Llobregat, Barcelona 08907, Spain. ¹⁰Department of Medicine, Division of Cardiology, Stanford University School of Medicine, Stanford, CA 94305, USA. ¹¹Institució Catalana de Recerca i Estudis Avançats (ICREA), Barcelona, Catalonia, Spain. ¹²Division of Biological Sciences, University of California at San Diego, La Jolla, CA 92037, USA. ¹³Howard Hughes Medical Institute, The Salk Institute for Biological Studies, La Jolla, CA 92037, USA.

*These authors contributed equally to this work.

†Corresponding author. E-mail: ryan.lister@uwa.edu.au (R.L.); mbehrens@salk.edu (M.M.B.); ecker@salk.edu (J.R.E.)

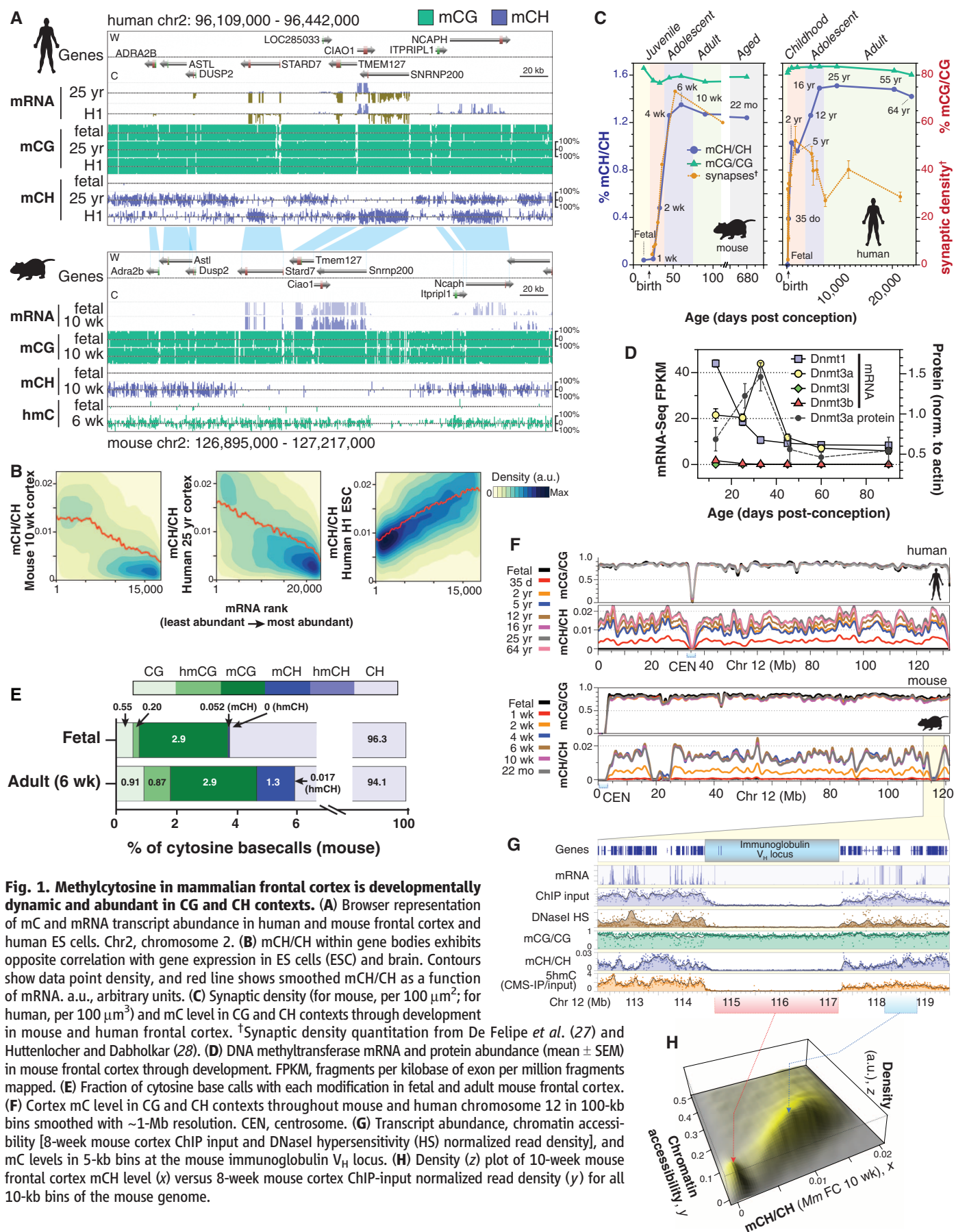


Fig. 1. Methylcytosine in mammalian frontal cortex is developmentally dynamic and abundant in CG and CH contexts. (A) Browser representation of mC and mRNA transcript abundance in human and mouse frontal cortex and human ES cells. Chr2, chromosome 2. (B) mCH/CH within gene bodies exhibits opposite correlation with gene expression in ES cells (ESC) and brain. Contours show data point density, and red line shows smoothed mCH/CH as a function of mRNA. a.u., arbitrary units. (C) Synaptic density (for mouse, per 100 μm^2 ; for human, per 100 μm^3) and mC level in CG and CH contexts through development in mouse and human frontal cortex. [†]Synaptic density quantitation from De Felipe *et al.* (27) and Huttenlocher and Dabholkar (28). (D) DNA methyltransferase mRNA and protein abundance (mean \pm SEM) in mouse frontal cortex through development. FPKM, fragments per kilobase of exon per million fragments mapped. (E) Fraction of cytosine base calls with each modification in fetal and adult mouse frontal cortex. (F) Cortex mC level in CG and CH contexts throughout mouse and human chromosome 12 in 100-kb bins smoothed with ~ 1 -Mb resolution. CEN, centrosome. (G) Transcript abundance, chromatin accessibility [8-week mouse cortex ChIP input and DNaseI hypersensitivity (HS) normalized read density], and mC levels in 5-kb bins at the mouse immunoglobulin V_H locus. (H) Density (z) plot of 10-week mouse frontal cortex mCH level (x) versus 8-week mouse cortex ChIP-input normalized read density (y) for all 10-kb bins of the mouse genome.

paucity of CG PMDs in these brain methylomes could indicate that lamina-associated domains are altered or much less frequent in the brain.

The adult mammalian brain contains the highest levels of hmC that have been observed (15), accounting for about 40% of methylated CG sites in cerebellar Purkinje cells (30). hmC accumulates during early postnatal brain development in mice (31, 32), becoming enriched in highly expressed genes (33). Given the evidence that hmC can be an intermediate in an active DNA demethylation pathway (16, 17), high-resolution analysis of the genomic distribution of hmC is needed to understand its role in the control of DNA methylation dynamics through brain development. Standard bisulfite-sequencing data does not distin-

guish between methylated and hydroxymethylated sites, so methylcytosines identified by MethylC-Seq analysis represent the sum of these two contributions. Therefore, we used Tet-assisted bisulfite sequencing [TAB-Seq (34)], a base-resolution technique that distinguishes hmC from C and mC genome-wide, to profile hmC in mouse fetal and adult frontal cortex (Fig. 1A). Integration of the genome-wide profiles of mC and hmC enabled a detailed breakdown of the methylated subset of the genome at these distinct developmental stages (Fig. 1E). hmC constitutes 0.20% of total cytosine base calls in fetal cortex and increases to 0.87% in adult cortex. This modification appears to be restricted to the CG context, as also observed in human and mouse ES cells (34); after correction

for false detection, we estimated that 0.017% of cytosine base calls were hmCH genome-wide (99% confidence interval: 0 to 0.059%), and significant hmCH was detected at few individual sites (fig. S2, A and B). The overwhelming presence of hmC in the CG context (99.98%) in mouse adult and fetal frontal cortex is consistent with recent findings in human ES cells, where 99.89% of hmC is in the CG context (34). hmC was present at many highly methylated CG sites (fig. S2C). Therefore, although only a small fraction of all cytosines throughout the genome are methylated (mCG = 2.9%, mCH = 1.3%, hmC = 0.87%), mCH and hmC constitute major, and nonoverlapping, components of the methylated fraction of the genome in adult frontal cortex (mCG = 57.2%,

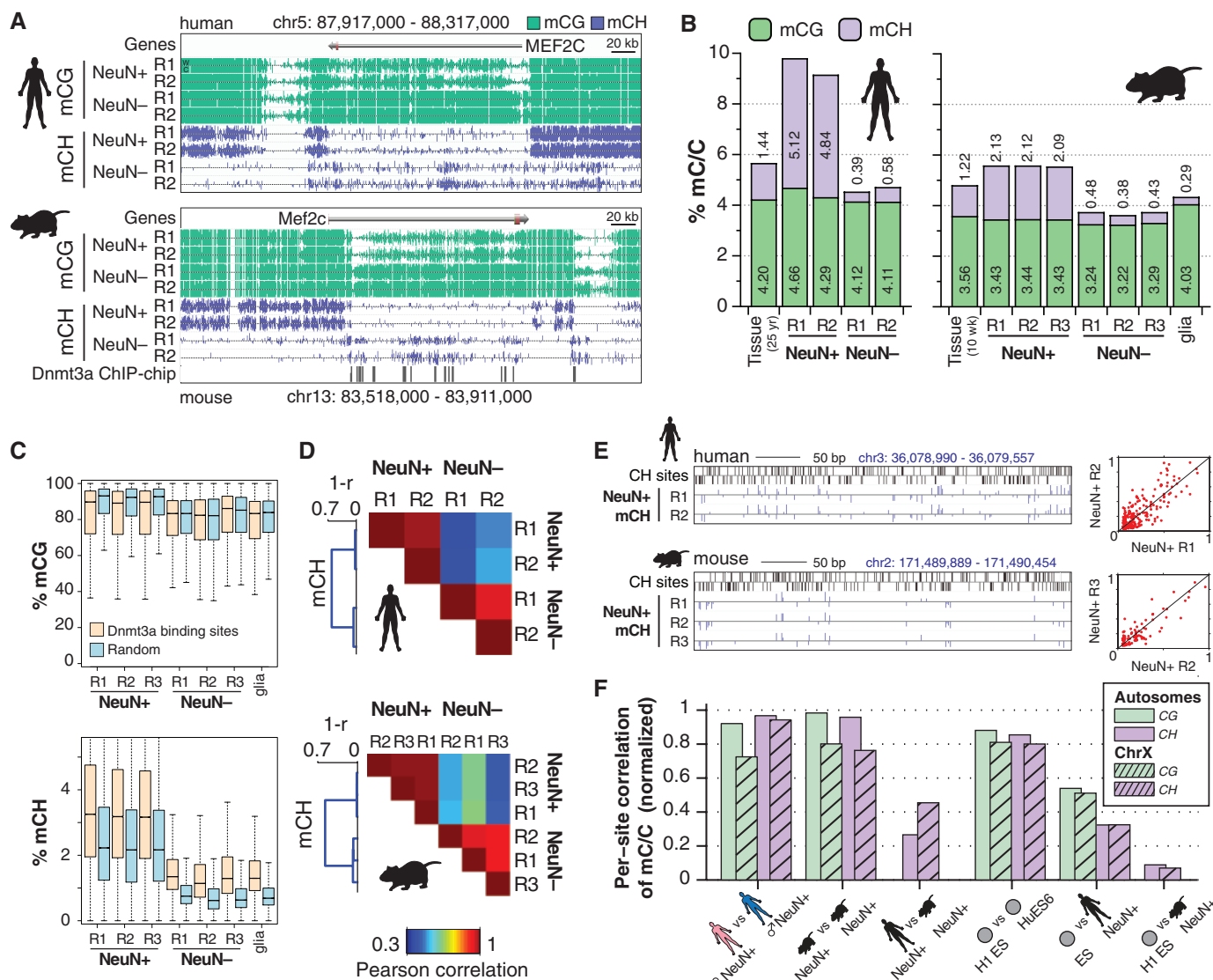


Fig. 2. mCH is positionally conserved and is the dominant form of DNA methylation in human neurons. (A) Browser representation of mCG and mCH in NeuN+ and NeuN- cells. Human NeuN+/NeuN- samples: R1, 53-year-old female; R2, 55-year-old male. Mouse NeuN+/NeuN- samples: R1, 7-week males; R2, 6-week females; R3, 12-month females (not shown). (B) Percentage of methylated base calls in each sequence context throughout the genome. (C) Box and whisker plot of mCG and mCH level in neurons and glia at genomic

regions bound by Dnmt3a versus a random set. Whiskers indicate 1.5 times the interquartile range. (D) mCH correlation between NeuN+ and NeuN- cells in mouse and human, measured in 10-kb bins. (E) Browser representation of mCH sites in neurons. Scatter plots (right) show consistent mCH/CH at all single sites in a 20-kb window overlapping the example region (left). (F) Correlation analysis of methylation state at single sites between neurons and ES cells in human and mouse. Correlation values are normalized by a simulation (62).

mCH = 25.6%, hmC = 17.2%). These data suggest that the steady-state population of hmC in the adult brain is not an intermediate stage in the demethylation of mCH. However, these steady-state measurements do not preclude the possibility that hmCH could be rapidly turned over after conversion from mCH, leading to negligible detected hmCH despite Tet-mediated demethylation at CH sites.

Protection of Inaccessible Genomic Regions from de Novo Methylation

mCH accumulates in parallel across most of the genome (Fig. 1F). However, we found numerous (36 in human, 34 in mouse) noncentromeric, megabase-sized regions that do not accumulate mCH. These regions, which we termed mCH deserts, are enriched for large gene clusters that encode proteins involved in immunity and recep-

tors required for sensory neuron function (table S2). One mCH desert spans the immunoglobulin V_H locus, which encodes variable domains of the immunoglobulin heavy chain that rearrange in B lymphocytes. The V_H locus is transcriptionally quiescent in the frontal cortex of 10-week-old mice, and the chromatin state is highly inaccessible, as inferred from deoxyribonuclease I (DNaseI) hypersensitivity profiling (35) and chromatin immunoprecipitation (ChIP) input sequence read density data (36, 37) (Fig. 1G). In contrast, mCG is not depleted in mCH deserts.

Genome-wide detection of hmC by cytosine 5-methylenesulphonate immunoprecipitation (CMS-IP) (38, 39) revealed that hmC is also strongly depleted in the V_H locus. mCH deserts are observed at other loci in the genome, including olfactory receptor gene clusters that form heterochromatic aggregates required for mono-

allelic receptor expression in olfactory sensory neurons (40, 41). Genome-wide comparison of mCH/CH with chromatin accessibility, as inferred from ChIP input read density (36, 37), for all 10-kb windows of the mouse genome revealed two discrete groups of genomic regions (Fig. 1H). Low-accessibility regions tend to contain minimal mCH, whereas more-accessible regions of the genome show a proportional relationship between genome accessibility and mCH levels. Thus, although mCG is unaffected in these regions, lower chromatin accessibility appears to be highly inhibitory to deposition of mCH and hmC, potentially via inaccessibility to de novo methyltransferases and Tet mC hydroxylases. Furthermore, this indicates that accumulation of mCH and hmC during mammalian brain development occurs via processes that are at least partly independent from methylation at CG dinucleotides.

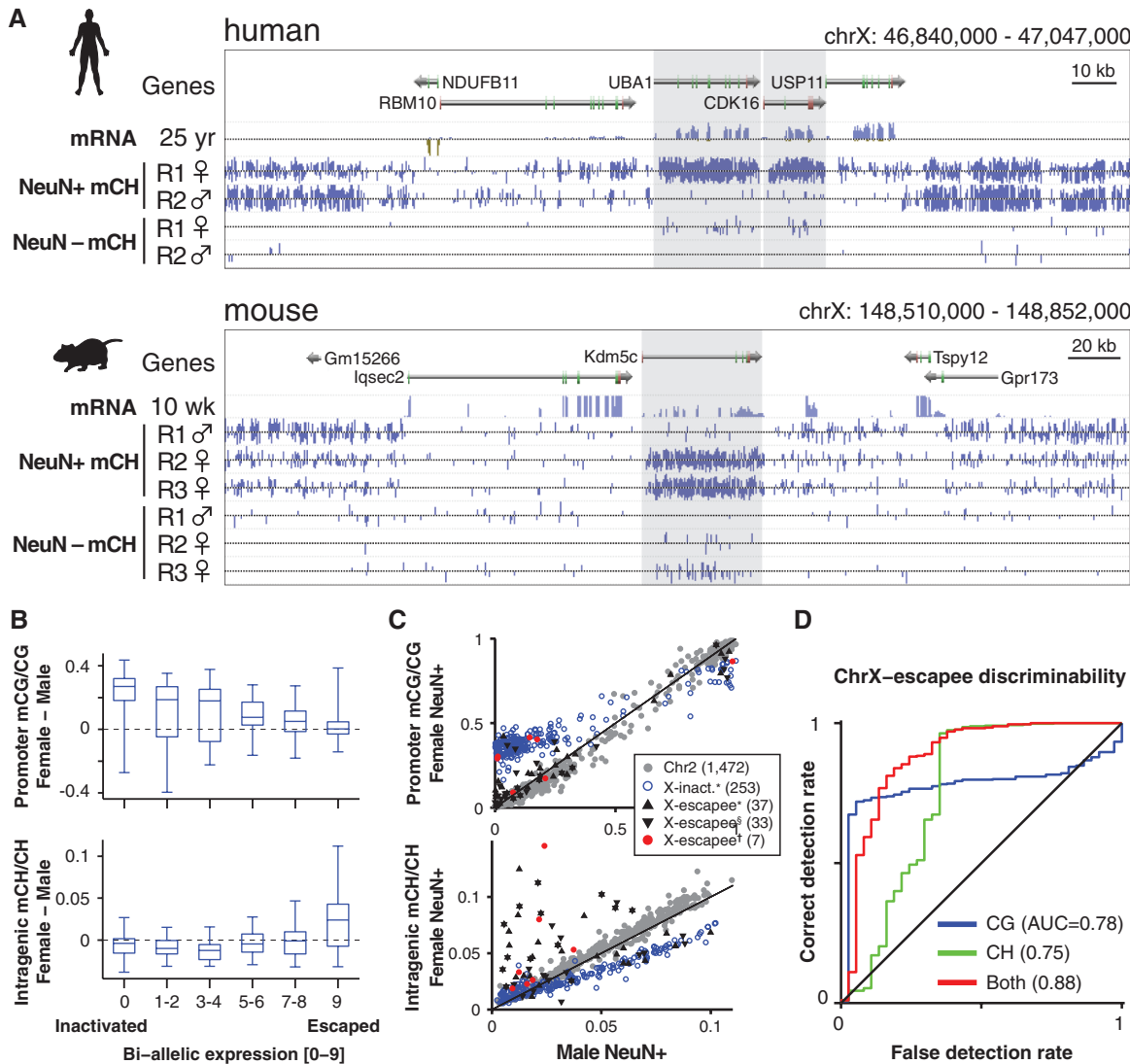


Fig. 3. mCH is enriched in genes that escape X inactivation. (A) Browser representation showing mCH-hypermethylated female human and mouse genes that escape X inactivation (shaded genes). (B) Box and whisker plots of gender differences in promoter mCG and intragenic mCH in inactivated and escapee genes on human chrX. (C) Scatter plot of gender differences in mCG and mCH

in human chrX genes. Reported X inactivated and escapee genes: *Carrel and Willard (49); †Sharp *et al.* (50); ‡predicted escapee genes, and autosomal (Chr2) genes are indicated. (D) Discriminability analysis of genes that escape female X inactivation using mC data, showing correct versus false detection rate mapped for all possible mC/C thresholds.

Cell Type–Specific DNA Methylation Patterns in Neurons and Glia

The diversity of neuronal and glial cells in the frontal cortex raises the question of which features of DNA methylation are found in specific cell types. We isolated populations of nuclei by fluorescence-activated cell sorting that were highly enriched for neurons (NeuN+) or glia (NeuN–) from human and mouse adult frontal cortex tissue. An additional glial population was isolated from mice expressing enhanced green fluorescent protein (eGFP) under the S100b promoter. MethylC-Seq revealed differences in the com-

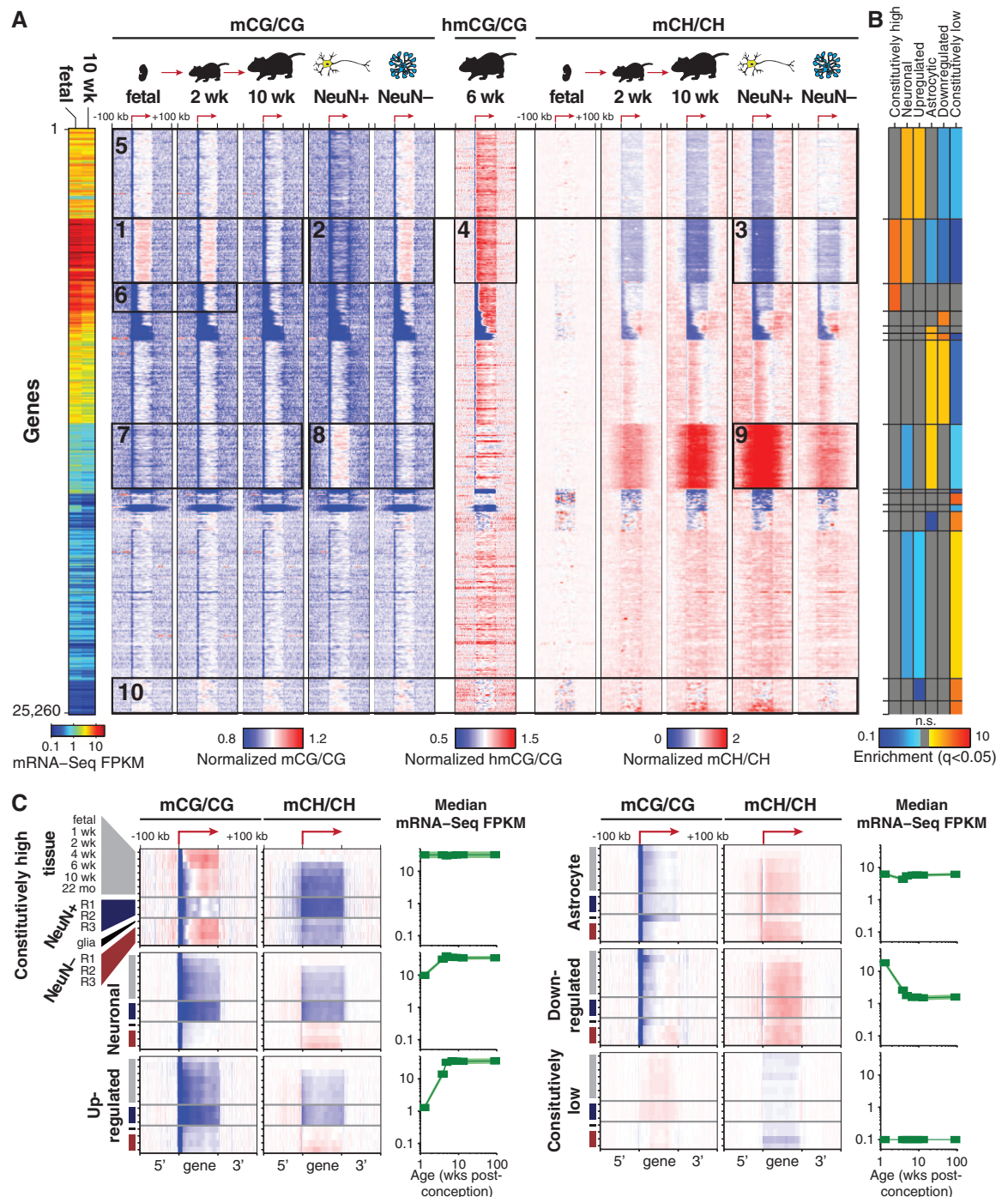
position and patterning of mCG and mCH in neurons and glia (Fig. 2A). Whereas differential mCG between neurons and glia was restricted to localized regions, neurons were globally enriched for mCH compared with glia. Indeed, we discovered that the level of mCH in glia is similar to that of fetal and early postnatal cortical tissue, whereas adult neurons have the greatest frequency of mCH that has been observed in mammalian cells. This indicates that the rapid developmental increase in mammalian brain mCH that coincides with the period of synaptogenesis is primarily due to mCH accumulation in neurons. Further-

more, our data show that in human neurons mCH is the dominant form of methylation in the genome: It is more abundant than mCG and occurs in 5% of CH and 10% of CA sites (Fig. 2B and fig. S1, A, B, and H). Of the total methylated fraction of adult human neuronal genomes, mCH accounts for ~53%, whereas mCG constitutes ~47%.

Although sparse in glia, mCH enrichment occurs within genes that are CH-hypomethylated in neurons, such as *Mef2c* (Fig. 2A), a transcriptional activator that plays critical roles in learning and memory, neuronal differentiation (42),

Fig. 4. Cell type–specific and developmental differences in mC between mouse neurons and glia. (A) Heat-map representation of 25,260 mouse genes organized in gene sets identified by *k*-means clustering using normalized genic mCG and mCH levels in adult developmental and NeuN+ and NeuN– samples. Left-hand plot shows mRNA abundance.

(B) Enrichment or depletion of each cluster for developmental and cell-type specific gene sets. n.s., not significant (FET, FDR < 0.05). (C) mCG and mCH throughout gene body and flanking 100 kb for indicated gene sets. Transcript abundance (mRNA-Seq FPKM) over mouse development is shown for the same gene sets. Color scales are as in (A).



synaptic plasticity (43), and regulation of synapse number and function (44). Genome-wide surveys identified 174 mouse genes in which glia were hypermethylated relative to neurons in the CH context (table S3). Unbiased gene ontology analysis revealed that these glial hyper-mCH genes are highly enriched for roles in neuronal and synaptic development and function (table S3). These genes also overlapped significantly with a set of 461 genes expressed at higher levels in neurons than in astrocytes (13-fold higher overlap than chance, $P < 10^{-30}$, Fisher exact test, FET) (45) and 233 developmentally up-regulated genes (7.5-fold, $P < 10^{-7}$, FET). These genes show hypomethylation of CG and CH in neurons and hypermethylation of CH in glia (fig. S3A), consistent with a potential role of mCH in transcriptional repression of neuronal genes in the glial genome. Furthermore, genes associated with oligodendrocyte or epithelial function accumulate mCH through development (fig. S3B), with oligodendrocyte up-regulated genes showing intragenic mCH hypermethylation in neurons and hypomethylation in glia, whereas epithelial genes

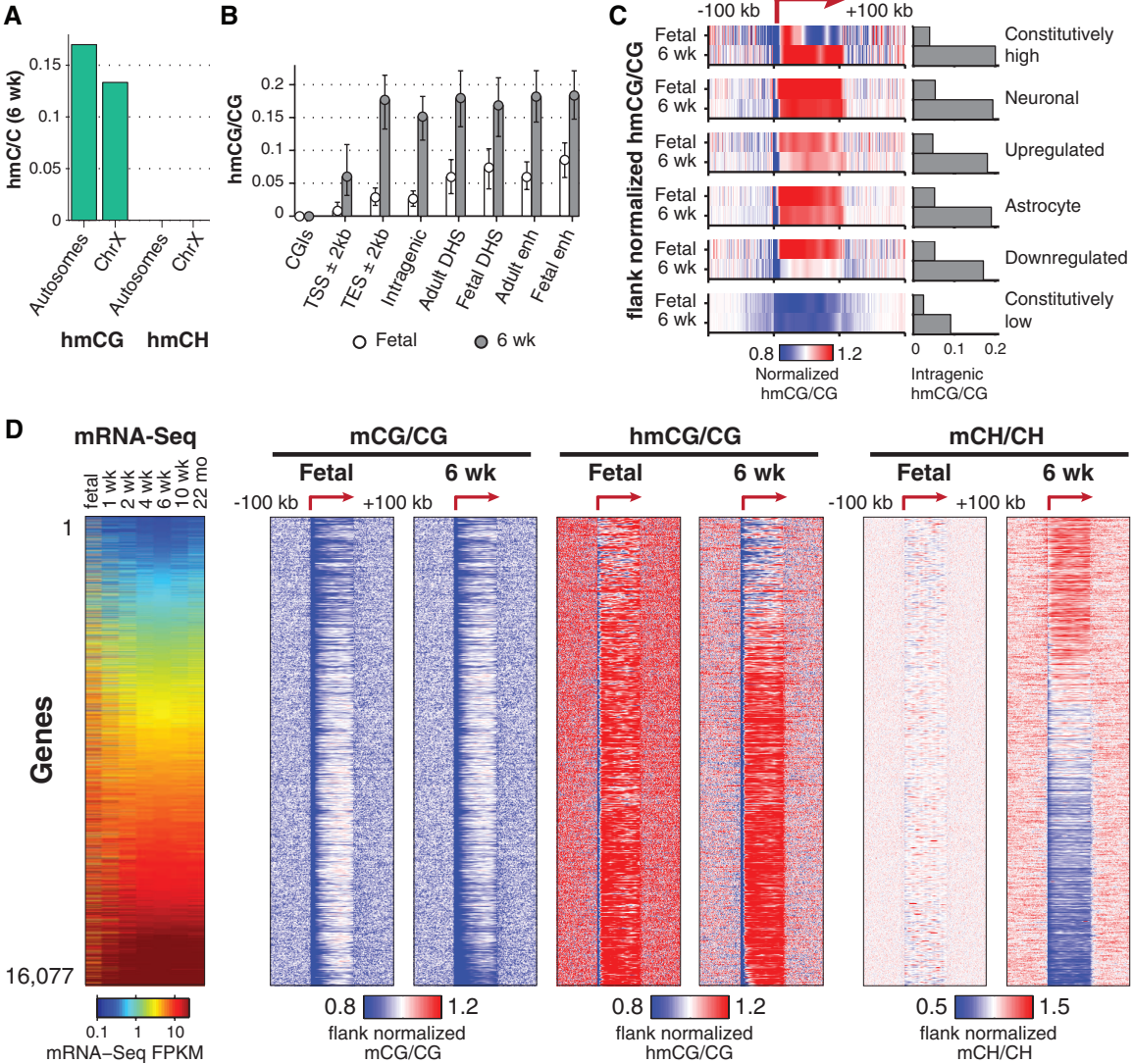
display mCH hypermethylation in both neuronal and glial populations. Consistent with CH methylation requiring Dnmt3a, glial hyper-mCH genes frequently intersect areas of the genome bound by Dnmt3a in mouse postnatal neural stem cells (46). Dnmt3a-binding regions are greatly enriched for mCH, particularly in glia, whereas mCG is not enriched in Dnmt3a-binding regions in glia and is depleted in neurons (Fig. 2C). Thus, there is an association with Dnmt3a binding sites specific to mCH and not mCG, suggesting partial independence between these two marks.

mCH Position Is Highly Conserved

We examined whether the position of DNA methylation is stochastic or precisely controlled at different genomic scales. The level of mCH in 10-kb windows throughout the genome was highly reproducible between independent samples of the same cell type, with lower, but substantial, correlation between cell types (Fig. 2D). Closer inspection revealed consistency between the methylation level at individual mCH sites in neurons from different individuals in both mice and hu-

mans (Fig. 2E). At single-base resolution (fig. S4), perfect correlation between individuals would not be observed even if the true methylation level were identical at each site because of the stochastic effect of a finite number of sequenced reads. To correct for this, we normalized the observed correlation by that of simulated data sets with the same coverage per site as each of our experimental samples but with identical methylation levels (Fig. 2F and fig. S4). To assess statistical significance, we used a permutation test, which compared the data correlation with the correlation after randomly shuffling the relative positions of CH sites in each sample (fig. S4). This revealed that autosomal CG and CH sites have nearly identical methylation levels in neuronal populations isolated from different individuals of the same species. Observed differences could be explained by stochastic sampling rather than true individual variation. Unexpectedly, normalized per-site correlation is higher for mCH than mCG between neuronal populations isolated from the frontal cortices of different human individuals, and mouse neuronal mCG and mCH per-site

Fig. 5. hmCG is enriched within active genomic regions in fetal and adult mouse brain. (A) hmCG level in 6-week mouse frontal cortex for autosomes and ChrX. (B) Median hmCG level within genomic features (error bars 32nd to 68th percentile). enh, enhancer. (C) Median normalized hmCG throughout gene body and flanking 100 kb for indicated gene sets. Bars show absolute hmCG/CG levels within gene bodies for each class. (D) mC and hmC throughout gene body and flanking 100 kb for each. Transcript abundance (mRNA-Seq FPKM) during mouse development is also shown (left).



correlations are equivalent. Per-site correlation between two human ES cell lines (H1 and HUES6) is also high (>0.8) for both mCG and mCH.

The high interindividual correlation of mCH at the kilobase and single-site scales indicates that methylation of CH positions, particularly in mammalian neurons, is a highly controlled process. It is not consistent with a stochastic event that takes place at any available CH position in a particular genomic region that accumulates mCH. Comparison of mCH between human and mouse neurons at conserved exonic CH positions revealed a low but significant interspecies correlation (Fig. 2F; $P < 0.005$, shuffle test), possibly indicating conservation of the cellular processes that precisely target or restrict mCH at these positions. Last, per-site mCG and mCH correlation between human ES cells and neurons is significantly lower, likely because of differences in the processes governing methylation of particular genomic features in the distinct cell types, for example, enrichment and depletion of mCH in highly transcribed genes in ES cells and neurons, respectively (Fig. 1, A and B).

The precise conservation of mCH position may be partly caused by the physical configuration of DNA within nucleosomes. Consistent with this, neuronal mCH patterns contain robust periodic components at the scale of nucleosome spacing [~ 170 base pairs (bp), fig. S5A] and the DNA helix coil length (~ 10.5 bp, fig. S5B). Such periodic components may arise from sequence-dependent constraints on mCH position, which would be the same in every neuronal cell. Alternatively, epigenetic heterogeneity within the population of NeuN⁺ nuclei in our sample may lead to stronger correlation for CH sites located on the same physical chromosome, compared with the correlation between the same locations on chromosomes from different cells. To test this, we measured the cross-correlation within individual reads, revealing a contribution of within-chromosome correlation to the periodic methylation pattern (fig. S5C).

Gender-Specific DNA Methylation Patterns on the X Chromosome

Interindividual correlation of mCG and mCH on chromosome X (ChrX) is frequently lower than on autosomes (Fig. 2F), prompting a closer analysis of ChrX mC patterns. ChrX mCG and mCH levels were generally lower in females compared with males, presumably because of the effect of ChrX inactivation (fig. S5, F and G) (47, 48). However, a subset of genes in both humans and mice have significantly greater intragenic mCH levels in females compared with males (Fig. 3A). Inspection of these genes revealed that most were previously found to escape inactivation in human females (X-escapees), displaying biallelic expression (49) and a reduction in promoter mCG hypomethylation, a DNA methylation signature of inactivated alleles (50). Quantification of human gender differences in neuronal DNA methylation for ChrX genes previously characterized as show-

ing biallelic expression (49) revealed that females have reduced promoter mCG and a large increase in intragenic mCH but not intragenic mCG (Fig. 3, B and C, and fig. S5, D and E). The sequence composition of mCH is very similar in the whole genome, within autosomal gene bodies, and within X-chromosome inactivated and escapee gene bodies (fig. S5H). Analysis of gender-specific methylation in additional human cell types revealed that female promoter mCG hypomethylation is observed at X-escapee genes in glia and human embryonic stem cells (fig. S6). Intragenic mCH hypermethylation of X-escapees was also observed in female glia, albeit to a lesser extent than in neurons, but was not present in ES cells. Thus, X-escapee mCH hypermethylation may be a feature that is specific to neural cell types. Although both promoter CG hypomethylation and intragenic CH hypermethylation provide significant information for discriminating X-escapees [Fig. 3D, discriminability index (area under the curve, AUC) = 0.75 and 0.78, respectively], combining both mCG and mCH measurements boosts discriminability (AUC = 0.88). By using this intragenic mCH hypermethylation signature, we identified seven new putative X-escapee genes (table S4). On the basis of these data, we hypothesize that intragenic CH hypermethylation in neurons may play a compensatory role in genes that fail to acquire repressive CG hypermethylation in the promoter region, restoring equal gene expression between male and female cells (51).

Distinct Genic DNA Methylation States Demarcate Functionally Relevant Gene Clusters

DNA methylation within promoter regions and in gene bodies is implicated in regulation of gene expression (22, 52), suggesting that the precisely conserved, cell type-specific DNA methylation patterns may be related to specific neuronal and glial cellular processes. We therefore used an unbiased approach to classify patterns of mCG and mCH within each annotated gene body and in flanking regions extending 100 kb up- or downstream. After normalizing the methylation pattern around each autosomal gene by the local baseline mCG or mCH level in each adult neuronal or glial sample, we combined these features into a large data matrix containing 4200 individual DNA methylation measurements for each gene [seven samples, two contexts (CG and CH), 300 1-kb bins within and around each gene]. Using principal component (PC) analysis, we extracted five methylation features (PCs) that together account for 46% of the total data set variance (fig. S7A). Gene sets with specific neuronal or astrocytic expression, as well as ChrX genes, segregate within PC space (fig. S6B). We then used *k*-means clustering to classify all genes into 15 clusters on the basis of their mCG and mCH patterns (Fig. 4A and fig. S8). Several dominant patterns of DNA methylation and transcript abundance and dynamics between developmental and cellular states are evident. A cluster of genes that progressively loses gene-body mCG and mCH through development

contains constitutively highly expressed genes that are strongly enriched for neuronal function and depleted for astrocyte-specific roles (Fig. 4A, box 1). These genes show intragenic mCG enrichment in glia and depletion in neurons (box 2), indicating that glial gene body mCG resembles that of the neural precursor cells that predominate the fetal brain. This indicates that the loss of mCG in brain tissue during development is due to CG hypomethylation in mature neurons. These constitutively highly expressed genes enriched for neuronal function also show extensive intragenic mCH hypomethylation in neurons in contrast to glia (box 3), and they are enriched for hmCG (box 4) as previously described (32, 33). Genes that are not as highly transcribed, but that are associated with neuronal function and are developmentally up-regulated, also show intragenic mCG and mCH hypomethylation in neurons but not glia (box 5). For these gene sets, mCG and mCH enrichment or depletion is precisely localized to transcribed regions, suggesting that this modification of genic mC is tightly coupled to transcription. Notably, the bodies of constitutively high genes that are not enriched for neuronal function (box 6) do not show marked fetal/glial mCG enrichment or neuronal mCH depletion, indicating that this differential methylation is specific for genes enriched for neuronal function and not simply an association with particular levels of transcriptional activity. Genes associated with astrocyte function show an opposite pattern to genes associated with neuronal function: a progressive increase in intragenic mCG and mCH in frontal cortex tissue over development, neuronal mCG and mCH hypermethylation, and glial mCG and mCH hypomethylation (Fig. 4A, boxes 7 to 9). Last, genes with constitutively low expression do not show developmental or cell type-specific DNA methylation patterns (box 10), demonstrating that dynamic DNA methylation in genes is highly associated with differential transcriptional activity in mammalian brain development and neural cell specialization.

Each of the gene clusters identified in our unbiased analysis was significantly enriched or depleted for cell type-specific function [neuronal or astrocytic genes (45)] or particular expression patterns (constitutively high or low expression, developmentally up- or down-regulated) (Fig. 4B). Profiling the median mCG and mCH of genes within each of these categories allows direct comparison of developmental and cell type-specific DNA methylation in mouse (Fig. 4C) and human (fig. S3C). This analysis recapitulates many of the conclusions of the unbiased clustering (Fig. 4A).

The inverse relationship observed between genic mCH level and transcriptional activity is consistent with a model whereby intragenic accumulation of mCH impedes transcriptional activity. Alternatively, the process of transcription could interfere with mCH de novo methylation or induce active mCH demethylation, although these are not consistent with the DNMT3A-dependent intragenic mCH in human embryonic stem cells that is positively correlated with gene expression

[illegible]

(22, 23). Overall, glial mCG and mCH patterns closely resemble those of the fetal and the early postnatal brain, indicating that DNA methylation in early mammalian brain developmental stages may be a default state that largely persists through to maturity in glial cells, whereas neuronal differentiation and maturation involve extensive re-configuration of the DNA methylome that is highly associated with cell type-specific changes in transcriptional activity.

hmCG Is Enriched Within Active Genomic Regions in Fetal and Adult Mouse Brain

Our base-resolution analysis of hmC using TAB-Seq revealed that intragenic and global mCG levels are largely equivalent between chromosomes, whereas hmCG/CG is 22% lower on the male ChrX, consistent with previous reports from enrichment based detection of hmC (32, 33) (Fig. 5A). Analysis of hmCG levels in different genomic regions revealed that, although adult hmCG/CG is similar across transcriptional end sites and intragenic, DNaseI-hypersensitive (DHS), and enhancer regions, the fetal frontal cortex shows a relative enrichment of hmCG in DHS regions and enhancers, in particular enhancer regions that are unique to the fetal developmental stage (Fig. 5B). The inverse pattern can be observed for adult mCG levels, which are lower in DHS regions and enhancers (fig. S9, A and B), suggesting that regions of relatively high hmCG levels in the fetal brain show relatively low mCG levels in the adult brain. Analysis of intragenic hmCG enrichment relative to flanking genomic regions, for cell type-specific or developmentally dynamic gene sets (Fig. 5C), showed that neuronal and astrocyte gene bodies that are highly enriched with hmCG in adult are also highly enriched at the fetal stage.

Thus, despite lower absolute levels of intragenic hmCG in the fetal stage, the adult patterns of hmCG enrichment at these cell type-specific genes are already forming in utero. Constitutively lowly expressed genes show intragenic depletion of hmCG, in contrast to constitutively highly transcribed genes, which show localized enrichment of hmCG throughout part or all of the gene body. Developmentally down-regulated genes show enrichment of hmCG in the fetal frontal cortex but not in adults, indicating that reduced transcription is accompanied by a loss of hmCG enrichment. Overall, transcriptional activity is associated with intragenic hmCG enrichment, as reported (33), with in utero establishment of adult hmCG patterns for cell type-specific genes and loss of hmCG enrichment associated with developmentally coupled transcriptional down-regulation.

Measurement of mC and hmC in all genes in fetal and adult mouse frontal cortex indicated that both mCG and hmCG are depleted at promoters and in gene bodies of lowly expressed genes, whereas hmCG is enriched throughout the gene bodies of more highly transcribed genes (Fig. 5D). The most highly expressed genes in the adult frontal cortex show intragenic mCG hypomethylation (Figs. 4 and 5D) but still retain high intra-

genic hmCG. Ranking all genes by transcript abundance, it is evident that the highest mean intragenic hmCG levels, which occur in the most highly transcribed genes, correspond to hmCG/CG ~ 0.25 and mCG/CG ~ 0.5 (fig. S10D). Frontal cortex development is accompanied by increased enrichment of hmCG at intragenic regions that are already hyper-hydroxymethylated at the fetal stage (Fig. 5D and fig. S10), demonstrating that adult patterns of genic hmC are already evident in the immature fetal brain.

CG Differentially Methylated Regions Enriched in Regulatory Regions

Because differences in genic mCG were observed over development and between neuronal and glial cell populations (Fig. 4), we scanned the human and mouse methylomes to comprehensively identify CG differentially methylated regions (CG-DMRs) throughout the genome. CG-DMRs were identified between fetal and adult frontal cortex, neurons and glia, and combined into four sets: neuronal and glial hyper- and hypo-methylated CG-DMRs. In total, 267,799 human and 142,835 mouse CG-DMRs were identified (median lengths: for mouse, 473 bp; human, 533 bp), revealing several predominant dynamics in mCG during brain development and cellular specialization (Fig. 6A and fig. S11). Neuronal CG-DMRs are the most numerous in both mice and humans, because of the very distinct mCG patterns that emerge during neuronal differentiation and maturation. At these sites, CG methylation in adult neurons is distinct compared with those in glial and/or fetal and early postnatal development frontal cortex tissue samples. Neuronal hypermethylated CG-DMRs also show mCH hypermethylation (fig. S11). In mouse, mCG/CG within neuronal hypomethylated CG-DMRs declines to a stable level by 1 week after birth. In contrast, neuronal hypermethylated CG-DMRs do not begin to change until 1 week after birth, after which they accumulate mCG until 2 to 4 weeks of age. These data indicate that increases in neuronal mCG occur during synaptogenesis after most decreases in neuronal mCG have already occurred. Furthermore, we found that hydroxymethylation in the adult cortex is highest in CG-DMRs that show neuronal hypermethylation and is depleted from CG-DMRs that display neuronal hypomethylation (Fig. 6A). This suggests that hmCG may be most abundant in neurons, rather than glial cells, in the frontal cortex.

Analysis of the genomic features in which CG-DMRs are located revealed that although half are found within gene bodies, they are not common within promoters and transcriptional start and end regions. Instead, they are disproportionately located at DHS regions and enhancers unique to fetal or adult brain (Fig. 6B). Closer inspection of the enrichment and depletion of these CG-DMRs revealed that fetal enhancers and DHS sites unique to the fetal brain are enriched for hypermethylation in adult brain but not in the fetal brain (Fig. 6C). In contrast, adult enhancers and unique adult DHS sites are highly associated with CG hyper-

methylation in fetal stages but are not associated with hypermethylated CG-DMRs in the adult brain and in neurons. Thus, developmentally dynamic enhancers and DHS sites in frontal cortex have dynamic CG methylation that is depleted where chromatin accessibility and regulatory element activity increase, consistent with a range of human cell lines (53).

To characterize gene functions associated with the CG-DMRs, we analyzed the association between proximal genes (transcriptional start site within 5 kb of the DMR) and cell type-specific or developmentally dynamic gene sets (fig. S12A). We observed an inverse relationship between methylation and gene function. Genes associated with neuronal function and up-regulation during development are enriched for promoter hypermethylation in glia and hypomethylation in neurons, whereas genes down-regulated during brain development and those related to astrocyte function are enriched for promoter hypermethylation in neurons and hypomethylation in glia. Genes that are constitutively expressed at either high or low levels are not associated with promoter/transcription start site CG-DMRs, indicating that dynamic CG methylation is highly associated with changes in transcriptional activity and cell type-specific transcriptional regulation.

Because the majority of all developmentally dynamic CG-DMRs are associated with DHS sites, we examined the directional relationships between dynamic mCG and DNA accessibility states over development (Fig. 6D). Notably, DHS sites unique to fetal frontal cortex overlap with 28% of CG-DMRs that gain methylation through development (Adult>Fetal). However, these sites only overlap 7.3% of CG-DMRs that lose mCG during development (Fetal>Adult). Similarly, DHS sites unique to adult frontal cortex rarely overlap Adult>Fetal CG-DMRs. A similar analysis of developmentally dynamic enhancers active in only one of the developmental stages (37) (Fig. 6E) showed that enhancer activation is associated with mCG hypomethylation of the enhancer, whereas enhancer inactivation is associated with enhancer mCG hypermethylation.

This inverse relationship between genome accessibility and mCG level at putative functional regions of the genome suggests that nuclear factors that bind the region and increase accessibility may cause localized reduction in mCG, as previously reported for a small number of DNA binding proteins (54). Alternatively, mCG hypermethylation may cause reduced genome accessibility by direct inhibition of DNA-protein interactions or induction of chromatin compaction, with loss of mCG enabling increased chromatin accessibility and genome interaction with DNA binding factors.

Discrete regions that show increased or decreased CG methylation through development are associated with specific local chromatin modifications. We found that CG-methylated regions of the fetal frontal cortex that become hypomethylated in the adult (Fig. 6F, Fetal>Adult) gain

localized histone modifications characteristic of active enhancers (H3K4me1 and H3K27ac) and increased DNaseI hypersensitivity in the adult. In addition, these regions have reduced accumulation of mCH (Fig. 6F), consistent with an overall decrease in mC linked to increased genome accessibility and enhancer activity. In contrast, genomic regions that gain mCG during development (Adult>Fetal) lose localized enrichment of H3K4me1, H3K27ac, and DNaseI hypersensitivity and show increased mCH. These changes indicate inactivation of these genomic regions through brain development and suggest that this inactivation is associated with increased local mCG.

A Hydroxymethylation Signature of Developmentally Activated Regions

Adult>Fetal CG-DMRs show broad low-level hmCG enrichment flanking the CG-DMR and a localized depletion of hmC at the center in both fetal and adult genomes (Fig. 6F), and the absolute abundance of hmC is several-fold lower in fetal compared with adult frontal cortex (Fig. 1E). This suggests that although Adult>Fetal CG-DMRs gain mCG through development, they tend to be refractory to conversion to hmC, potentially because of lower accessibility to the Tet hydroxylases. In contrast, Fetal>Adult CG-DMRs have a local enrichment of both mCG and hmCG in the fetal cortex that becomes a local depletion in the adult. Two enrichment-based genome-wide hmC profiling techniques, CMS-IP (38) and biotin-glucosyl tagging (31), confirmed the localized enrichment of hmC at Fetal>Adult CG-DMRs (fig. S12B). The localized enrichment of hmC at these inaccessible and quiescent genomic regions, which lose mCG and hmCG later in development, indicates that they may be premodified with hmCG in the fetal stage to create a dormant state that is poised for subsequent demethylation and activation at a later developmental stage. Closer inspection of base-resolution hmC data revealed that 4% of the hmCG bases that have significantly higher hmC levels in fetal compared with adult [false discovery rate (FDR) 0.05] directly overlap with Fetal>Adult CG-DMRs, far exceeding the number expected by chance (0.5%). This indicates that despite lower global levels of hmC in the fetal brain, developmentally demethylated CG-DMRs are enriched for hmCG bases that are more highly hydroxymethylated in fetal than in adult brain (Fig. 6G). The localized enrichment of mCG at these CG-DMRs in the fetal cortex indicates that CG-demethylation has not yet taken place.

If fetal hmCG is poised at dormant genomic regions in order to facilitate active DNA demethylation at later developmental stages, then the Tet hydroxylase enzymes that catalyze conversion of mC to hmC should be necessary for mCG hypomethylation in the adult frontal cortex at these regions. To test this, we performed MethylC-Seq of genomic DNA from frontal cortex tissue of adult *Tet2*^{-/-} mice. Adult>Fetal CG-DMRs, which gain mCG through development, are largely unaffected in *Tet2*^{-/-} compared with wild-type adult mice

(Fig. 6, H and I; 3.6% hypermethylated, FET, FDR 0.05). By contrast, a substantial fraction of Fetal>Adult CG-DMRs are hypermethylated in *Tet2*^{-/-} (19.7%) versus wild type. The mutant shows a small but significant increase in mCG at Fetal>Adult CG-DMRs (Fig. 6I and fig. S12C) (*Tet2*^{-/-}: 7.9% ± 4.6%, $P < 10^{-11}$, Wilcoxon signed rank test). The partial effect of the mutation on CG methylation is not unexpected given that all three *Tet* genes are expressed in the brain (fig. S9C) and may exhibit some functional redundancy. Additionally, a genome-wide search identified 14,340 CG-DMRs hypermethylated in *Tet2*^{-/-} relative to wild type (6 weeks, 10 weeks, and 22 months), >fourfold more numerous than hypomethylated CG-DMRs (3099). This further indicates a role for Tet2 in mediating mCG demethylation during brain development.

Discussion

The essential role of frontal cortex in behavior and cognition requires the coordinated interaction, via electrical and chemical signaling, of multiple neuronal cell types and a diverse population of glial cells. Individual brain cells have unique roles within circuits that are defined by their location and pattern of connections as well as by their molecular identity. The development and maturation of the brain's physical structure and the refinement of the molecular identities of neurons and glial cells occur in parallel in a finely orchestrated process that starts early during the embryonic period and continues, in humans, well into the third decade of life (55, 56). An early postnatal burst of synaptogenesis is followed by activity-dependent pruning of excess synapses during adolescence (28, 57, 58). This process forms the basis for experience-dependent plasticity and learning in children and young adults (59), and its disruption leads to behavioral alterations and neuropsychiatric disorders (60). During this period, profound transcriptional changes lead to the appearance of adult electrophysiological characteristics in neocortical neurons.

Our study suggests a key role of DNA methylation in brain development and function. First, CH methylation accumulates significantly in neurons through early childhood and adolescence, becoming the dominant form of DNA methylation in mature human neurons. This shows that the period of synaptogenesis, during which the neural circuit matures, is accompanied by a parallel process of large-scale reconfiguration of the neuronal epigenome. Indeed, central nervous system deletion of *Dnmt3a* during late gestation induces motor deficits, and animals die prematurely (61). However, mice with a postnatal deletion restricted to the pyramidal cell population (complete recombination around 1 month old) do not show overt behavioral or transcriptional alterations (2). Our data suggest that expression of *Dnmt3a* specifically around the second postnatal week may be critical for establishing a normal brain DNA methylation profile and allowing healthy brain development.

Second, the precise positioning of mCG and mCH marks, which are conserved between individuals and across humans and mice, is consistent with a functional role. Whether this is the case, or whether the conserved patterns are instead a reflection of conserved nucleosome position or chromatin structure, requires further investigation. Third, the relationship between DNA methylation patterns and the function of neuron- or astrocyte-specific gene sets suggests a role for DNA methylation in distinguishing these two broad classes of cortical cells. DNA methylation could therefore play a key role in sculpting more-specific cellular identities. If this is the case, we expect that purified subpopulations will reveal high specificity of methylation at specific sites for particular cell types. Thus, the observation that most CH sites with nonzero methylation are methylated in ~20 to 25% of sampled cells (fig. S1H) could be explained by the heterogeneity of these brain circuits rather than by stochastic methylation within each cell. These conclusions obtained from our genome-wide, base-resolution, cell type-specific DNA methylomes for brain cells through key stages of development are the first steps toward unraveling the genetic program and experience-dependent epigenetic modifications leading to a fully differentiated nervous system.

References and Notes

1. E. Borrelli, E. J. Nestler, C. D. Allis, P. Sassone-Corsi, Decoding the epigenetic language of neuronal plasticity. *Neuron* **60**, 961–974 (2008). doi: [10.1016/j.neuron.2008.10.012](https://doi.org/10.1016/j.neuron.2008.10.012); pmid: [19109904](https://pubmed.ncbi.nlm.nih.gov/19109904/)
2. J. Feng et al., Dnmt1 and Dnmt3a maintain DNA methylation and regulate synaptic function in adult forebrain neurons. *Nat. Neurosci.* **13**, 423–430 (2010). doi: [10.1038/nn.2514](https://doi.org/10.1038/nn.2514); pmid: [20228804](https://pubmed.ncbi.nlm.nih.gov/20228804/)
3. C. A. Miller, J. D. Sweatt, Covalent modification of DNA regulates memory formation. *Neuron* **53**, 857–869 (2007). doi: [10.1016/j.neuron.2007.02.022](https://doi.org/10.1016/j.neuron.2007.02.022); pmid: [17359920](https://pubmed.ncbi.nlm.nih.gov/17359920/)
4. S. Numata et al., DNA methylation signatures in development and aging of the human prefrontal cortex. *Am. J. Hum. Genet.* **90**, 260–272 (2012). doi: [10.1016/j.ajhg.2011.12.020](https://doi.org/10.1016/j.ajhg.2011.12.020); pmid: [22305529](https://pubmed.ncbi.nlm.nih.gov/22305529/)
5. M. Suderman et al., Conserved epigenetic sensitivity to early life experience in the rat and human hippocampus. *Proc. Natl. Acad. Sci. U.S.A.* **109** (suppl. 2), 17266–17272 (2012). doi: [10.1073/pnas.1121260109](https://doi.org/10.1073/pnas.1121260109); pmid: [23045659](https://pubmed.ncbi.nlm.nih.gov/23045659/)
6. K. D. Siegmund et al., DNA methylation in the human cerebral cortex is dynamically regulated throughout the life span and involves differentiated neurons. *PLoS ONE* **2**, e895 (2007). doi: [10.1371/journal.pone.0000895](https://doi.org/10.1371/journal.pone.0000895); pmid: [17878930](https://pubmed.ncbi.nlm.nih.gov/17878930/)
7. K. Martinowich et al., DNA methylation-related chromatin remodeling in activity-dependent BDNF gene regulation. *Science* **302**, 890–893 (2003). doi: [10.1126/science.1090842](https://doi.org/10.1126/science.1090842); pmid: [14593184](https://pubmed.ncbi.nlm.nih.gov/14593184/)
8. J. U. Guo et al., Neuronal activity modifies the DNA methylation landscape in the adult brain. *Nat. Neurosci.* **14**, 1345–1351 (2011). doi: [10.1038/nn.2900](https://doi.org/10.1038/nn.2900); pmid: [21874013](https://pubmed.ncbi.nlm.nih.gov/21874013/)
9. I. B. Zovkic, M. C. Guzman-Karlsson, J. D. Sweatt, Epigenetic regulation of memory formation and maintenance. *Learn. Mem.* **20**, 61–74 (2013). doi: [10.1101/lm.026575.112](https://doi.org/10.1101/lm.026575.112); pmid: [23322554](https://pubmed.ncbi.nlm.nih.gov/23322554/)
10. J. M. Levenson et al., Evidence that DNA (cytosine-5) methyltransferase regulates synaptic plasticity in the hippocampus. *J. Biol. Chem.* **281**, 15763–15773 (2006). doi: [10.1074/jbc.M511767200](https://doi.org/10.1074/jbc.M511767200); pmid: [16606618](https://pubmed.ncbi.nlm.nih.gov/16606618/)
11. A. M. M. Oliveira, T. J. Hemstedt, H. Bading, Rescue of aging-associated decline in Dnmt3a2 expression restores

- cognitive abilities. *Nat. Neurosci.* **15**, 1111–1113 (2012). doi: [10.1038/nn.3151](https://doi.org/10.1038/nn.3151); pmid: [22751036](https://pubmed.ncbi.nlm.nih.gov/22751036/)
12. P. Moretti *et al.*, Learning and memory and synaptic plasticity are impaired in a mouse model of Rett syndrome. *J. Neurosci.* **26**, 319–327 (2006). doi: [10.1523/JNEUROSCI.2623-05.2006](https://doi.org/10.1523/JNEUROSCI.2623-05.2006); pmid: [16399702](https://pubmed.ncbi.nlm.nih.gov/16399702/)
 13. N. W. Penn, R. Suwalski, C. O'Riley, K. Bojanowski, R. Yura, The presence of 5-hydroxymethylcytosine in animal deoxyribonucleic acid. *Biochem. J.* **126**, 781–790 (1972). pmid: [4538516](https://pubmed.ncbi.nlm.nih.gov/4538516/)
 14. N. W. Penn, Modification of brain deoxyribonucleic acid base content with maturation in normal and malnourished rats. *Biochem. J.* **155**, 709–712 (1976). pmid: [949331](https://pubmed.ncbi.nlm.nih.gov/949331/)
 15. D. Globisch *et al.*, Tissue distribution of 5-hydroxymethylcytosine and search for active demethylation intermediates. *PLoS ONE* **5**, e15367 (2010). doi: [10.1371/journal.pone.0015367](https://doi.org/10.1371/journal.pone.0015367); pmid: [21203455](https://pubmed.ncbi.nlm.nih.gov/21203455/)
 16. J. U. Guo, Y. Su, C. Zhong, G.-L. Ming, H. Song, Hydroxylation of 5-methylcytosine by TET1 promotes active DNA demethylation in the adult brain. *Cell* **145**, 423–434 (2011). doi: [10.1016/j.cell.2011.03.022](https://doi.org/10.1016/j.cell.2011.03.022); pmid: [21496894](https://pubmed.ncbi.nlm.nih.gov/21496894/)
 17. Y.-F. He *et al.*, Tet-mediated formation of 5-carboxylcytosine and its excision by TDG in mammalian DNA. *Science* **333**, 1303–1307 (2011). doi: [10.1126/science.1210944](https://doi.org/10.1126/science.1210944); pmid: [21817016](https://pubmed.ncbi.nlm.nih.gov/21817016/)
 18. C.-X. Song *et al.*, Genome-wide profiling of 5-formylcytosine reveals its roles in epigenetic priming. *Cell* **153**, 678–691 (2013). doi: [10.1016/j.cell.2013.04.001](https://doi.org/10.1016/j.cell.2013.04.001); pmid: [23602153](https://pubmed.ncbi.nlm.nih.gov/23602153/)
 19. L. Shen *et al.*, Genome-wide analysis reveals TET- and TDG-dependent 5-methylcytosine oxidation dynamics. *Cell* **153**, 692–706 (2013). doi: [10.1016/j.cell.2013.04.002](https://doi.org/10.1016/j.cell.2013.04.002); pmid: [23602152](https://pubmed.ncbi.nlm.nih.gov/23602152/)
 20. W. Xie *et al.*, Base-resolution analyses of sequence and parent-of-origin dependent DNA methylation in the mouse genome. *Cell* **148**, 816–831 (2012). doi: [10.1016/j.cell.2011.12.035](https://doi.org/10.1016/j.cell.2011.12.035); pmid: [22341451](https://pubmed.ncbi.nlm.nih.gov/22341451/)
 21. K. E. Varley *et al.*, Dynamic DNA methylation across diverse human cell lines and tissues. *Genome Res.* **23**, 555–567 (2013). doi: [10.1101/gr.147942.112](https://doi.org/10.1101/gr.147942.112); pmid: [23325432](https://pubmed.ncbi.nlm.nih.gov/23325432/)
 22. R. Lister *et al.*, Human DNA methylomes at base resolution show widespread epigenomic differences. *Nature* **462**, 315–322 (2009). doi: [10.1038/nature08514](https://doi.org/10.1038/nature08514); pmid: [19829295](https://pubmed.ncbi.nlm.nih.gov/19829295/)
 23. M. J. Ziller *et al.*, Genomic distribution and inter-sample variation of non-CpG methylation across human cell types. *PLoS Genet.* **7**, e1002389 (2011). doi: [10.1371/journal.pgen.1002389](https://doi.org/10.1371/journal.pgen.1002389); pmid: [22174693](https://pubmed.ncbi.nlm.nih.gov/22174693/)
 24. R. Lister *et al.*, Highly integrated single-base resolution maps of the epigenome in Arabidopsis. *Cell* **133**, 523–536 (2008). doi: [10.1016/j.cell.2008.03.029](https://doi.org/10.1016/j.cell.2008.03.029); pmid: [18423832](https://pubmed.ncbi.nlm.nih.gov/18423832/)
 25. R. Lister *et al.*, Hotspots of aberrant epigenomic reprogramming in human induced pluripotent stem cells. *Nature* **471**, 68–73 (2011). doi: [10.1038/nature09798](https://doi.org/10.1038/nature09798); pmid: [21289626](https://pubmed.ncbi.nlm.nih.gov/21289626/)
 26. B. H. Ramsahoye *et al.*, Non-CpG methylation is prevalent in embryonic stem cells and may be mediated by DNA methyltransferase 3a. *Proc. Natl. Acad. Sci. U.S.A.* **97**, 5237–5242 (2000). doi: [10.1073/pnas.97.10.5237](https://doi.org/10.1073/pnas.97.10.5237); pmid: [10805783](https://pubmed.ncbi.nlm.nih.gov/10805783/)
 27. J. De Felipe, P. Marco, A. Fairén, E. G. Jones, Inhibitory synaptogenesis in mouse somatosensory cortex. *Cereb. Cortex* **7**, 619–634 (1997). doi: [10.1093/cercor/7.7.619](https://doi.org/10.1093/cercor/7.7.619); pmid: [9373018](https://pubmed.ncbi.nlm.nih.gov/9373018/)
 28. P. R. Huttenlocher, A. S. Dabholkar, Regional differences in synaptogenesis in human cerebral cortex. *J. Comp. Neurol.* **387**, 167–178 (1997). doi: [10.1002/\(SICI\)1096-9861\(19971020\)387:2<167::AID-CNE1>3.0.CO;2-Z](https://doi.org/10.1002/(SICI)1096-9861(19971020)387:2<167::AID-CNE1>3.0.CO;2-Z); pmid: [9336221](https://pubmed.ncbi.nlm.nih.gov/9336221/)
 29. B. P. Berman *et al.*, Regions of focal DNA hypermethylation and long-range hypomethylation in colorectal cancer coincide with nuclear lamina-associated domains. *Nat. Genet.* **44**, 40–46 (2012). doi: [10.1038/ng.969](https://doi.org/10.1038/ng.969); pmid: [22120008](https://pubmed.ncbi.nlm.nih.gov/22120008/)
 30. S. Kiaucionis, N. Heintz, The nuclear DNA base 5-hydroxymethylcytosine is present in Purkinje neurons and the brain. *Science* **324**, 929–930 (2009); [10.1126/science.1169786](https://doi.org/10.1126/science.1169786); doi: [10.1126/science.1169786](https://doi.org/10.1126/science.1169786); pmid: [19372393](https://pubmed.ncbi.nlm.nih.gov/19372393/)
 31. C.-X. Song *et al.*, Selective chemical labeling reveals the genome-wide distribution of 5-hydroxymethylcytosine. *Nat. Biotechnol.* **29**, 68–72 (2011). doi: [10.1038/nbt.1732](https://doi.org/10.1038/nbt.1732); pmid: [21151123](https://pubmed.ncbi.nlm.nih.gov/21151123/)
 32. K. E. Szulwach *et al.*, 5-hmC-mediated epigenetic dynamics during postnatal neurodevelopment and aging. *Nat. Neurosci.* **14**, 1607–1616 (2011). doi: [10.1038/nn.2959](https://doi.org/10.1038/nn.2959); pmid: [22037496](https://pubmed.ncbi.nlm.nih.gov/22037496/)
 33. M. Mellén, P. Ayata, S. Dewell, S. Kiaucionis, N. Heintz, MeCP2 binds to 5hmC enriched within active genes and accessible chromatin in the nervous system. *Cell* **151**, 1417–1430 (2012). doi: [10.1016/j.cell.2012.11.022](https://doi.org/10.1016/j.cell.2012.11.022); pmid: [23260135](https://pubmed.ncbi.nlm.nih.gov/23260135/)
 34. M. Yu *et al.*, Base-resolution analysis of 5-hydroxymethylcytosine in the mammalian genome. *Cell* **149**, 1368–1380 (2012). doi: [10.1016/j.cell.2012.04.027](https://doi.org/10.1016/j.cell.2012.04.027); pmid: [22608086](https://pubmed.ncbi.nlm.nih.gov/22608086/)
 35. J. A. Stamatoyannopoulos *et al.*, An encyclopedia of mouse DNA elements (Mouse ENCODE). *Genome Biol.* **13**, 418 (2012). doi: [10.1186/gb-2012-13-8-418](https://doi.org/10.1186/gb-2012-13-8-418); pmid: [22889292](https://pubmed.ncbi.nlm.nih.gov/22889292/)
 36. R. K. Auerbach *et al.*, Mapping accessible chromatin regions using Sono-Seq. *Proc. Natl. Acad. Sci. U.S.A.* **106**, 14926–14931 (2009). doi: [10.1073/pnas.0905443106](https://doi.org/10.1073/pnas.0905443106); pmid: [19706456](https://pubmed.ncbi.nlm.nih.gov/19706456/)
 37. Y. Shen *et al.*, A map of the cis-regulatory sequences in the mouse genome. *Nature* **488**, 116–120 (2012). doi: [10.1038/nature11243](https://doi.org/10.1038/nature11243); pmid: [22763441](https://pubmed.ncbi.nlm.nih.gov/22763441/)
 38. W. A. Pastor *et al.*, Genome-wide mapping of 5-hydroxymethylcytosine in embryonic stem cells. *Nature* **473**, 394–397 (2011). doi: [10.1038/nature10102](https://doi.org/10.1038/nature10102); pmid: [21552279](https://pubmed.ncbi.nlm.nih.gov/21552279/)
 39. Y. Huang, W. A. Pastor, J. A. Zepeda-Martínez, A. Rao, The anti-CMS technique for genome-wide mapping of 5-hydroxymethylcytosine. *Nat. Protoc.* **7**, 1897–1908 (2012). doi: [10.1038/nprot.2012.103](https://doi.org/10.1038/nprot.2012.103); pmid: [23018193](https://pubmed.ncbi.nlm.nih.gov/23018193/)
 40. A. Magklara *et al.*, An epigenetic signature for monoallelic olfactory receptor expression. *Cell* **145**, 555–570 (2011). doi: [10.1016/j.cell.2011.03.040](https://doi.org/10.1016/j.cell.2011.03.040); pmid: [21529909](https://pubmed.ncbi.nlm.nih.gov/21529909/)
 41. E. J. Clowney *et al.*, Nuclear aggregation of olfactory receptor genes governs their monogenic expression. *Cell* **151**, 724–737 (2012). doi: [10.1016/j.cell.2012.09.043](https://doi.org/10.1016/j.cell.2012.09.043); pmid: [23141535](https://pubmed.ncbi.nlm.nih.gov/23141535/)
 42. H. Li *et al.*, Transcription factor MEF2C influences neural stem/progenitor cell differentiation and maturation in vivo. *Proc. Natl. Acad. Sci. U.S.A.* **105**, 9397–9402 (2008). doi: [10.1073/pnas.0802876105](https://doi.org/10.1073/pnas.0802876105); pmid: [18599437](https://pubmed.ncbi.nlm.nih.gov/18599437/)
 43. M. W. Akhtar *et al.*, In vivo analysis of MEF2 transcription factors in synapse regulation and neuronal survival. *PLoS ONE* **7**, e34863 (2012). doi: [10.1371/journal.pone.0034863](https://doi.org/10.1371/journal.pone.0034863); pmid: [22496871](https://pubmed.ncbi.nlm.nih.gov/22496871/)
 44. A. C. Barbosa *et al.*, MEF2C, a transcription factor that facilitates learning and memory by negative regulation of synapse numbers and function. *Proc. Natl. Acad. Sci. U.S.A.* **105**, 9391–9396 (2008). doi: [10.1073/pnas.0802679105](https://doi.org/10.1073/pnas.0802679105); pmid: [18599438](https://pubmed.ncbi.nlm.nih.gov/18599438/)
 45. J. D. Cahoy *et al.*, A transcriptome database for astrocytes, neurons, and oligodendrocytes: a new resource for understanding brain development and function. *J. Neurosci.* **28**, 264–278 (2008). doi: [10.1523/JNEUROSCI.4178-07.2008](https://doi.org/10.1523/JNEUROSCI.4178-07.2008); pmid: [18171944](https://pubmed.ncbi.nlm.nih.gov/18171944/)
 46. H. Wu *et al.*, Dnmt3a-dependent nonpromoter DNA methylation facilitates transcription of neurogenic genes. *Science* **329**, 444–448 (2010). doi: [10.1126/science.1190485](https://doi.org/10.1126/science.1190485); pmid: [20651149](https://pubmed.ncbi.nlm.nih.gov/20651149/)
 47. T. Mohandas, R. S. Sparkes, L. J. Shapiro, Reactivation of an inactive human X chromosome: Evidence for X inactivation by DNA methylation. *Science* **211**, 393–396 (1981). doi: [10.1126/science.6164095](https://doi.org/10.1126/science.6164095); pmid: [6164095](https://pubmed.ncbi.nlm.nih.gov/6164095/)
 48. K. Plath, S. Mlynarczyk-Evans, D. A. Nusinow, B. Panning, Xist RNA and the mechanism of X chromosome inactivation. *Annu. Rev. Genet.* **36**, 233–278 (2002). doi: [10.1146/annurev.genet.36.042902.092433](https://doi.org/10.1146/annurev.genet.36.042902.092433); pmid: [12429693](https://pubmed.ncbi.nlm.nih.gov/12429693/)
 49. L. Carrel, H. F. Willard, X-inactivation profile reveals extensive variability in X-linked gene expression in females. *Nature* **434**, 400–404 (2005). doi: [10.1038/nature03479](https://doi.org/10.1038/nature03479); pmid: [15772666](https://pubmed.ncbi.nlm.nih.gov/15772666/)
 50. A. J. Sharp *et al.*, DNA methylation profiles of human active and inactive X chromosomes. *Genome Res.* **21**, 1592–1600 (2011). doi: [10.1101/gr.112680.110](https://doi.org/10.1101/gr.112680.110); pmid: [21862626](https://pubmed.ncbi.nlm.nih.gov/21862626/)
 51. C. M. Johnston *et al.*, Large-scale population study of human cell lines indicates that dosage compensation is virtually complete. *PLoS Genet.* **4**, e9 (2008). doi: [10.1371/journal.pgen.0040009](https://doi.org/10.1371/journal.pgen.0040009); pmid: [18208332](https://pubmed.ncbi.nlm.nih.gov/18208332/)
 52. A. K. Maunakea *et al.*, Conserved role of intragenic DNA methylation in regulating alternative promoters. *Nature* **466**, 253–257 (2010). doi: [10.1038/nature09165](https://doi.org/10.1038/nature09165); pmid: [20613842](https://pubmed.ncbi.nlm.nih.gov/20613842/)
 53. R. E. Thurman *et al.*, The accessible chromatin landscape of the human genome. *Nature* **489**, 75–82 (2012). doi: [10.1038/nature11232](https://doi.org/10.1038/nature11232); pmid: [22955617](https://pubmed.ncbi.nlm.nih.gov/22955617/)
 54. M. B. Stadler *et al.*, DNA-binding factors shape the mouse methylome at distal regulatory regions. *Nature* **480**, 490–495 (2011). pmid: [22170606](https://pubmed.ncbi.nlm.nih.gov/22170606/)
 55. Z. Petanjek *et al.*, Extraordinary neonety of synaptic spines in the human prefrontal cortex. *Proc. Natl. Acad. Sci. U.S.A.* **108**, 13281–13286 (2011). doi: [10.1073/pnas.1105108108](https://doi.org/10.1073/pnas.1105108108); pmid: [21788513](https://pubmed.ncbi.nlm.nih.gov/21788513/)
 56. B. Kolb *et al.*, Experience and the developing prefrontal cortex. *Proc. Natl. Acad. Sci. U.S.A.* **109** (suppl. 2), 17186–17193 (2012). doi: [10.1073/pnas.1121251109](https://doi.org/10.1073/pnas.1121251109); pmid: [23045653](https://pubmed.ncbi.nlm.nih.gov/23045653/)
 57. H. T. Chugani, A critical period of brain development: Studies of cerebral glucose utilization with PET. *Prev. Med.* **27**, 184–188 (1998). doi: [10.1006/pmed.1998.0274](https://doi.org/10.1006/pmed.1998.0274); pmid: [9578992](https://pubmed.ncbi.nlm.nih.gov/9578992/)
 58. P. Levitt, Structural and functional maturation of the developing primate brain. *J. Pediatr.* **143** (suppl.), S35–S45 (2003). doi: [10.1067/S0022-3476\(03\)00400-1](https://doi.org/10.1067/S0022-3476(03)00400-1); pmid: [14597912](https://pubmed.ncbi.nlm.nih.gov/14597912/)
 59. M. V. Johnston, Plasticity in the developing brain: implications for rehabilitation. *Dev. Disabil. Res. Rev.* **15**, 94–101 (2009). doi: [10.1002/ddrr.64](https://doi.org/10.1002/ddrr.64); pmid: [19489084](https://pubmed.ncbi.nlm.nih.gov/19489084/)
 60. P. J. Uhlhaas, W. Singer, The development of neural synchrony and large-scale cortical networks during adolescence: Relevance for the pathophysiology of schizophrenia and neurodevelopmental hypothesis. *Schizophr. Bull.* **37**, 514–523 (2011). doi: [10.1093/schbul/sbr034](https://doi.org/10.1093/schbul/sbr034); pmid: [21505118](https://pubmed.ncbi.nlm.nih.gov/21505118/)
 61. S. Nguyen, K. Meletis, D. Fu, S. Jhaveri, R. Jaenisch, Ablation of de novo DNA methyltransferase Dnmt3a in the nervous system leads to neuromuscular defects and shortened lifespan. *Dev. Dyn.* **236**, 1663–1676 (2007). doi: [10.1002/dvdy.21176](https://doi.org/10.1002/dvdy.21176); pmid: [17477386](https://pubmed.ncbi.nlm.nih.gov/17477386/)
 62. Materials and methods are available as supplementary materials on Science Online.

Acknowledgments: We thank W. F. Loomis for critical reading of this manuscript; J. Chambers for technical assistance with animal breeding; D. Chambers for technical assistance with cell sorting; M. Lutz and T. Berggren for provision of the HUES6 cells; F. Yue, G. Hon, and B. Ren for providing mapped mouse ChIP-Seq data and assistance with TAB-Seq; and A. Nimmerjahn for providing the S100b-eGFP mice. Human brain tissue was obtained from the National Institute of Child Health and Human Development Brain and Tissue Bank for Developmental Disorders at the University of Maryland, Baltimore, Maryland, the IDIBELL Biobank, which is part of the BrainNet Europe Bank funded by the European Commission (LSHM-CT-2004-503039). We thank the Stamatoyannopoulos laboratory (University of Washington) and the Mouse ENCODE Consortium for generating and providing access to the DNase hypersensitivity data sets (35). This work was supported by a National Institutes of Mental Health grant to M.M.B. and J.R.E. (MH094670); the Howard Hughes Medical Institute to T.J.S. and J.R.E.; the Gordon and Betty Moore Foundation (GMBF3034) to J.R.E.; NIH grant HG006827 to C.H.; NIH RO1 grants AI44432, HD065812, and CA151535; grant RM-01729 from the California Institute of Regenerative Medicine; and Translational Research grant

TRP 6187-12 from the Leukemia and Lymphoma Society (to A.R.). R.L. was supported by an Australian Research Council Future Fellowship. Support was also provided by the Government of Western Australia through funding for the Western Australia CoE for Computational Systems Biology. E.A.M. was supported by the Center for Theoretical Biological Physics, University of California San Diego, and NIH (National Institute of Neurological Diseases and Stroke grant K99NS080911). W.A.P. was supported by a predoctoral graduate research

fellowship from the NSF. Analyzed data sets can be accessed at http://neomorph.salk.edu/brain_methylomes. Sequence data can be downloaded from National Center for Biotechnology Information GEO (GSE47966). Tet2 mutant mice are available under a material transfer agreement from the La Jolla Institute for Allergy and Immunology. Correspondence and requests for materials should be addressed to R.L. (ryan.lister@uwa.edu.au), M.M.B. (mbehrens@salk.edu), and J.R.E. (ecker@salk.edu).

Supplementary Materials

www.sciencemag.org/content/341/6146/1237905/suppl/DC1
Materials and Methods
Figs. S1 to S12
Tables S1 to S5
References (63–78)

15 March 2013; accepted 7 June 2013
10.1126/science.1237905

Imaging of the CO Snow Line in a Solar Nebula Analog

Chunhua Qi,^{1*†} Karin I. Öberg,^{2*‡} David J. Wilner,¹ Paola D'Alessio,³ Edwin Bergin,⁴ Sean M. Andrews,¹ Geoffrey A. Blake,⁵ Michiel R. Hogerheijde,⁶ Ewine F. van Dishoeck^{6,7}

Planets form in the disks around young stars. Their formation efficiency and composition are intimately linked to the protoplanetary disk locations of “snow lines” of abundant volatiles. We present chemical imaging of the carbon monoxide (CO) snow line in the disk around TW Hya, an analog of the solar nebula, using high spatial and spectral resolution Atacama Large Millimeter/Submillimeter Array observations of diazenylium (N_2H^+), a reactive ion present in large abundance only where CO is frozen out. The N_2H^+ emission is distributed in a large ring, with an inner radius that matches CO snow line model predictions. The extracted CO snow line radius of ~ 30 astronomical units helps to assess models of the formation dynamics of the solar system, when combined with measurements of the bulk composition of planets and comets.

Condensation fronts in protoplanetary disks, where abundant volatiles deplete out of the gas phase and are incorporated into solids, are believed to have played a critical role in the formation of planets in the solar system (1, 2), and similar “snow lines” in the disks around young stars should affect the ongoing formation of exoplanets. Snow lines can enhance particle growth and thus planet formation efficiencies because of (i) substantial increases in solid mass surface densities exterior to snow line locations, (ii) continuous freeze-out of gas diffusing across the snow line (cold-head effect), (iii) pile-up of dust just inside of the snow line in pressure traps, and (iv) an increased “stickiness” of icy grains compared with bare ones, which favors dust coagulation (3–7). Experiments and theory on these processes have been focused on the H_2O snow line, but the results should be generally applicable to snow lines of abundant volatiles, with the exception that the stickiness of different icy grain mantles varies. The locations of snow lines of the most abundant volatiles— H_2O , CO_2 , and CO—with respect to the planet-forming zone may also regulate the bulk composition of planets (8). Determining snow line locations is therefore key to probing grain growth—and thus, planetesimal and planet formation efficiencies—and elemental and molecular compositions of planetesimals and planets forming in protoplanetary disks, including the solar nebula.

According to the solar system’s composition and disk theory, the H_2O snow line developed at ~ 3 astronomical units (AU, where 1 AU is the average distance from the Earth to the Sun) from the early Sun during the epoch of chondrite assembly (9). In other protoplanetary disks, the snow line locations are determined by the disk midplane temperature structures, which are set by a time-dependent combination of the luminosity of the central star, the presence of other heating sources, the efficiencies of dust and gas cooling, and the intrinsic condensation temperatures of different volatiles. Because of the low condensation temperature of CO, the CO snow line occurs at radii of tens of AU around solar-type stars: this larger-sized scale makes the CO transition zone the most accessible to direct observations. The CO snow line is also important in its own right because CO ice is a starting point for a complex, prebiotic chemistry (10). Also, without incorporating an enhanced grain growth ef-

iciency beyond that expected for bare silicate dust, observations of centimeter-sized dust grains in disks, including in TW Hya (11), are difficult to reproduce in the outer disk. Condensation of CO is very efficient below the CO freeze-out temperature, with a sticking efficiency close to unity according to experiments (12), and a CO condensation-based dust growth mode may thus be key to explaining these observations.

Protoplanetary disks have evolving radial and vertical temperature gradients, with a warmer surface where CO remains in the gaseous state throughout the disk, even as it is frozen in the cold, dense region beyond the midplane snow line (13). This means that the midplane snow line important for planet formation constitutes a smaller portion of a larger condensation surface. Because the bulk of the CO emission comes from the disk surface layers, this presents a challenge for locating the CO midplane snow line. Its location has been observationally identified toward only one system, the disk around HD 163296, based on millimeter (or sub-millimeter) interferometric observations of multiple CO rotational transitions and isotopologues at high spatial resolution, interpreted through detailed modeling of the disk dust and gas physical structure (14). An alternative approach to constrain the CO snow line, suggested in (15) and pursued here, is to image molecular emission from a species that is abundant only where CO is highly depleted from the gas phase.

N_2H^+ emission is expected to be a robust tracer of CO depletion because the presence of gas phase CO both slows down N_2H^+ formation and speeds up N_2H^+ destruction. N_2H^+ forms through reactions between N_2 and H_3^+ , but most H_3^+ will instead transfer a proton to CO as long as the more abundant CO remains in the gas phase. The most important destruction mechanism for N_2H^+ is proton transfer to a CO molecule, whereas

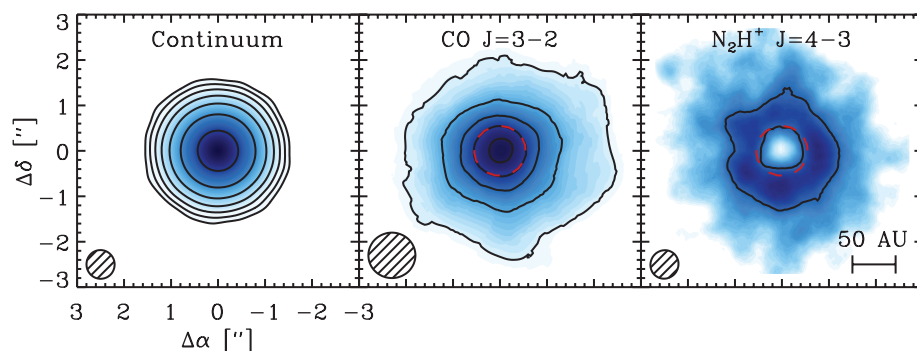


Fig. 1. Observed images of dust, CO, and N_2H^+ emission toward TW Hya. (Left) ALMA 372-GHz continuum map, extracted from the line-free channels of the N_2H^+ observations. Contours mark [5, 10, 20, 40, 80, 160, 320] millijansky (mJy) beam^{-1} , and the root mean square (RMS) is $0.2 \text{ mJy beam}^{-1}$. (Center) Image of CO $J = 3-2$ emission acquired with the SMA (24). Contours mark (1–5) $\text{Jy km s}^{-1} \text{ beam}^{-1}$, and the RMS is $0.1 \text{ Jy km s}^{-1} \text{ beam}^{-1}$. (Right) ALMA image of $\text{N}_2\text{H}^+ J = 4-3$ integrated emission with a single contour at $150 \text{ mJy km s}^{-1} \text{ beam}^{-1}$, and the RMS is $10 \text{ mJy km s}^{-1} \text{ beam}^{-1}$. The synthesized beam sizes are shown in each bottom left corner. The red dashed circle marks the best-fit inner radius of the N_2H^+ ring from a modeling of the visibilities. This inner edge traces the onset of CO freeze-out according to astrochemical theory and thus marks the CO snow line in the disk midplane.

¹Harvard-Smithsonian Center for Astrophysics, Cambridge, MA 02138, USA. ²Departments of Chemistry and Astronomy, University of Virginia, Charlottesville, VA 22904, USA. ³Centro de Radioastronomía y Astrofísica, Universidad Nacional Autónoma de México (UNAM), 58089 Mexico City, Mexico. ⁴Department of Astronomy, University of Michigan, Ann Arbor, MI 48109, USA. ⁵Division of Geological and Planetary Sciences, California Institute of Technology, Pasadena, CA 91125, USA. ⁶Leiden Observatory, Leiden University, 2300 RA Leiden, Netherlands. ⁷Max Planck Institute for Extraterrestrial Physics, 85748 Garching, Germany.

*These authors contributed equally to this work.

†Corresponding author. E-mail: cqi@cfa.harvard.edu

‡Present address: Harvard-Smithsonian Center for Astrophysics, Cambridge, MA 02138, USA.

in the absence of CO, N_2H^+ is destroyed through a much slower dissociative recombination reaction. These simple astrochemical considerations predict a correlation between N_2H^+ and CO depletion, or equivalently an anticorrelation between N_2H^+ and gas-phase CO. The latter has been observed in many prestellar and protostellar environments, confirming the basic theory (16, 17). In disks, N_2H^+ should therefore be present at large abundances only inside the vertical and horizontal thermal layers where CO vapor is condensing—that is, beyond the CO snow line. Molecular line surveys of disks have shown that N_2H^+ is only present in disks cold enough to entertain CO freeze-out (18), and marginally resolved observations hint at a N_2H^+ emission offset from the stellar position (15), which is in agreement with the models of disk chemistry (19). Detailed imaging of N_2H^+ emission in protoplanetary disks at the scales needed to directly reveal CO snow lines with sufficient sensitivity has previously been out of reach.

We used the Atacama Large Millimeter/Submillimeter Array (ALMA) to obtain images of emission from the 372-GHz dust continuum and the N_2H^+ $J = 4 - 3$ rotational line (where J is the rotational quantum number) from the disk around TW Hya (Fig. 1 and fig. S1) (20). TW Hya is the closest (54 ± 6 pc) and as such is the most intensively studied pre-main-sequence star with a gas-rich circumstellar disk (21, 22). According to previous observations of dust and CO emission, and the recent detection of HD line

emission (23), this 3 million- to 10 million-year-old, 0.8 solar mass (M_\odot) T Tauri star (spectral type K7) is known to be surrounded by an almost face-on ($\sim 6^\circ$ inclination) massive $\sim 0.04 M_\odot$ gas-rich disk. The disk size in millimeter dust is ~ 60 AU, with a more extended (>100 AU) disk in gas and micrometer-sized dust (24). Both the disk mass and size conform well with solar nebula estimates—the minimum mass of the solar nebula is $0.01 M_\odot$, based on planet masses and compositions (9)—and the disk around TW Hya may thus serve as a template for planet formation in the solar nebula. Our images show that N_2H^+ emission is distributed in a ring with an inner diameter of 0.8 to 1.2 arc sec (based on visual inspection), corresponding to a physical inner radius of 21 to 32 AU. In contrast, CO emission is detected down to radial scales of ~ 2 AU (25). The clear difference in morphology between the N_2H^+ and CO emission can be simply explained by the presence of a CO midplane snow line at the observed inner edge of the N_2H^+ emission ring. The different morphologies cannot be explained by a lack of ions in the inner disk, based on previous spatially and spectrally resolved observations of another ion, HCO^+ (22). These HCO^+ observations had lower sensitivity and angular resolution than those of the N_2H^+ observations, but they are sufficient to exclude a central hole comparable in size with that seen in N_2H^+ .

To associate the inner-edge radius of the N_2H^+ emission with a midplane temperature, and thus

a CO freeze-out temperature, requires a model of the disk density and temperature structure. We adopted the model presented in (22), updated to conform with recent observations of the accretion rate and grain settling (figs. S2 to S4 and table S1) (20). In the context of this disk structure model, the N_2H^+ inner-edge location implies that N_2H^+ becomes abundant where the midplane temperature drops to 16 to 20 K. This is in agreement with expectations for the CO freeze-out temperature on the basis of the outcome of the laboratory experiments and desorption modeling by (12), who found CO condensation/sublimation temperatures of 16 to 18 K under interstellar conditions, assuming heat-up rates of 1 K per 10^2 to 10^6 years. In outer-disk midplanes, condensation temperatures are expected to be at most a few degrees higher because of a weak dependence on density (26). If CO condenses onto H_2O ice rather than existing CO ice, the condensation temperature will increase further, but this will only affect the first few monolayers of ice and is not expected to change the location where the majority of CO freezes out. Some CO may also remain in the gas phase below the CO freeze-out temperature in the presence of efficient nonthermal desorption, especially ultraviolet (UV) photodesorption (27), but this is expected to be negligible in the disk midplane at 30 AU because of UV shielding by upper-disk layers. UV photodesorption may affect the vertical CO snow surface location, however, and thus, describing the radial and vertical condensation surfaces with a single freeze-out temperature may not be possible.

To locate the inner edge of the N_2H^+ ring more quantitatively, we simulated the N_2H^+ emission with a power-law column density distribution and compared this with the data. We assumed the disk material orbits the central star in Keplerian motion and fixed the geometric and kinematic parameters of the disk that affect its observed spatio-kinematic behavior (22). We used the same updated density and temperature disk structure model (20) and assumed that the N_2H^+ column density structure could be approximated as a radial power law with inner and outer edges, whereas vertically the abundance was taken to be constant between the lower (toward midplane) and upper (toward surface) boundaries. This approach crudely mimics the results of detailed astrochemical modeling of disks, which shows that molecules are predominantly present in well-defined vertical layers (13, 19), and has been used to constrain molecular abundance structures in a number of previous studies (15, 22). The inner and outer radii, power-law index, and column density at 100 AU were treated as free parameters. We calculated a grid of synthetic N_2H^+ visibility data sets using the RATRAN code (28) to determine the radiative transfer and molecular excitation and compared them with the N_2H^+ observations. We obtained the best-fit model by minimizing χ^2 , the weighted difference between the data and the model with the real and imaginary part of the

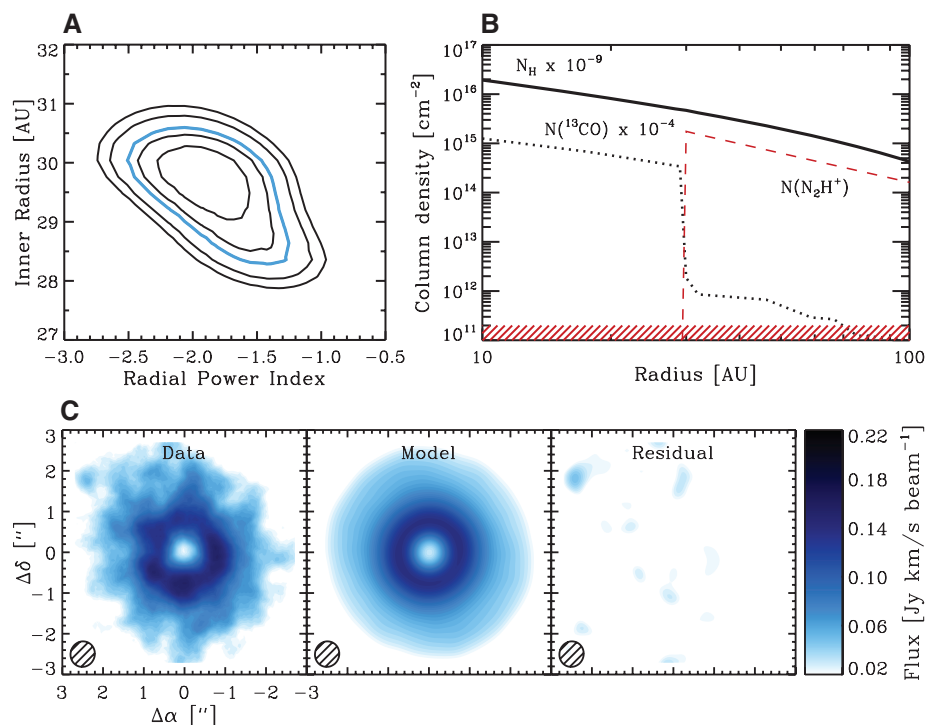


Fig. 2. Model results for the N_2H^+ abundance structure toward TW Hya. (A) The χ^2 fit surface for the power-law index and inner radius of the N_2H^+ abundance profile. Contours correspond to the 1σ to 5σ errors, and the blue contour marks 3σ . (B) The best-fit N_2H^+ column density structure, shown together with the total gas column density and the best-fit ^{13}CO column density for CO freeze-out at 17 K. The shaded region marks the N_2H^+ 1σ detection limit. (C) N_2H^+ observations, simulated observations of the best-fit N_2H^+ model, and the imaged residuals, calculated from the visibilities.

complex visibility measured in the (u, v) plane sampled by the ALMA observations of N_2H^+ .

As demonstrated in Fig. 2A, the inner radius is well constrained to 28 to 31 AU (3σ). This edge determination was aided by the nearly face-on viewing geometry because this minimizes the impact of the detailed vertical structure on the disk-modeling outcome. Furthermore, the Keplerian kinematics of the gas help to constrain the size scale at a level finer than the spatial resolution implied by the synthesized beam size. As a result, the fitted inner radius is robust to the details of the density and temperature model (table S2) (20). In the context of this model, the best-fit N_2H^+ inner radius corresponds to a CO midplane snow line at a temperature of 17 K. The best-fit N_2H^+ column density profile is presented in Fig. 2B together with the best-fit ^{13}CO profile, assuming a CO freeze-out temperature of 17 K (20) (fig. S5 and table S3). We fit ^{13}CO emission [obtained with the Submillimeter Array (20)] because the main isotopologue CO lines are optically thick. The N_2H^+ column density contrast across the CO snow line is at least an order of magnitude (20). Simulated ALMA observations of the best-fit N_2H^+ $J=4-3$ model are shown in Fig. 2C, demonstrating the excellent agreement.

Our quantitative analysis thus confirms the predictions that N_2H^+ traces the snow line of the abundant volatile, CO. Furthermore, the agreement between the quantitative analysis and the visual estimate of the N_2H^+ inner radius demonstrates that N_2H^+ imaging is a powerful tool to determine the CO snow line radii in disks, whose density and temperature structures have not been modeled in detail. N_2H^+ imaging with ALMA may therefore be used to provide statistics on how snow line locations depend on parameters of interest for planet formation theory, such as the evolutionary stage of the disks.

The locations of snow lines in solar nebula analogs such as TW Hya are also important to understand the formation dynamics of the solar system. The H_2O snow line is key to the formation of Jupiter and Saturn (29), whereas CH_4 and CO freeze-out enhanced the solid surface density further out in the solar nebula, which may have contributed to the feeding zones of Uranus and Neptune (30), depending on exactly where these ice giants formed. In the popular Nice model for the dynamics of the young solar system, Uranus formed at the largest radius of all planets, at ~ 17 AU (31), and most comets and Kuiper Belt objects formed further out, to ~ 35 AU. The plausibility of this scenario can be assessed by using the bulk compositions of these bodies together with knowledge of the CO snow line location. In particular, Kuiper Belt objects contain CO and the even more volatile N_2 (32, 33), which implies that they must have formed beyond the CO snow line. Comets exhibit a range of CO abundances, some of which seem to be primordial, which suggests that the CO snow line was located in the outer part of their formation region of 15 to 35 AU (34). This is consistent with the CO snow line

radius that we have determined in the TW Hya disk. However, in the context of the Nice model this CO snow line radius is too large for the ice giants and suggests that their observed carbon enrichment has a different origin than the accretion of CO ice (30). A caveat is that H_2O ice can trap CO, although this process is unlikely to be efficient enough to explain the observations. In either case, the CO snow line locations in solar nebula analogs such as TW Hya offer independent constraints on the early history of the solar system.

References and Notes

1. J. S. Lewis, *Science* **186**, 440–443 (1974).
2. D. J. Stevenson, J. I. Lunine, *Icarus* **75**, 146–155 (1988).
3. F. J. Ciesla, J. N. Cuzzi, *Icarus* **181**, 178–204 (2006).
4. A. Johansen *et al.*, *Nature* **448**, 1022–1025 (2007).
5. E. Chiang, A. N. Youdin, *Annu. Rev. Earth Planet. Sci.* **38**, 493–522 (2010).
6. B. Gundlach, S. Kilias, E. Beitz, J. Blum, *Icarus* **214**, 717–723 (2011).
7. K. Ros, A. Johansen, *Astron. Astrophys.* **552**, A137 (2013).
8. K. I. Öberg, R. Murray-Clay, E. A. Bergin, *Astrophys. J.* **743**, L16 (2011).
9. C. Hayashi, *Prog. Theor. Phys.* **70** (suppl.), 35–53 (1981).
10. E. Herbst, E. F. van Dishoeck, *Annu. Rev. Astron. Astrophys.* **47**, 427–480 (2009).
11. D. J. Wilner, P. D'Alessio, N. Calvet, M. J. Claussen, L. Hartmann, *Astrophys. J.* **626**, L109–L112 (2005).
12. S. E. Bisschop, H. J. Fraser, K. I. Öberg, E. F. van Dishoeck, S. Schlemmer, *Astron. Astrophys.* **449**, 1297–1309 (2006).
13. Y. Aikawa, E. Herbst, *Astron. Astrophys.* **351**, 233 (1999).
14. C. Qi *et al.*, *Astrophys. J.* **740**, 84 (2011).
15. C. Qi, K. I. Öberg, D. J. Wilner, *Astrophys. J.* **765**, 34 (2013).
16. E. A. Bergin, J. Alves, T. Huard, C. J. Lada, *Astrophys. J.* **570**, L101–L104 (2002).
17. J. K. Jørgensen, *Astron. Astrophys.* **424**, 589 (2004).
18. K. I. Öberg *et al.*, *Astrophys. J.* **734**, 98 (2011).
19. C. Walsh, H. Nomura, T. J. Millar, Y. Aikawa, *Astrophys. J.* **747**, 114 (2012).
20. Materials and methods are available as supplementary materials on Science Online.
21. J. H. Kastner, B. Zuckerman, D. A. Weintraub, T. Forveille, *Science* **277**, 67–71 (1997).
22. C. Qi, D. J. Wilner, Y. Aikawa, G. A. Blake, M. R. Hogerheijde, *Astrophys. J.* **681**, 1396–1407 (2008).
23. E. A. Bergin *et al.*, *Nature* **493**, 644–646 (2013).
24. S. M. Andrews *et al.*, *Astrophys. J.* **744**, 162 (2012).
25. K. A. Rosenfeld *et al.*, *Astrophys. J.* **757**, 129 (2012).
26. D. Hollenbach, M. J. Kaufman, E. A. Bergin, G. J. Melnick, *Astrophys. J.* **690**, 1497–1521 (2009).
27. K. Willacy, *Astrophys. J.* **660**, 441–460 (2007).
28. M. R. Hogerheijde, F. F. S. van der Tak, *Astron. Astrophys.* **362**, 697 (2000).
29. M. Lecar, M. Podolak, D. Sasselov, E. Chiang, *Astrophys. J.* **640**, 1115–1118 (2006).
30. S. E. Dodson-Robinson, K. Willacy, P. Bodenheimer, N. J. Turner, C. A. Beichman, *Icarus* **200**, 672–693 (2009).
31. K. Tsiganis, R. Gomes, A. Morbidelli, H. F. Levison, *Nature* **435**, 459–461 (2005).
32. T. C. Owen *et al.*, *Science* **261**, 745–748 (1993).
33. S. C. Tegler *et al.*, *Astrophys. J.* **751**, 76 (2012).
34. M. J. Mumma, S. B. Charnley, *Annu. Rev. Astron. Astrophys.* **49**, 471–524 (2011).

Acknowledgments: We are grateful to S. Schnee for data calibration and reduction assistance. C.Q. thanks the Smithsonian Astrophysical Observatory (SAO) Radio Telescope Data Center (RTDC) staff for their generous computational support. C.Q., K.I.O., and D.J.W. acknowledge grant NNX11AK63 from NASA Origins of Solar Systems. P.D. acknowledges a grant from Programa de Apoyo a Proyectos de Investigación e Innovación Tecnológica–UNAM. E.B. acknowledges support from NSF grant 1008800. This Report makes use of the following ALMA data: ADS JAO. ALMA#2011.0.00340.S. ALMA is a partnership of the European Southern Observatory (ESO) (representing its member states), NSF (USA), and the National Institute of Natural Sciences (Japan), together with the National Research Council (Canada) and the National Science Council and Academia Sinica's Institute of Astronomy and Astrophysics (ASIAA) (Taiwan), in cooperation with the Republic of Chile. The Joint ALMA Observatory is operated by ESO, Associated Universities, Inc. (AUI)/National Radio Astronomy Observatory, and the National Astronomical Observatory of Japan. We also make use of the Submillimeter Array (SMA) data: project #2004-214 (principal investigator, C.Q.). The SMA is a joint project between SAO and ASIAA and is funded by the Smithsonian Institution and the Academia Sinica.

Supplementary Materials

www.sciencemag.org/cgi/content/full/science.1239560/DC1
Materials and Methods
Figs. S1 to S5
Tables S1 to S3
References (35–52)

23 April 2013; accepted 2 July 2013

Published online 18 July 2013;

10.1126/science.1239560

A Quantum Many-Body Spin System in an Optical Lattice Clock

M. J. Martin,^{1,2,*} M. Bishof,^{1,2} M. D. Swallows,^{1,2,†} X. Zhang,^{1,2} C. Benko,^{1,2} J. von-Stecher,^{1,2,§} A. V. Gorshkov,³ A. M. Rey,^{1,2,†} Jun Ye^{1,2,†}

Strongly interacting quantum many-body systems arise in many areas of physics, but their complexity generally precludes exact solutions to their dynamics. We explored a strongly interacting two-level system formed by the clock states in ^{87}Sr as a laboratory for the study of quantum many-body effects. Our collective spin measurements reveal signatures of the development of many-body correlations during the dynamical evolution. We derived a many-body Hamiltonian that describes the experimental observation of atomic spin coherence decay, density-dependent frequency shifts, severely distorted lineshapes, and correlated spin noise. These investigations open the door to further explorations of quantum many-body effects and entanglement through use of highly coherent and precisely controlled optical lattice clocks.

Strongly correlated quantum many-body systems have become a major focus of modern science. Researchers are using quantum-degenerate atomic gases (1–6), ultra-

cold polar molecules (7–9), and ensembles of trapped ions (10, 11) to realize previously unidentified quantum phases of matter and simulate complex condensed matter systems. Another prom-

using system is optical atomic clocks that use fermionic alkaline earth atoms. The most stable of these clocks now operate near the quantum noise limit (12), with an accuracy surpassing that of the cesium standard (13). With atom-light coherence times reaching several seconds, permitting optical spectral resolution well below 1 Hz (Fig. 1A), even very weak interactions (such as fractional energy level shifts of order $\geq 1 \times 10^{-16}$) can dominate the dynamics of these systems, and the corresponding complex spectrum can be probed precisely. Atomic interactions in optical lattice clocks were first studied in the context of density-dependent frequency shifts, which were attributed to *s*-wave collisions allowed by inhomogeneous excitation (14–17); *p*-wave interactions were assumed to be suppressed because of the ~ 1 μ K sample temperature. More recently, in an optical clock based on ^{171}Yb atoms at ~ 10 μ K, *p*-wave interactions were reported to lead to two-body losses and density shifts (18, 19). At the same time, even at ~ 1 μ K inelastic *p*-wave losses were observed in the ^{87}Sr system (20). The importance of many-body interactions in these clocks has been recognized theoretically (15–17), but measuring them experimentally has been challenging.

In this paper, we report the observation of quantum many-body effects in a high-density ^{87}Sr optical clock in a one-dimensional (1D) optical lattice. In a prior experiment (21), a strongly interacting regime (in which atom-laser and atom-atom interactions are energetically comparable) was reached by tightly confining the atoms in a 2D optical lattice, at the expense of reducing the occupancy to one or two atoms per site. In this work, we probed a strongly interacting system with an average of 20 atoms per disk-shaped 1D-lattice site and developed a detailed understanding of the complex many-body quantum dynamics. The role of *s*-wave collisions is suppressed by operating in the strongly interacting regime with highly homogeneous atom-laser coupling, making *p*-wave interactions, which operate collectively, dominant. The experimental observation of such quantum magnetic behavior at micro-Kelvin temperatures is made possible because the motional degrees of freedom are effectively frozen during the clock interrogation. Only the internal electronic degrees of freedom (pseudo-spin) are relevant, and these can be initialized in a pure state.

We considered an optical lattice clock that uses the $^1S_0 \rightarrow ^3P_0$ (henceforth $|g\rangle \rightarrow |e\rangle$) clock transition in nuclear spin-polarized ^{87}Sr . It comprises an array of quasi-2D trap sites loaded with atoms at micro-Kelvin temperatures. The tight lattice confinement along the longitudinal direction *Z* freezes the dynamics and the population distribution across the trap sites. A single site populated with *N* atoms is modeled as a slightly anharmonic 2D oscillator with radial (longitudinal) frequency $\nu_R = 450$ Hz ($\nu_Z = 80$ kHz).

As shown in Fig. 1B, atoms within a given trap site can elastically interact with one another

through the *p*-wave channel. Because all trap frequencies are much greater than the characteristic *p*-wave interaction energy, the motional degrees of freedom are effectively frozen, and interactions thus manifest themselves in the electronic $|g\rangle \leftrightarrow |e\rangle$ degrees of freedom that define our spin system (22). Fermi statistics guarantee that no two atoms within a given trap site occupy the same motional state. We initialized our nuclear spin-polarized gas with all atoms in the ground state $|g\rangle$, and this initial state can be expressed as a collective spin state with $S = N/2$, where $S(S+1)$ is the eigenvalue of the observable

$$\vec{S} \cdot \vec{S} \text{ and } \hat{S}^{\tau=x,y,z} = \sum_{j=1}^N \hat{S}_j^{\tau}$$

are the collective spin operators. In the presence of the interatomic interactions and homogenous laser excitation, the collective nature of the system is maintained via two mechanisms. The first is the presence of a protective energy gap between collective spin manifolds (Fig. 1C), which prevents transitions away from the $S = N/2$ manifold (22). The second is the relatively small spread in mode-dependent interaction parameters with respect to the gap. Using the collective spin operators, we can thus describe the spin dynamics with the following Hamiltonian:

$$\hat{H}^{\text{eff}}/\hbar = -\delta\hat{S}^z - \Omega\hat{S}^x + \chi(\hat{S}^z)^2 + C(N-1)\hat{S}^z + J^{-1}\vec{S} \cdot \vec{S} + \mathcal{O}(S^2)^3 \quad (1)$$

where δ is the laser detuning from atomic resonance, Ω is the Rabi frequency of the driving laser, $\chi = (V_{gg} + V_{ee} - 2V_{eg})/2$, and $C = (V_{ee} - V_{gg})/2$. V_{gg} , V_{ee} , and V_{eg} represent *p*-wave interaction parameters between the three possible electronic symmetric states, $|gg\rangle$, $|ee\rangle$, and $\frac{1}{\sqrt{2}}(|ge\rangle + |eg\rangle)$ (Fig.

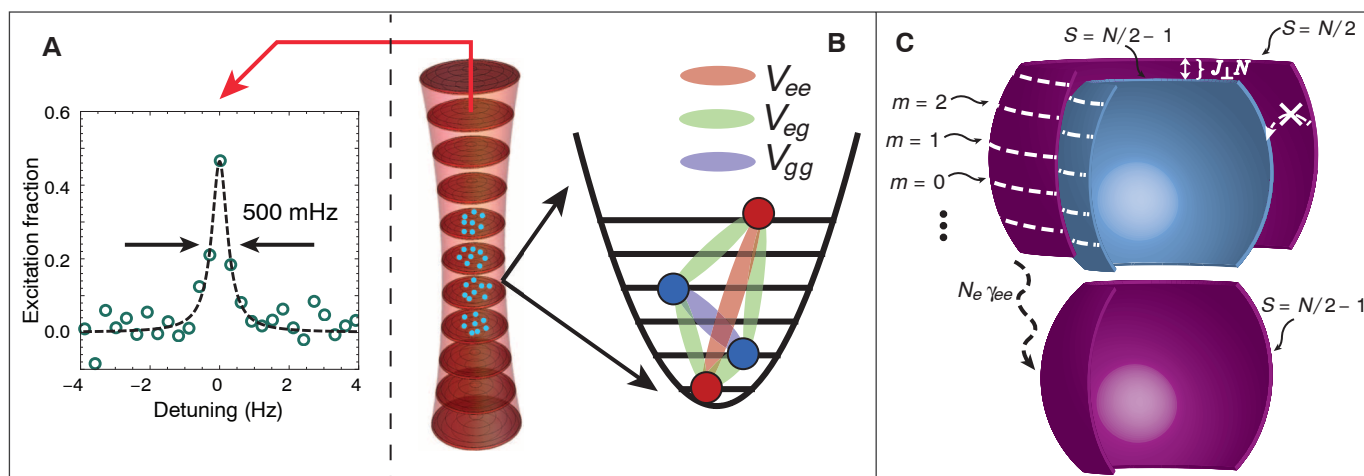


Fig. 1. Diagram of the interacting many-body system. (A) Spectroscopy of the ^{87}Sr clock transition in a 1D optical lattice, showing 500-mHz spectral resolution. The density is more than an order of magnitude lower than the typical operating condition. (B) Several hundred sites of the 1D vertical optical lattice are substantially occupied during the experiment. The average lattice occupancy is 20 atoms for the peak total atom number. Interactions between atoms are parametrized by the spin-dependent interaction parameters, $V_{gg} \propto b_{gg}^3$ (blue), $V_{eg} \propto b_{eg}^3$ (green), and $V_{ee} \propto b_{ee}^3$ (pink), with b^3 being the

p-wave scattering volumes (22). (C) The many-body Hamiltonian has eigenstates comprising maximally symmetric superpositions (Dicke states, for which $S = N/2$) of electronic ground and excited states (purple shells). Slight inhomogeneities in the coupling strengths allow the maximally symmetric manifold to be coupled to the next lowest manifold with $S = N/2 - 1$ (nested blue shell), but this coupling is prevented by an energy gap resulting from the $J^{-1}\vec{S} \cdot \vec{S}$ term in the Hamiltonian. Two-body inelastic losses connect maximally symmetric manifolds of $S \rightarrow S - 1$ and thus are not a strong decoherence mechanism.

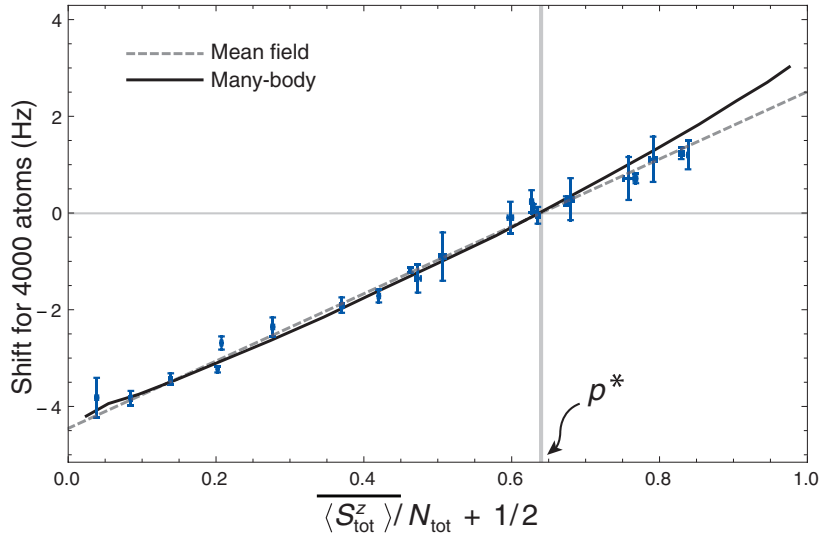


Fig. 2. Density shift in Ramsey spectroscopy fit with the full many-body solution. Because of the perturbative nature of this measurement, the mean-field approximation (dashed line) to the many-body theory agrees well with the data. The exact many-body solution in the absence of losses (solid curve) agrees best with the data only for lower values of total average spin $\langle \hat{S}_{\text{tot}}^z \rangle / N_{\text{tot}}$ because of the nonlinear $(\hat{S}^z)^3$ term in the Hamiltonian. The zero crossing occurs at an average excitation fraction, given by $\langle \hat{S}_{\text{tot}}^z \rangle / N_{\text{tot}} + 1/2$, of $p^* = 0.64(1)$. From the zero crossing and the measured slope, we extract χ and C .

1B). J^\perp is responsible for the energy gap (22). We find that the weak modification of the motional degrees of freedom by interactions can be accounted for as a term of order $(S^z)^3$. Equation 1 links the spin dynamics of interacting thermal fermions at micro-Kelvin temperatures to those of two-mode Bose-Einstein condensates (BECs), and it has been shown both theoretically (23, 24) and experimentally (25–27) to give rise to nontrivial many-body correlations and quantum noise-squeezed states. The validity of the collective model has been tested against the full multimode model with good agreement (22).

In the presence of excited-state inelastic loss, which has been observed in ^{87}Sr (20), our system becomes a many-body open quantum system. To capture the full many-body dynamics observed in the experiment, we solved a master equation in the presence of a two-body decay that is largely independent of the thermal occupation. The mode-independent losses preserved the collective nature of the system to leading order (Fig. 1C) and allowed us to solve the master equation efficiently for up to 50 atoms (22).

To determine the interaction parameters that characterize our spin Hamiltonian, Eq. 1, we mea-

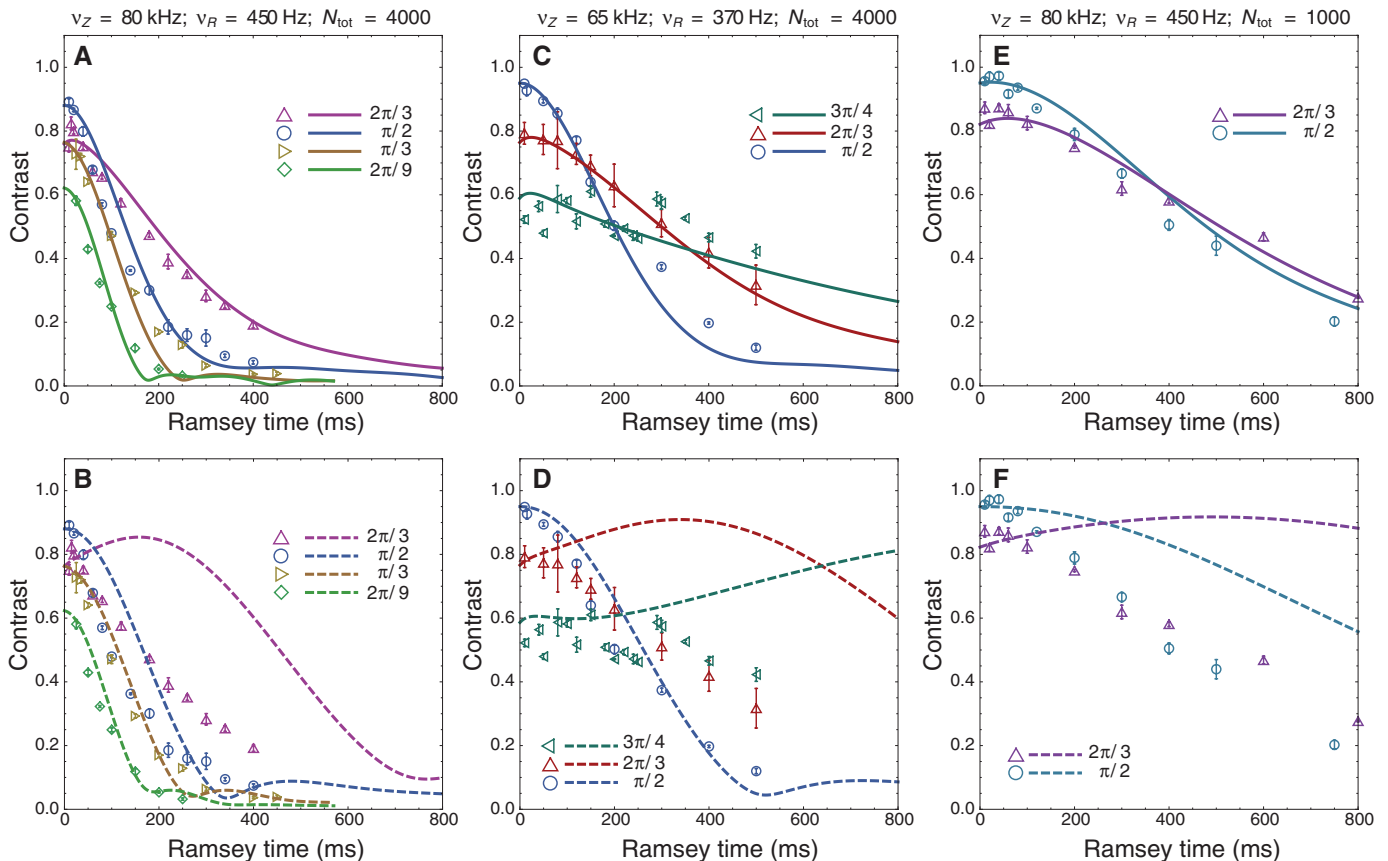


Fig. 3. Ramsey fringe contrast decay for varying initial pulse areas and experimental conditions. The pulse area values for the data and corresponding theory are given in the legends of the plots. Error bars represent the statistical error of each contrast measurement and thus do not account for systematic drifts that occur over the course of the experiment. The solid lines (top) are the many-body calculations, whereas the dashed lines (bottom) are using the mean-field

approximation of the theory. The many-body model and the mean-field approximation agree in the limit of small initial pulse area (Bloch vector polar angle) but disagree for pulse areas $\geq \pi/2$. This is an important confirmation of the dominance of many-body effects in this parameter regime. (A and B) $\nu_Z = 80$ kHz, $\nu_R = 450$ Hz, and $N_{\text{tot}} = 4000$; (C and D) $\nu_Z = 65$ kHz, $\nu_R = 370$ Hz, and $N_{\text{tot}} = 4000$; and (E and F) $\nu_Z = 80$ kHz, $\nu_R = 450$ Hz, and $N_{\text{tot}} = 1000$.

sured the density-dependent frequency shift of the clock transition using a modified Ramsey spectroscopy sequence. The initial pulse area $\theta_1 = \Omega T_R$, chosen so that $0 < \theta_1 < \pi$, controls the initial value of $\langle \hat{S}_{\text{tot}}^z \rangle$. Here, \hat{S}_{tot}^z is the sum of \hat{S}^z over the hundred relevant sites, so that $-N_{\text{tot}}/2 \leq \langle \hat{S}_{\text{tot}}^z \rangle \leq N_{\text{tot}}/2$, where N_{tot} is the total number of atoms loaded into the lattice. In the presence of two-body losses, $\langle \hat{S}_{\text{tot}}^z \rangle$ is not constant; thus, we used its time average, $\langle \hat{S}_{\text{tot}}^z \rangle$, to compare with theory. We extracted $\langle \hat{S}_{\text{tot}}^z \rangle$ from independent measurements periodically inserted into the clock sequence. The duration of the dark time, τ_{dark} , was fixed at 80 ms, and the final pulse area was set to $\pi/2$. We measured the shift by modulating the density by a factor of ~ 2 (Fig. 2).

Simple mean-field analysis of Eq. 1 (neglecting cubic terms and losses), in which the time-dependent operators are replaced by their expectation values, reveals that the average interaction experienced by a single atom behaves as an effective magnetic field along Z , $B(N) = NC + 2\chi\langle \hat{S}^z \rangle$, where $\langle \hat{S}^z \rangle = -(N/2)\cos\theta_1$. The mean-field density-dependent frequency shift $\Delta\nu(N) = B(N)/(2\pi)$ scales linearly with the excitation fraction and agrees with experimental observations (Fig. 2). Additionally, we fit an exact solution of Eq. 1 to the data. Both fits are shown in Fig. 2. To compare with the experiment, we always performed an average over the atom number distribution across the lattice sites. From this measurement, we extracted $\chi = 2\pi \times 0.20(4)$ Hz and $C = -0.3\chi$.

As a further step, we directly measured the spectrum of the many-body Hamiltonian with subherz spectral resolution and as a function of the drive strength, parameterized by the Rabi frequency Ω . We found that for $\Omega \gg N\chi$, the lineshapes are perturbatively shifted. However, for $\Omega \lesssim N\chi$, the lineshapes become significantly distorted, and the onset of an interaction blockade mechanism is observed, reflecting the dominant effect of strong interactions on the many-body spectrum. The observed Rabi lineshapes can be fully reproduced with the mean-field treatment by using the interaction parameters extracted from the density shift measurements. In this case, a full many-body treatment of the master equation agrees with the mean-field predictions.

To explore the development of many-body correlations during the full many-body dynamical evolution, we measured the Ramsey fringe contrast, which can undergo a periodic series of collapses and revivals, reflecting the quantized structure of the many-body spectrum. The results require a beyond-mean-field treatment. The mean-field model at the single-site level (with fixed N) predicts no decay of the Ramsey fringe contrast because when correlations are neglected, the interactions lead only to a pure precession of the collective Bloch vector (22). By taking the average over atom distributions among lattice sites and properly treating two-body loss during the Ramsey dark time, the mean-field model does show a decay of the contrast. However, this decay is associated mainly with dephasing arising from different precession rates exhibited by sites with different N .

For the Ramsey sequence designed to measure the fringe contrast effects, the pulse durations are < 6 ms, satisfying $\Omega \gg N\chi$, to suppress interaction effects during the pulses. We applied the final $\pi/2$ readout pulse with a variable relative optical phase of 0° to 360° and recorded the fraction of excited atoms as a function of the readout phase. The contrast of the resulting fringe was extracted in a manner that was insensitive to the frequency noise of the ultrastable clock laser (22).

We explored three distinct experimental conditions in order to rule out single-particle decoherence mechanisms and thoroughly test the model. The first condition represents the typical operating parameters of the lattice clock, with $N_{\text{tot}} = 4 \times 10^3$ and $\nu_Z = 80$ kHz. In the second case, we reduced the lattice intensity so that $\nu_Z = 65$ kHz, which results in a reduction of the density by a factor of ~ 1.8 . Last, we maintained $\nu_Z = 80$ kHz but reduced the atom number to $N_{\text{tot}} = 1 \times 10^3$. Under all conditions, the full many-body density matrix model reproduces the experimental observations well (Fig. 3, A, C, and E). The inclusion of the $(\hat{S}^z)^3$ correction improves the theory-experiment agreement, especially for pulse areas $\theta_1 > \pi/2$ and for the high-density conditions (22). We also observed a striking breakdown of the mean-field model for $\theta_1 \gtrsim \pi/2$, where many-body corrections are dominant (Fig. 3, B, D, and F).

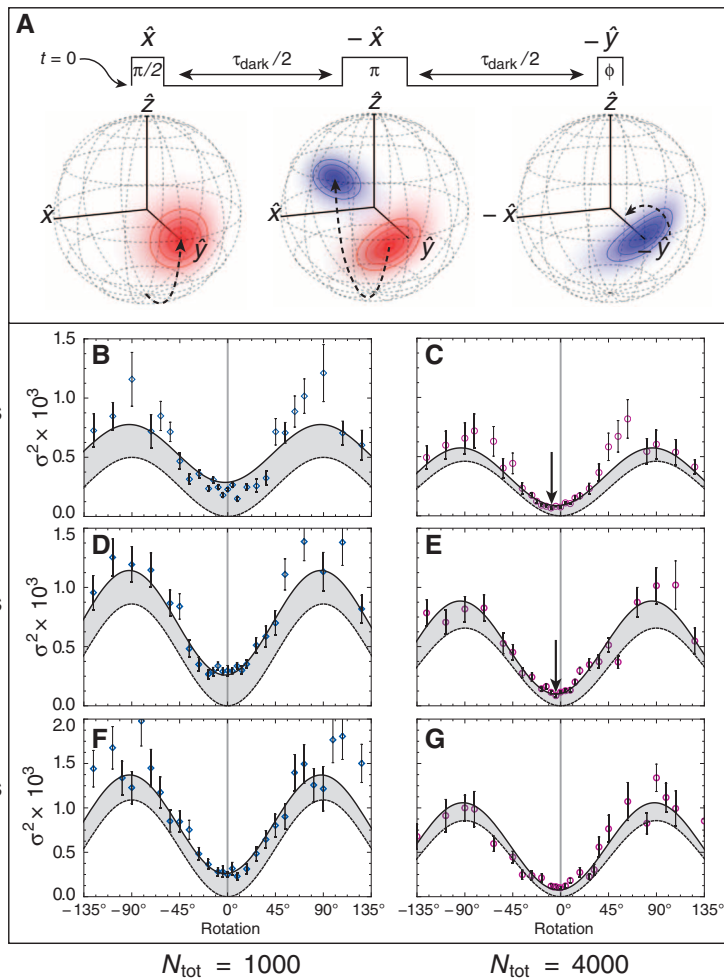


Fig. 4. Spin noise versus quadrature. (A) An initial pulse prepares a coherent state along \hat{y} , which then evolves for $\tau_{\text{dark}}/2$. An echo pulse then rotates the many-body state 180° about $-\hat{x}$. After an additional evolution time of $\tau_{\text{dark}}/2$, a final pulse rotates the state about $-\hat{y}$, and the spin noise is measured. The π -pulse has duration τ_{π} . The many-body state depicted here represents the spin evolution of a 20-atom ensemble in a single trap site, with $\tau_{\text{dark}} = 40$ ms. To remove spurious effects due to slow drifts in atom number, the data are processed as detailed in (22) in order to remove the potential bias. For (B to G), the dashed line is the pure laser noise extracted from a fit to the data. The solid line is the laser noise plus the full many-body prediction of the spin noise. This full theory is simultaneously fit to both the low- and high-atom-number curves so as to extract the laser noise for a given dark time. Vertical arrows indicate significantly phase-shifted minima in the experimentally measured spin noise, which is consistent with the predictions of the many-body theory. π -pulse times and τ_{dark} values are indicated at left, and total atom number is indicated at bottom.

The frequency shift, lineshape, and Ramsey fringe contrast are quantities that all depend on the first-order expectation values of the spin operators $\langle \hat{S}^{x,y,z} \rangle$. We next turned our attention to the distribution of quantum noise, which depends on the second-order moments of the spin operators, such as $\langle (\hat{S}^x)^2 \rangle - \langle \hat{S}^x \rangle^2$ and $\langle \hat{S}^x \hat{S}^z + \hat{S}^z \hat{S}^x \rangle - 2\langle \hat{S}^x \rangle \langle \hat{S}^z \rangle$. Given that the form of the Hamiltonian in Eq. 1 is known to produce squeezed and entangled states (23), the distribution of the spin noise becomes a compelling measurement to probe many-body correlations beyond the mean field.

To minimize single-particle dephasing effects (for example, arising from the distribution of site occupancies), we added a spin-echo pulse to the Ramsey sequence. As a result, the sensitivity to low-frequency laser noise was reduced at the expense of increased sensitivity to high-frequency laser noise. With atoms initialized in $|g\rangle$, we followed the pulse sequence (Fig. 4) so as to manipulate and measure the spin noise of the many-body state. For each value of the final rotation angle, representing a specific quadrature in which we measured the spin noise, we repeatedly recorded $\langle \hat{S}_{\text{tot}}^z \rangle / N_{\text{tot}}$ via measurements of the final atomic excitation fraction after the Ramsey sequence. From the data, we determined $\sigma \equiv \langle (\hat{S}_{\text{tot}}^z)^2 \rangle / N_{\text{tot}}^2 - \langle \hat{S}_{\text{tot}}^z \rangle^2 / N_{\text{tot}}^2$ by analyzing the pair variance for successive measurement of $\langle \hat{S}_{\text{tot}}^z \rangle / N_{\text{tot}}$. The quantum limit of σ^2 is important for defining the ultimate stability of lattice clocks (12). For an ideal coherent spin state of the entire ensemble, the standard quantum limit (SQL) of σ^2 is given by $\sigma_{\text{sql}}^2 = p(1-p)/N_{\text{tot}}$, where p is the probability of finding an atom in the excited state and can be estimated as $p = \langle \hat{S}^z \rangle / N_{\text{tot}} + 1/2$.

We performed measurements for different N_{tot} and τ_{dark} —the total atom number and Ramsey free evolution time, respectively—in order to probe the time evolution of the spin noise distribution. Long π pulses were used to reduce the sensitivity to spurious high-frequency components of laser noise. For $N_{\text{tot}} = 1 \times 10^3$, the quantum noise contribution to the spin noise is comparable with that of the laser noise (Fig. 4); however, with $N_{\text{tot}} = 4 \times 10^3$ the laser noise is responsible for a larger fraction of the noise in repeated measurements of $\langle \hat{S}^z \rangle$.

There are qualitative differences between the low- and high-atom-number cases; for example, for $N_{\text{tot}} = 4 \times 10^3$ with $\tau_{\text{dark}} = 20$ and 40 ms we observed a phase shift for the minimum of the spin noise. To compare the predictions of the full many-body master equation with the experiment, we added the effect of laser noise in quadrature with the calculated spin quantum noise. In the absence of laser noise, the theory predicts a small degree of sub-SQL squeezing. This effect is masked by laser noise in both the theoretical prediction for the total spin noise and in our experimental observations but gives rise to a shift of the spin noise minimum with respect to measurement quadrature. We additionally treated the effects of interactions during the laser pulses. The theory predicts the direction and magnitude

of the phase shift of the noise minimum in agreement with the experimental observations (Fig. 4), in addition to significantly enhanced spin noise for rotations near $\pm 90^\circ$. Despite the presence of laser noise, the measurements of the total spin noise are consistent with the many-body spin model.

Although the investigation described here is restricted to nuclear-spin-polarized gases, exploration of similar many-body effects in a clock making use of additional nuclear spin degrees of freedom with $SU(N)$ symmetry may allow investigation of unconventional frustrated quantum magnetism (28–30).

References and Notes

1. M. Greiner, O. Mandel, T. Esslinger, T. W. Hänsch, I. Bloch, *Nature* **415**, 39–44 (2002).
2. I. Bloch, W. Zwerger, *Rev. Mod. Phys.* **80**, 885–964 (2008).
3. Y.-J. Lin, R. L. Compton, K. Jiménez-García, J. V. Porto, I. B. Spielman, *Nature* **462**, 628–632 (2009).
4. G. B. Jo et al., *Science* **325**, 1521–1524 (2009).
5. S. Will et al., *Nature* **465**, 197–201 (2010).
6. J. Simon et al., *Nature* **472**, 307–312 (2011).
7. K. K. Ni et al., *Science* **322**, 231–235 (2008).
8. M. H. G. de Miranda et al., *Nat. Phys.* **7**, 502–507 (2011).
9. A. Chotia et al., *Phys. Rev. Lett.* **108**, 080405 (2012).
10. K. Kim et al., *Nature* **465**, 590–593 (2010).
11. J. W. Britton et al., *Nature* **484**, 489–492 (2012).
12. T. L. Nicholson et al., *Phys. Rev. Lett.* **109**, 230801 (2012).
13. A. D. Ludlow et al., *Science* **319**, 1805–1808 (2008).
14. G. K. Campbell et al., *Science* **324**, 360–363 (2009).
15. A. M. Rey, A. V. Gorshkov, C. Rubbo, *Phys. Rev. Lett.* **103**, 260402 (2009).
16. K. Gibble, *Phys. Rev. Lett.* **103**, 113202 (2009).
17. Z. H. Yu, C. J. Pethick, *Phys. Rev. Lett.* **104**, 010801 (2010).

18. N. D. Lemke et al., *Phys. Rev. Lett.* **107**, 103902 (2011).
19. A. Ludlow et al., *Phys. Rev. A* **84**, 052724 (2011).
20. M. Bishof et al., *Phys. Rev. A* **84**, 052716 (2011).
21. M. D. Swallows et al., *Science* **331**, 1043–1046 (2011).
22. Materials and methods are available as supplementary materials on Science Online.
23. A. Sørensen, L. M. Duan, J. I. Cirac, P. Zoller, *Nature* **409**, 63–66 (2001).
24. M. Kitagawa, M. Ueda, *Phys. Rev. A* **47**, 5138–5143 (1993).
25. J. Estève, C. Gross, A. Weller, S. Giovanazzi, M. K. Oberthaler, *Nature* **455**, 1216–1219 (2008).
26. C. Gross, T. Zibold, E. Nicklas, J. Estève, M. K. Oberthaler, *Nature* **464**, 1165–1169 (2010).
27. B. Lücke et al., *Science* **334**, 773–776 (2011).
28. A. V. Gorshkov et al., *Nat. Phys.* **6**, 289–295 (2010).
29. C. Wu, J.-P. Hu, S.-C. Zhang, *Phys. Rev. Lett.* **91**, 186402 (2003).
30. M. A. Cazalilla, A. F. Ho, M. Ueda, *New J. Phys.* **11**, 103033 (2009).

Acknowledgments: We thank S. Blatt, J. Thomsen, W. Zhang, T. Nicholson, J. Williams, B. Bloom, and S. Campbell for technical help and A. D. Ludlow, K. R. A. Hazzard, M. Foss-Feig, A. J. Daley, and J. K. Thompson for discussions. The work is supported by the National Institute of Standards and Technology, Defense Advanced Research Projects Agency Optical Lattice Emulator Program administered by Army Research Office, NSF, and Air Force Office of Scientific Research. M.B. acknowledges support from the National Defense Science and Engineering Graduate fellowship program. A.V.G. acknowledges support from NSF IQIM, the Lee A. DuBridge Foundation, and the Gordon and Betty Moore Foundation.

Supplementary Materials

www.sciencemag.org/cgi/content/full/341/6146/632/DC1

Materials and Methods

Supplementary Text

Figs. S1 to S5

References (31–44)

22 February 2013; accepted 1 July 2013

10.1126/science.1236929

Writing and Deleting Single Magnetic Skyrmions

Niklas Romming, Christian Hanneken, Matthias Menzel, Jessica E. Bickel,* Boris Wolter, Kirsten von Bergmann,† André Kubetzka,† Roland Wiesendanger

Topologically nontrivial spin textures have recently been investigated for spintronic applications. Here, we report on an ultrathin magnetic film in which individual skyrmions can be written and deleted in a controlled fashion with local spin-polarized currents from a scanning tunneling microscope. An external magnetic field is used to tune the energy landscape, and the temperature is adjusted to prevent thermally activated switching between topologically distinct states. Switching rate and direction can then be controlled by the parameters used for current injection. The creation and annihilation of individual magnetic skyrmions demonstrates the potential for topological charge in future information-storage concepts.

Magnetic skyrmions (I) are topologically stable, particle-like spin configurations that carry a characteristic topological charge S , which is essentially a measure of the magnetization curvature. For a surface area A ,

S is defined as $S = \frac{1}{4\pi} \int_A \mathbf{n} \cdot \left(\frac{\partial \mathbf{n}}{\partial x} \times \frac{\partial \mathbf{n}}{\partial y} \right) dx dy$, where

\mathbf{n} is the normalized magnetization vector and x and y are the spatial coordinates. A single

skyrmion carries a quantized charge of $S = +1$; for an antiskyrmion, the charge is $S = -1$. In contrast, a spin spiral and the ferromagnetic (FM)

Institute of Applied Physics, University of Hamburg, D-20355 Hamburg, Germany.

*Present address: Department of Physics, Mount Holyoke College, 50 College Street, South Hadley, MA 01075, USA.

†Corresponding author. E-mail: kubetzka@physnet.uni-hamburg.de (A.K.); kbergman@physnet.uni-hamburg.de (K.v.B.)

state are topologically trivial with $S = 0$. Transitions between such topologically distinct states are forbidden within a continuous description of \mathbf{n} , but in a real system with magnetic moments on an atomic lattice, strict topological protection does not exist. Instead, the states are separated by a finite energy barrier. Magnetic skyrmions typically arrange in two-dimensional (2D) lattices (2–4). An important prerequisite for their formation is broken inversion symmetry, which is fulfilled not only for samples with chiral crystal structure (4–9), but also for magnetic film systems, in which the top and bottom interfaces are different (10–12). In recent years, magnetic skyrmions have been observed in a number of systems with broken crystal inversion symmetry ranging from metallic and semiconducting (4–7) to insulating (8, 9). Each of these systems displays a spin spiral phase in zero field (Fig. 1A), resulting from a competition of magnetic exchange and Dzyaloshinskii-Moriya interaction, and can be driven into a hexagonal skyrmion lattice phase (Fig. 1B) by the application of an external magnetic field B . In contrast to the spin spiral state, which is magnetically compensated, the hexagonal skyrmion lattice exhibits a net magnetization and is, therefore, favored by the Zeeman energy. By further increasing the magnetic field, the parallel alignment of the magnetic moments becomes energetically more and more favorable, until the skyrmion phase is eventually saturated to the FM phase (Fig. 1C) (5). Both of these phase transitions are accompanied by a change of topological charge. In thin films, the skyrmion lattice

phase space increases as the thickness of the sample is decreased (7). In such 2D systems, the diameter of the skyrmions can exceed the film thickness (5, 7), which may be favorable for controlled skyrmion manipulation by surface techniques. At the ultimate limit, a single atomic layer of Fe on Ir(111) exhibits a skyrmion lattice, even in the absence of an external field. This skyrmion lattice has square symmetry and a period of only 1 nm (12); however, driving it into a different topological state has been challenging.

The manipulation of skyrmion lattices may require substantially smaller current densities compared with the manipulation of domain walls in conventional ferromagnetic systems, which makes skyrmions a promising candidate for spintronic applications (13–18). However, even though single skyrmions were observed experimentally (5), and the creation of skyrmions by radial currents was studied theoretically (19), the manipulation or creation of individual skyrmions has presented difficulties. To design an ultrathin film system exhibiting skyrmions that can be manipulated with a local probe, we cover the Fe layer on Ir(111) with an additional atomic layer of Pd (20). We thereby modify the top interface and, thus, the magnetic interactions within the film. As Pd is known to be easily polarized by adjacent magnetic moments (21), we expect the resulting PdFe bilayer to behave as a single magnetic entity.

Figure 1 shows the magnetic field dependence of the PdFe bilayer on Ir(111) at a temperature T of 8 K. In zero field (Fig. 1D), the spin-polarized

scanning tunneling microscopy (SP-STM) image (20) reveals a spin spiral ground state with a period of 6 to 7 nm. When the magnetic field is increased to $B = +1$ T (Fig. 1E), skyrmions can be observed coexisting with remaining areas of spiral ordering. Even higher values of B lead to a pure hexagonal skyrmion lattice (Fig. 1F) and, eventually, to saturation of the film to a FM phase (Fig. 1G); here only a few single skyrmions, pinned at atomic defects, remain at $B = +2$ T. This field-dependent behavior is similar to previously studied systems (5), and the transitions are reversible at $T = 8$ K: Removing the field leads to qualitatively the same magnetic structure as in Fig. 1D, with small variations in the details of the spiral position and direction.

Figure 2A depicts a comparable sample at $B = +1$ T, this time measured at $T = 4.2$ K. Whereas the trend of skyrmion formation at the cost of the spiral phase is similar, fewer skyrmions are observed compared with the measurement at $T = 8$ K (see Fig. 1E). This may be partly due to a small shift with temperature of the critical magnetic field needed for the phase transition (4, 5, 7) or to small differences in the local environment. However, the main reason is reduced thermal energy, which prevents the system from reaching energetically lower states. A change of B at $T = 4.2$ K may not necessarily lead to the lowest-energy state; instead, a metastable state may be preserved. We demonstrated a transition from a metastable to a lower-energy state by depositing energy into the system by tunneling with higher-energy electrons: After scanning the surface area at an increased bias voltage of $U = +1$ V, the spin spiral has locally transformed into skyrmions (Fig. 2B). A higher degree of control can be achieved by injecting higher-energy electrons locally, as in Fig. 2, C and D, where skyrmions are imprinted into the ferromagnetic phase; by voltage sweeps with the STM tip held stationary, skyrmions can be created one by one below the tip or in close vicinity (Fig. 2E). Apparently, atomic defects act as preferred nucleation and pinning sites (see also fig. S2). In such a writing process, a topological charge S is created. The field-dependent potential can be sketched as in Fig. 2F, where B_0 is the field at which the two states are energetically degenerate. For $B < B_0$, the energetically lower state is the skyrmion ($S = 1$); for $B > B_0$, it is the FM state ($S = 0$). When we start from the FM state and lower the external field to $B < B_0$ (as in Fig. 2C), the system can be transferred to the skyrmion state only if the remaining energy barrier is overcome, either by thermal fluctuations or if energy is supplied by other means (e.g., by the tunneling electrons).

For magnetic field values close to B_0 , skyrmions can be created and annihilated reversibly. In this way, topological charge can be used to store information, as demonstrated in Fig. 3: By locally injecting electrons, we can generate any desired skyrmion configuration for the four pinning sites within the area. In the series of

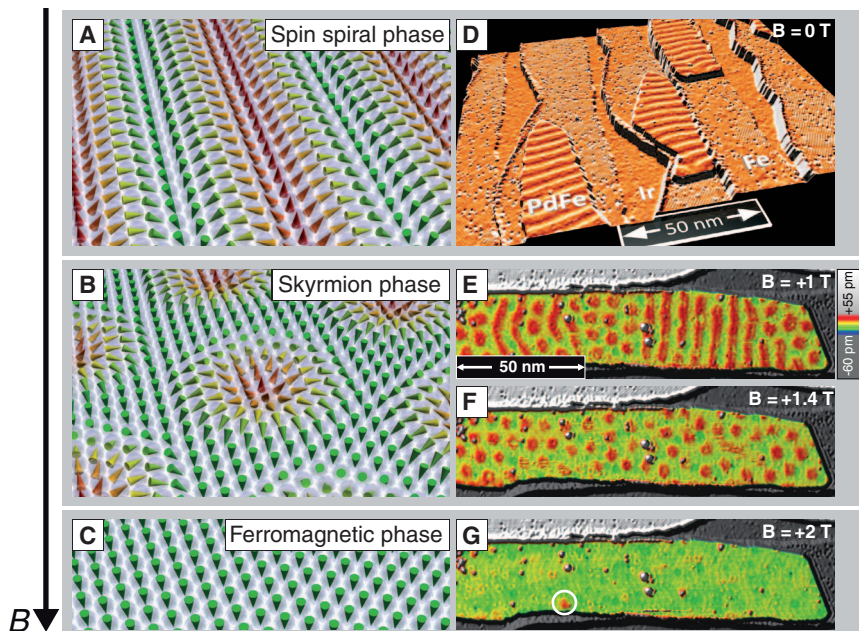


Fig. 1. Magnetic field dependence of the PdFe bilayer on the Ir(111) surface at $T = 8$ K. (A to C) Perspective sketches of the magnetic phases. (D) Overview SP-STM image, perspective view of constant-current image colored with its derivative. (E to G) PdFe bilayer at different magnetic fields ($U = +50$ mV, $I = 0.2$ nA, magnetically out-of-plane sensitive tip). (E) Coexistence of spin spiral and skyrmion phase. (F) Pure skyrmion phase. (G) Ferromagnetic phase. A remaining skyrmion is marked by the white circle.

difference SP-STM images in Fig. 3, B to E, the skyrmions are annihilated one by one until no skyrmion is present (in Fig. 3F); skyrmions are

then created in a different sequence until the starting configuration is reached again (Fig. 3, G to J). The writing and deleting was done between the

images by local voltage sweeps. This series demonstrates that the skyrmions can be addressed individually and independently, even in close proximity to one another.

Whereas controlled skyrmion creation and annihilation is demonstrated, the intermediate magnetization states during the switching process cannot be imaged directly because of the limited time resolution in our experiment. We consider the following mechanisms that may contribute to switching (22, 23): (i) thermal noise, (ii) a local temperature increase caused by the injected power (Joule heating), (iii) nonthermal excitations from the injected electrons, and (iv) spin-transfer torque (STT). The latter depends on the spin-polarization of the tunnel current and its direction. To discriminate between these different contributions, we performed measurements as a function of bias voltage U , tunnel current I , and applied magnetic field B (23, 24): With the tip held stationary above atomic pinning sites, we recorded the time evolution of the system (20). The observed magnetic telegraph noise (see insets in Fig. 4) occurs because of repetitive switching between a skyrmion ($S = 1$) and the FM state ($S = 0$). From each measurement, typically consisting of 1000 switching events, the switching rate f and the probability to observe a skyrmion P can be extracted (22). We find that the switching process is very sensitive to the energy of the tunneling electrons eU (where e is the elementary charge) (Fig. 4A): At $U = 300$ mV, switching occurs, on average, once every 15 s at $I = 300$ nA. Toward lower bias voltages, switching becomes increasingly rare, which facilitates nonperturbing imaging. For higher voltages, the rate increases rapidly, allowing efficient skyrmion manipulation. In contrast, the current dependence at fixed bias voltage (Fig. 4B) is much weaker. The switching rate depends linearly on I within the investigated current

Fig. 2. Manipulation of the magnetic states of the PdFe bilayer at $T = 4.2$ K.

(A and B) SP-STM images at $B = +1$ T ($U = +100$ mV, $I = 0.5$ nA, magnetically in-plane sensitive tip). Whereas (A) shows the sample in its initial magnetic state after sweeping the field up from $B = 0$ T to $+1$ T, in (B) the spin spiral has locally transformed into skyrmions after supplying energy by a higher-voltage STM scan with $U = +1$ V, $I = 0.5$ nA. (C) SP-STM image of the initial state at $B = +1.8$ T after sweeping the magnetic field down from $+3$ T. Four skyrmions are marked by circles ($U = +100$ mV, $I = 1$ nA, magnetically out-of-plane sensitive tip). (D) Successive population of the island with skyrmions by injecting higher-energy electrons through local voltage sweeps (20) (fig. S2). (E) Concept of skyrmion manipulation with local currents from an STM tip. (F) Sketch of the field-dependent potential for a skyrmion (Sk; $S = 1$) and the FM state ($S = 0$). B_0 is the field where the two states are energetically degenerate.

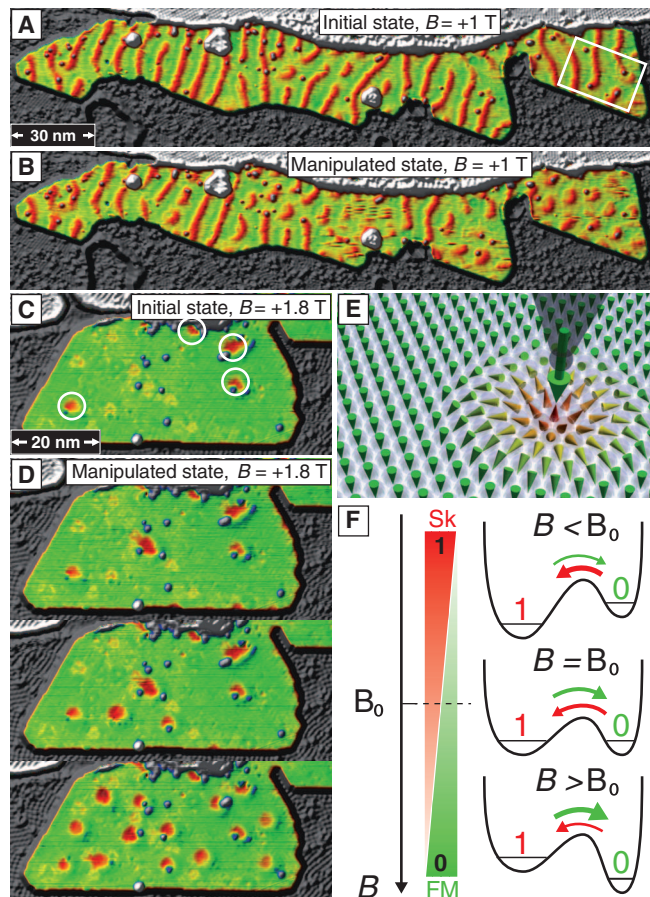
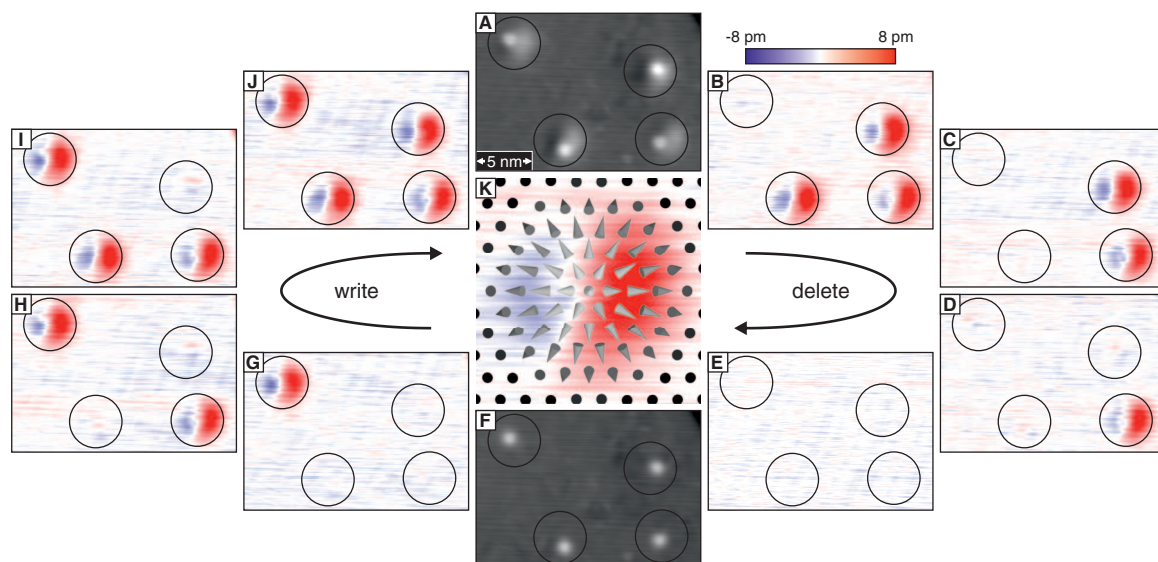


Fig. 3. Creation and annihilation of single skyrmions.

(A) Constant-current image of a sample region with four defects (see box in Fig. 2A), each hosting a skyrmion marked by a circle containing ~ 270 surface atoms ($U = +250$ mV, $I = 1$ nA, $B = +3.25$ T, $T = 4.2$ K, magnetically in-plane sensitive tip). (B to E) Sequence of difference SP-STM images [with respect to (F)] showing the selective erasing of all four skyrmions using local voltage sweeps (feedback loop switched off while bias voltage was increased to $+750$ mV). (F) The sample area without skyrmions (constant-current image) and (G to J) their successive rewriting (difference images). (K) Schematic spin configuration with distances twice the atomic lattice, superimposed on the experimental data: The asymmetric appearance of the skyrmions results from a canted SP-STM tip magnetization in this experiment.



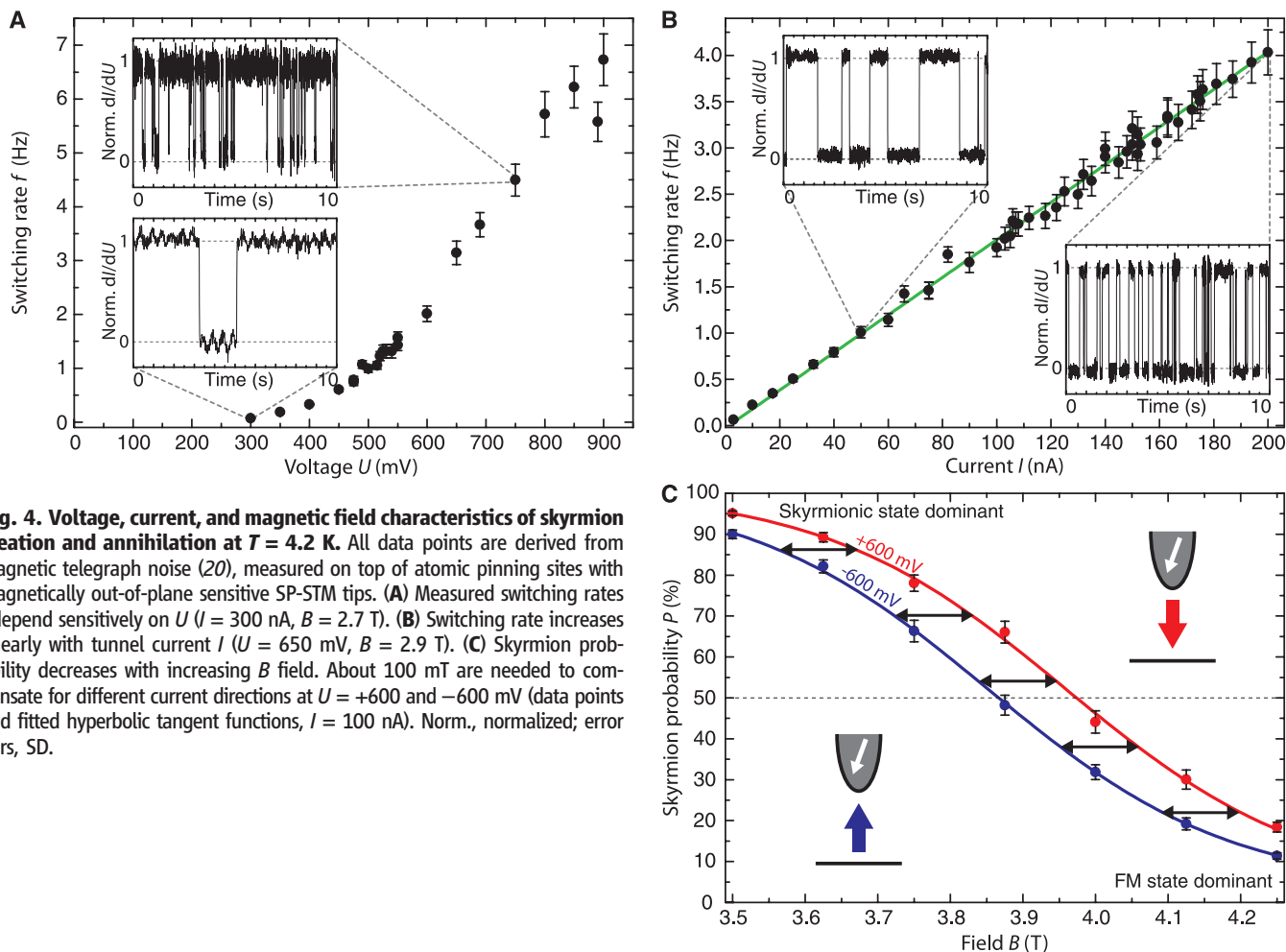


Fig. 4. Voltage, current, and magnetic field characteristics of skyrmion creation and annihilation at $T = 4.2$ K. All data points are derived from magnetic telegraph noise (20), measured on top of atomic pinning sites with magnetically out-of-plane sensitive SP-STM tips. **(A)** Measured switching rates f depend sensitively on U ($I = 300$ nA, $B = 2.7$ T). **(B)** Switching rate increases linearly with tunnel current I ($U = 650$ mV, $B = 2.9$ T). **(C)** Skyrmion probability decreases with increasing B field. About 100 mT are needed to compensate for different current directions at $U = +600$ and -600 mV (data points and fitted hyperbolic tangent functions, $I = 100$ nA). Norm., normalized; error bars, SD.

range, which means that, on average, the number of electrons needed for switching, $I/(fe)$, is constant, independent of I . We found that, in the limit of low bias and low current, the switching rate approaches zero, which shows that thermally activated switching (i) does not play a role at $T = 4.2$ K. The injected power IU is also not a decisive quantity for the switching process. At constant power, the switching rates still depend critically on U . Thus, local thermal heating (ii) can be ruled out as a driving mechanism. Instead, the energy of the injected electrons $|eU|$ (iii) appears to be the dominant factor determining the switching rate. Figure 4C shows the magnetic field-dependent skyrmion probability P for the two current directions, while $|eU|$ and $|I|$ are fixed. As expected, P decreases with increasing B (Fig. 2F). More importantly, the data points show a uniform shift of $\Delta B \approx 100$ mT upon current reversal. Because all other parameters are fixed, this indicates that ΔB results from a difference of the STT (iv) at the chosen bias voltages (23). Along with the external field B , the STT is, thus, a means to control the directionality of the switching. Whereas the switching trajectory within the energy landscape and the coupling of the spin-polarized tunnel current to the magnetic states re-

main to be identified for the optimization of the switching process, our work demonstrates the feasibility of using spin-polarized tunnel currents for the controlled manipulation of individual skyrmions.

References and Notes

1. T. H. R. Skyrme, *Nucl. Phys.* **31**, 556–569 (1962).
2. A. Bogdanov, A. Hubert, *J. Magn. Magn. Mater.* **138**, 255–269 (1994).
3. U. K. Rößler, A. N. Bogdanov, C. Pfleiderer, *Nature* **442**, 797–801 (2006).
4. S. Mühlbauer et al., *Science* **323**, 915–919 (2009).
5. X. Z. Yu et al., *Nature* **465**, 901–904 (2010).
6. W. Münzer et al., *Phys. Rev. B* **81**, 041203 (2010).
7. X. Z. Yu et al., *Nat. Mater.* **10**, 106–109 (2011).
8. T. Adams et al., *Phys. Rev. Lett.* **108**, 237204 (2012).
9. S. Seki, X. Z. Yu, S. Ishiwata, Y. Tokura, *Science* **336**, 198–201 (2012).
10. M. Bode et al., *Nature* **447**, 190–193 (2007).
11. P. Ferriani et al., *Phys. Rev. Lett.* **101**, 027201 (2008).
12. S. Heinze et al., *Nat. Phys.* **7**, 713–718 (2011).
13. F. Jonietz et al., *Science* **330**, 1648–1651 (2010).
14. N. S. Kiselev, A. N. Bogdanov, R. Schäfer, U. K. Rößler, *J. Phys. D Appl. Phys.* **44**, 392001 (2011).
15. J. Zang, M. Mostovoy, J. H. Han, N. Nagaosa, *Phys. Rev. Lett.* **107**, 136804 (2011).
16. T. Schulz et al., *Nat. Phys.* **8**, 301–304 (2012).
17. X. Z. Yu et al., *Nat. Commun.* **3**, 988 (2012).
18. A. Fert, V. Cros, J. Sampaio, *Nat. Nanotechnol.* **8**, 152–156 (2013).
19. Y. Tchoe, J. H. Han, *Phys. Rev. B* **85**, 174416 (2012).
20. Materials and methods are available as supplementary materials on Science Online.
21. W. Weber, D. A. Wesner, G. Güntherodt, U. Linke, *Phys. Rev. Lett.* **66**, 942–945 (1991).
22. S. Krause, L. Berbil-Bautista, G. Herzog, M. Bode, R. Wiesendanger, *Science* **317**, 1537–1540 (2007).
23. A. A. Khajetoorians et al., *Science* **339**, 55–59 (2013).
24. S. Loth, S. Baumann, C. P. Lutz, D. M. Eigler, A. J. Heinrich, *Science* **335**, 196–199 (2012).

Acknowledgments: We thank S. Krause, A. A. Khajetoorians, A. Sonntag, S. Heinze, B. Dupé, and Ch. Hübner for discussions. We acknowledge financial support from the Deutsche Forschungsgemeinschaft via grants SFB668 and GrK 1286, the European Union via the European Research Council Advanced Grant FUROR, and the Hamburg Cluster of Excellence NANOSPINTRONICS.

Supplementary Materials

www.sciencemag.org/cgi/content/full/341/6146/636/DC1
Materials and Methods
Figs. S1 and S2
References (25–29)

15 May 2013; accepted 11 July 2013
10.1126/science.1240573

A Semi-Floating Gate Transistor for Low-Voltage Ultrafast Memory and Sensing Operation

Peng-Fei Wang,^{1*†} Xi Lin,¹ Lei Liu,² Qing-Qing Sun,^{1*} Peng Zhou,¹ Xiao-Yong Liu,¹ Wei Liu,² Yi Gong,² David Wei Zhang^{1*}

As the semiconductor devices of integrated circuits approach the physical limitations of scaling, alternative transistor and memory designs are needed to achieve improvements in speed, density, and power consumption. We report on a transistor that uses an embedded tunneling field-effect transistor for charging and discharging the semi-floating gate. This transistor operates at low voltages (≤ 2.0 volts), with a large threshold voltage window of 3.1 volts, and can achieve ultra-high-speed writing operations (on time scales of ~ 1 nanosecond). A linear dependence of drain current on light intensity was observed when the transistor was exposed to light, so possible applications include image sensing with high density and performance.

Metal-oxide semiconductor field-effect transistors (MOSFETs) and floating-gate (FG) MOSFETs are the two main semi-

conductor devices used in high-speed computing. The dimensions of MOSFETs are approaching their physical limitations for acceptable perform-

ance, and the scaling along Moore's law is slowing down (1–3). Further improvements of transistors and memory cells such as static random access memory (SRAM) and dynamic random access memory (DRAM) (4) are needed to continue to improve device performance. Tunneling field-effect transistors (TFETs) that have a gate over the tunneling junction have been intensively investigated for application in low-power logic circuits (5–8). Although Si-based TFETs have very limited drive currents, they have excellent sub-threshold swing and off-leakage current, which is very attractive for ultra-low-power logic applications (9). Here we report on the fabrication of a semi-floating gate (SFG) transistor with an embedded TFET. The gate-controlled band-to-band

¹State Key Laboratory of ASIC and System, School of Microelectronics, Fudan University, Shanghai, China. ²Oriental Semiconductor, Suzhou, China.

*These authors contributed equally to this work.
†Corresponding author. E-mail: pfw@fudan.edu.cn

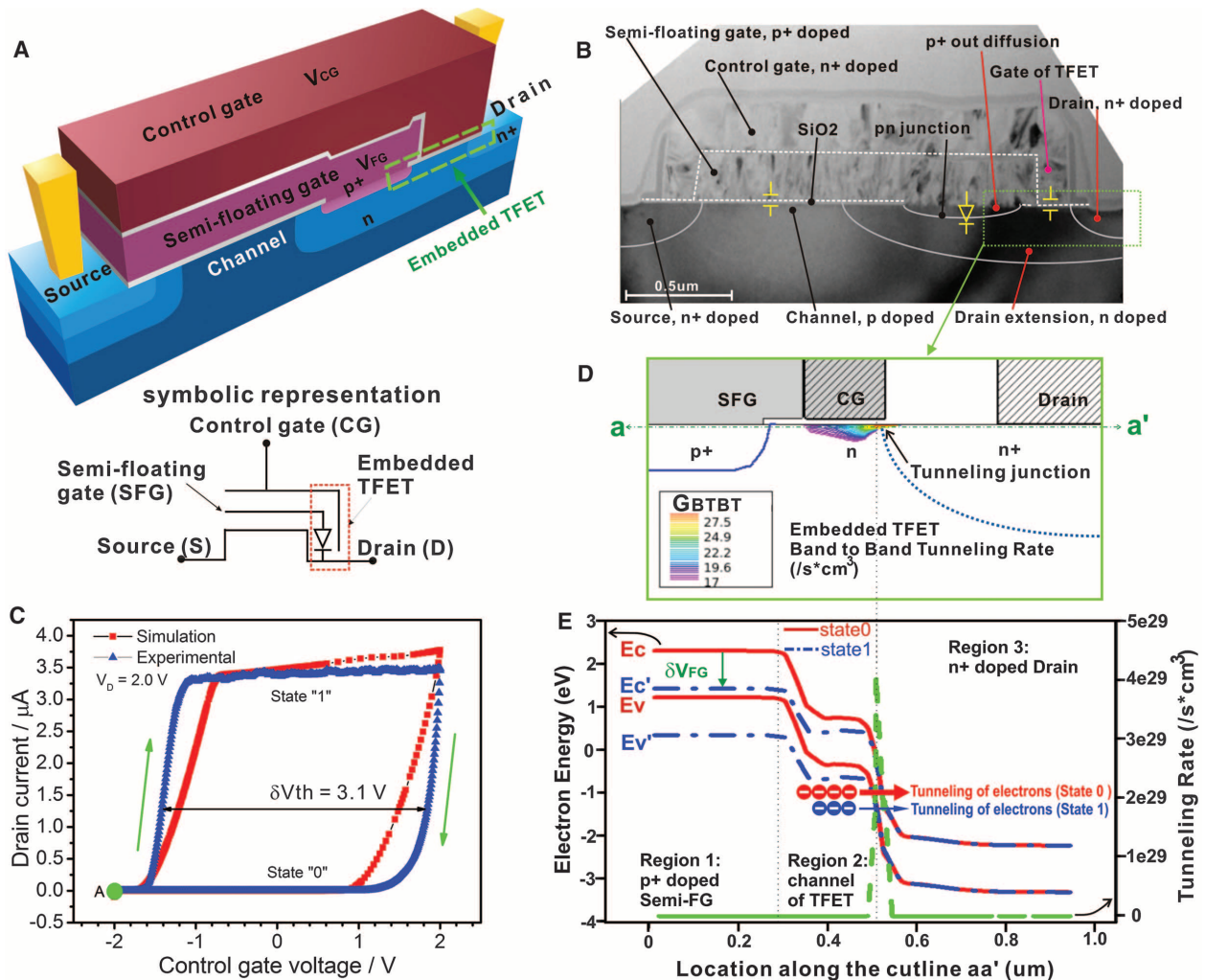


Fig. 1. Device structure and the working principle of the SFG transistor. (A) Schematic view of an SFG memory cell. A pn junction diode between the FG and D makes the FG semi-floating. The device's symbolic representation is also shown. (B) Cross-sectional view of the fabricated device. The CG is extended over the pn diode. A TFET is formed and connects the semi-FG to the D. (C) Simulated

and measured transfer characteristics for states 1 and 0. A large V_{th} window of 3.1 V between 1 and 0 is realized with low operation voltages. (D) Contour of BTBT generation rate during the writing-1 operation. (E) Band diagrams (red and blue lines) and BTBT generation rate (green line) along the cutline aa' shown in Fig. 1D. The tunneling generation rate is highest where the band bending is strongest.

tunneling effect of the TFET enables high-speed writing operation (1.3 ns) of the SFG with low operating voltages (2.0 V). The operation voltage is much lower than that of FG-MOSFETs, and the operation speed is comparable to that of six-transistor SRAM (6T-SRAM).

The SFG transistor has a pn junction diode between the FG and drain (D), which makes the FG semi-floating (Fig. 1A). The fabricated transistor consists of a D region, a source region, a control gate (CG), and a semi-FG (Fig. 1B). A diode is formed between the p^+ floating gate and the n^+ -doped D. The CG is extended over the pn diode. A TFET is formed and connects SFG to the D.

The measured and simulated D current to CG voltage (I_D - V_{CG}) curves are shown in Fig. 1C. The threshold voltage (V_{th}) of a single device was -1.6 V for logic state “1” and 1.5 V for logic state “0” when V_{CG} was swept from -2 V to 2 V and back to -2 V, respectively. A change in threshold voltage (δV_{th}) of about 3.1 V was observed. The simulated behavior fits well with the experimental results using the simulation structure given in fig. S3 (10).

The V_{th} of a SFG transistor was controlled by regulating the amount of charge stored inside the SFG. During the writing-1 operation, the device was biased, with a positive V_D and a negative V_{CG} (i.e., $V_D = 2$ V and $V_{CG} = -2$ V

at point A of Fig. 1C). Because of the negative V_{CG} of -2 V, the n -doped D extension region under the gate of the TFET was inverted to a p^+ channel. Tunneling occurred at the p^+ channel/ n^+ D tunneling junction, as depicted in the band-to-band generation rate contour of Fig. 1D. According to Kane’s model, the band-to-band tunneling generation rate (G_{BTBT}) is expressed as

$$G_{BTBT} = A_{BTBT} \times \frac{E_g^2}{E} \times \exp(-B_{BTBT} \times \frac{E_g^3}{E}), \text{ where}$$

A_{BTBT} and B_{BTBT} are constants, E_g is the band-gap energy, and E is the magnitude of the electric field (11). The corresponding energy band diagrams and G_{BTBT} along the cutline aa’ during

Fig. 2. Demonstration of the memory functions of the SFG transistors. The operation sequence is writing-0, reading, writing-1, and then reading. (A and B) Measured voltages and D current with 1.3-ns writing-1 and writing-0 operations. The target pulse width is 0.6 ns. The actual peak width at half height is increased to 1.3 ns when the rising and falling edges are included (fig. S5A).

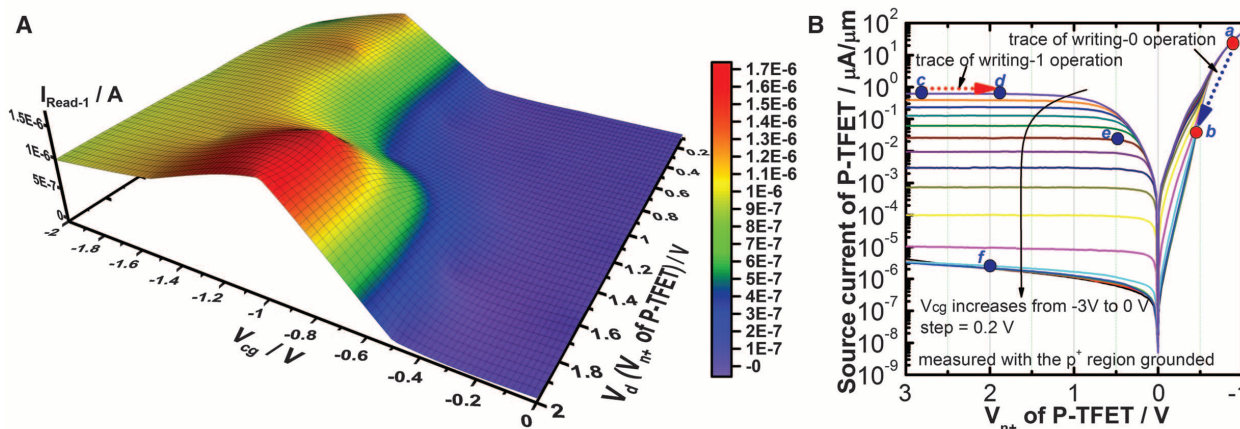
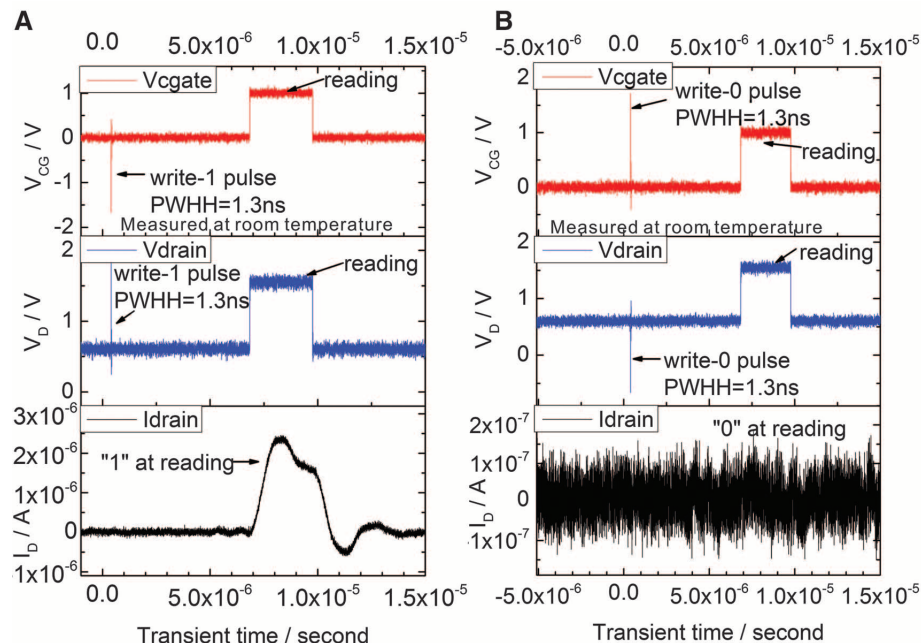


Fig. 3. Impact of p-type TFET (P-TFET) on the device writing and reading operations. (A) Measured reading-1 current of transistors written with various V_D and V_{CG} . The writing-1 duration is as long as 50 ms, so that some of the transistors have reached the self-limiting status of logic 1 (Fig. 1C). With small V_{CG} , the writing-1 operation becomes very slow even with V_D of 2 V. (B) Output charac-

teristics of a typical P-TFET. In order to emulate the voltage setting of the embedded TFET of the SFG, the measurement of P-TFET is with the p^+ region grounded and the voltage on the n^+ region sweeping. The current through a P-TFET with lower V_D (i.e., point e with $V_D = 0.5$ V and $V_{CG} = -2$ V) can be several orders of magnitude larger than that with higher V_D (i.e., point f with $V_D = 2$ V and $V_{CG} = -0.5$ V).

the writing-1 operation are displayed in Fig. 1D. A peak of tunneling generation rate can be seen where the band bending is the strongest. Because the D was biased with 2 V, electrons tunneled from the valance band of the p^+ channel to the conduction band of the n^+ D region, and current flowed from D to SFG (fig. S3A). The current through TFET will raise the FG potential V_{FG} by δV_{FG} . The energy bands in the SFG region moved accordingly in Fig. 1E. Because of the capacitive coupling effect, δV_{FG} caused a change in V_{th} .

During the writing-0 operation, V_{CG} increased and the pn junction between the SFG and n-doped D extension was forward-biased. The current flowing from the SFG to the n-doped D extension discharged the SFG capacitor (fig. S3B). After the discharging process, 0 was written and the threshold voltage increased.

The memory function of the SFG transistor was investigated by applying two channel voltage-pulse signals on CG and D, respectively. A 0 could be written into the transistor with V_D of -1 V and V_{CG} of 2 V for 3 ms [fig. S6A (10)]. During the subsequent reading operation, a very small D current of 30 nA was measured with $V_D = 2$ V and $V_{CG} = 2$ V and indicated that logic 0 was written into this cell. After a writing-1 operation at $V_D = 2$ V and $V_{CG} = -2$ V for 3 ms, the threshold voltage was lowered and a large D current of about 2 μ A was measured with $V_D = 2$ V and $V_{CG} = 2$ V. As a gain cell, the read operation was nondestructive. The wafer map of the reading-1 D current of 40 test devices showed

that high uniformity was observed on these transistors across the whole wafer.

High-speed memory properties were evaluated by reducing the pulses to nanosecond durations. As displayed in fig. S5A, the measured pulses for the writing-1 and writing-0 operations were with the peak width at half height (PWHH) of 1.3 ns. The measured voltage pulse signals for the writing-1 and writing-0 operations and the readout current signals are shown in Fig. 2, A and B. After the 1.3-ns writing-1 operation, a D current signal of about 2 μ A was measured, indicating that 1 was successfully written and read out (Fig. 2A). The readout D current was much lower than that of the 1 cell (34 nA) after the 1.3-ns writing-0 operation (Fig. 2B).

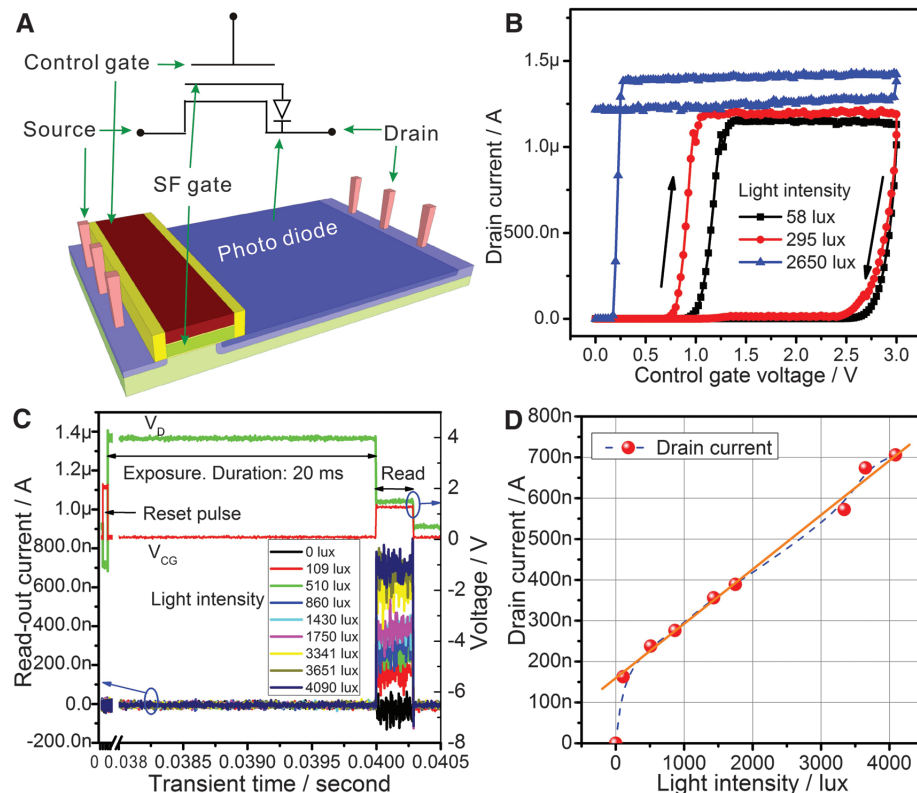
The high-speed and low-voltage operation capabilities of the SFG are the result of introducing an embedded tunneling transistor instead of the tunneling oxide layer of flash memory in a conventional FG-MOSFET structure. In Fig. 3A, the dependence of reading-1 current on the V_D and V_{CG} of the writing-1 operation is displayed. With a 50-ms writing time, logic 1 could not be written by increasing V_D to 2.0 V and keeping V_{CG} at 0 V. However, 1 was successfully written with a low V_D of 0.1 V and a V_{CG} of -2.0 V. These results indicate that V_{CG} plays a dominating role during the writing-1 operation. As shown in Fig. 1D, the BTBT effect is turned on by applying the negative V_{CG} , and the embedded TFET works as a p-type TFET (P-TFET) (12). When V_{CG} equaled 0 V, the tunneling effect of P-TFET was suppressed, and the writing-1 operation became

very slow for the weak reverse diode current. When V_{CG} equaled -2 V, the BTBT of P-TFET was turned on. Logic 1 could be written even with a V_D as low as 0.1 V within a 50-ms time period.

In a SFG transistor, the embedded P-TFET was realized by using an asymmetric doping design (fig. S1). The gate-on-source-only overlay design also weakened the N-channel TFET response (13). The functions of P-TFET during the writing operations are schematically illustrated in its typical output characteristics (Fig. 3B). During the writing-0 operation, the pn junction of P-TFET was forward-biased, and the large forward diode current quickly discharged the SFG capacitor. Accordingly, the device working point moved from point *a* to *b* in Fig. 3B. During the writing-1 operation, the negative gate voltage of TFET resulted in a tunneling current around 0.7 μ A/ μ m. The tunneling current flowed from the D to charge the SFG capacitor and in turn reduced the voltage drop between D and SFG. Accordingly, the device working point moved from point *c* to *d* and 1 was written.

Because the operation mechanism was changed from Fowler-Nordheim tunneling through SiO_2 to the BTBT in the TFET for the SFG transistor, much lower voltages were needed, and the operation endurance was greatly improved as compared with that of the conventional FG-MOSFET. In fig. S6B, the device operation endurance was investigated by repeating the full operation sequences. Almost no degradation was observed for 10^{12} cycles of operation (less than 11%). The extrapolated endurance reached 10^{15} , which is far

Fig. 4. Device structure and measurements of the SFG transistor-based single-transistor image sensor. (A) Schematic view of a SFG image sensor. A photodiode is used to charge and discharge the semi-FG. (B) Measured current-voltage (*I*-*V*) characteristics of the SFG transistor under exposure to different light intensities. V_{th} decreases with the increasing light intensity. (C) Transient operation sequence and readout current of the SFG image sensor. Because of the tiny photocurrent, the exposure time is increased to 20 ms. The speed is much slower than the nanosecond-level writing-1 operation when using P-TFET for charging the semi-FG. (D) Dependence of readout D current on the light intensity. High linear dependence of the readout current on the intensity of light exposure is observed.



beyond the endurance of 10^6 for the conventional FG memory cell. Moreover, the measured disturb margin of this device met the requirements of memory array operation (fig. S7).

Compared with 6T-SRAM, the transistor number is reduced to one with the SFG memory cell, whereas the speed is comparable. As a result, the unit memory cell size and the cost of the chip can be greatly reduced. The power consumption would also be greatly reduced, because the write current is below $1\ \mu\text{A}$. For comparison, the 1T1C DRAM cell needs a write current of over $10\ \mu\text{A}$ to quickly charge and discharge the capacitor of $25\ \text{fF}$ (14).

When the pn junction between the SFG and D of a SFG transistor was exposed to light, the photogenerated carriers induced a tiny photocurrent. As indicated in the device symbol shown in Fig. 4A, the V_{th} of the SFG transistor will change accordingly when the photogenerated carriers are collected by the SFG. The SFG device can then be modified for light sensing by enlarging the area of the photodiode for better light sensitivity. Using the image-sensing SFG transistor, an imaging array was configured (fig. S8). The imaging function of the SFG transistor was evaluated by setting V_{CG} to $0\ \text{V}$ during light exposure, using photocurrent as the major writing-1 mechanism. It can be seen from Fig. 4B that a single device has different threshold voltages when it is exposed to different light intensities. The SFG transistor locally amplifies the photogenerated current to a large change in D current for each transistor, whereby the active pixel image-sensing function is realized. In Fig. 4C, the SFG transistor was operated in the image-sensing operation mode, with a sequence of “reset - exposure - read”. Dur-

ing the reset operation, the SFG was initialized to a low potential by a reset pulse of $V_{\text{CG}} = 2\ \text{V}$ and $V_{\text{D}} = -1\ \text{V}$. During the exposure stage, the pn junction between SFG and D was reverse-biased and V_{CG} was set to $0\ \text{V}$. After an exposure operation of $20\ \text{ms}$, a reading operation was executed with $V_{\text{CG}} = 1.28\ \text{V}$ and $V_{\text{D}} = 1.5\ \text{V}$. The readout D current of the reading operation is summarized in Fig. 4D. The D current at the reading operation increases linearly with the increasing light intensity from 109 to $4090\ \text{lux}$. Thus, an active pixel image sensor (APS) function was realized with a single SFG cell. For comparison, the CMOS image-sensing technology uses three MOSFETs plus a photodiode to compose a functional APS. Using the SFG cell as an APS cell, the pixel density of the image-sensing chip can be increased, and the reading operation becomes nondestructive.

As an emerging fundamental semiconductor device, the SFG transistor concept opens up possibilities for innovations for many technologies, such as DRAM, SRAM, TFET, and APS. The SFG transistor may become a fundamental semiconductor device after MOSFET (15) and FG-MOSFET (16), given its merits such as ultra-high-speed memory function and an active image-sensing function.

References and Notes

1. M. leong, B. Doris, J. Kedzierski, K. Rim, M. Yang, *Science* **306**, 2057–2060 (2004).
2. Y. Taur, *IEEE Spectr.* **36**, 25–29 (1999).
3. A. Heinrich, S. Loth, *Science* **332**, 1039–1040 (2011).
4. A. Makarov, V. Sverdlov, S. Selberherr, *Microelectron. Reliab.* **52**, 628–634 (2012).

5. J. Koga, A. Toriumi, *IEEE Electron Device Lett.* **20**, 529–531 (1999).
6. C. Aydin *et al.*, *Appl. Phys. Lett.* **84**, 1780–1782 (2004).
7. W. Hansch, C. Fink, J. Schulze, I. Eisele, *Thin Solid Films* **369**, 387–389 (2000).
8. C. Anghel, A. Hraizii, A. Gupta, A. Amara, A. Vladimirescu, *IEEE Trans. Electron. Dev.* **58**, 1649–1654 (2011).
9. A. M. Ionescu, H. Riel, *Nature* **479**, 329–337 (2011).
10. Materials and methods are available as supplementary materials on Science Online.
11. E. O. Kane, *J. Phys. Chem. Solids* **12**, 181–188 (1960).
12. P.-F. Wang *et al.*, *Solid-State Electron.* **48**, 2281–2286 (2004).
13. K.-H. Kao *et al.*, *IEEE Trans. Electron. Dev.* **59**, 2070–2077 (2012).
14. I.-G. Kim, S.-H. Park, J.-S. Yoon, D.-J. Kim, J.-Y. Noh, *et al.*, *IEDM Tech. Dig.* **13**, 319–322 (2005).
15. C. Hu, *Modern Semiconductor Devices for Integrated Circuits* (Pearson Education, Upper Saddle River, NJ, ed. 1, 2009).
16. D. Kahng, S. M. Sze, *Bell Syst. Tech. J.* **46**, 1288–1295 (1967).

Acknowledgments: This research was partially supported by the National Natural Science Foundation of China (grant no. 61176074), the National Science and Technology Major Project of China (grant no. 2009ZX02039-003), and the Key Technologies Research and Development Program of Jiangsu Province (grant no. BE2009055, SISPAK). The authors are grateful to M.-F. Li, S.-J. Ding, and A.-Q. Jiang (Fudan University) for discussions on device concepts and measurements.

Supplementary Materials

www.sciencemag.org/cgi/content/full/341/6146/640/DC1
Materials and Methods
Figs. S1 to S8
References

23 May 2013; accepted 27 June 2013
10.1126/science.1240961

Active Atmosphere-Ecosystem Exchange of the Vast Majority of Detected Volatile Organic Compounds

J.-H. Park,^{1,2*} A. H. Goldstein,^{1,3†} J. Timkovsky,² S. Fares,^{1,4} R. Weber,¹ J. Karlik,⁵ R. Holzinger²

Numerous volatile organic compounds (VOCs) exist in Earth's atmosphere, most of which originate from biogenic emissions. Despite VOCs' critical role in tropospheric chemistry, studies for evaluating their atmosphere-ecosystem exchange (emission and deposition) have been limited to a few dominant compounds owing to a lack of appropriate measurement techniques. Using a high-mass resolution proton transfer reaction–time of flight–mass spectrometer and an absolute value eddy-covariance method, we directly measured 186 organic ions with net deposition, and 494 that have bidirectional flux. This observation of active atmosphere-ecosystem exchange of the vast majority of detected VOCs poses a challenge to current emission, air quality, and global climate models, which do not account for this extremely large range of compounds. This observation also provides new insight for understanding the atmospheric VOC budget.

About 90% of atmospheric volatile organic compounds (VOCs) originate from biogenic sources (BVOCs) (1). VOCs play a critical role in tropospheric chemistry and are associated with ozone production and secondary

organic aerosol (SOA) formation, which affect human health, regional air quality, and the global climate (2–4). Once VOCs are emitted, they either undergo oxidation until they form carbon dioxide, deposition to a surface, or transformation

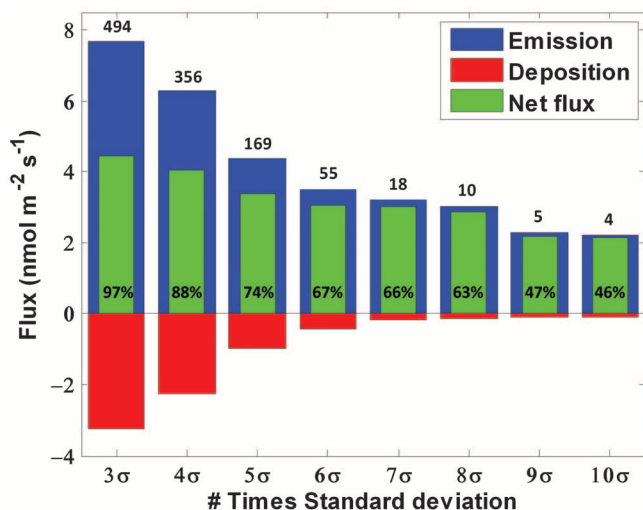
into SOAs (5). A few studies have shown that unmeasured BVOCs were responsible for O_3 chemical loss and missing OH reactivity (6–8). Previous BVOC flux field observations mainly focused on a few dominant BVOCs such as methanol, isoprene, and terpenes, and the number of compounds for which fluxes could be simultaneously measured was generally limited to 18 compounds (9). Owing to technical measurement limitations, understanding of VOC deposition remains limited, yet this loss process may dominate the removal of atmospheric VOCs (5, 10). Deposition of only a few oxygenated VOCs (OVOCs) has been previously observed in forests (11).

¹Department of Environmental Science, Policy, and Management, University of California at Berkeley, Berkeley, CA 94720, USA. ²Institute for Marine and Atmospheric Research Utrecht, Princetonplein 5, 3584 CC, Utrecht, Netherlands. ³Department of Civil and Environmental Engineering, University of California at Berkeley, Berkeley, CA 94720, USA. ⁴Consiglio per la ricerca e la sperimentazione in agricoltura—Research Center for the Soil-Plant System, Rome, Italy. ⁵University of California Cooperative Extension, Bakersfield, CA 93307, USA.

*Present address: Institute of Arctic and Alpine Research (INSTAAR), University of Colorado at Boulder, Boulder, CO 80309, USA.

†Corresponding author. E-mail: ahg@berkeley.edu

Fig. 1. Flux contribution by identified ions that had a flux exceeding S/N of three or more. Sigma (σ) indicates standard deviation of the noise. Blue, red, and green bars indicate the estimated 24-hour mean total emission, estimated 24-hour mean total deposition, and observed 24-hour mean net exchange, respectively. The number of ions in each bin is indicated above. The percentage shown in the green bars indicates the flux contribution to total net flux of 555 ions on a molar basis.



We present results of direct flux measurement over an orange grove in California's Central Valley during the summer of 2010 (12). We used a proton transfer reaction–time of flight–mass spectrometer (PTR-TOF-MS) (13, 14), collected VOC concentration data at 5 Hz, and evaluated the data using the eddy-covariance (EC) method. We calculated mixing ratios and fluxes for 555, mostly organic, ions with mass-to-charge ratios (m/z) between 31 and 1263 (hereafter referred to as “ions”), as described by Holzinger *et al.* (15). The detection of fluxes for ions that are only emitted or only deposited is straightforward, but determination of fluxes for ions that experience both emission and deposition and for which the net flux is small is more challenging. The flux detection method that we used computes the “absolute value” of covariance between measured vertical wind speed and ion-mixing ratios, effectively adding absolute value signals for emis-

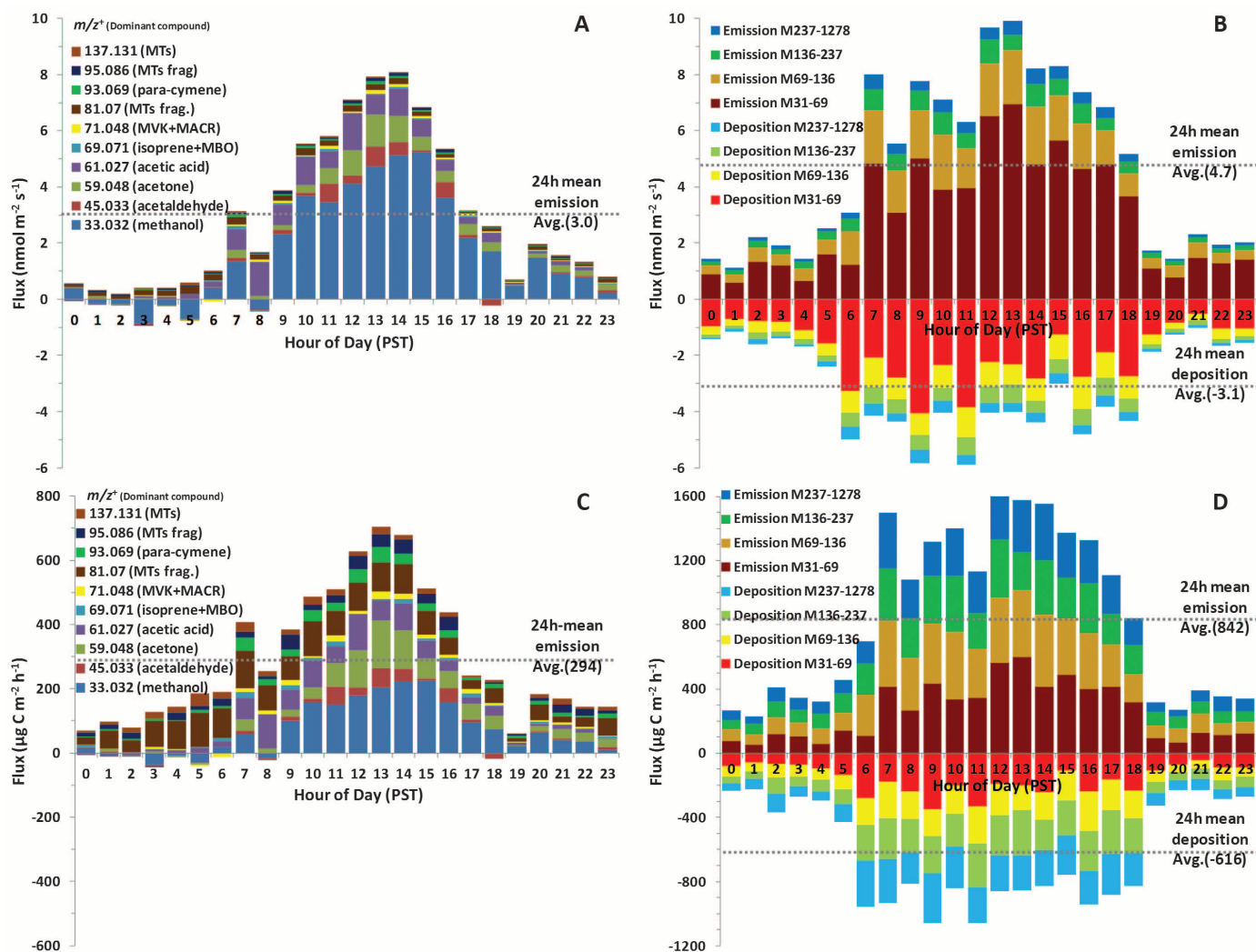


Fig. 2. BVOC diurnal emission and deposition fluxes. On a molar basis for (A) 10 major compounds, (B) four different mass ranges categorized as m/z 31-69 ($n = 61$), m/z 69-136 ($n = 141$), m/z 136-237 ($n = 141$), and m/z 237-1278 ($n = 141$), and on a carbon mass basis for (C) 10

major masses and (D) four classes. Staged bar plots of 10 masses and four classes with the largest fluxes are shown as diurnal cycles with m/z (or m/z range) indicated in the legend. The scale of the y axis in (C) is half that of (D).

sion and deposition to more easily detect when bidirectional exchange is occurring (16). Noise levels (N) were computed in the same way but with vertical wind data that were time shifted. The measured ions were categorized by their signal-to-noise ratios (S/N), and the detection limit for flux was defined as $S/N \geq 3$. Of the 555 ions analyzed, 494 ions ($\sim 89\%$) passed the $S/N = 3$ filter. Figure 1 shows the number of ions that passed this and more stringent filters ($S/N = 4$ to 10).

The net flux was calculated by EC for all ions. On a molar basis, the net flux (Fig. 1, green bars) of 494 ions contributed 97% of the total net flux of $4.43 \text{ nmol m}^{-2} \text{ s}^{-1}$ for all 555 ions observed. Deposition for ions above $S/N = 3$ was substantial, with a total magnitude of $-3.24 \text{ nmol m}^{-2} \text{ s}^{-1}$, which is 42% of the total emission of ions above $S/N = 3$, and exceeding the total emission of $3.03 \text{ nmol m}^{-2} \text{ s}^{-1}$ of the 10 ions that passed the $S/N = 8$ filter and constitute the 10 dominant BVOC fluxes measured. This result supports the idea that many unexplored VOCs exist in the atmosphere and are actively exchanged with ecosystems (5, 10).

Most BVOC flux field observations only measure the dominant VOCs that are included in our top 10 major compounds exceeding $S/N = 8$. These dominant compounds were almost exclusively emitted throughout the day, except for small deposition of a few compounds in the early morning and evening (Fig. 2A). The 24-hour mean net flux of these 10 major compounds contributed 63% to the observed total (Figs. 1 and 2A). We classified all other 484 ions above $S/N = 3$ (but below $S/N = 8$) into four groups by size, including m/z ranges of M31-69 ($n = 61$ observed), M69-136 ($n = 141$), M136-237 ($n = 141$), and M237-1278 ($n = 141$), respectively. The m/z of 237 has been previously observed in the gas phase by PTR-MS as a β -caryophyllene oxidation product (17); however, none of the other ions in the group M237-1278 has been reported before. The results for compounds in this group are uncertain because they are less volatile and sticky and are currently not well understood. Thus, further research in this m/z range is recommended. All 484 of these ions were observed to have fluxes that were bidirectional throughout the day (Fig. 2B). Both emission and deposition

fluxes were at their maxima during daytime; by contrast, the concentrations were generally lower during day and higher at night owing to buildup in the shallow nighttime boundary layer (table S2) (16). Although their 24-hour mean total net flux was an emission ($1.61 \text{ nmol m}^{-2} \text{ s}^{-1}$) and smaller than the total net emission of the summed 10 major compounds ($2.82 \text{ nmol m}^{-2} \text{ s}^{-1}$) described above, their 24-hour mean estimated emission was ~ 1.6 times as large as that of the 10 major compounds. Their 24-hour mean estimated deposition was of similar magnitude to the net emission of the 10 major compounds (Fig. 2, A and B, and table S1) (16). A 24-hour mean net deposition occurred for 186 ions, but no single ions accounted for more than 1.6% of the total estimated deposition on a molar basis.

We did not find any ions depositing uniformly throughout the day. More ions with net deposition were observed in the higher m/z group (Fig. 3 and table S1) (16), suggesting that heavier (presumably lower vapor pressure) molecules deposit more efficiently. For the 186 ions observed to have net deposition, the exchange velocity (or deposition velocity) was calculated

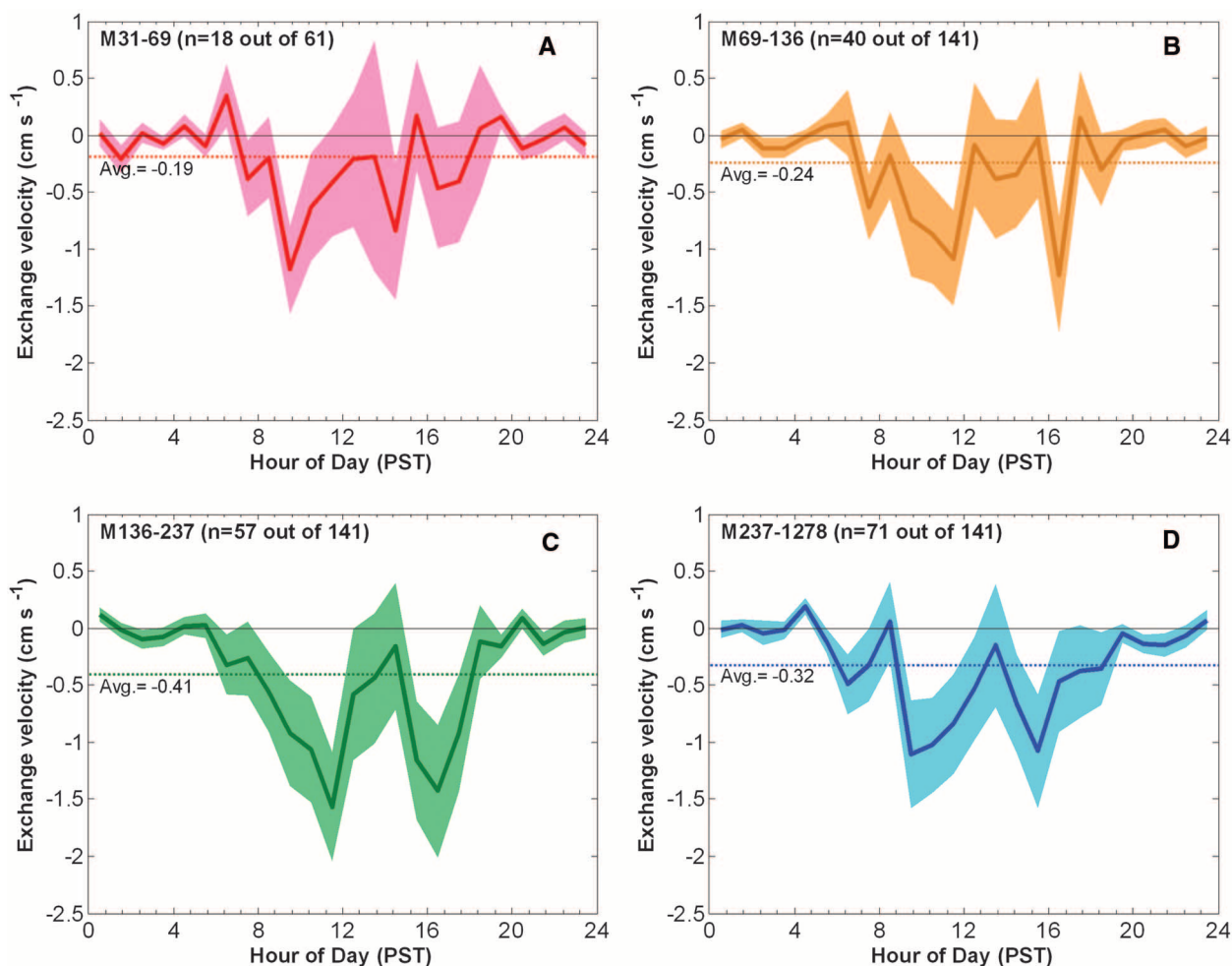


Fig. 3. Mean diurnal cycle of exchange velocity for depositing species in m/z categories. Range 31-69 (A), 69-136 (B), 136-237 (C), and 237-1278 (D). Dotted lines indicate the 24-hour mean exchange velocity for each group; the shaded area indicates SEM.

according to V_{ex} = flux/ambient concentration, and the diurnal trends were examined (16). On the basis of this analysis, a 24-hour mean V_{ex} in M136-237 of -0.41 cm s^{-1} was the fastest deposition rate, and the maximum hourly deposition was between -1 and -1.5 cm s^{-1} for all groups. During daytime, two V_{ex} minima usually appeared, first in the morning hours from 09:00 to 12:00 PST and second in the afternoon hours from 14:00 to 17:00 PST. Surprisingly, slower V_{ex} in the hours from 12:00 to 15:00 was observed for all groups (Fig. 3). This implies that direct emission from the ecosystem and/or within-canopy photochemical production reduces the net deposition when both temperature and sunlight intensity are at a maximum. Recently, Karl *et al.* (11) observed deposition of methyl vinyl ketone (MVK) and methacrolein (MACR) and a few other OVOCs, including acetaldehyde, to deciduous forests, but those accounted for only a small fraction of what we observed as deposition. In contrast to Karl *et al.*'s results, we observed MVK and MACR to have bidirectional flux that resulted in net emission. For these compounds, we unambiguously observed emissions during daytime, with small deposition in the early morning, and found excellent agreement with vertical gradient observations performed simultaneously at the site using a separate instrument (fig. S2) (16). The exchange velocity range we observed for the 186 depositing ions (Fig. 3) was generally lower or at the low end of the values reported above deciduous forests (11).

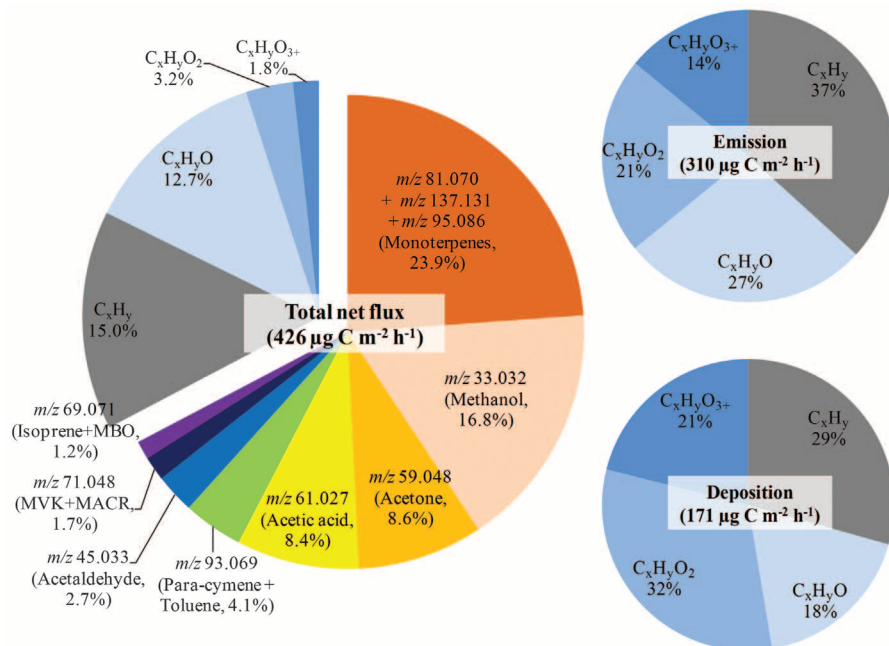
In contrast to our molar-basis analysis above, when considering carbon mass flux, the heavier ions observed are generally more important. We estimated carbon mass fluxes for each group by conservatively assuming 2, 5, 10, and 15 carbon atoms on average for ions in the groups M31-69,

M69-136, M136-237, and M237-1278, respectively. Our estimated carbon emission from the sum of all 484 observed ions ($842 \mu\text{g C m}^{-2} \text{ hour}^{-1}$) is 2.8 times as large as the sum of the 10 major compounds ($294 \mu\text{g C m}^{-2} \text{ hour}^{-1}$), and the estimated carbon deposition was twice as large (Fig. 2, C and D) as the net emission of the 10 major compounds, suggesting that carbon mass flux of these 484 ions is even more substantial on a carbon mass basis than on a molar basis. This estimate is conservative and likely an underestimate because more carbons may be expected in each class than the carbon numbers we assumed, and another fraction of carbon is not accounted for owing to fragmentation in the PTR-TOF-MS (16). The estimated total emission of the M31-69 group was the largest, and estimated total emissions decreased as the m/z group number increased. The deposition was almost equivalent among the four groups except for M69-136, for which the deposition was slightly lower (Fig. 2D and table S1) (16).

We used the high-mass resolution molecular weight observations to identify chemical formulas for 162 observed hydrocarbons and oxidized hydrocarbons by selecting the ions exceeding $S/N = 3$, smaller than m/z 237, and consisting of only carbon (C), hydrogen (H), and oxygen (O) atoms within a mass range tolerance of $\pm 3 \text{ mD}$ (table S2) (16). The 24-hour mean total net flux for these 162 identified ions contributed 77% to the total on a molar basis. Using the molecular formula from 152 ions identified (excluding 10 dominant ions), we calculated carbon mass fluxes and summarized them in groups of pure hydrocarbons (C_xH_y) and oxygenated hydrocarbons containing one, two, and three or more oxygen atoms (i.e., $\text{C}_x\text{H}_y\text{O}$, $\text{C}_x\text{H}_y\text{O}_2$, $\text{C}_x\text{H}_y\text{O}_3$). A 24-hour mean net emission flux of $426 \mu\text{g C m}^{-2} \text{ hour}^{-1}$ was estimated, and the total net flux of 152 ions accounted for about one-third of the total (Fig. 4, left pie chart). Pure hydrocarbons (C_xH_y ; $n = 40$) constituted 15% of the total carbon flux of these 162 ions, and ions containing one to three or more oxygens ($\text{C}_x\text{H}_y\text{O}$: $n = 30$; $\text{C}_x\text{H}_y\text{O}_2$: $n = 44$; and $\text{C}_x\text{H}_y\text{O}_3$: $n = 38$) contributed 12.7, 3.2, and 1.8%, respectively. Although the summed flux of these 152 ions was a net emission of $139 \mu\text{g C m}^{-2} \text{ hour}^{-1}$, it is instructive to look separately at the contributions of oxygenated hydrocarbons and pure hydrocarbons to the estimated total emissions and depositions. For estimated total emission in each category, oxygenated hydrocarbons were dominant, but pure hydrocarbon (C_xH_y) emission was individually the largest, followed by $\text{C}_x\text{H}_y\text{O}$, $\text{C}_x\text{H}_y\text{O}_2$, and $\text{C}_x\text{H}_y\text{O}_3$, indicating that the vast array of unknown VOCs were either photochemically produced below the measurement height or directly emitted from the ecosystem, and were larger than the emission of the 10 dominant and commonly measured compounds. Thus, this fuller range of compounds provides an extremely important contribution to the total observed emissions (Fig. 4). Moreover, we also estimated greater deposition fluxes for oxygenated hydrocarbons (71%) than for pure hydrocarbons (29%), and $\text{C}_x\text{H}_y\text{O}_2$ deposition exceeded C_xH_y deposition (Fig. 4). This result is consistent with the idea that less-oxygenated VOCs are emitted from the ecosystem, whereas secondary compounds produced through atmospheric photochemical process and containing more oxygen atoms are preferentially removed by dry deposition.

Our results show that the mass balance of VOCs in the orange orchard ecosystem is highly incomplete when considering only emission and deposition of commonly measured dominant

Fig. 4. Flux contribution by chemical composition. Individual VOC and VOC-group contribution to the total flux for ions to which an empirical formula has been attributed (162 ions) are shown in pie chart on the left. The 10 major masses were specifically identified, and the remaining 152 m/z ratios were categorized by number of oxygens in the molecule as C_xH_y , $\text{C}_x\text{H}_y\text{O}$, $\text{C}_x\text{H}_y\text{O}_2$, and $\text{C}_x\text{H}_y\text{O}_3$. The two pie charts on the right show the contribution of categorized ions to the estimated emission (top) and deposition (bottom). MBO, 2-methyl-3-butene-2-ol.



BVOCs. The contribution from hundreds of individually minor compounds is important. Future research is required to determine if this is also true for ecosystems that emit larger quantities of isoprene and/or monoterpenes.

The minor species with lower fluxes and concentrations are not in current BVOC emission models, but their sizes, chemical formulae, and sum suggest that they should be important for SOA formation and regional photochemistry. Their presence in the atmosphere may also account for a sizable amount of the missing OH chemical reactivity and O₃ chemical loss observed in plant environments.

References and Notes

1. A. Guenther *et al.*, *J. Geophys. Res. Atmos.* **100**, 8873 (1995).
2. W. L. Chameides, R. W. Lindsay, J. Richardson, C. S. Kiang, *Science* **241**, 1473–1475 (1988).

3. M. O. Andreae, P. J. Crutzen, *Science* **276**, 1052–1058 (1997).
4. M. S. Jang, N. M. Czoschke, S. Lee, R. M. Kamens, *Science* **298**, 814–817 (2002).
5. A. H. Goldstein, I. E. Galbally, *Environ. Sci. Technol.* **41**, 1514–1521 (2007).
6. M. R. Kurpius, A. H. Goldstein, *Geophys. Res. Lett.* **30**, 1371 (2003).
7. P. Di Carlo *et al.*, *Science* **304**, 722–725 (2004).
8. R. Holzinger, A. Lee, K. T. Paw, A. H. Goldstein, *Atmos. Chem. Phys.* **5**, 67–75 (2005).
9. T. M. Ruuskanen *et al.*, *Atmos. Chem. Phys.* **11**, 611–625 (2011).
10. M. Hallquist *et al.*, *Atmos. Chem. Phys.* **9**, 5155–5236 (2009).
11. T. Karl *et al.*, *Science* **330**, 816–819 (2010).
12. J.-H. Park *et al.*, *Atmos. Chem. Phys.* **13**, 1439–1456 (2013).
13. A. Jordan *et al.*, *Int. J. Mass Spectrom.* **286**, 122–128 (2009).
14. M. Graus, M. Müller, A. Hansel, *J. Am. Soc. Mass Spectrom.* **21**, 1037–1044 (2010).
15. R. Holzinger, A. Kasper-Giebl, M. Staudinger, G. Schauer, T. Rockmann, *Atmos. Chem. Phys.* **10**, 10111–10128 (2010).

16. See supplementary materials on Science Online.
17. A. Lee *et al.*, *J. Geophys. Res. Atmos.* **111**, 21 (2006).

Acknowledgments: This work was supported by the Netherlands Organization for Scientific Research (NWO) under the ALW-Middelgroot program (grant 834.08.002), the California Air Resources Board (Award 06-329), the Citrus Research Board, and the University of Utrecht short stay fellowship program. We thank the Gorden Ranch for hosting this study and for the assistance provided by the University of California Lindcove Research and Extension station.

Supplementary Materials

www.sciencemag.org/cgi/content/full/341/6146/643/DC1
Materials and Methods
Figs. S1 to S4
Tables S1 to S3
References (18–28)

11 January 2013; accepted 2 July 2013
10.1126/science.1235053

Social Influence Bias: A Randomized Experiment

Lev Muchnik,¹ Sinan Aral,^{2*} Sean J. Taylor³

Our society is increasingly relying on the digitized, aggregated opinions of others to make decisions. We therefore designed and analyzed a large-scale randomized experiment on a social news aggregation Web site to investigate whether knowledge of such aggregates distorts decision-making. Prior ratings created significant bias in individual rating behavior, and positive and negative social influences created asymmetric herding effects. Whereas negative social influence inspired users to correct manipulated ratings, positive social influence increased the likelihood of positive ratings by 32% and created accumulating positive herding that increased final ratings by 25% on average. This positive herding was topic-dependent and affected by whether individuals were viewing the opinions of friends or enemies. A mixture of changing opinion and greater turnout under both manipulations together with a natural tendency to up-vote on the site combined to create the herding effects. Such findings will help interpret collective judgment accurately and avoid social influence bias in collective intelligence in the future.

We rely on ratings contributed by others to make decisions about which hotels, books, movies, political candidates, news, comments, and stories are worth our time and money (1). Given the widespread use and economic value of rating systems (2–4), it is important to consider whether they can successfully harness the wisdom of crowds to accurately aggregate individual information. Do they produce useful, unbiased, aggregate information about the quality of the item being rated? Or, as suggested by the experiments of Salganik *et al.* (5), are outcomes path dependent, yielding different aggregate ratings for items of equivalent quality?

Collective intelligence has recently been heralded as a harbinger of accelerated human potential (6). But, social influence on individuals' perceptions of quality and value could create herding effects that lead to suboptimal market outcomes (7, 8); rich-get-richer dynamics that exaggerate inequality (9–12); a group think mentality that distorts the truth (13); and measurable disruptions in the wisdom of crowds (14). If perceptions of quality are biased by social influence, attempts to aggregate collective judgment and socialize choice could be easily manipulated, with dramatic consequences for our markets, our politics, and our health.

The recent availability of population-scale data sets on rating behavior and social communication enable novel investigations of social influence (1, 15–20). Unfortunately, our understanding of the impact of social influence on collective judgment is limited because empirically distinguishing influence from uninfluenced agree-

ment on true quality is nearly impossible in observational data (21–27). For example, popular products may be popular because of the irrational effect of past positive ratings, or alternatively, the best products may become popular because they are of the highest quality. We must distinguish these explanations to determine the extent to which social influence creates irrational herding.

We therefore designed and analyzed a large-scale randomized experiment to quantify the effects of social influence on users' ratings and discourse on a social news aggregation Web site, where users contribute news articles and discuss them. Users of the site that we studied write comments in response to posted articles, and other users can then “up-vote” or “down-vote” these comments, yielding an aggregate current rating for each posted comment equal to the number of up-votes minus the number of down-votes. Users do not observe the comment scores before clicking through to comments—each impression of a comment is always accompanied by that comment's current score, tying the comment to the score during users' evaluation—and comments are not ordered by their popularity, mitigating selection bias on high (or low) rated comments. Similar scoring mechanisms are widely used on the Web to reward users for supplying insightful or interesting analysis, while penalizing those posting irrelevant, redundant, or low-quality comments. The vast majority of interuser relations occur on the Web site, in contrast to Web sites whose members also interact offline. The data therefore provide a unique opportunity to comprehensively study social influence bias in rating behavior.

Over 5 months, 101,281 comments submitted on the site were randomly assigned to one of three treatment groups: up-treated, down-treated, or control. Up-treated comments were artificially given an up-vote (a +1 rating) upon the comment's creation, whereas down-treated comments were given a down-vote (a –1 rating) upon the comment's creation. Users were unaware of the

¹School of Business Administration, The Hebrew University of Jerusalem, Mount Scopus, Jerusalem, 91905 Israel. ²MIT Sloan School of Management, 100 Main Street, Cambridge, MA 02142, USA. ³NYU Stern School of Business, 44 West 4th Street, New York, NY 10012, USA.

*Corresponding author. E-mail: sinana@mit.edu

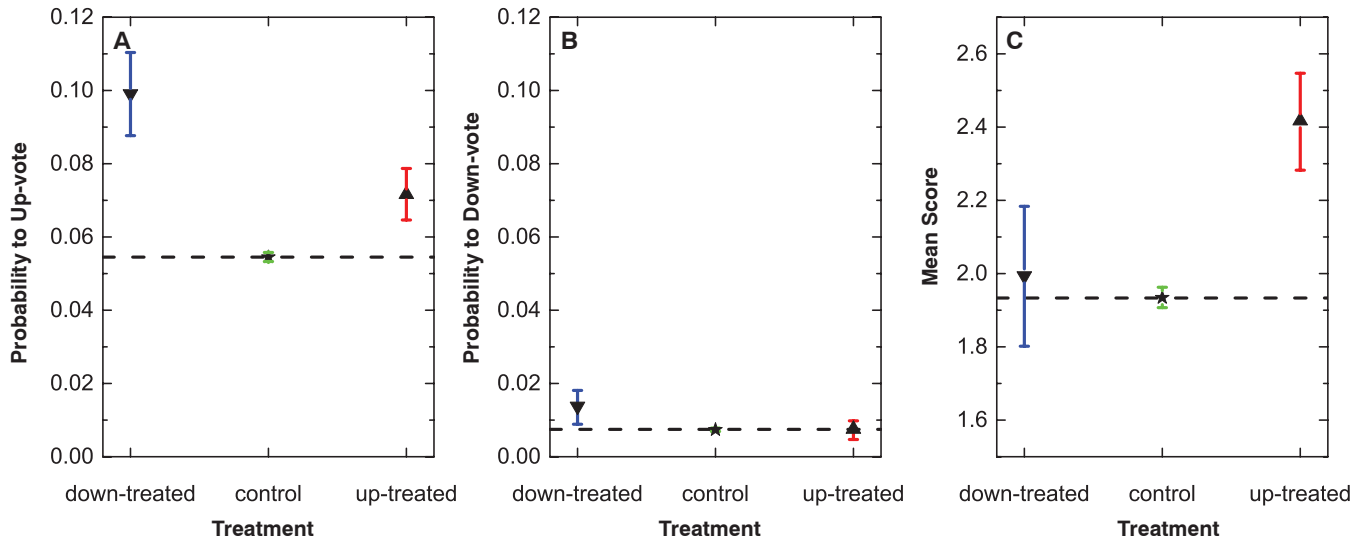


Fig. 1. Effect of manipulation on voting behavior. The positively manipulated treatment group (up-treated), the negatively manipulated treatment group (down-treated), and the control group (dotted line) are shown. The probabilities to up-vote (A) and down-vote (B) positively manipulated, negatively manipulated, and control group comments are shown by the first unique viewer; 95% confidence intervals are inferred from Bayesian logistic regression with commenter, rater, and commenter-

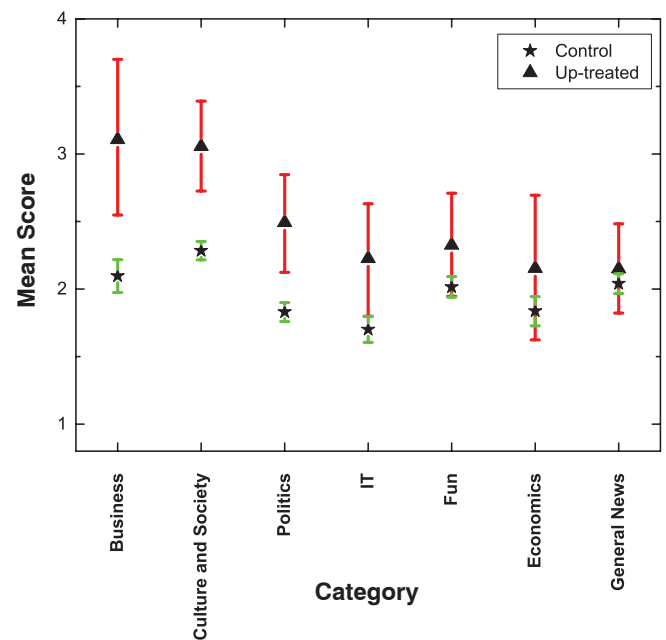
rater random effects. (C) The mean final scores of positively manipulated, negatively manipulated, and control group comments are shown with 95% confidence intervals inferred from Bayesian linear regression of the final comment score with commenter random effects. Final mean scores on this Web site are measured as the number of up-votes minus the number of down-votes. We discuss the implications of this measurement in greater detail in the supplementary materials.

manipulation and unable to trace votes to any particular user. As a result of the randomization, comments in the control and treatment groups were identical in expectation along all dimensions that could affect users' rating behavior except for the current rating. This manipulation created a small random signal of positive or negative judgment by prior raters for randomly selected comments that have the same quality in expectation, enabling estimates of the effects of social influence holding comment quality and all other factors constant. The 101,281 experimental comments (of which 4049 were positively treated and 1942 were negatively treated to reflect the natural proportions of up- and down-votes on the site) were viewed more than 10 million times and rated 308,515 times by subsequent users.

We may sample users multiple times, and nonrandom heterogeneity may exist in users' comment-generating process, their selection of comments to vote on, and in relationships between commenters and raters. We therefore estimated hierarchical Bayesian models of voting behavior and specified commenter, rater, and commenter-rater pair random effects; i.e., the confidence intervals are based on repeated resampling, creating a distribution of parameter estimates from which the 95% confidence bands are derived (see materials and methods in the supplementary materials).

We first compared the probabilities that comments in each group would be up-voted or down-voted by the first viewer after the manipulation. These probabilities measure the immediate effect of current ratings on users' rating behavior. We then analyzed comments' long-run ratings distributions and final mean scores by aggregating

Fig. 2. Effects of topic on herding. Mean final scores of positively manipulated and control group comments are shown with 95% confidence intervals inferred from Bayesian linear regression of the final comment score with commenter random effects across the seven most active topic categories on the site, ordered by the magnitude of the difference between the mean final score of positively manipulated comments and the mean final score of control comments in each category.



all users' ratings for comments in the three groups over time.

Figure 1A shows the immediate up-vote and down-vote probabilities for the first viewer of comments in each of the three categories. Up-votes were 4.6 times as common as down-votes on this site, with 5.13% of all comments receiving an up-vote by the first viewer of the comment and only 0.82% of comments receiving a down-vote by the first viewer. The up-vote treatment significantly increased the probability of up-voting by the first viewer by 32% over

the control group ($P = 1.0 \times 10^{-6}$) (Fig. 1A). Up-treated comments were not down-voted significantly more or less frequently than the control group, so users did not tend to correct the upward manipulation. In the absence of a correction, positive herding accumulated over time.

The positive manipulation created a positive social influence bias that persisted over our 5-month observation window, generating accumulating herding effects that increased comments' final mean ratings by 25% relative to the final mean ratings of control group comments (χ^2 test;

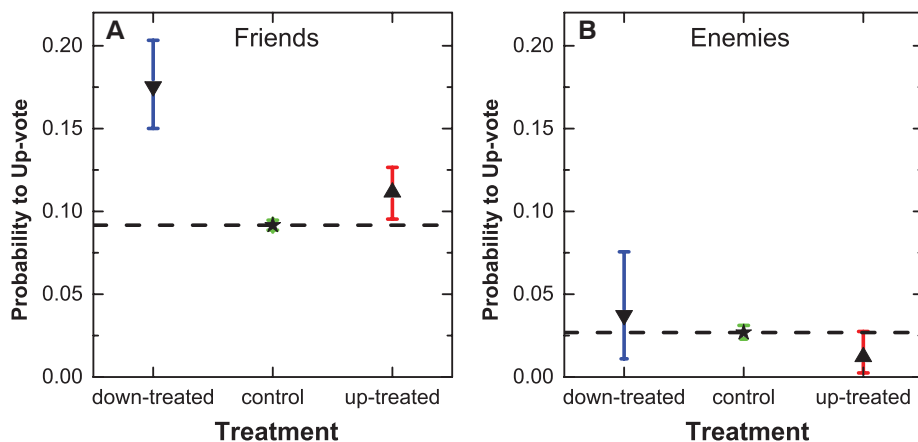


Fig. 3. Effects of friendship on rating behavior. The figure shows the probability of a friend (A) and enemy (B) of the commenter to up-vote positively manipulated, negatively manipulated, and control group comments. Friends and enemies are defined as users who had previously clicked a button on the Web site labeling the commenter as someone they “liked” or “disliked,” respectively.

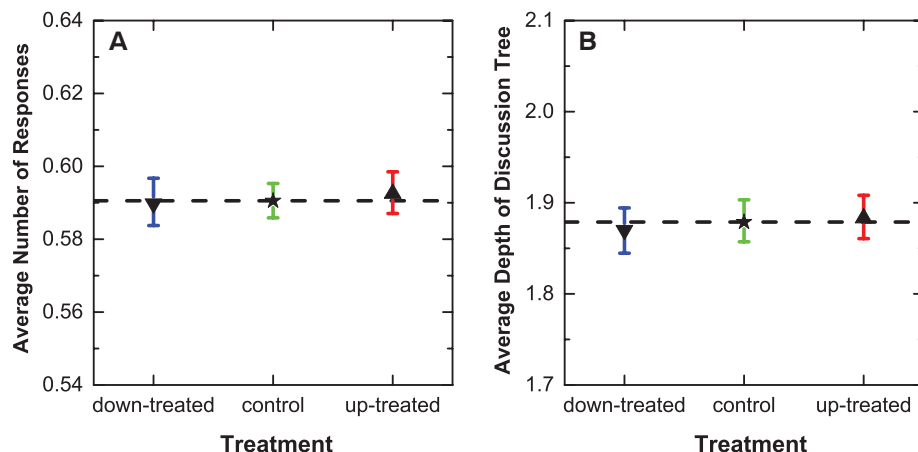


Fig. 4. Effects on subsequent discourse. The figure displays the average number of responses (A) and the average depth of the discussion tree (B) that developed in response to positively manipulated, negatively manipulated, and control group comments; 95% confidence intervals are inferred from Bayesian linear regressions with author random effects.

$P = 2.3 \times 10^{-11}$) (Fig. 1C), and Kolmogorov-Smirnov (K-S) tests showed that the final score distribution of up-treated comments was significantly shifted toward higher scores (K-S test statistic: 0.083; $P = 1.2 \times 10^{-23}$). Comments in the up-treated group were also significantly more likely than those in the control group to accumulate exceptionally high scores. Up-treated comments were 30% more likely to reach or exceed a score of 10 (6.4% versus 4.9% in the control group, χ^2 test; $P = 2.0 \times 10^{-5}$). The small manipulation of a single random up-vote when the comment was created resulted in significantly higher accumulated ratings due to social influence.

Positive and negative social influence created asymmetric herding effects. The probability of down-treated comments receiving subsequent down-votes was 0.014, whereas the probability of control comments receiving a down-vote was 0.007; a significant difference (χ^2 test; $P = 1.1 \times$

10^{-3}) (Fig. 1B). However, this effect was offset by a larger correction effect. The probability that a down-treated comment would subsequently be up-voted was 0.099, whereas the probability that a control comment would be up-voted was significantly different at 0.054 (χ^2 test; $P = 1.0 \times 10^{-30}$) (Fig. 1A). This correction neutralized social influence in the ratings of negatively manipulated comments, and their final mean ratings were not statistically different from the control group’s final mean ratings (Fig. 1C).

We next estimated changes in the final mean score for up-treated comments compared to control comments in the seven most active topic categories on the Web site. We found significant positive herding effects for comment ratings in “politics,” “culture and society,” and “business,” but no detectable herding behavior for comments in “economics,” “IT,” “fun,” and “general news” (Fig. 2). These differences are not due to the frequency of commenting in these categories, as

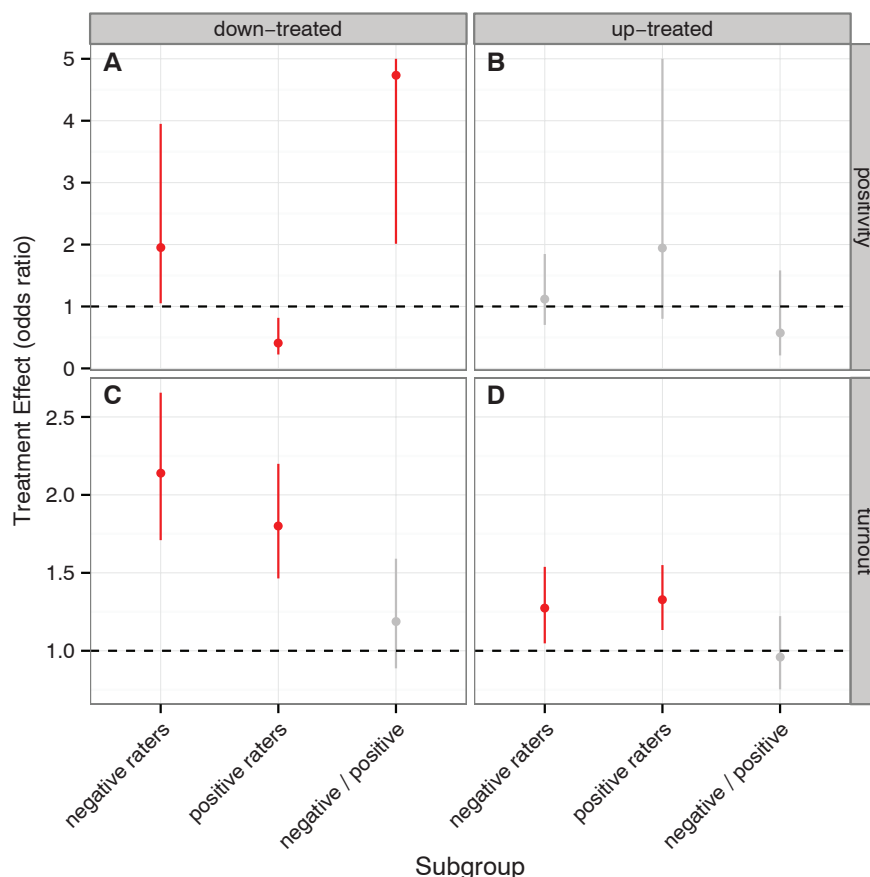
categories with significant differences in control and treatment ratings and those with no significant differences had similar levels of activity. There was no significant negative herding in any category.

Friendship also moderated the impact of social influence on rating behavior (Fig. 3, A and B). The Web site has a feature whereby users can indicate that they “like” or “dislike” other users, forming “friends” and “enemies” social preference graphs. Unsurprisingly, friends of the commenter were more likely to up-vote a comment than those who disliked him or her (9.2% versus 2.7%, χ^2 test; $P = 2.7 \times 10^{-49}$) [compare the average (dotted line) in Fig. 3A to the average (dotted line) in Fig. 3B]. Friends also tended to herd on current positive ratings (friends’ probability to up-vote a positively manipulated comment: 0.122 versus friends’ probability to up-vote a control comment: 0.092; χ^2 test; $P = 1.4 \times 10^{-2}$) and to correct comments with negatively manipulated ratings (friends’ probability to up-vote a negatively manipulated comment: 0.176 versus friends’ probability to up-vote a control comment: 0.092; χ^2 test; $P = 4.0 \times 10^{-12}$) (Fig. 3A), mirroring the cooperation found in human social networks (28). By contrast, enemies of the commenter were not susceptible to social influence. Enemies’ ratings were unaffected by our treatments, possibly because of the small sample of potential first ratings by enemies (though there are a substantial number of enemies in the community, they are less active) (Fig. 3B).

Finally, social influence in ratings behavior did not affect discourse in our setting during the 5-month observation period. Neither the positive nor the negative manipulation affected the average number of replies (Fig. 4A) or the average depth of the discussion tree created in response to a comment (Fig. 4B).

Several data-generating processes could explain our findings. A selection effect could inspire different populations of voters to turn out to rate the item (selective turnout)—for example, if the negative manipulation inspired voters who tend to down-vote (negative voters) to vote in higher proportion. Alternatively, prior ratings could bias users’ voting behavior by changing their opinions about comment quality and therefore their votes (opinion change). We analyzed changes in turnout (the likelihood of rating rather than just viewing comments) and changes in positivity (the proportion of positive ratings) across subgroups in our study population to identify variance in our results explained by turnout effects and opinion change, respectively. We divided raters and commenters, on the basis of their rating history, along four subgroup dimensions by their positivity (proportion of positive votes), the commenters’ quality (prior scores of their comments), the frequency with which a rater rated a particular commenter, and whether raters were friends or enemies with commenters. We then compared treatment effects with expected voting behavior in these subgroups. Our analysis revealed several

Fig. 5. Effects on turnout versus positivity. The figure displays treatment effects of the negative and positive manipulation on turnout (the likelihood of rating) and positivity (the proportion of positive votes) for negative (positive) raters, defined as active raters (with at least 100 votes on control comments) who display less than (greater than) the median proportion of positive votes on control comments. Results displayed in red are statistically significant at the 95% level, whereas results displayed in gray are not. (A) Treatment effect of the negative manipulation on positivity; (B) treatment effect of the positive manipulation on positivity; (C) treatment effect of the negative manipulation on turnout; and (D) treatment effect of the positive manipulation on turnout. In each panel, the first estimate is the treatment effect on negative raters, the second estimate is the treatment effect on positive raters, and the third estimate is the ratio of the treatment effects on negative/positive raters. The treatment effects displayed are odds ratios of the treatment effect on the treated compared to the control for negative and positive raters. The negative manipulation created countervailing opinion change for positive and negative raters, increasing the positivity of negative raters and decreasing the positivity of positive raters, whereas both treatments increased turnout uniformly across both subgroups.



behavioral mechanisms that together explain the experimental results (see “Estimating Behavioral Mechanisms” in the supplementary text).

First, both treatments increased turnout (by 82 and 28% for first viewers of down- and up-treated comments, respectively), but neither created differential turnout for different types of voters. This suggests that selection, or differential turnout by voter type (e.g., selecting different proportions of positive or negative voters, or frequent or infrequent voters), cannot explain our results. Second, we found statistically significant opinion change in two of the four subgroup dimensions. The positive treatment created a systematic increase in the proportion of positive ratings for raters with little prior experience rating the particular commenter whose comment was manipulated (a 7% increase in the ratio of positive to negative votes and a 50% increase in the probability of up-votes for these raters) and no decrease in positivity in any subgroup. This implies that positive opinion change explains part of the variation in positive herding. The negative treatment, by contrast, created countervailing opinion change for positive and negative raters, cancelling out any aggregate-level evidence of opinion change (Fig. 5). This in part explains why we find no aggregate trend in either direction for the negative treatment. Third, both treatments created a uniform increase in turnout across voter types. This overall increase in turnout, com-

bined with a general preference for positivity on the site, created a tendency toward positive ratings under both treatments. Prior work has shown a preference for positivity in ratings in other contexts (1), which suggests that these results will generalize. Together, these findings suggest that a mixture of changing opinion and the natural tendency to up-vote together with greater turnout under both manipulations, combine to create the herding effects we see (see “Estimating Behavioral Mechanisms” in the supplementary text).

Our results demonstrate that whereas positive social influence accumulates, creating a tendency toward ratings bubbles, negative social influence is neutralized by crowd correction (29). Our findings suggest that social influence substantially biases rating dynamics in systems designed to harness collective intelligence. Future research that further explores the mechanisms driving individual and aggregate ratings—especially in in vivo social environments—will be essential to our ability to interpret collective judgment accurately and to avoid social influence bias in collective intelligence. We anticipate that our experiment will inspire more sophisticated analyses of social influence bias in electoral polling, stock market prediction, and product recommendation and that these results will be used to adapt rating and review technologies to account for social influence bias in their outputs.

References and Notes

1. J. A. Chevalier, D. Mayzlin, *J. Mark. Res.* **43**, 345–354 (2006).
2. D. G. Pope, *J. Health Econ.* **28**, 1154–1165 (2009).
3. C. Dellarocas, *Manage. Sci.* **49**, 1407–1424 (2003).
4. L. Cabral, A. Hortacsu, “The dynamics of seller reputation: Theory and evidence from eBay.” National Bureau of Economic Research, working paper w10363 (2004).
5. M. J. Salganik, P. S. Dodds, D. J. Watts, *Science* **311**, 854–856 (2006).
6. A. W. Woolley, C. F. Chabris, A. Pentland, N. Hashmi, T. W. Malone, *Science* **330**, 686–688 (2010).
7. S. Bikhchandani, D. Hirshleifer, I. Welch, *J. Polit. Econ.* **100**, 992 (1992).
8. D. Hirshleifer, in *The New Economics of Human Behaviour*, M. Tommasi, K. Ierulli, Eds. (Cambridge Univ. Press, Cambridge, UK, 1995), pp. 188–215.
9. R. K. Merton, *Social Theory and Social Structure* (Free Press, New York, 1968).
10. H. A. Simon, *Biometrika* **42**, 425 (1955).
11. A.-L. Barabási, R. Albert, *Science* **286**, 509–512 (1999).
12. J.-P. Onnela, F. Reed-Tsochas, *Proc. Natl. Acad. Sci. U.S.A.* **107**, 18375–18380 (2010).
13. I. L. Janis, *Groupthink: Psychological Studies of Policy Decisions and Fiascoes* (Cengage Learning, Boston, MA, ed. 2, 1982).
14. J. Lorenz, H. Rauhut, F. Schweitzer, D. Helbing, *Proc. Natl. Acad. Sci. U.S.A.* **108**, 9020–9025 (2011).
15. C. Danescu-Niculescu-Mizil, G. Kossinets, J. Kleinberg, L. Lee, How opinions are received by online communities: A case study on amazon.com helpfulness votes, in *Proceedings of the 18th International Conference on World Wide Web* (Association for Computing Machinery, New York, 2009), pp. 141–150.

16. C. A. Hidalgo, R. A. Castro, C. Rodriguez-Sickert, *New J. Phys.* **8**, 52 (2006).
17. E. Bakshy, B. Karrer, L. A. Adamic, Social influence and the diffusion of user created content, in *Proceedings of the 10th ACM Conference on Electronic Commerce* (Association for Computing Machinery, New York, 2009), pp. 325–334.
18. J. Leskovec, A. Singh, J. Kleinberg, Patterns of influence in a recommendation network, in *Advances in Knowledge Discovery and Data Mining, Lecture Notes in Computer Science* (Springer, Berlin, Heidelberg, 2006), vol. 3918, pp. 380–389.
19. F. Wu, B. A. Huberman, *Internet and Network Economics* **5385**, 334–341 (2008).
20. N. Archak, A. Ghose, P. G. Ipeirotis, *Manage. Sci.* **57**, 1485–1509 (2011).
21. C. F. Manski, *Rev. Econ. Stud.* **60**, 531–542 (1993).
22. S. Aral, L. Muchnik, A. Sundararajan, *Proc. Natl. Acad. Sci. U.S.A.* **106**, 21544–21549 (2009).
23. S. Aral, *Mark. Sci.* **30**, 217–223 (2011).
24. S. Aral, D. Walker, *IEEE Intell. Syst.* **26**, 91–96 (2011).
25. S. Aral, D. Walker, *Manage. Sci.* **57**, 1623–1639 (2011).
26. S. Aral, D. Walker, *Science* **337**, 337–341 (2012).
27. C. R. Shalizi, A. C. Thomas, *Sociol. Methods Res.* **40**, 211–239 (2011).
28. C. L. Apicella, F. W. Marlowe, J. H. Fowler, N. A. Christakis, *Nature* **481**, 497–501 (2012).
29. D. Centola, R. Willer, M. Macy, *Am. J. Sociol.* **110**, 1009–1040 (2005).

Acknowledgments: We thank D. Eckles and D. Watts for invaluable discussions. This work was supported by a Microsoft Research faculty fellowship (S.A.) and by NSF Career Award 0953832 (S.A.). The research was approved by the New York University institutional review board. There are legal obstacles to making the data available and revealing the name of the Web site, but code is available upon request. All of the user

data that we analyzed is publicly available, except the treatment assignment and the random identifier that links a deidentified user to a vote, and therefore does not contain any other information that cannot be obtained by crawling the Web site. The randomized testing that the Web site performed is covered by the Web site's terms of service. Opt-in permissions were granted by the users when they registered for the Web site. No data on nonregistered users was collected.

Supplementary Materials

www.sciencemag.org/cgi/content/full/341/6146/647/DC1
Materials and Methods
Supplementary Text
Tables S1 to S21
Figs. S1 to S16
References (30–57)

14 May 2013; accepted 16 July 2013
10.1126/science.1240466

Pluripotent Stem Cells Induced from Mouse Somatic Cells by Small-Molecule Compounds

Pingping Hou,^{1*} Yanqin Li,^{1*} Xu Zhang,^{1,2*} Chun Liu,^{1,2*} Jingyang Guan,^{1*} Honggang Li,^{1*} Ting Zhao,^{1†} Junqing Ye,^{1,2†} Weifeng Yang,^{3†} Kang Liu,^{1†} Jian Ge,^{1,2†} Jun Xu,^{1†} Qiang Zhang,^{1,2†} Yang Zhao,^{1†} Hongkui Deng^{1,2†}

Pluripotent stem cells can be induced from somatic cells, providing an unlimited cell resource, with potential for studying disease and use in regenerative medicine. However, genetic manipulation and technically challenging strategies such as nuclear transfer used in reprogramming limit their clinical applications. Here, we show that pluripotent stem cells can be generated from mouse somatic cells at a frequency up to 0.2% using a combination of seven small-molecule compounds. The chemically induced pluripotent stem cells resemble embryonic stem cells in terms of their gene expression profiles, epigenetic status, and potential for differentiation and germline transmission. By using small molecules, exogenous “master genes” are dispensable for cell fate reprogramming. This chemical reprogramming strategy has potential use in generating functional desirable cell types for clinical applications.

Pluripotent stem cells, such as embryonic stem cells (ESCs), can self-renew and differentiate into all somatic cell types. Somatic cells can be reprogrammed to become pluripotent via nuclear transfer into oocytes or through the ectopic expression of defined factors (1–4). However, exogenous pluripotency-associated factors, especially *Oct4*, are indispensable for establishing pluripotency (5–7), and previous reprogramming strategies have raised concerns regarding the clinical applications (8, 9). Small molecules have advantages because they can be cell permeable, nonimmunogenic, more cost-effective, and more easily synthesized, preserved, and standard-

ized. Moreover, their effects on inhibiting and activating the function of specific proteins are often reversible and can be finely tuned by varying the concentrations. Here, we identified small-molecule combinations that were able to drive the reprogramming of mouse somatic cells toward pluripotent cells.

To identify small molecules that facilitate cell reprogramming, we searched for small molecules that enable reprogramming in the absence of *Oct4* using *Oct4* promoter-driven green fluorescent protein (GFP) expression (OG) mouse embryonic fibroblasts (MEFs), with viral expression of *Sox2*, *Klf4*, and *c-Myc*. After screening up to 10,000 small molecules (table S1A), we identified Forskolin (FSK), 2-methyl-5-hydroxytryptamine (2-Me-5HT), and D4476 (table S1B) as chemical “substitutes” for *Oct4* (Fig. 1, A and B, and figs. S1 and S2). Previously, we had developed a small-molecule combination “VC6T” [VPA, CHIR99021 (CHIR), 616452, Tranylcypromine], that enables reprogramming with a single gene, *Oct4* (6). We next treated OG-MEFs with VC6T plus the chem-

ical substitutes of *Oct4* in the absence of transgenes. We found that VC6T plus FSK (VC6TF) induced some GFP-positive clusters expressing E-cadherin, a mesenchyme-to-epithelium transition marker, reminiscent of early reprogramming by transcription factors (10, 11) (Fig. 1C and fig. S3). However, the expression of *Oct4* and *Nanog* was not detectable, and their promoters remained hypermethylated, suggesting a repressed epigenetic state (fig. S3).

To identify small molecules that facilitate late reprogramming, we used a doxycycline (DOX)-inducible *Oct4* expression screening system, adding DOX only in the first 4 to 8 days (6). Small-molecule hits, including several cAMP agonists (FSK, Prostaglandin E2, and Rolipram) and epigenetic modulators [3-deazaneplanocin A (DZNep), 5-Azacytidine, sodium butyrate, and RG108], were identified in this screen (fig. S4 and table S1B).

To achieve complete chemical reprogramming without the *Oct4*-inducible system, these small molecules were further tested in the chemical reprogramming of OG-MEFs without transgenes. When DZNep was added 16 days after treatment with VC6TF (VC6TFZ), GFP-positive cells were obtained more frequently by a factor of up to 65 than those treated with VC6TF, forming compact, epithelioid, GFP-positive colonies without clear-cut edges (Fig. 1, D and E, and fig. S5). In these cells, the expression levels of most pluripotency marker genes were elevated but were still lower than in ESCs, suggesting an incomplete reprogramming state (fig. S6). After switching to 2i-medium with dual inhibition (2i) of glycogen synthase kinase-3 and mitogen-activated protein kinase signaling after day 28 posttreatment, certain GFP-positive colonies developed an ESC-like morphology (domed, phase-bright, homogeneous with clear-cut edges) (Fig. 1F) (12, 13). These colonies could be further cultured for more than 30 passages, maintaining an ESC-like morphology (Fig. 1, G and H). We refer to these 2i-competent, ESC-like, and GFP-positive cells as chemically induced pluripotent stem cells (CiPSCs).

Next, we optimized the dosages and treatment duration of the small molecules and were able to generate 1 to 20 CiPSC colonies from 50,000

¹College of Life Sciences and Peking-Tsinghua Center for Life Sciences, Peking University, Beijing 100871, China. ²School of Chemical Biology and Biotechnology, Peking University Shenzhen Graduate School, Shenzhen 518055, China. ³Beijing Vitalstar Biotechnology Co., Ltd., Beijing 100012, China.

*These authors contributed equally to this work.

†These authors contributed equally to this work.

‡Corresponding author. E-mail: hongkui_deng@pku.edu.cn (H.D.); yangzhao@pku.edu.cn (Y.Z.)

initially plated MEFs (fig. S7). After an additional screen, we identified some small-molecule boosters of chemical reprogramming, among which, a synthetic retinoic acid receptor ligand, TTNPB, enhanced chemical reprogramming efficiency up to a factor of 40, to a frequency comparable to transcription factor–induced reprogramming (up to 0.2%) (fig. S8 and table S1B). Furthermore,

using the small-molecule combination VC6TFZ, we obtained CiPSC lines from mouse neonatal fibroblasts (MNFs), mouse adult fibroblasts (MAFs), and adipose-derived stem cells (ADSCs) with OG cassettes by an efficiency lower by a factor of ~10 than that obtained from MEFs (fig. S9 and table S3). Moreover, we induced CiPSCs from wild-type MEFs without OG cassettes or

any other genetic modifications by a comparable efficiency to that achieved from MEFs with OG cassettes (fig. S9). The CiPSCs were also confirmed to be viral-vector free by genomic polymerase chain reaction (PCR) and Southern blot analysis (fig. S10). The established CiPSC lines were then further characterized. They grew with a doubling

Fig. 1. Generation of CiPSCs by small-molecule compounds. (A and B) Numbers of iPSC colonies induced from MEFs infected by SKM (A) or SK (B) plus chemicals or *Oct4*. Error bars, mean \pm SD ($n = 3$ biological repeat wells). (C) Morphology of MEFs for chemical reprogramming on day 0 (D0) and a GFP-positive cluster generated using VC6TF on day 20 (D20) after chemical treatment. (D) Numbers of GFP-positive colonies induced after DZNep treatment on day 36. Error bars, mean \pm SD ($n = 2$ biological repeat wells). (E to G) Morphology of a compact, epithelioid, GFP-positive colony on day 32 (D32) after treatment (E), a primary CiPSC colony on day 40 (D40) after treatment (F), and passaged CiPSC colonies (G). (H) Schematic diagram illustrating the process of CiPSC generation. Scale bars, 100 μ m. For (D), cells for reprogramming were replated on day 12.

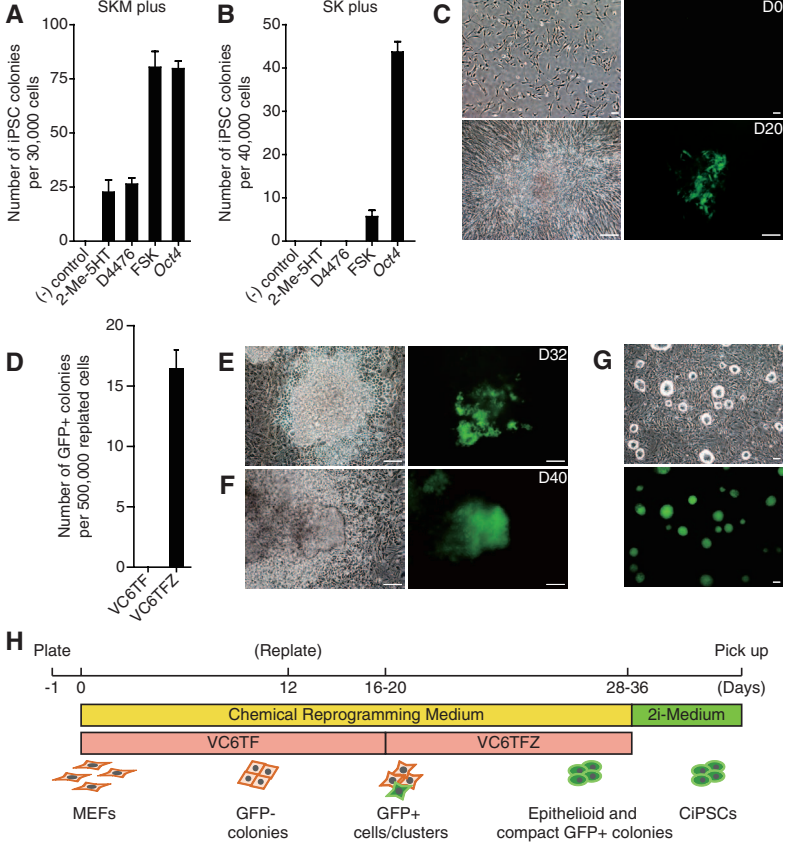
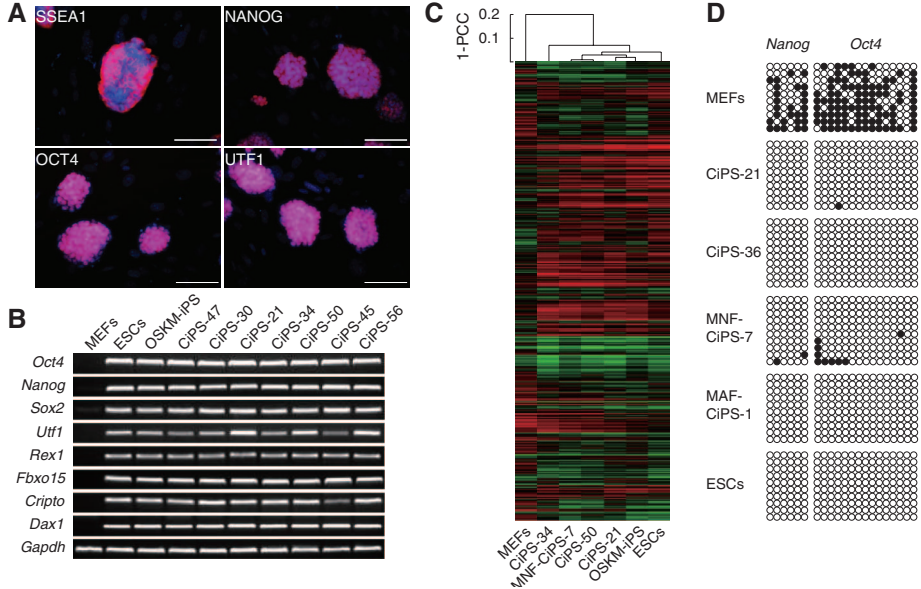


Fig. 2. Characterization of CiPSCs. (A and B) Pluripotency marker expression as illustrated by immunofluorescence (A, clone CiPS-25) and RT-PCR (B). Scale bars, 100 μ m. (C) Hierarchical clustering of global transcriptional profiles. 1-PCC, Pearson correlation coefficient. (D) Bisulfite genomic sequencing of the *Oct4* and *Nanog* promoter regions. MNF-CiPS-7, MNF-derived CiPSC line no. 7; MAF-CiPS-1, MAF-derived CiPSC line no. 1.



time (14.1 to 15.1 hours) similar to that of ESCs (14.7 hours), maintained alkaline phosphatase activity, and expressed pluripotency markers, as detected by immunofluorescence and reverse transcription (RT)-PCR (Fig. 2, A and B, and fig. S11). The gene expression profiles were similar in CiPSCs, ESCs, and OSKM-iPSCs (iPSCs induced by *Oct4*, *Sox2*, *Klf4*, and *c-Myc*) (Fig. 2C and fig. S12). DNA methylation state and histone modifications at *Oct4* and *Nanog* promoters in CiPSCs were similar to that in ESCs (Fig. 2D and fig. S13). In addition, CiPSCs maintained a normal karyotype and genetic integrity for up to 13 passages (fig. S14 and table S2).

To characterize their differentiation potential, we injected CiPSCs into immunodeficient (SCID) mice. The cells were able to differentiate into tissues of all three germ layers (Fig. 3A and fig. S15). When injected into eight-cell embryos or blastocysts, CiPSCs were capable of integration into organs of all three germ layers, including gonads and transmission to subsequent generations (Fig. 3, B to E, and fig. S16). Unlike chimeric mice generated from iPSCs induced by transcription factors including *c-Myc* (14), the chimeric mice generated from CiPSCs were 100% viable and apparently healthy for up to 6 months (Fig. 3F). These observations suggest that the CiPSCs were fully reprogrammed into pluripotency (table S3).

We next determined which of these small molecules were critical in inducing CiPSCs. We found four essential small molecules whose individual withdrawal from the cocktails generated significantly reduced GFP-positive colonies

and no CiPSCs (Fig. 4, A to C). These small molecules (C6FZ) include: CHIR (C), a glycogen synthase kinase 3 inhibitor (15); 616452 (6), a transforming growth factor-beta inhibitor (16); FSK (F), a cAMP agonist (fig. S17) (17); and DZNep (Z), an *S*-adenosylhomocysteine (SAH) hydrolase inhibitor (figs. S18 and S19) (18, 19). Moreover, C6FZ was able to induce CiPSCs from both MEFs and MAFs, albeit by an efficiency lower by a factor of 10 than that induced by VC6TFZ (fig. S20 and table S3).

To better understand the pluripotency-inducing properties of these small molecules, we profiled the global gene expression during chemical reprogramming and observed the sequential activation of certain key pluripotency genes, which was validated by real-time PCR and immunofluorescence (fig. S21). The expression levels of two pluripotency-related genes, *Sall4* and *Sox2*, were most significantly induced in the early phase in response to VC6TF, as was the expression of several extra-embryonic endoderm (XEN) markers *Gata4*, *Gata6*, and *Sox17* (Fig. 4, D to F, and figs. S22 to S24). The expression of *Sall4* was enhanced most significantly as early as 12 hours after small-molecule treatment, suggesting that *Sall4* may be involved in the first step toward pluripotency in chemical reprogramming (fig. S22B). We further examined the roles of the endogenous expression of these genes in chemical reprogramming, using gene overexpression and knockdown strategies. We found that the concomitant overexpression of *Sall4* and *Sox2* was able to activate an *Oct4* promoter-driven luciferase reporter (fig. S25)

and was sufficient to replace C6F in inducing *Oct4* expression and generating iPSCs (Fig. 4, G and H, and fig. S26). The endogenous expression of *Sall4*, but not *Sox2*, requires the activation of the XEN genes, and vice versa (fig. S27). This suggests a positive feedback network formed by *Sall4*, *Gata4*, *Gata6*, and *Sox17*, similar to that previously described in mouse XEN formation (20). Moreover, knockdown of *Sall4* or these XEN genes impaired *Oct4* activation and the subsequent establishment of pluripotency (fig. S28), inconsistent with our previous finding that *Gata4* and *Gata6* can contribute to inducing pluripotency (21). Taken together, these findings revealed a *Sall4*-mediated molecular pathway that acts in the early phase of chemical reprogramming (Fig. 4L). This step resembles a *Sall4*-mediated dedifferentiation process in vivo during amphibian limb regeneration (22).

We next investigated the role of DZNep, which was added in the late phase of chemical reprogramming. We found that *Oct4* expression was enhanced significantly after the addition of DZNep in chemical reprogramming (Fig. 4D), and DZNep was critical for stimulating the expression of *Oct4* but not the other pluripotency genes (Fig. 4I). As an SAH hydrolase inhibitor, DZNep elevates the concentration ratio of SAH to *S*-adenosylmethionine (SAM) and may thereby repress the SAM-dependent cellular methylation process (fig. S18) (18, 19). Consistently, DZNep significantly decreased DNA and H3K9 methylation at the *Oct4* promoter, which may account for its role in *Oct4* activation (Fig. 4, J and K) (23, 24). As master pluripotency genes, *Oct4* and *Sox2* may thereby activate other pluripotency-related genes and fulfill the chemical reprogramming process, along with the activation of *Nanog* and the silencing of *Gata6*, in the presence of 2i (12, 13, 25, 26) (Fig. 4F and fig. S29). In summary, as a master switch governing pluripotency, *Oct4* expression, which is kept repressed in somatic cells by multiple epigenetic modifications, is unlocked in chemical reprogramming by the epigenetic modulator DZNep and stimulated by C6F-induced expression of *Sox2* and *Sall4* (Fig. 4L).

Our proof-of-principle study demonstrates that somatic reprogramming toward pluripotency can be manipulated using only small-molecule compounds (fig. S30). It reveals that the endogenous pluripotency program can be established by the modulation of molecular pathways non-specific to pluripotency via small molecules rather than by exogenously provided “master genes.” These findings increase our understanding about the establishment of cell identities and open up the possibility of generating functionally desirable cell types in regenerative medicine by cell fate reprogramming using specific chemicals or drugs, instead of genetic manipulation and difficult-to-manufacture biologics. To date, the complete chemical reprogramming approach remains to be further improved to reprogram human somatic cells and ultimately meet the needs of regenerative medicine.

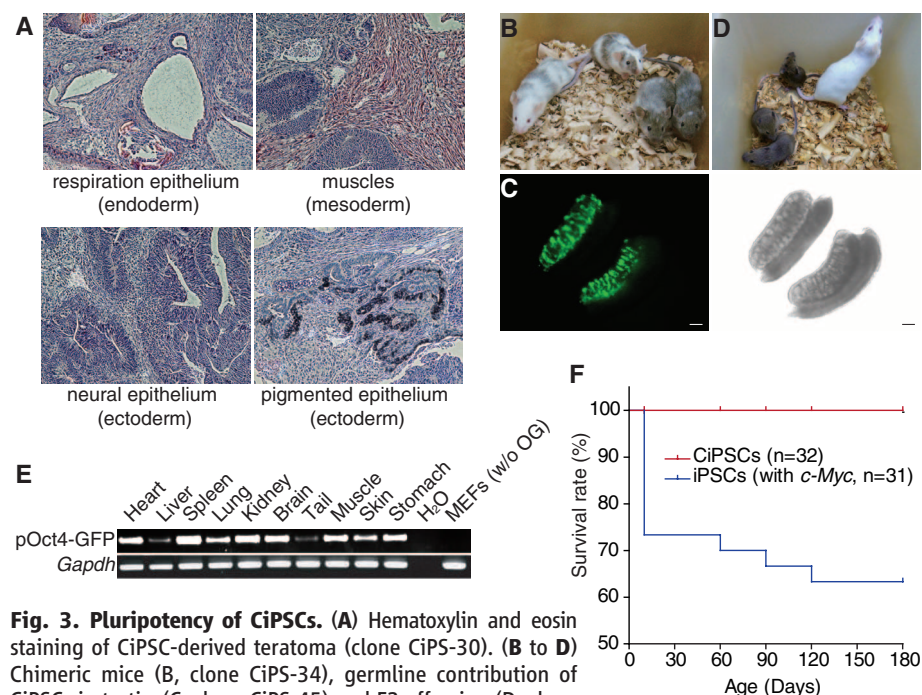
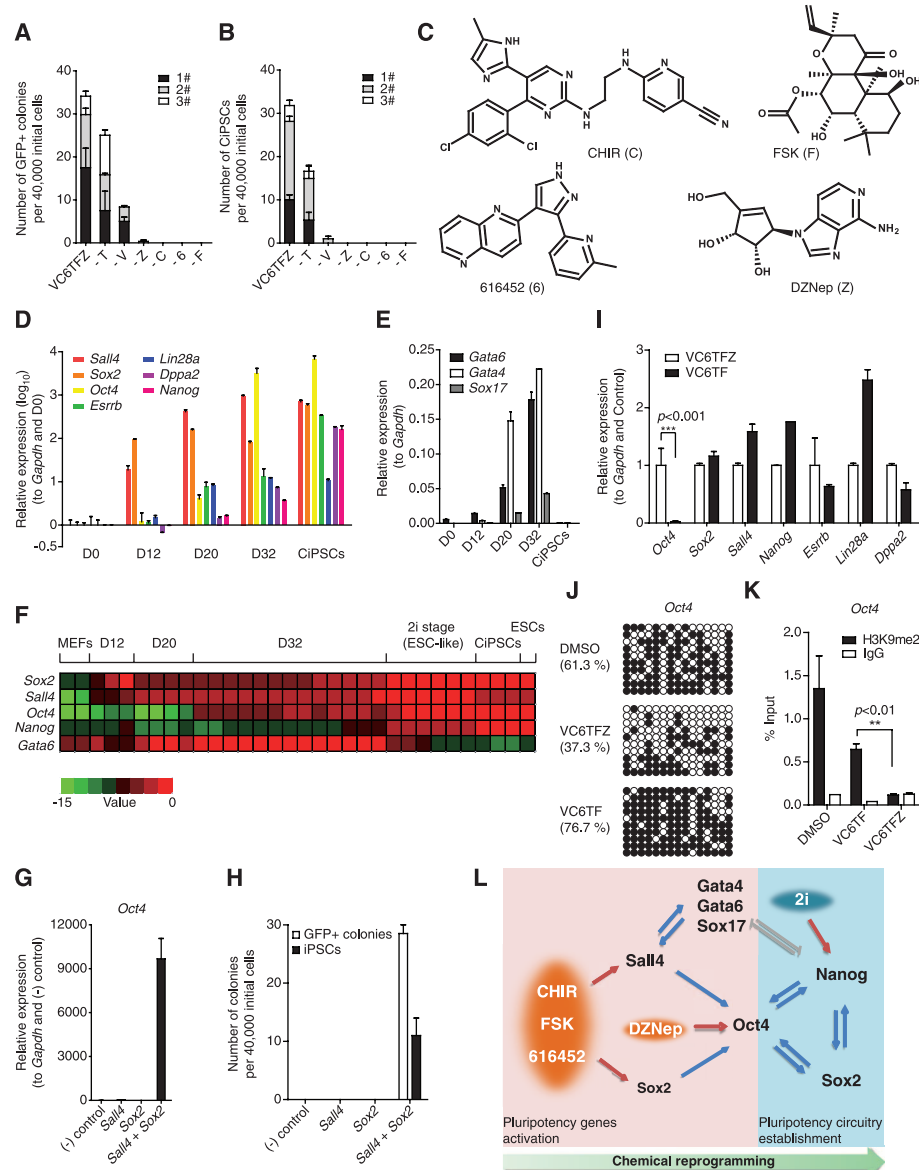


Fig. 3. Pluripotency of CiPSCs. (A) Hematoxylin and eosin staining of CiPSC-derived teratoma (clone CiP5-30). (B to D) Chimeric mice (B, clone CiP5-34), germline contribution of CiPSCs in testis (C, clone CiP5-45) and F2 offspring (D, clone CiP5-34). Scale bars, 100 μm. (E) Genomic PCR analyzing pOct4-GFP cassettes in the tissues of chimeras. (F) Survival curves of chimeras. *n*, total numbers of chimeras studied.

Fig. 4. Stepwise establishment of the pluripotency circuitry during chemical reprogramming.

(A and B) Numbers of GFP-positive (A) and CiPSC (B) colonies induced by removing individual chemicals from VC6TFZ. The results of three independent experiments are shown with different colors (white, gray, and black). (C) Structures of the essential chemicals. (D and E) The expression of pluripotency-related genes (D) and *Gata6*, *Gata4*, and *Sox17* (E) as measured by real-time PCR. (F) Gene expression heat map at the single colony level. The value indicates the \log_2 -transformed fold change (relative to *Gapdh* and normalized to the highest value). (G and H) *Oct4* activation (G) and numbers of GFP-positive and iPSC colonies (H) induced by the overexpression of *Sall4* and *Sox2*, with C6F removed from VC6TFZ. (I to K) The expression of pluripotency-related genes (I), DNA methylation (J), and H3K9 dimethylation (K) states of the *Oct4* promoter in the presence and absence of DZNep on day 32. (L) Schematic diagram illustrating the stepwise establishment of the pluripotency circuitry during chemical reprogramming. Error bars, mean \pm SD ($n \geq 2$ biological repeats).



References and Notes

1. Wilmut, A. E. Schieke, J. McWhir, A. J. Kind, K. H. Campbell, *Nature* **385**, 810–813 (1997).
2. K. Takahashi, S. Yamanaka, *Cell* **126**, 663–676 (2006).
3. S. Yamanaka, H. M. Blau, *Nature* **465**, 704–712 (2010).
4. M. Stadtfeld, K. Hochedlinger, *Genes Dev.* **24**, 2239–2263 (2010).
5. S. Zhu, W. Wei, S. Ding, *Annu. Rev. Biomed. Eng.* **13**, 73–90 (2011).
6. Y. Li et al., *Cell Res.* **21**, 196–204 (2011).
7. W. Li et al., *Proc. Natl. Acad. Sci. U.S.A.* **109**, 20853–20858 (2012).
8. K. Saha, R. Jaenisch, *Cell Stem Cell* **5**, 584–595 (2009).
9. S. M. Wu, K. Hochedlinger, *Nat. Cell Biol.* **13**, 497–505 (2011).
10. R. Li et al., *Cell Stem Cell* **7**, 51–63 (2010).
11. P. Samavarchi-Tehrani et al., *Cell Stem Cell* **7**, 64–77 (2010).
12. J. Silva et al., *PLoS Biol.* **6**, e253 (2008).
13. T. W. Theunissen et al., *Curr. Biol.* **21**, 65–71 (2011).
14. M. Nakagawa, N. Takizawa, M. Narita, T. Ichisaka, S. Yamanaka, *Proc. Natl. Acad. Sci. U.S.A.* **107**, 14152–14157 (2010).
15. Q. L. Ying et al., *Nature* **453**, 519–523 (2008).
16. N. Maherali, K. Hochedlinger, *Curr. Biol.* **19**, 1718–1723 (2009).
17. P. A. Insel, R. S. Ostrom, *Cell. Mol. Neurobiol.* **23**, 305–314 (2003).
18. P. K. Chiang, *Pharmacol. Ther.* **77**, 115–134 (1998).
19. R. K. Gordon et al., *Eur. J. Biochem.* **270**, 3507–3517 (2003).
20. C. Y. Lim et al., *Cell Stem Cell* **3**, 543–554 (2008).
21. J. Shu et al., *Cell* **153**, 963–975 (2013).
22. A. W. Neff, M. W. King, A. L. Mescher, *Dev. Dyn.* **240**, 979–989 (2011).
23. N. Feldman et al., *Nat. Cell Biol.* **8**, 188–194 (2006).
24. J. Chen et al., *Nat. Genet.* **45**, 34–42 (2013).
25. L. A. Boyer et al., *Cell* **122**, 947–956 (2005).
26. C. Chazaud, Y. Yamanaka, T. Pawson, J. Rossant, *Dev. Cell* **10**, 615–624 (2006).

Acknowledgments: We thank X. Zhang, J. Wang, C. Han, Z. Hou, J. Liu, and L. Ai for technical assistance. This work was supported by grants from the National 973 Basic Research Program of China (2012CB966401 and

2010CB945204), the Key New Drug Creation and Manufacturing Program (2011ZX09102-010-03), the National Natural Science Foundation of China (90919031), the Ministry of Science and Technology (2011AA020107, 2011DFA30730 and 2013DFG30680), the Beijing Science and Technology Plan (Z121100005212001), the Ministry of Education of China (111 project), and a Postdoctoral Fellowship of Peking-Tsinghua Center for Life Sciences. Microarray and RNA-seq data are deposited in the Gene Expression Omnibus (GEO) database (accession no. GSE48243). The authors have filed a patent for the small-molecule combinations used in the chemical reprogramming reported in this paper.

Supplementary Materials

www.sciencemag.org/cgi/content/full/science.1239278/DC1
Materials and Methods

Figs. S1 to S30

Tables S1 to S5

References (27–37)

17 April 2013; accepted 11 July 2013

Published online 18 July 2013;

10.1126/science.1239278

Nuclear Pore Scaffold Structure Analyzed by Super-Resolution Microscopy and Particle Averaging

Anna Szymborska,¹ Alex de Marco,² Nathalie Daigle,¹ Volker C. Cordes,³ John A. G. Briggs,² Jan Ellenberg^{1*}

Much of life's essential molecular machinery consists of large protein assemblies that currently pose challenges for structure determination. A prominent example is the nuclear pore complex (NPC), for which the organization of its individual components remains unknown. By combining stochastic super-resolution microscopy, to directly resolve the ringlike structure of the NPC, with single particle averaging, to use information from thousands of pores, we determined the average positions of fluorescent molecular labels in the NPC with a precision well below 1 nanometer. Applying this approach systematically to the largest building block of the NPC, the Nup107-160 subcomplex, we assessed the structure of the NPC scaffold. Thus, light microscopy can be used to study the molecular organization of large protein complexes in situ in whole cells.

Methods used to determine the structures of large complexes in situ, for example, electron tomography, currently lack the resolution for direct molecular assignments. Consequently, structure determination of very large protein assemblies, such as the nuclear pore complex (NPC), is extremely challenging. The NPC channel mediates nucleocytoplasmic transport, consists of several hundred proteins termed nucleoporins (Nups), and has an estimated mass of 110 MD (1). Despite progress in the crystallization of individual Nups (2, 3) and electron tomographic reconstruction of the whole NPC (4, 5), it remains unclear how the individual proteins are organized within the complex. Super-resolution (SR) fluorescence microscopy should be able to fill this gap, because it combines specific molecular labeling with a very high resolution (6). However, SR imaging of biological structures in situ is currently limited to a resolution of ~15 nm (6–8). We reasoned that it should be possible to improve the precision of SR microscopy by combining many SR images of individual complexes using single-particle averaging and applied this approach to address the structural organization of the NPC.

We first established a robust methodological pipeline by using Nup133, a stable component of the NPC scaffold. Stochastic localization microscopy (7–12) of antibody-labeled Nup133 achieved about one order of magnitude better resolution than state-of-the-art confocal microscopy (Fig. 1, A and B) and revealed that Nup133 molecules are organized in a ring, consistent with previous observations of the transmembrane Nup gp210

(13). The large field of view of the SR light microscope allowed us to record the entire lower surface of a mammalian nucleus, typically containing several hundred pores with their transport axes oriented along the optical axis. Next, we developed a single-particle averaging routine that allowed us to combine information from thousands of pores (Fig. 1, C to F) (14). After passing stringent quality control (figs. S1 and S2), the particles were aligned and summed to generate an average image of the respective fluorescent

label in the NPC (Fig. 1, C and D). From the mean radial intensity profile of the image, we could determine the average position of the fluorescent label with respect to the center of the pore with a standard deviation of 0.1 nm (Fig. 1, E and F, and fig. S3). Applying the averaging pipeline to simulated particles showed that our method underestimated the real position of the label by 0.3 nm owing to incomplete decoration of the pore ring (fig. S4). Thus, we could determine the average radial position of the fluorescent label with a precision of 0.1 nm and an accuracy of 0.3 nm.

Next, we applied our method to systematically probe the molecular organization of the human NPC scaffold, which is primarily composed of multiple copies of the Nup107-160 subcomplex, a stable assembly of nine Nups. On the basis of structural homology, the organization of the human (hs) subcomplex is generally assumed to be similar to the yeast (y) Nup84 subcomplex, which resembles a 40-nm-long letter Y (15, 16). The positions and orientations of the yeast proteins within the Y shape have been assigned on the basis of biochemical and crystallographic data (17) (Fig. 2A). The stalk of the complex is formed by yNup133 (hsNup133) at the foot, followed by yNup84 (hsNup107) and yNup145C-ySec13 (hsNup96-hsSec13) at the central branch point. The two arms contain yNup120 (hsNup160) and yNup85-ySeh1 (hsNup85-hsSeh1), respectively. The human complex additionally contains Nup37, which localizes to the Nup160 arm, and Nup43, whose position is thus far undetermined.

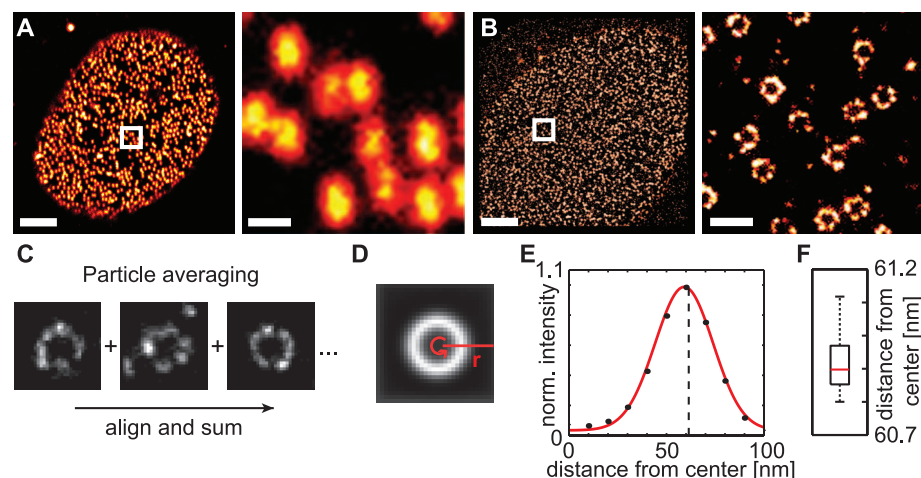


Fig. 1. SR microscopy combined with single-particle averaging. (A) Confocal and (B) SR microscopy of U2OS cells stained with Nup133 antibody raised against the full-length protein (FL), showing the lower surface of the nucleus (left) and a magnified 2- μm^2 area (right). Scale bars (SB) indicate 3 μm and 300 nm, respectively. (C) Examples of Nup133-FL-labeled pores that passed quality control. (D) Average image of the NPC, generated by summing of 8698 quality-controlled and translationally aligned particles. The mean radial intensity profile of the image was calculated by averaging the line profile r in all directions. (E) Normalized mean radial intensity profile (black points) fitted with circularly convolved Gaussian (red line). Summing of several two-dimensional (2D) Gaussian peaks in a circle results in an apparent shift of the peak toward the center of the pore. The true mean radial position of the fluorescence label (dashed line) can be determined from the fit. (F) Precision of determining the radial position was estimated by cross-validation, performed by averaging 17 sets of 500 pores each (red line marks the median). The standard deviation of the distribution is 0.1 nm. The whiskers on the box plot encompass 99.3% of the distribution.

¹Cell Biology and Biophysics Unit, European Molecular Biology Laboratory, Meyerhofstrasse 1, 69117 Heidelberg, Germany.

²Structural and Computational Biology Unit, European Molecular Biology Laboratory, Meyerhofstrasse 1, 69117 Heidelberg, Germany. ³Max Planck Institute for Biophysical Chemistry, Am Fassberg 11, 37077 Göttingen, Germany.

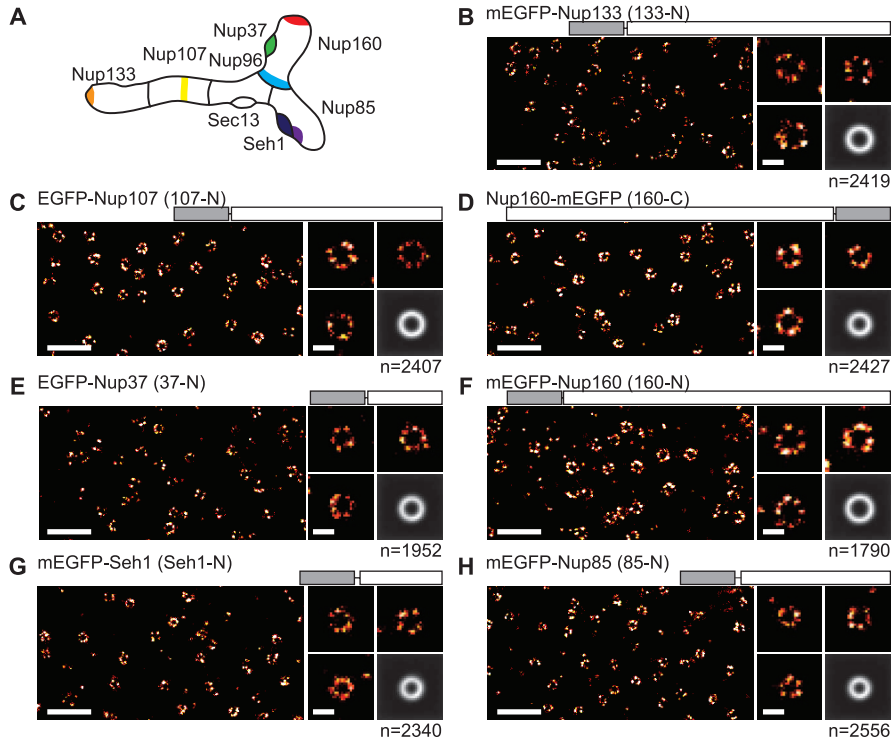
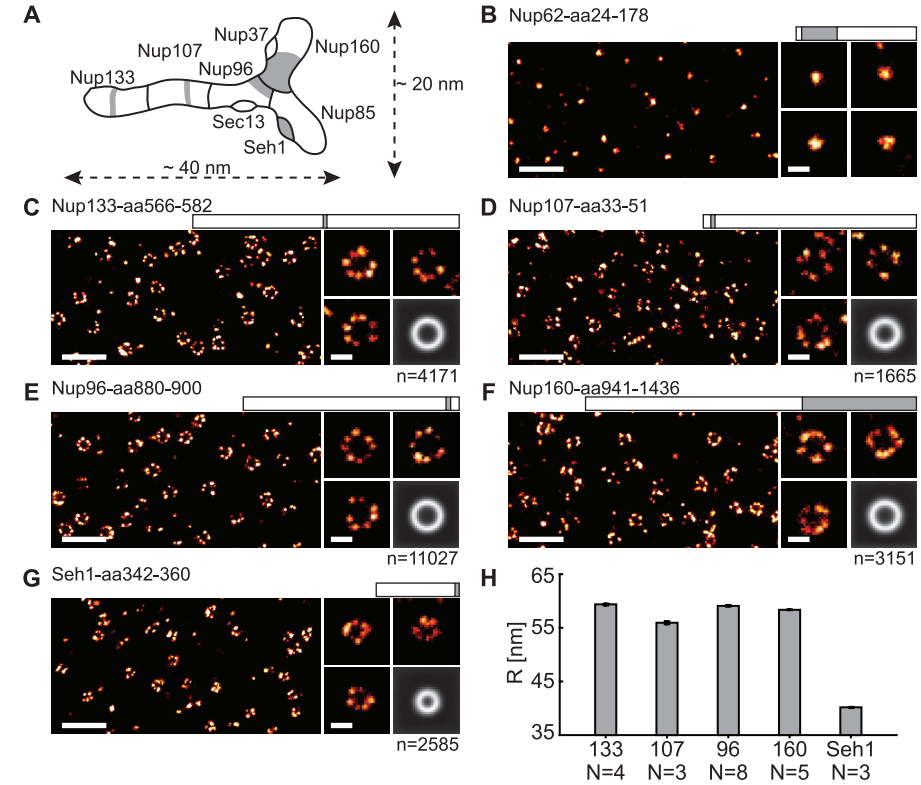
*Corresponding author. E-mail: jan.ellenberg@embl.de

At least three contradictory models for the orientation of the Nup107-160 subcomplex have been proposed, each making different predictions for the radial position of its components at the

scale of nanometers (18–20) (fig. S5). To address this, we first attempted to localize endogenous Nup107-160 complex members by using antibodies. We could specifically label the stalk

(Nup133 and Nup107), the central branch point (Nup96), and each arm of the Y (Seh1 and Nup160). As expected, all five components of the subcomplex appeared as ring structures in SR images

Fig. 2. Systematic immunolabeling of the Nup107-160 complex. (A) Schematic representation of the current model of the human Nup107-160 complex based on homology to the yeast Nup84 subcomplex (Nup43 is omitted, because its position is not known). The dimensions of the yeast complex are indicated. The approximate positions of the antigens of the antibodies used in this study are indicated in gray. (B to G) SR images of NPCs stained with antibodies against Nup62 (B), Nup133 (C), Nup107 (D), Nup96 (E), Nup160 (F), and Seh1 (G). The bars above the images show the position of the antigen (aa) with respect to the rest of the amino acid (aa) sequence. For each antibody, a representative 4.5-μm² area of the lower surface of the nucleus (left) is shown, as well as four (B) or three [(C) to (G)] exemplary high-quality pores (right). The lower right panel in (C) to (G) shows the average image, generated from *n* number of aligned pores. SB, 0.5 μm and 0.1 μm. (H) Average radial positions *R* of the antibody-stained Nups measured in *N* independent experiments. The error bars represent SEM of the experiments. From left to right: Nup133-aa566-582 *R* = 59.4 ± 0.2 nm (SEM), Nup107-aa33-51 *R* = 55.9 ± 0.3 nm, Nup96-aa880-900 *R* = 59.0 ± 0.1 nm, Nup160-aa941-1436 *R* = 58.3 ± 0.2 nm, Seh1-aa342-360 *R* = 40.4 ± 0.3 nm. Positions of Nup107 and Seh1 are significantly different from all other positions with a *t* test *P* value *P* < 0.01.



(I) Average radial positions *R* of the GFP-tagged Nups measured in *N* independent experiments. From left to right: 133-N *R* = 50.1 ± 0.2 nm, 107-N *R* = 48.2 ± 0.2 nm, 160-C *R* = 42.6 ± 0.2 nm, 37-N *R* = 45.5 ± 0.0 nm, 160-N *R* = 52.5 ± 0.2 nm, Seh1-N *R* = 39.9 ± 0.3 nm, 85-N *R* = 38.2 ± 0.2 nm. All positions are significantly different from all others with a *t* test *P* < 0.01.

(Fig. 2, C to G), in contrast to Nup62, a component of the central transport channel, which appeared as a spot (Fig. 2B). Differences in the diameters of some of the Nup107-160 components were evident in single SR images without averaging (Fig. 2, C to G). After averaging, we found that Nup133 is the outermost epitope, followed by Nup96, then Nup160, Nup107, and lastly Seh1 (Fig. 2H and fig. S6). The antibody-based localizations suggested that the stalk and the Nup160 arm of the Y are largely peripheral, whereas the Nup85-Seh1 arm reaches far to the center of the pore.

Despite the subnanometer precision and accuracy in determining the mean position of the fluorescent label, the substantial size of the primary and secondary antibody complexes could potentially offset the fluorescent dye from the targeted epitope. In addition, we could not obtain antibodies of sufficient quality for SR imaging against several Nup107-160 complex members. To systematically determine the positions of the components of the subcomplex with higher accuracy, we labeled a collection of seven Nup-green fluorescent protein (GFP) fusions with dye-coupled small anti-GFP nanobodies (21) (Fig. 3). To ensure high incorporation of the GFP-tagged protein into the pore and control for functionality, we depleted the endogenous Nups by RNA interference (14). Overall, the nanobody measurements resulted in a radial order of Nup107-160 complex members very similar to those obtained by using immunolabeling of endogenous Nups. The differences in absolute distances between the two labeling strategies that we observed for Nup133, Nup107, and Nup160 are consistent with the size difference between the nanobody and the bulky primary and secondary antibody pair, which becomes nonnegligible at this resolution.

The small error and well-defined average profile we measured for each protein suggested that they have very similar radial distances on the cytoplasmic and nucleoplasmic face of the pore, consistent with their symmetric localization along the transport axis (22), and that all copies of the subcomplex lie in a very similar orientation within the NPC (Fig. 3I). According to our subnanometer positional constraints for seven nanobody-labeled Nups, the Nup107-160 complex is arranged with its stalk tilting from the periphery slightly toward the center and splits at the branching point from where the Nup85-Seh1 arm reaches toward the center of the pore, whereas the Nup160-Nup37 arm stretches back toward the periphery (Fig. 4A and figs. S5D and S7). Our data are consistent with aspects of a previous computational model (20, 23) and with fluorescence anisotropy measurements (24), both of which proposed that the long axis of the Y-shaped complex is perpendicular to the direction of transport. Furthermore, our positional data does not support the “fence-like coat” (19, 25) (fig. S5B) or the “lattice” models (18, 26) (fig. S5C).

Comparison with the high-resolution human NPC cryogenic electron microscopy (cryo-EM) structure (5) placed most of our molecular positions in the electron density of the cytoplasmic and nucleoplasmic rings and excluded their localization in the spoke ring (Fig. 4B). The Nup85-Seh1 arm localizes at about the same radial distance as the eight pairs of central protrusions discernible in the cytoplasmic ring, while the rest of the Y shape overlaps with the ring backbone (Fig. 4C). Thus, a head-to-tail arrangement of Nup107-160 complex in cytoplasmic and nucleoplasmic rings, along the circumference of the pore, is the most likely model to explain our data. The model allows for the two proposed stoichiometries of 8 or 16 copies of the Nup107-160

complex per cytoplasmic or nucleoplasmic ring (22, 27, 28) (fig. S5D).

Although the alignment method we used to study the organization of the NPC relied on the intrinsic rotational symmetry of the complex, we demonstrated that it can be extended to asymmetric structures by aligning single particles on a molecular reference labeled in a second color without a loss of precision (figs. S8 and S9).

We combined stochastic SR microscopy with single-particle averaging to investigate the structure of a large protein complex, the NPC, in situ in whole cells. Our data provide direct evidence for the orientation of the Nup107-160 subcomplex within the pore and discriminate between contradictory models of the structural organization of the NPC scaffold. More generally, our results demonstrate that the average positions of fluorescence labels in protein complexes suitable for particle averaging can be determined by light microscopy with a precision well below 1 nm. This approach is potentially valuable to address structural biology questions pertaining to large protein complexes and organelles, including centrioles and the centrosome, endosomes, coated vesicles, and the kinetochore, because it bridges the gap between atomic resolution methods and label-free in situ techniques.

References and Notes

1. R. Reichelt *et al.*, *J. Cell Biol.* **110**, 883–894 (1990).
2. A. Hoeltz, E. W. Debler, G. Blobel, *Annu. Rev. Biochem.* **80**, 613–643 (2011).
3. S. G. Brohawn, J. R. Partridge, J. R. R. Whittle, T. U. Schwartz, *Structure* **17**, 1156–1168 (2009).
4. M. Beck, V. Lucic, F. Förster, W. Baumeister, O. Medalia, *Nature* **449**, 611–615 (2007).
5. T. Maimon, N. Elad, I. Dahan, O. Medalia, *Structure* **20**, 998–1006 (2012).
6. L. Schermelleh, R. Heintzmann, H. Leonhardt, *J. Cell Biol.* **190**, 165–175 (2010).
7. M. J. Rust, M. Bates, X. Zhuang, *Nat. Methods* **3**, 793–796 (2006).
8. J. Fölling *et al.*, *Nat. Methods* **5**, 943–945 (2008).
9. E. Betzig *et al.*, *Science* **313**, 1642–1645 (2006).
10. S. T. Hess, T. P. K. Girirajan, M. D. Mason, *Biophys. J.* **91**, 4258–4272 (2006).
11. H. Bock *et al.*, *Appl. Phys. B* **88**, 161–165 (2007).
12. M. Heilemann *et al.*, *Angew. Chem. Int. Ed.* **47**, 6172–6176 (2008).
13. A. Löschberger *et al.*, *J. Cell Sci.* **125**, 570–575 (2012).
14. For details, see supplementary materials available on Science Online.
15. M. Lutzmann, R. Kunze, A. Buerer, U. Aebi, E. Hurt, *EMBO J.* **21**, 387–397 (2002).
16. M. Kampmann, G. Blobel, *Nat. Struct. Mol. Biol.* **16**, 782–788 (2009).
17. S. Bilokapic, T. U. Schwartz, *Curr. Opin. Cell Biol.* **24**, 86–91 (2012).
18. S. G. Brohawn, N. C. Leksa, E. D. Spear, K. R. Rajashankar, T. U. Schwartz, *Science* **322**, 1369–1373 (2008).
19. K.-C. Hsia, P. Stavropoulos, G. Blobel, A. Hoeltz, *Cell* **131**, 1313–1326 (2007).
20. F. Alber *et al.*, *Nature* **450**, 695–701 (2007).
21. J. Ries, C. Kaplan, E. Platonova, H. Eghlidi, H. Ewers, *Nat. Methods* **9**, 582–584 (2012).
22. M. P. Rout *et al.*, *J. Cell Biol.* **148**, 635–652 (2000).
23. J. Fernandez-Martinez *et al.*, *J. Cell Biol.* **196**, 419–434 (2012).
24. M. Kampmann, C. E. Atkinson, A. L. Mattheyses, S. M. Simon, *Nat. Struct. Mol. Biol.* **18**, 643–649 (2011).
25. E. W. Debler *et al.*, *Mol. Cell* **32**, 815–826 (2008).
26. S. Bilokapic, T. U. Schwartz, *Proc. Natl. Acad. Sci. U.S.A.* **109**, 15241–15246 (2012).

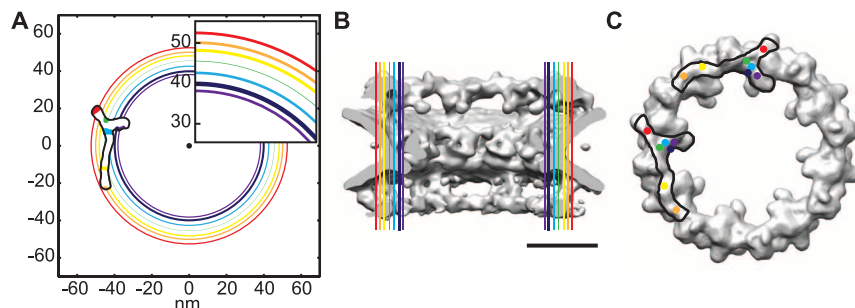


Fig. 4. SR imaging-based model for the orientation of the Y-shaped complex in the NPC scaffold. (A) Average positions of (m)EGFP fusions of Nups 133-N (orange), 107-N (yellow), 160-C (light blue), 37-N (green), 160-N (red), Seh1-N (dark blue), and 85-N (purple) in the plane of the nuclear envelope, based on the spatial constraints from SR measurements of nanobody stained pores magnified in the inset. The line thickness represents the 95% confidence interval for the mean position of each tagged Nup. The schematic model of the Nup107-160 complex from Fig. 3A is brought into line with the measured positions. A cartoon illustrating the two equally possible opposite-handed models is shown in fig. S5D. (B) The mean positions of Nups overlaid to scale on the EM structure of the human NPC, viewed along the transport axis; SB, 40 nm. (C) Two possible arrangements of the Nup107-160 complexes traced in the electron density of the cytoplasmic ring of the nuclear pore consistent with our measurements; the dots are drawn in the measured radial position and adjusted manually along the circumference of the pore to mark the stalk and both arms of the Y shape.

27. J. M. Cronshaw, A. N. Krutchinsky, W. Zhang, B. T. Chait, M. J. Matunis, *J. Cell Biol.* **158**, 915–927 (2002).
28. A. Ori *et al.*, *Mol. Syst. Biol.* **9**, 648 (2013).

Acknowledgments: We gratefully acknowledge V. Doye, I. Mattaj, J. Köser, and M. Platani for the kind gifts of antibodies; the GSD development team of Leica Microsystems (especially M. Dyba, J. Fölling, W. Fouquet, and G. Simonutti); the European Molecular Biology Laboratory (EMBL) Advanced Light Microscopy Facility (especially S. Terjung, B. Neumann, and J. Bulkescher) and the EMBL Protein Expression and Purification Core for support; M. Bates

for advice on SR microscopy; O. Medalia for the human NPC electron density maps; M. Beck and H. Bui for help with rendering the EM density and Nup85 cDNA; S. Yoshimura for Nup160 cDNA; F. Nedelec, A. Picco, and W. Huber for help with data analysis; S. Streichan and the Ellenberg group for help with the analysis implementation (especially W. Xiang, P. Strnad, J. Roberti, S. Otsuka, and J. Hossain); and J. Ries for comments on the manuscript and Alexa Fluor 647 nanobody. This work was supported by funding from the German Research Council to J.E. (DFG EL 246/3-2 within the priority program SPP1175). The data presented here are tabulated in the main paper and the supplementary materials.

Supplementary Materials
www.sciencemag.org/cgi/content/full/science.1240672/DC1
Materials and Methods
Supplementary Text
Figs. S1 to S9
Tables S1 to S3
References (29–43)

17 May 2013; accepted 26 June 2013
Published online 11 July 2013;
10.1126/science.1240672

Polyploids Exhibit Higher Potassium Uptake and Salinity Tolerance in *Arabidopsis*

Dai-Yin Chao,¹ Brian Dilkes,² Hongbing Luo,² Alex Douglas,¹ Elena Yakubova,² Brett Lahner,² David E. Salt^{1*}

Genome duplication (or polyploidization) has occurred throughout plant evolutionary history and is thought to have driven the adaptive radiation of plants. We found that the cytotype of the root, and not the genotype, determined the majority of heritable natural variation in leaf potassium (K) concentration in *Arabidopsis thaliana*. Autopolyploidy also provided resistance to salinity and may represent an adaptive outcome of the enhanced K accumulation of plants with higher ploidy.

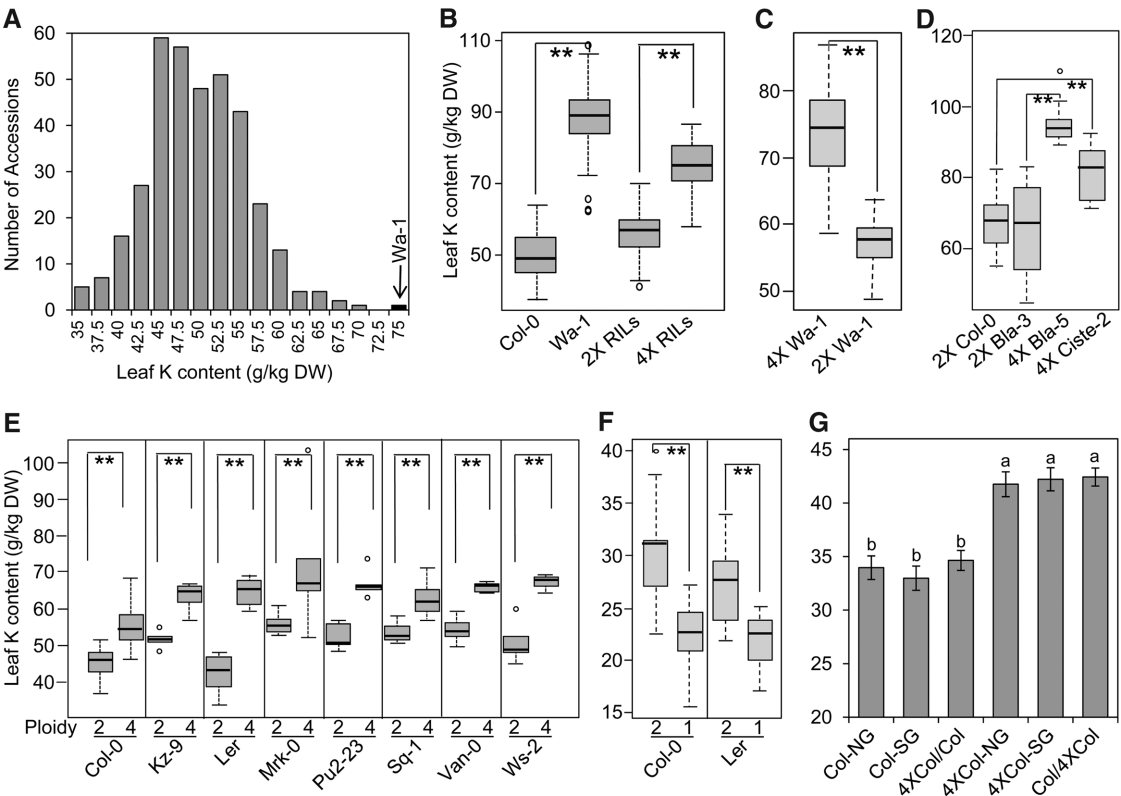
Polyploidy, the quality of possessing multiple complete sets of chromosomes, is pervasive within land plants, suggesting

an adaptive benefit though no mechanisms have been established (1). Soil discontinuities, such as boundaries between soil types, may

underlie plant-selective constraints. In an analysis of the elemental composition of leaves from a set of 349 *Arabidopsis thaliana* accessions (2), the autotetraploid accession Wa-1 (from Warsaw, Poland) had the highest concentration of leaf potassium (K) (Fig. 1A) and the K analog rubidium (Rb) (fig. S1A). Recombinant inbred lines (RILs) between the diploid accession Col-0 and the autotetraploid Wa-1 (3) contain diploids and tetraploids with recombinant genotypes (4). All 89 RILs were phenotyped for the leaf concentration of K and Rb by inductively coupled plasma mass

¹Institute of Biological and Environmental Sciences, University of Aberdeen, Cruickshank Building, St. Machar Drive, Aberdeen, AB24 3UU, UK. ²Department of Horticulture and Landscape Architecture, Purdue University, West Lafayette, IN 47907, USA.
*Corresponding author. E-mail: david.salt@abdn.ac.uk

Fig. 1. Ploidy contributes to K accumulation in *A. thaliana* leaves. (A) Leaf K concentration among 349 accessions. The arrow and back bar indicate the tetraploid, Wa-1. DW, dry weight. (B to F) Box plots (the minimum, first quartile, median, third quartile, and maximum are shown, with data >1.5 interquartile ranges denoted with circles) for leaf K concentration in Col-0 × Wa-1 RILs (B), Wa-1 and diploid Wa-1 (C), natural tetraploid accessions (D), natural diploids and derived tetraploids (E), and natural diploids and derived haploids (F). (G) Leaf K concentration of grafted diploid and tetraploid plants. NG, nongrafted; SG, self-grafted; Col/4XCol, grafted with Col-0 as scion and 4XCol-0 as rootstock; 4XCol/Col, grafted with 4XCol-0 as scion and Col-0 as rootstock. Asterisks in (B) to (F) indicate the significance of pairwise comparisons (Student's *t* test; **P* < 0.05; ***P* < 0.01). Letters above the bars in (G) indicate statistically different groups (one-way analysis of variance with groupings by Tukey's HSD with a 95% confidence interval). 2X, diploid; 4X, tetraploid. Data were collected from 6 to 18 biological replicates for



each accession, cytotype or graft, and represented in (G) as mean ± SE. All leaf K concentration data are accessible using the digital object identifiers (DOIs) 10.4231/T9H41PBV and 10.4231/T93X84K7 (see <http://dx.doi.org>).

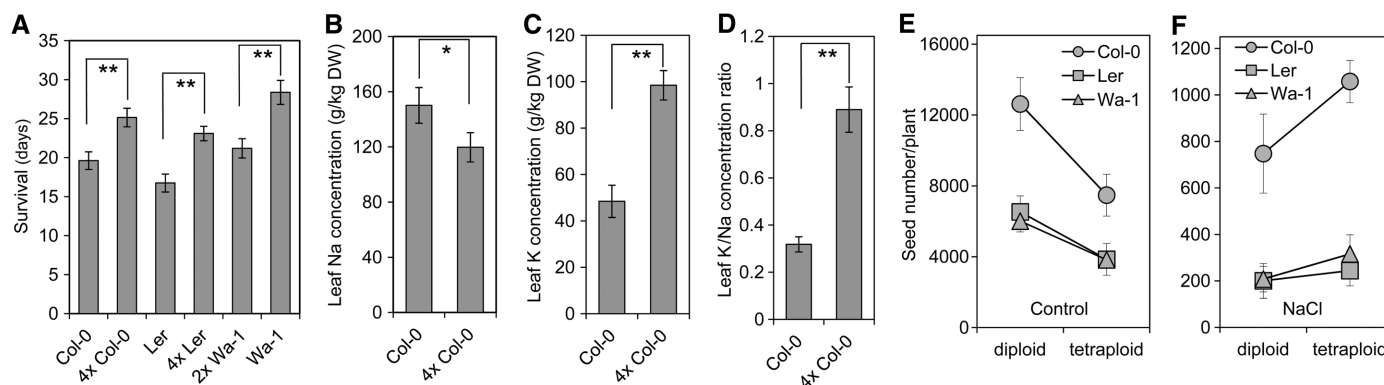


Fig. 2. Tetraploidy promotes *A. thaliana* salinity tolerance. (A) Survival of diploid and tetraploid plants after irrigation with 200 mM NaCl. Leaf concentrations of Na (B) and K (C) and the K/Na concentration ratio (D) of plants after 2 weeks of irrigation with 200 mM NaCl. (E and F) Seed production of diploid and tetraploid plants without (E) and with irrigation with 100 mM NaCl (F). 2X, diploid; 4X tetraploid. Data represent means of measurements from biological rep-

licates [(A) $n = 40$ replicates; (B) to (D) $n = 12$; (E) and (F) $n = 5$ to 6] \pm SE. (A to D) Data were analyzed with a Student's t test; * $P < 0.05$; ** $P < 0.01$. (E and F) Data were analyzed with a log-normal Poisson generalized linear mixed model (table S2), which identifies a significant two-way interaction between salinity treatment and cytotype ($P < 0.001$), but no significant interaction between salinity and genotype ($P = 0.051$).

spectrometry (ICP-MS). Ploidy was a significant determinant (logarithm of the odds ratio for linkage = 28) of leaf K concentration, accounting for 57.2% of the variation in the RILs, and increased K by 32% compared with the diploids (Fig. 1B). A diploid Wa-1, derived by haploid induction (5), had reduced leaf K and Rb concentrations (Fig. 1C and fig. S1B), confirming that tetraploidy increased leaf K. A minor portion (9.9%) of the variation in leaf K in the RILs was accounted for by a quantitative trait locus (QTL) on chromosome 2. Wa-1 contributed the allele for increased leaf K. No obvious candidate genes are present in the genomic region of this QTL.

We used flow cytometry to identify two additional natural autotetraploids, Bla-5 (from Blanes, Spain) and Ciste-2 (from Cisterna di Latina, Italy), from a screen of 344 accessions (table S1) (4) (see also supplementary materials and methods). These autotetraploids also had elevated leaf K and Rb compared with the diploid Col-0 and with Bla-3 (from Blanes, Spain), a close diploid relative of Bla-5 (Figs. 1D and fig. S1B). To test for genotype by ploidy interaction, eight diploid and colchicine-doubled tetraploid pairs were evaluated for leaf K and Rb. All autotetraploids were phenotypically similar to their diploid progenitor, and all eight had elevated leaf K and Rb (Fig. 1E and fig. S1B). Examination of haploid Col-0 and Ler, prepared by haploid induction (5), revealed that haploidy reduced leaf K compared with diploid progenitors (Fig. 1F). Thus, leaf K in *A. thaliana* was directly related to ploidy level. We used reciprocal grafting (6) to show that the elevated leaf K and Rb observed in tetraploid Col-0 was present in diploid leaves on shoots grafted to tetraploid roots (Fig. 1G and fig. S2), whereas leaves from tetraploid

shoots grafted to diploid roots showed the same leaf K as diploid Col-0 (Fig. 1G and fig. S2). These results establish that leaf K is controlled by root ploidy, independently of the ploidy of the shoot.

Increased K/Na ratios enhance salinity tolerance in plants (7). We grew diploid and tetraploid Ler, Col-0, and Wa-1 with nutrient media supplemented with 200 mM NaCl. Plant survival after NaCl treatment was used as a measure of salinity tolerance (6). Tetraploids showed an increased rate of survival compared with diploids (Fig. 2A). In a separate experiment, tetraploid NaCl-treated plants were shown to have elevated leaf K and reduced Na compared with diploids (Fig. 2, B to D). This suggests that enhanced salinity tolerance in tetraploids was associated with both elevated leaf K and reduced leaf Na accumulation. To assess the reproductive success of tetraploids and diploids in a saline environment, Ler, Col-0, and Wa-1 plants were grown to maturity with sublethal salinity treatment (100 mM NaCl) and seed production was determined as a proxy for fitness. In the untreated controls, the diploid cytotypes for all three genotypes produced more seeds than the tetraploids ($P < 0.001$) (Fig. 2E), as observed previously (4). As expected, salinity treatment reduced the seed production of all genotypes, regardless of cytotype ($P < 0.001$), though there was no significant interaction between genotype and salinity treatment. On the other hand, the interaction between cytotype and salinity treatment was significant ($P < 0.001$), with tetraploids of all genotypes producing significantly more seeds than diploids under elevated salinity ($P < 0.001$) (Fig. 2F). Thus, polyploidy can provide a reproductive advantage in saline environments.

Soils with high Na concentration are prevalent in many regions of the world. We propose that under saline conditions, polyploids, with their improved ability to accumulate K and exclude Na, may have a fitness advantage that could contribute to the establishment and persistence of polyploid populations.

References and Notes

1. C. Parisod, R. Holderegger, C. Brochmann, *New Phytol.* **186**, 5–17 (2010).
2. I. Baxter *et al.*, *PLoS Genet.* **6**, e1001193 (2010).
3. C. L. Schiff, I. W. Wilson, S. C. Somerville, *Plant Pathol.* **50**, 690–701 (2001).
4. I. M. Henry *et al.*, *Genetics* **170**, 1979–1988 (2005).
5. M. Ravi, S. W. Chan, *Nature* **464**, 615–618 (2010).
6. A. Rus *et al.*, *PLoS Genet.* **2**, e210 (2006).
7. R. Munns, M. Tester, *Annu. Rev. Plant Biol.* **59**, 651–681 (2008).

Acknowledgments: We thank S. Chan for diploid Wa-1 and the haploid inducer, C. P. Huang for help with microscopy, and T. Graham and E. Svedin for flow cytometry results. We acknowledge support from the NIH (grant R01GM078536) and the European Commission (grant PCIG9-GA-2011-291798). ICP-MS data for Fig. 1, A to F, and fig. S1 are stored at www.ionomicshub.org. All other data are available as supplementary materials on Science Online. D.-Y.C., B.D., and D.E.S. conceived and designed the experiments; D.-Y.C., H.L., B.L., and E.Y. performed the experiments; D.-Y.C., B.D., B.L., A.D., and D.E.S. analyzed the data; and D.-Y.C., B.D., and D.E.S. wrote the manuscript.

Supplementary Materials

www.sciencemag.org/cgi/content/full/science.1240561/DC1
Materials and Methods
Figs. S1 and S2
Tables S1 and S2
References (8–10)
Databases S1 to S4

15 May 2013; accepted 15 July 2013
Published online 25 July 2013;
10.1126/science.1240561

Spatial Dynamics of Chromosome Translocations in Living Cells

Vassilis Roukos,¹ Ty C. Voss,² Christine K. Schmidt,^{1*} Seungtaek Lee,³
Darawalee Wangsa,⁴ Tom Misteli^{1†}

Chromosome translocations are a hallmark of cancer cells. We have developed an experimental system to visualize the formation of translocations in living cells and apply it to characterize the spatial and dynamic properties of translocation formation. We demonstrate that translocations form within hours of the occurrence of double-strand breaks (DSBs) and that their formation is cell cycle-independent. Translocations form preferentially between prepositioned genome elements, and perturbation of key factors of the DNA repair machinery uncouples DSB pairing from translocation formation. These observations generate a spatiotemporal framework for the formation of translocations in living cells.

Despite the prevalence and functional importance of chromosome translocations, the sequence and timing of events leading to their formation are largely unknown (1–3). To directly visualize the formation of chromosome translocations in living cells, we generated NIH3T3duo cells, which contain integrated into chromosome 7 the ISceI restriction endonuclease site adjacent to an array of the Lac-operator DNA sequence (LacO, 256 copies) and three integrations on chromosomes 1 and 10 (integrations on two chromosome homologs) of the TetO-ISceI-TetO array (TetO, 96 copies) (fig. S1, A and B). The LacO and TetO arrays can be visualized by stable expression of GFP-Lac repressor (LacR) or mCherry-Tet repressor (TetR) proteins, respectively (Fig. 1A and movie S1) (4). To induce double-strand breaks (DSBs), we introduced ISceI by transfection into NIH3T3duo cells; after 12 hours, LacO-ISceI and TetO-ISceI arrays colocalized with the DNA damage sensor 53BP1 and phosphorylated histone H2AX (γ H2AX), a marker of DSBs, indicating the efficient generation of DSBs (fig. S1C). Negligible colocalization of the arrays with 53BP1 or γ H2AX was observed after expression of the ISceID44A (Asp⁴⁴ → Ala) mutant, which lacks endonuclease activity (5); 53BP1 and γ H2AX strongly accumulated at 12 hours and declined gradually thereafter, indicative of successful DNA repair (fig. S1C). Efficient cutting and repair was confirmed by ligation-mediated real-time polymerase chain reaction (LM-PCR) (fig. S1D) (4).

To capture the formation of a translocation in individual cells, we used ultrahigh-throughput imaging (uHTI) (fig. S2A) (6). Upon introduction of ISceI, but not of the inactive ISceID44A mutant, the percentage of NIH3T3duo cells with colocalized (defined as <3 pixel distance, pixel size 320 nm; fig. S2, B and C) GFP-LacR and mCherry-

TetR arrays (Fig. 1B) increased from background levels of ~2% in nontransfected cells to $7.5 \pm 0.9\%$ after 24 hours ($P < 10^{-4}$) and reached a plateau of $12.1 \pm 1.2\%$ after 36 hours ($P < 10^{-3}$) (Fig. 1C). Formation of translocations was confirmed by real-time PCR (fig. S2D) and sequencing of translocation junctions (fig. S2E). Translocation frequency increased from ~1:2000 cells at 12 hours after ISceI expression to ~1:400 at 24 hours and ~1:300 at 36 hours (Fig. 1D). These data indicate that upon induction of DSBs, a considerable population of DSBs becomes paired, but that only a fraction is illegitimately repaired to form translocations. No differences in GFP-LacR or mCherry-TetR pairing frequency were observed in individual G₁-, S-, or G₂/M-phase cells ($P > 0.05$, Fig. 1E), identified by measuring the integrated intensity of 4',6-diamidino-2-phenylindole (DAPI) staining of single cells in three dimensions (fig. S3, A to D) (6). The absence of cell cycle dependence of translocation formation was confirmed by PCR of LacO-TetO translocations in cells analyzed by fluorescence-activated cell sorting (FACS) (fig. S3E), ($P > 0.05$, Fig. 1F) and in cells arrested in G₁ or at the G₂/M boundary by contact inhibition or nocodazole treatment, respectively (Fig. 1G, $P > 0.05$; fig. S3, A and F). We conclude that the formation of chromosome translocations is cell cycle-independent.

To observe translocation events in living cells, we used uHTI time-lapse microscopy to simultaneously track GFP-LacO and mCherry-TetO arrays in several thousand cells for up to 24 hours (Fig. 2, A and B) (6). The fraction of cells with paired arrays increased with time in cell populations transfected with ISceI, but not with ISceID44A (fig. S4A). Tracking of individual cells by time-lapse microscopy demonstrated that after generation of DSBs by ISceI, DSBs sampled the nuclear space by nondirectional, saltatory motion (Fig. 2; fig. S4, B and C). Some DSB pairs moved into spatial proximity and underwent cycles of local transient pairing and dissociation (fig. S4, B and C, and movie S2). A subset of transiently paired DSBs eventually engaged in persistent pairing, resulting in the stable juxtaposition of the LacO and TetO arrays over several hours, suggestive of

translocation formation (Fig. 2, A and B, and movies S3 and S4). Stable joining of LacO and TetO arrays by translocation is indicated by the coordinated motion of the two arrays over several hours (fig. S5A and movies S4 and S5). The two intrachromosomal ends marked by TetO, generated by the ISceI cut, moved in unison to the area of pairing with the LacO (Fig. 2, A and B, and movies S3 and S4). The number of the detected TetO arrays per cell, but not of the LacO arrays ($P = 0.036$), was higher in cells with paired LacO and TetO arrays ($P < 3.7 \times 10^{-7}$, fig. S5B), indicating that the two TetO sequences flanking the break separated after completion of repair toward the formation of a translocation. This observation suggests that the two intrachromosomal breaks do not separate before translocation, and that the choice of the chromosomal partners involved in the joining takes place after the chromosomal partners are in close proximity. The absence of separation of the two chromosome ends generated by a single ISceI cut provides a cell biological explanation for the occurrence of reciprocal translocations, because it would be highly unlikely that both broken chromosome ends find their two corresponding translocation partners, if the two chromosome ends separated prior to congregation with other DSBs.

Covisualization of the repair factor 53BP1 revealed its recruitment to individual DSBs and the coalescence of individual foci to form a single repair center (Fig. 2C). The combined 53BP1 focus was then resolved over time, presumably as a consequence of completed DNA repair to generate a translocation (Fig. 2C).

Single-particle tracking to monitor the movement of the fluorescently tagged LacO and TetO arrays after expression of ISceI showed that, in agreement with previous reports in mammalian cells (7, 8) but distinct from their behavior in yeast (9, 10), the mean squared displacement of DSBs in mammalian cells displayed motion properties similar to those of intact chromosomal loci (Fig. 3A). In contrast, the motion properties of translocating arrays were significantly faster (Fig. 3B) with a mean squared change in distance $\Delta r^2 = 25 \mu\text{m}^2$ after 8 hours for translocating arrays versus $\sim 10 \mu\text{m}^2$ for nontranslocating arrays.

To directly address the role of spatial positioning in translocation formation, we determined the relative positions of translocating DSBs prior to persistent pairing. The increase in paired arrays (8% at 24 hours, 13% at 48 hours, 15% at 60 hours; fig. S6A) was mirrored by a reduction in the population of cells with array separations of 2 to 6 μm (fig. S6A); this finding suggests that the majority of paired arrays arise by association of pairs within this distance range. In support of preferential pairing of proximal DSBs, reverse tracking of LacO-TetO arrays that persistently formed pairs in time-lapse movies (≥ 3 -hour colocalization; <960 nm apart) showed that more than 80% of translocating arrays were found within less than 2.5 μm of each other 5 hours before their permanent joining (Fig. 3C) and that translocating

¹National Cancer Institute, Bethesda, MD 20892, USA. ²High-Throughput Imaging Facility, National Cancer Institute, Bethesda, MD 20892, USA. ³PerkinElmer Health Sciences Inc., 940 Winter Street, Waltham, MA 02451, USA. ⁴Genetics Branch, National Cancer Institute, Bethesda, MD 20892, USA.

*Present address: Gurdon Institute and Department of Biochemistry, University of Cambridge, Cambridge CB2 1QN, UK. †Corresponding author. E-mail: misteli@mail.nih.gov

DSBs were separated by an average distance of $\sim 1.5 \mu\text{m}$ 4 hours before their persistent joining, whereas array pairs that colocalized only temporarily, and thus do not reflect translocation events, were separated by $\sim 3 \mu\text{m}$ during the same time period (Fig. 3D and fig. S6B). Although the vast majority of persistent colocalizations originated

from proximally ($< 3 \mu\text{m}$) located DSBs (Fig. 3, C and D), we also detected the occurrence of $\sim 10\%$ of persistent pairs from distally positioned DSBs (Fig. 2B, Fig. 3C, and movie S4). We conclude that the vast majority of translocations form from pre-positioned proximal DSBs, although a small subset of translocations can be generated by DSBs,

which undergo long-range motion. These results unify the “contact-first” and “breakage-first” models for how spatial organization affects translocation formation (3, 11, 12).

To explore the role of DNA repair in DSB pairing and translocation formation, we inhibited key components of the DNA damage response

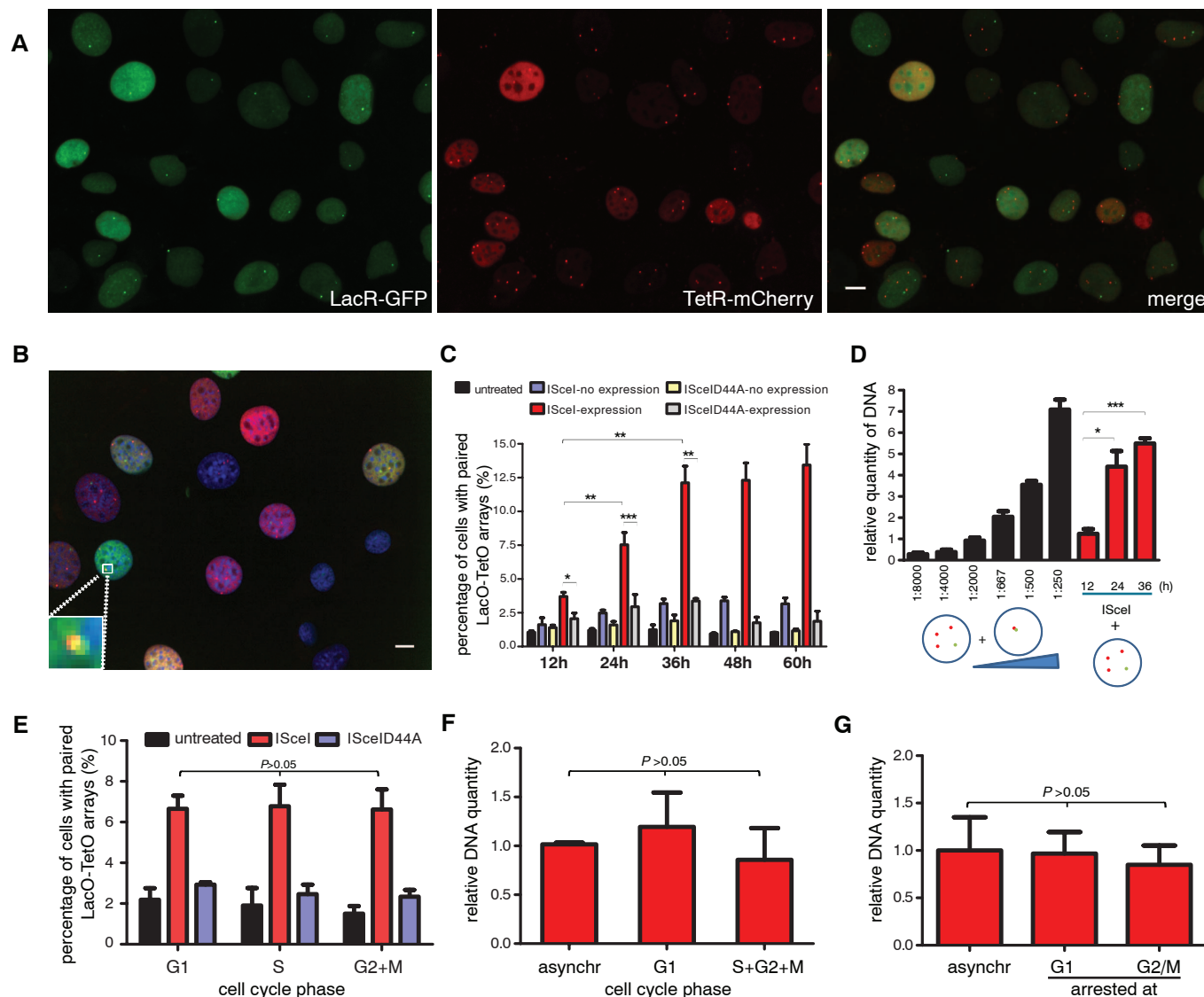


Fig. 1. An experimental system to visualize chromosome translocations in living cells. (A) NIH3T3duo cells containing an integrated LacO-*IScel* array and three TetO-*IScel*-TetO arrays, stably expressing GFP-LacR and mCherry-TetR, respectively. Scale bar, $10 \mu\text{m}$. (B) Colocalization of LacO (green) and TetO (red) arrays in NIH3T3duo cells 24 hours after expression of *IScel*. Scale bar, $10 \mu\text{m}$. (C) Percentages of the cells with paired LacO and TetO arrays in indicated cell populations. Values represent means \pm SD from at least three independent experiments (7500 to 16,500 cells with LacO and TetO analyzed per sample; $*P < 0.05$, $**P < 0.001$, $***P < 0.0001$, Student *t* test or χ^2 test). (D) Real-time PCR analysis for detection of Lac-Tet translocations in NIH3T3duo cells transfected with *IScel* or *IScelD44A* for the indicated times. PCR was performed using primers located in the Lac or Tet operator sequences. Standard curve was generated by spiking-in at the indicated ratios with NIH2/4 cells, which contain an integrated LacO-*IScel*-TetO array (4). Values are normalized to 1:2000 sample and represent means \pm SD from three independent experiments. $*P < 0.05$, $***P < 0.0001$, two-tailed Student *t* test. (E) Untreated

cells or cells transfected for 24 hours with the indicated plasmids were fixed and stained with DAPI and uHT1 was performed to assess the cell cycle status of individual cells (fig. S3, A and B). The percentage of cells with paired LacO-TetO arrays was determined. Values represent means \pm SD from three independent experiments; one-way analysis of variance (ANOVA) test or χ^2 test (*IScel* positive: G_1 , $n = 3620$; S , $n = 985$; G_2+M , $n = 1295$; *IScelD44A* positive: G_1 , $n = 1851$; S , $n = 1052$; G_2+M , $n = 891$). (F) NIH3T3duo cells transfected for 24 hours with *IScel* were stained with DAPI and sorted into G_1 or $S+G_2+M$ populations (fig. S3E). Identical numbers of gated G_1 , $S+G_2+M$, and asynchronous cells were used to extract DNA and perform real-time PCR. Values represent means \pm SD from two independent experiments ($P > 0.05$, one-way ANOVA). (G) Real-time PCR for LacO-TetO translocations in NIH3T3duo cells transfected with *IScel* for 24 hours and arrested in G_1 phase by contact inhibition or at the G_2/M boundary by treatment with nocodazole (fig. S3, A and F). Values represent means \pm SD from three experiments ($P > 0.05$, one-way ANOVA).

(DDR) machinery and monitored their effect on these processes. Inhibition of the major DNA repair and signaling kinases ATM (ataxia telangiectasia mutated) or ATR (ataxia telangiectasia and Rad3-related) by inhibitors or knockdown experiments using specific small interfering RNAs (siRNAs) (fig. S7A) had no effect on the fraction of the cells with paired DSBs ($P > 0.05$; Fig. 4, A and C). However, inhibition of DNA-dependent protein kinase (DNAPK) activity increased translocation frequency by almost an order of magnitude ($P < 10^{-4}$; Fig. 4B and fig. S7C), indicating uncoupling of DSB pairing from translocation formation. In line with a reported increase in the frequency of c-Myc and immunoglobulin heavy chain locus (IgH) translocations upon treatment of

ATM^{-/-} B cells treated with DNAPK inhibitor (13), inhibition of both ATM and DNAPK synergistically increased translocation frequency in NIH3T3duo cells (fig. S7B). In addition, when the catalytic subunit of DNAPK was eliminated by siRNA (fig. S7A), an increase in the frequency of translocations similar to the increase observed after Ku80 knockdown was observed (Fig. 4D) (14). Taken together, these data suggest that upon formation of DSBs and DSB pairing, DDR signaling acts downstream of the paired breaks to regulate the repair steps required for translocation formation, indicating that the kinase activity of DNAPK is essential to suppress translocations without affecting the physical pairing of DSBs. Consistent with this notion, DNAPK kinase

activity through autophosphorylation has been implicated in the regulation of DSB end processing, the complex dissociation from the break, and the inactivation of the enzyme (15, 16). In support of this idea, sequencing of the translocated junctions formed in the presence of DNAPK inhibitor indicated minimal end processing (fig. S7D).

Interference with the upstream repair machinery by Mirin, an inhibitor of the Mre11 component of the DNA damage-sensing MRN complex (17), or by small hairpin RNA (shRNA) against MRE11 (fig. S7A) reduced by a factor of 2 the fraction of the cells with paired Laco-TetO arrays ($P < 0.05$; Fig. 4, A and C) and translocation frequency by 23% ($P < 0.05$; Fig. 4B). Mirin suppressed the increase in frequency of translocations observed in

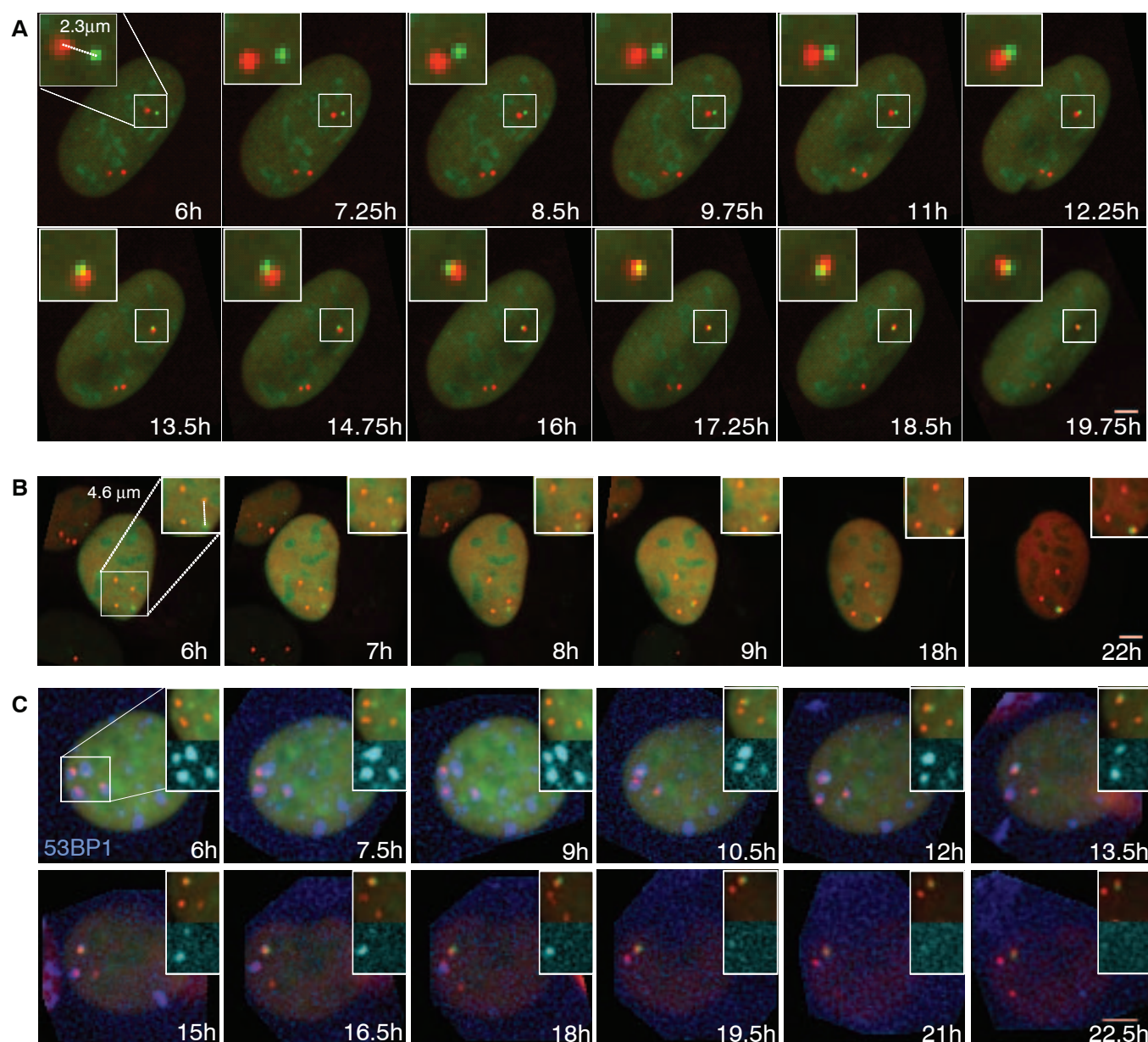


Fig. 2. Visualization of chromosome translocations by time-lapse microscopy. (A and B) Time-lapse microscopy of NIH3T3duo cells transfected with IScel. Maximal projected image sequences of representative movies show

pairing of (A) proximal and (B) distal DSBs. Scale bars, 5 μm. (C) Formation of a LacO (green)–TetO (red) translocation relative to repair foci in NIH3T3duo cells stably expressing BFP-53BP1 (blue). Scale bar, 5 μm.

the presence of the DNAPK inhibitor, which suggests that it acts upstream of DNAPK function (fig. S7B). We conclude that inhibition of Mre11 function reduces the efficiency of breaks to pair,

and that this effect results in decreased translocation frequency.

The experimental system described here serves as the basis for a comprehensive spatial and tem-

poral framework for the elucidation of the mechanisms involved in the formation of chromosome translocations and will enable in-depth analysis of translocation mechanisms in vivo.

Fig. 3. Dynamics of translocations in space and time. (A) Mean squared displacement (MSD) plots for LacO and TetO in cells transfected with ISceI or ISceID44A. Values represent means \pm SEM of pooled data from three independent experiments ($n = 66$ to 98). (B) Mean squared change in distance (Δd^2) between the LacO and the closest TetO array of cells with intact arrays (ISceID44A, $n = 34$), DSBs without pairing events (ISceI, $n = 33$), or persistent colocalization (ISceI, pairing ≥ 3 hours, $n = 43$). (C) Translocations occur predominantly from proximally located DSBs. Persistent LacO-TetO pairs (≥ 3 hours) were identified, and distance histograms between LacO and TetO arrays for the time of pairing ($t = 0$, light blue bar) and 5 hours before ($t = -5$ hours, red bars) were generated ($n = 40$). (D) Average LacO-TetO distances as a function of time before pairing for 1 hour, ≥ 3 hours, and ≥ 5 hours (all tracks, $n = 2897$; 1-hour transient interaction, $n = 1437$; at least 3 hours, $n = 615$; 5-hour pairing, $n = 157$). Values represent means \pm SD from two independent experiments.

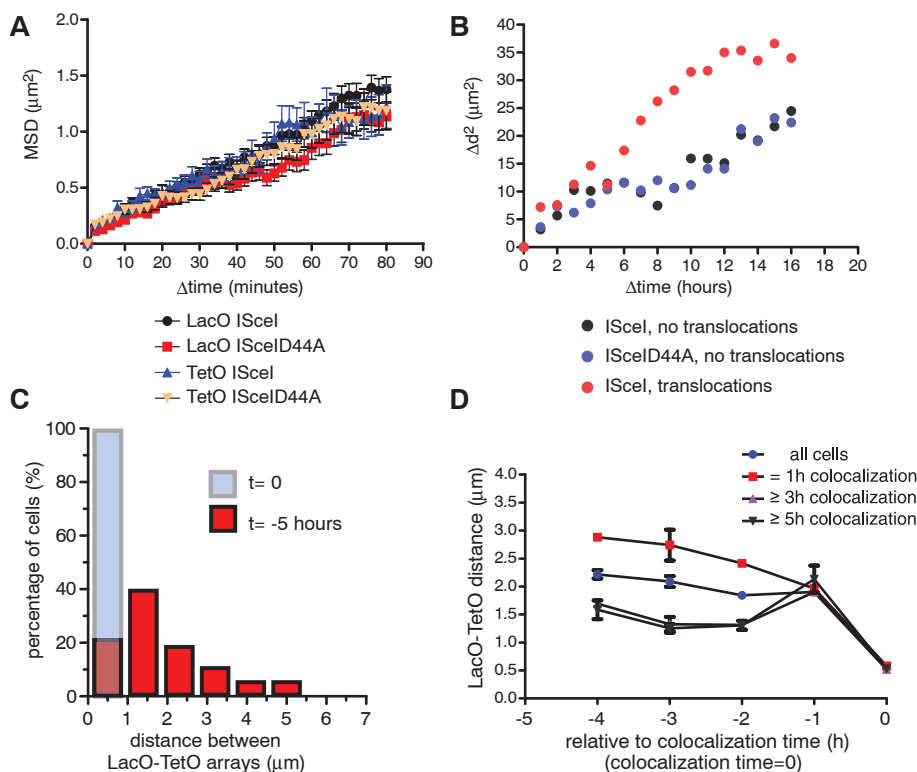
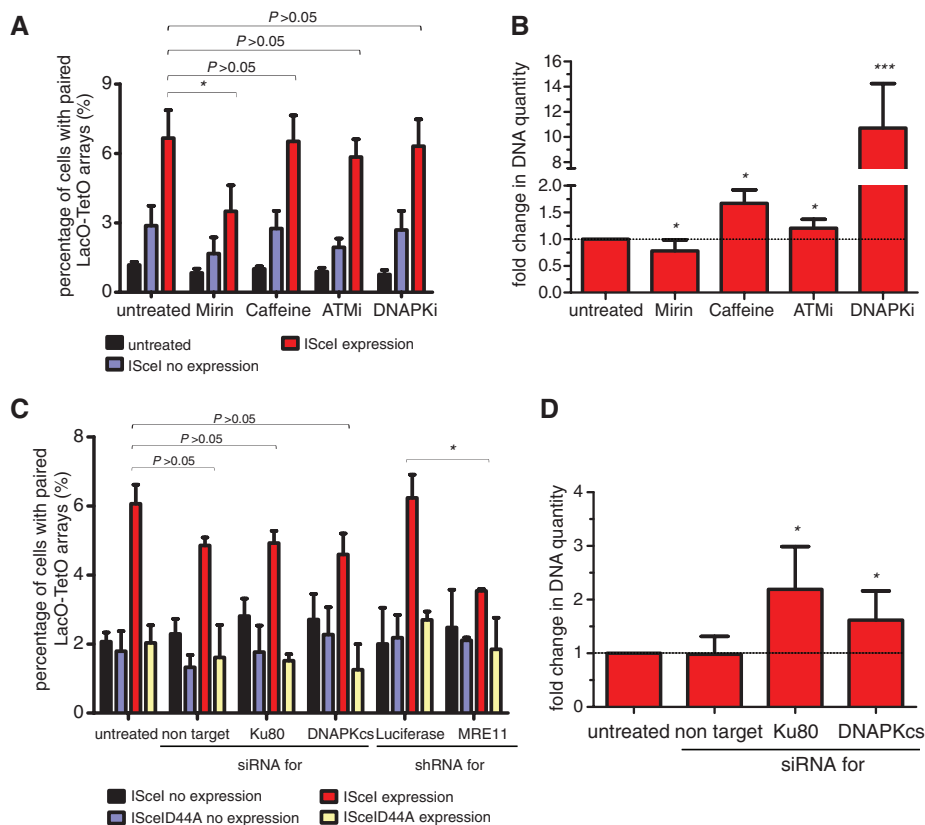


Fig. 4. Effects of DNA repair machinery on DSB pairing and translocation formation. (A) The percentage of NIH3T3duo cells with paired LacO-TetO arrays was assessed after ISceI or ISceID44A expression for 24 hours in the presence of the indicated inhibitors. Values represent means \pm SD from at least four independent experiments (Student t test or χ^2 test, $*P < 0.05$). (B) Real-time PCR on DNA from cells transfected with ISceI for 24 hours in the presence of the indicated inhibitors. The untreated sample was used as a control. Values represent means \pm SD from at least four independent experiments (Student t test, $*P < 0.05$, $***P < 0.0001$). (C) Percentage of cells with paired LacO-TetO arrays in cells treated with the indicated siRNAs or shRNAs as in (A) (Student t test, $*P < 0.05$). Values represent means \pm SD from at least two independent experiments. (D) Real-time PCR of NIH3T3duo cells treated with the indicated siRNAs performed as in (B) (Student t test, $*P < 0.05$).



References and Notes

1. F. Mitelman, B. Johansson, F. Mertens, *Nat. Rev. Cancer* **7**, 233–245 (2007).
2. T. Misteli, *Cold Spring Harb. Perspect. Biol.* **2**, a000794 (2010).
3. K. J. Meaburn, T. Misteli, E. Soutoglou, *Semin. Cancer Biol.* **17**, 80–90 (2007).
4. E. Soutoglou *et al.*, *Nat. Cell Biol.* **9**, 675–682 (2007).
5. Y. Niu, K. Tenney, H. Li, F. S. Gimble, *J. Mol. Biol.* **382**, 188–202 (2008).
6. See supplementary materials on Science Online.
7. M. J. Kruhlak *et al.*, *J. Cell Biol.* **172**, 823–834 (2006).
8. B. Jakob, J. Splinter, M. Durante, G. Taucher-Scholz, *Proc. Natl. Acad. Sci. U.S.A.* **106**, 3172–3177 (2009).
9. J. Miné-Hattab, R. Rothstein, *Nat. Cell Biol.* **14**, 510–517 (2012).
10. V. Dion, V. Kalck, C. Horigome, B. D. Towbin, S. M. Gasser, *Nat. Cell Biol.* **14**, 502–509 (2012).
11. B. E. Nelms, R. S. Maser, J. F. MacKay, M. G. Lagally, J. H. Petrini, *Science* **280**, 590–592 (1998).
12. J. A. Aten *et al.*, *Science* **303**, 92–95 (2004).
13. E. Callén *et al.*, *Mol. Cell* **34**, 285–297 (2009).
14. D. M. Weinstock, E. Brunet, M. Jasin, *Nat. Cell Biol.* **9**, 978–981 (2007).
15. J. A. Neal, K. Meek, *Mutat. Res.* **711**, 73–86 (2011).
16. N. Uematsu *et al.*, *J. Cell Biol.* **177**, 219–229 (2007).
17. A. Dupré *et al.*, *Nat. Chem. Biol.* **4**, 119–125 (2008).

Acknowledgments: We thank T. Tsukamoto, M. Jasin, E. Heard, D. Jullien, and M. Dundr for reagents; B. J. Taylor, S. Banerjee, J. Simone, and K. McKinnon for help with FACS experiments; T. Karpova (NCI Fluorescence Imaging Microscopy

Facility) for help with microscopy; and T. Ried and K. Meaburn for expertise with SKY analysis and FISH. This research was supported by the Intramural Research Program of the National Institutes of Health (NIH), NCI, Center for Cancer Research, and by an EMBO long-term fellowship (C.K.S.). We dedicate this work to the memory of Dr. Michael Potter, NCI, a giant in the field of chromosome translocations.

Supplementary Materials

www.sciencemag.org/cgi/content/full/341/6146/660/DC1
Materials and Methods

Figs. S1 to S7

Movies S1 to S5

References (18–40)

27 February 2013; accepted 10 July 2013

10.1126/science.1237150

Real-Time Dynamics of RNA Polymerase II Clustering in Live Human Cells

Ibrahim I. Cisse,^{1,2,3} Ignacio Izcedin,^{1,2} Sebastien Z. Causse,¹ Lydia Boudarene,^{1,2} Adrien Senecal,^{1,6} Leila Muresan,^{4*} Claire Dugast-Darzacq,^{1,5} Bassam Hajj,^{3†} Maxime Dahan,^{2,3,6‡} Xavier Darzacq^{1,3‡}

Transcription is reported to be spatially compartmentalized in nuclear transcription factories with clusters of RNA polymerase II (Pol II). However, little is known about when these foci assemble or their relative stability. We developed a quantitative single-cell approach to characterize protein spatiotemporal organization, with single-molecule sensitivity in live eukaryotic cells. We observed that Pol II clusters form transiently, with an average lifetime of 5.1 (\pm 0.4) seconds, which refutes the notion that they are statically assembled substructures. Stimuli affecting transcription yielded orders-of-magnitude changes in the dynamics of Pol II clusters, which implies that clustering is regulated and plays a role in the cell's ability to effect rapid response to external signals. Our results suggest that transient crowding of enzymes may aid in rate-limiting steps of gene regulation.

Transcription is believed to take place in the cell nucleus in local RNA polymerase II (Pol II)-enriched foci known as transcription factories. Clusters of Pol II have been observed in fixed cells (*1*); however, many aspects of transcription factories remain a matter of debate (*1–6*). Central questions are whether these foci are stable architectures to which DNA must translocate (*7*) or if they assemble and disassemble dynamically for transcription regulation in vivo.

Here, we engineered a human osteosarcoma cell line (U2OS) stably expressing the Pol II cat-

alytic subunit (RPB1) labeled (*8, 9*) with a photoconvertible fluorescent protein, Dendra2, replacing endogenous RPB1 (Fig. 1A and fig. S1). This cell line enabled superresolution imaging—fluorescence-based localization with an accuracy greater than the diffraction limit—of the distribution of Pol II in living cells by means of photoactivation localization microscopy (PALM) (*10, 11*). As illustrated in Fig. 1B, a nonhomogeneous distribution of Pol II was observed in living cells, which suggested Pol II clustering, comparable to Pol II distributions in fixed cells (fig. S2).

Pair-correlation PALM (pcPALM) analysis was recently used to infer spatial clustering of proteins at the cell membrane, with a correction for possible contributions of single-molecule fluorophore photophysics (*12*). pcPALM analysis on the PALM distribution of Dendra2–Pol II (fig. S3) yielded a correlation function best fitted by a spatial clustering model, both in living and fixed cells, but not in a control cell line expressing Dendra2 alone, which fitted the simpler model consistent with single-molecule homogeneous distribution (Fig. 1C and fig. S3). The average correlation radius obtained by pcPALM was 220 (\pm 17) nm in live cells, and 94 (\pm 4) nm in fixed cells (table S1); this difference can be explained by the observa-

tion that temporally distinct clustering events can occur at neighboring loci in vivo (fig. S7). Cluster sizes below the diffraction limit may explain why these structures remained uncharacterized in previous Pol II live-cell studies (*4, 5*).

PALM images are reconstructed from single detections collected over several minutes of imaging. In live-cell PALM, all the temporal information is lost in the final image. In order to discriminate between a deterministic organization model with static, dedicated Pol II clusters, which necessarily required gene translocation for activation, and a self-organization model with highly dynamic, de novo clustering of Pol II, we analyzed the temporal sequence of detections leading to a particular cluster. We investigated from the time-resolved single-molecule detection data whether the live-cell clusters have discernible and quantifiable temporal signatures indicative of their relative stability. We refer to this approach combining time-correlated detection counting and PALM as time-correlated PALM (tcPALM) (*13*).

For tcPALM analysis, we selected regions corresponding to individual high-density clusters in live-cell superresolution PALM images. For each selected Pol II cluster, we plotted the single-molecule detection profiles in the form of time series (Fig. 2, A and C) representing the rate of detection of Dendra2–Pol II fluorescence per frame. The detections did not seem uniformly distributed but appeared clustered in time. These temporal clustering events are more evident in the cumulative count of detections, where they appear as large steps (arrows in Fig. 2, B and D) in the representation. For comparison, in a fixed cluster, the cumulative detections from fixed-cell controls under identical conditions (see fig. S4A) exhibited a monotonic slope from the start of the acquisition, indicative of a local concentration of immobile proteins followed by a gradual plateau until the end of acquisition, signature of an exhaustion in detections from the static pool of proteins. By contrast, the live-cell cumulative detections showed a delayed slope onset, which suggested that the clusters dynamically assembled after acquisition started. Moreover, the slope abruptly turned into a plateau, indicative of a sudden disassembly of the cluster. Overall, these observations suggest that Pol II clustering in live cells exhibited transient dynamic signatures clearly distinct from static clusters.

¹Functional Imaging of Transcription, CNRS UMR8197, Ecole Normale Supérieure, Institut de Biologie de l'ENS, IBENS, Paris, 75005 France. ²Laboratoire Kastler Brossel, CNRS UMR8552, Département de Physique, Institut de Biologie de l'Ecole Normale Supérieure, 46 rue d'Ulm, 75230 Paris cedex 05, France. ³Transcription Imaging Consortium, Janelia Farm Research Campus, 19700 Helix Drive, Ashburn, VA 20147, USA. ⁴DYOGEN, CNRS, UMR8197, Ecole Normale Supérieure, Institut de Biologie de l'ENS, IBENS, Paris, 75005 France. ⁵Université Paris Diderot, Paris Cité Sorbonne, 75013 Paris, France. ⁶Université Pierre et Marie Curie—Paris 6, 75005 Paris, France.

*Present address: CNRS, Centre de Génétique Moléculaire, UPR3404, 91198 Gif-sur-Yvette, France.

†Present address: Laboratoire Physico-Chimie Curie, Institut Curie, CNRS UMR168, 75248 Paris, France.

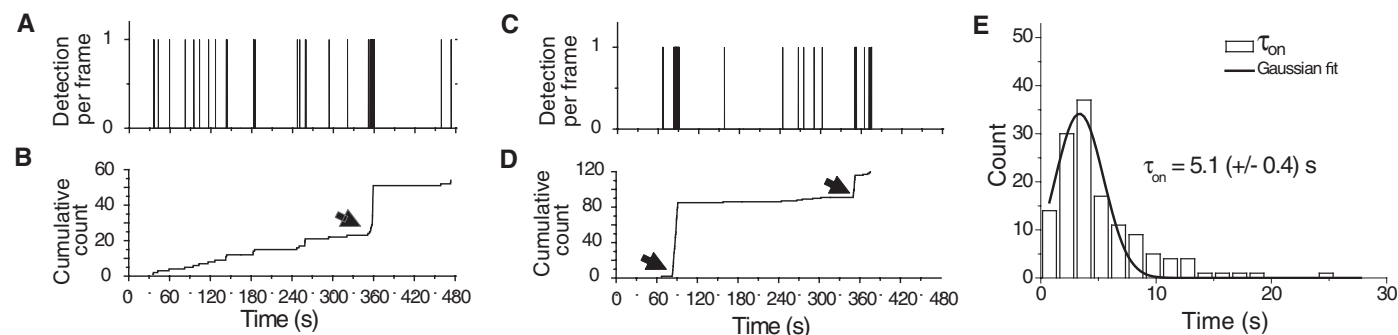
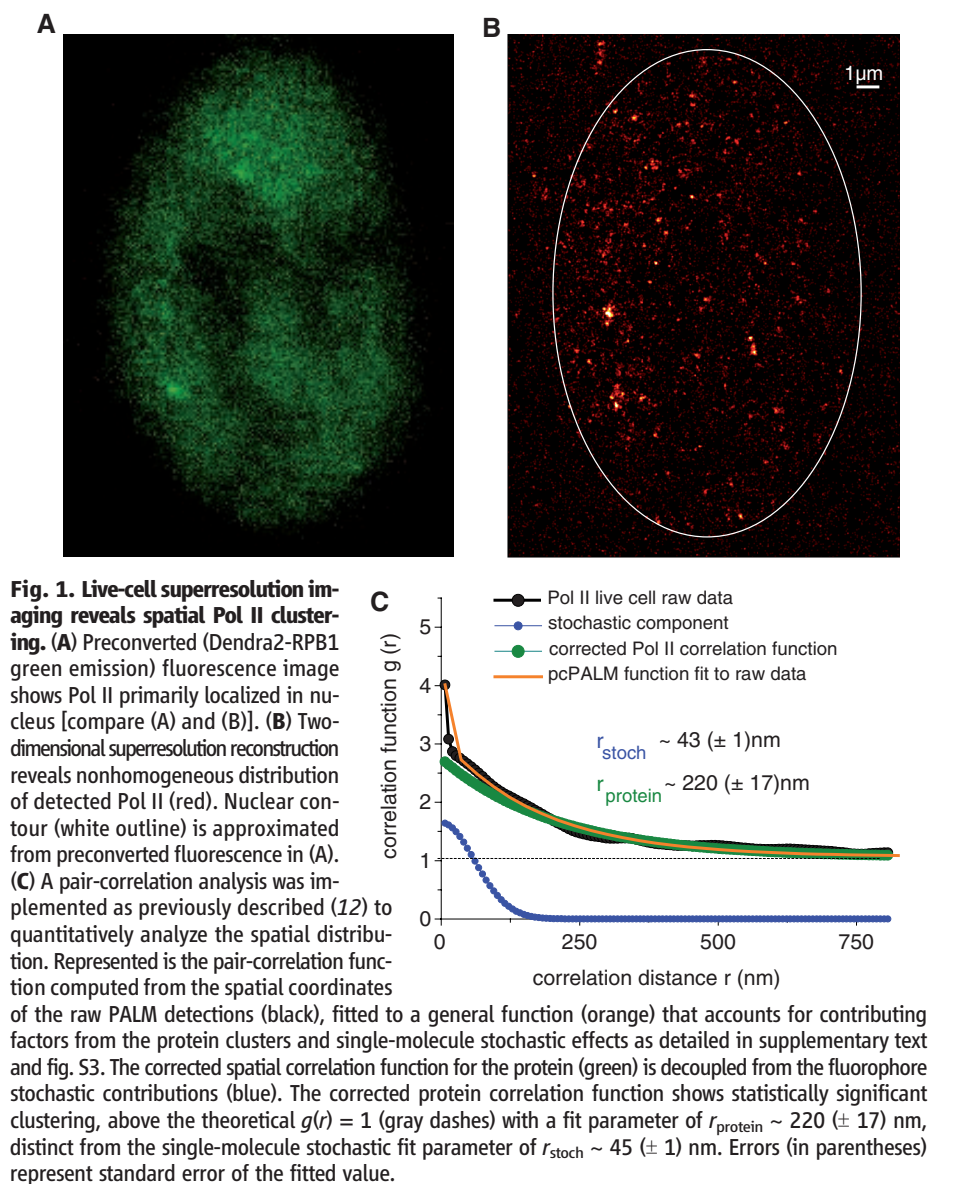
‡Corresponding author. E-mail: maxime.dahan@curie.fr (M.D.); darzacq@ens.fr (X.D.)

To quantify the apparent kinetics of Pol II clustering, we implemented a burst dwell-time analysis. We recorded both a dwell time (τ_{on}) cor-

responding to the apparent lifetime of a selected burst and the count of detections per burst (burst size). The time separating individual bursts (τ_{off})

was often larger than the imaging time (500 s) and, therefore, could not be determined precisely. For the bursts detected, we obtained a distribution of τ_{on} with an average lifetime of $5.1 (\pm 0.4)$ s, and spanning less than 30 s (Fig. 2E). This observation is consistent with our previous study (4) on an artificial gene array, where 99% of Pol II molecules interacted very transiently at the active locus. These results support de novo spatio-temporal clustering of Pol II, which is more consistent with a self-organization model of transcription.

We hypothesized that, if there is any relevance of Pol II clustering to transcription, it should be reflected by systematically changing the cell's transcriptional state. We therefore measured the cluster dynamics through serum induction, when specific response genes are transcribed at much higher efficiency (14–17). Similar to the normal growth case, temporal clustering events were observed after serum stimulation (Fig. 3, A and B). The average τ_{on} was $48 (\pm 9)$ s (Fig. 3C), an order-of-magnitude increase from normally grown cells. As shown in Fig. 3C, the distribution of τ_{on} revealed a variation of bursting lifetimes spanning up to two orders of magnitude. Larger clusters were also observed under serum stimulation (Fig. 3D). Depicted in the examples in Fig. 3, A and B, two clusters exhibiting comparable total detection counts might exhibit 10-fold difference in bursting lifetimes, which suggests that the apparent recruitment rate differs considerably from one locus to another. These observations are consistent with the notion that individual gene loci might exhibit different clustering kinetics. By contrast, Pol II clustering kinetics in serum-deprived cells showed relatively little difference from the kinetics measured in normally grown cells (fig. S5), which indicates that the orders-of-magnitude changes in Fig. 3 are unique to the serum stimulation. In addition, accumulation of Pol II could be observed at the transcription locus of an induction-responsive (β -actin) gene by colocalization analysis with endogenous mRNA imaged by fluorescence in situ hybridization (FISH) (fig. S6); therefore, individual Pol II clusters can be linked to a gene locus with active transcription. These results correlate



assembly (arrows) and disassembly (plateaus). (E) The distribution of apparent burst lifetimes (τ_{on}) is represented with a Gaussian fit. Average τ_{on} obtained was $5.1 (\pm 0.4)$ s, and the fit mean obtained was $4.2 (\pm 0.4)$ s. Errors (in parentheses) represent standard error of the mean. We analyzed 104 clusters from four cells.

assembly (arrows) and disassembly (plateaus). (E) The distribution of apparent burst lifetimes (τ_{on}) is represented with a Gaussian fit. Average τ_{on} obtained was $5.1 (\pm 0.4)$ s, and the fit mean obtained was $4.2 (\pm 0.4)$ s. Errors (in parentheses) represent standard error of the mean. We analyzed 104 clusters from four cells.

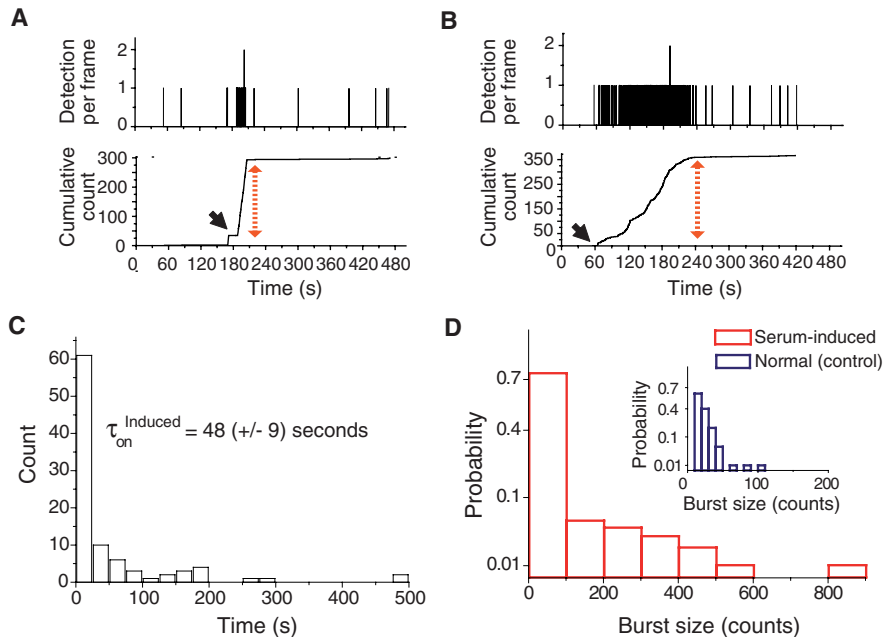


Fig. 3. Pol II cluster dynamics are dependent on transcription induction. (A and B) Time-dependent detection profiles of individual clusters show several fold higher detection counts (red arrow) during cluster formation (black arrows) with serum induction compared with clusters under normal cell growth (Fig. 2, A and C). (C) Distribution of apparent burst lifetimes (τ_{on}) has considerably broadened with an average τ_{on} for serum induction of $48 (\pm 9)$ s. (D) The probability distribution of burst sizes (detection counts per burst) for serum induction shows broadening with higher counts for burst events that were not present in clusters from normal growth cells (D, inset); the average burst size was $89 (\pm 14)$ and $23 (\pm 1)$ detection counts for serum-induced and normal growth cells, respectively. Errors (in parentheses) represent standard error of the mean. We analyzed 106 clusters from six cells.

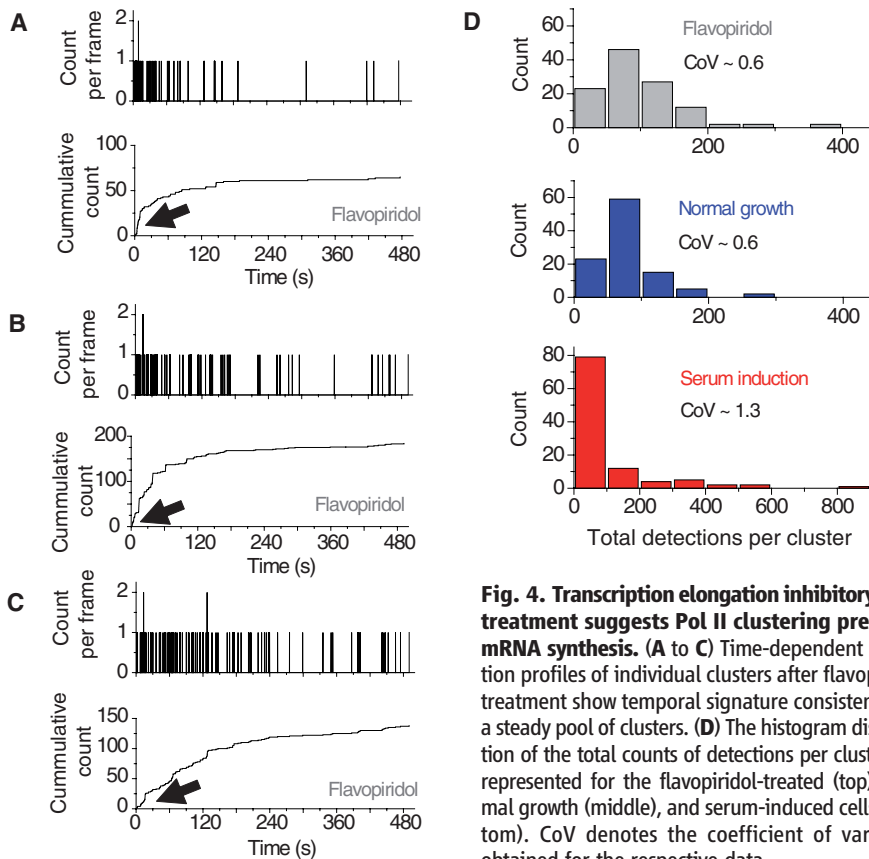


Fig. 4. Transcription elongation inhibitory drug treatment suggests Pol II clustering precedes mRNA synthesis. (A to C) Time-dependent detection profiles of individual clusters after flavopiridol treatment show temporal signature consistent with a steady pool of clusters. (D) The histogram distribution of the total counts of detections per cluster are represented for the flavopiridol-treated (top), normal growth (middle), and serum-induced cells (bottom). CoV denotes the coefficient of variation obtained for the respective data.

Pol II clustering dynamics to gene expression regulation at specific loci.

Next, we investigated whether Pol II clustering precedes or succeeds mRNA synthesis (transcription elongation). The inhibition of the positive elongation factor (P-TEFb) impedes productive elongation (4, 6, 18, 19). In chromatin immunoprecipitation (ChIP) experiments, P-TEFb inhibition did not affect polymerases accumulated at the promoter, whereas depletion in the transcribed region of genes was observed (18, 20). We hypothesized that, if clustering reflected an accumulation of the elongating Pol II, then P-TEFb inhibition should substantially reduce clustering. In contrast, upon treatment with the P-TEFb inhibitor flavopiridol (19, 21), Pol II clusters were more pronounced (Fig. 4). These results suggest that Pol II clustering occurs before promoter pause release (20), a regulatory step preceding productive transcription elongation.

After inhibition, 89% of clusters showed a stable signature, akin to fixed-cell static clusters (Fig. 4, A to C), with a slope onset in the cumulative detections from the start of acquisition followed by a gradual plateau. Furthermore, the histogram of the total counts of detections per cluster in flavopiridol-treated cells had a distribution comparable to that of normally grown cells. For both, the coefficient of variation was ~ 0.6 , which suggested that the same populations of gene loci are likely sampled in normal growth and after drug treatment. By contrast, these distributions are distinct from the serum-activated cluster dynamics, which resulted in a coefficient of variation two times larger (Fig. 4D). These results imply that the presence of Pol II clusters might depend on the presence of the preinitiation complex or initiating polymerases but not on elongation. We propose that such dynamic clustering of Pol II may play a role in facilitating and regulating macromolecular complex assembly during the rate-limiting (4, 5, 22, 23) transcription preinitiation and initiation steps (fig. S8).

Protein clustering has been reported in many cellular processes, including DNA replication, DNA repair, mRNA splicing, ribosomal RNA synthesis, and signal transduction. In many cases, macromolecular complex assembly is identified as a rate-limiting step, and detailed kinetic characterization could help elucidate the regulatory mechanisms. The PALM-based approach developed here can be broadly used for other proteins to study cellular processes with high spatial and temporal resolution, *in vivo*, with single-molecule sensitivity.

References and Notes

1. P. R. Cook, *Science* **284**, 1790–1795 (1999).
2. P. Fraser, W. Bickmore, *Nature* **447**, 413–417 (2007).
3. T. Misteli, *Cell* **128**, 787–800 (2007).
4. X. Darzacq et al., *Nat. Struct. Mol. Biol.* **14**, 796–806 (2007).
5. J. Yao, K. M. Munson, W. W. Webb, J. T. Lis, *Nature* **442**, 1050–1053 (2006).
6. H. Kimura, K. Sugaya, P. R. Cook, *J. Cell Biol.* **159**, 777–782 (2002).

7. H. Sutherland, W. A. Bickmore, *Nat. Rev. Genet.* **10**, 457–466 (2009).
8. M. Becker *et al.*, *EMBO Rep.* **3**, 1188–1194 (2002).
9. K. Sugaya, M. Vigneron, P. R. Cook, *J. Cell Sci.* **113**, 2679–2683 (2000).
10. E. Betzig *et al.*, *Science* **313**, 1642–1645 (2006).
11. S. T. Hess, T. P. K. Girirajan, M. D. Mason, *Biophys. J.* **91**, 4258–4272 (2006).
12. P. Sengupta *et al.*, *Nat. Methods* **8**, 969–975 (2011).
13. We note that, in live-cell PALM experiments, only a fraction of the molecules present can be localized; highly mobile or nonphotoactive molecules may be present but not detected. Therefore, tcPALM is not a measure of the total number of molecules present but rather an indication of the relative fluctuations of fluorescent molecules transiently present at a given locus.
14. R. E. Herrera, P. E. Shaw, A. Nordheim, *Nature* **340**, 68–70 (1989).
15. N. Mackman, B. J. Fowler, T. S. Edgington, J. H. Morrissey, *Proc. Natl. Acad. Sci. U.S.A.* **87**, 2254–2258 (1990).
16. H. R. Herschman, *Annu. Rev. Biochem.* **60**, 281–319 (1991).
17. V. M. Weake, J. L. Workman, *Nat. Rev. Genet.* **11**, 426–437 (2010).
18. Z. Ni *et al.*, *Mol. Cell. Biol.* **28**, 1161–1170 (2008).
19. O. Bensaude, *Transcription* **2**, 103–108 (2011).
20. P. B. Rahl *et al.*, *Cell* **141**, 432–445 (2010).
21. S.-H. Chao *et al.*, *J. Biol. Chem.* **275**, 28345–28348 (2000).
22. N. J. Fuda, M. B. Ardehali, J. T. Lis, *Nature* **461**, 186–192 (2009).
23. D. R. Larson, D. Zenklusen, B. Wu, J. A. Chao, R. H. Singer, *Science* **332**, 475–478 (2011).

Acknowledgments: We acknowledge J. T. Lis, I. Golding, R. Phillips, O. Bensaude, and E. Bertrand for valuable discussions. We thank members of the Darzacq, Dahan, and Howard Hughes Medical Institute–Janelia Farm Transcription Imaging Consortium groups for suggestions. I.I.C. was supported by fellowships from the European Molecular Biology Organization and the Foundation Pierre

Gilles de Gennes (FPGG). I.I. acknowledges the Netherlands Organization for Scientific Research and FPGG for financial support. A.S. was supported by La Ligue nationale contre le cancer. L.M. acknowledges support from Centre de Génétique Moléculaire UPR 3404. This work was supported by grants Agence Nationale de la Recherche Pol2Kinetics to X.D. and DYNAST to X.D. and M.D.; X.D. and M.D. acknowledge the support of Nikon France.

Supplementary Materials

www.sciencemag.org/cgi/content/full/science.1239053/DC1
Materials and Methods
Supplementary Text
Figs. S1 to S8
Table S1
References

11 April 2013; accepted 17 June 2013
Published online 4 July 2013;
10.1126/science.1239053

The Hologenomic Basis of Speciation: Gut Bacteria Cause Hybrid Lethality in the Genus *Nasonia*

Robert M. Brucker^{1*} and Seth R. Bordenstein^{1,2*}

Although the gut microbiome influences numerous aspects of organismal fitness, its role in animal evolution and the origin of new species is largely unknown. Here we present evidence that beneficial bacterial communities in the guts of closely related species of the genus *Nasonia* form species-specific phylosymbiotic assemblages that cause lethality in interspecific hybrids. Bacterial constituents and abundance are irregular in hybrids relative to parental controls, and antibiotic curing of the gut bacteria significantly rescues hybrid survival. Moreover, feeding bacteria to germ-free hybrids reinstates lethality and recapitulates the expression of innate immune genes observed in conventionally reared hybrids. We conclude that in this animal complex, the gut microbiome and host genome represent a coadapted “hologenome” that breaks down during hybridization, promoting hybrid lethality and assisting speciation.

Although the gut microbiome influences numerous fitness traits in animals, little attention has been given to how the microbiome is structured between closely related species and how the microbiome contributes to the origin of new species. By incorporating the microbiome into the biological species concept (1) and the Bateson-Dobzhansky-Muller model of hybrid incompatibilities (2), theoretical evidence specifies that negative epistasis between host genes and the host microbiome can accelerate the evolution of hybrid lethality and sterility (3).

We recently established that when environmental factors such as diet are controlled for, species of the *Nasonia* wasp complex harbor phylosymbiotic gut microbiotas—a term introduced here to denote microbial community relationships that recapitulate the phylogeny of their host (4). Similar to phylogenomics, phylosymbiosis asserts that the relationships of microbiomes

across host species maintain an ancestral signal of the host's evolution. The phylosymbiotic signal could be a consequence of host immune genes that rapidly evolve in a continual arms race with components of the microbiome.

We hypothesize that the phylosymbiotic gut microbiome within species breaks down in hybrids via epistatic interactions between the microbiome and nuclear and/or cytoplasmic genomes, leading to hybrid lethality. Using the parasitoid wasp genus *Nasonia*, we set out to experimentally determine the influence of the microbiome on hybrid lethality. The *Nasonia* genus consists of several species of haplodiploid parasitoid wasps that are readily hybridized. *Nasonia vitripennis* diverged approximately 1 million years ago from the ancestor of *Nasonia giraulti* and *Nasonia longicornis*, which themselves diverged less than 400,000 years ago (5). In the laboratory, all three species are reared on the fly host *Sarcophaga bullata* under identical conditions. *Nasonia* offspring are oviposited by the mother inside the puparium of the fly, where the eggs develop to adulthood before emerging from the fly host in about 14 days. In the absence of *Wolbachia* infections, reciprocal crosses between species produce fertile, diploid, F₁ hybrid

females (6). However, hybrid lethality is observed in F₂ male offspring, because they are haploid recombinants of their grandparents. Interspecies crosses of *N. vitripennis* and *N. giraulti* or *N. longicornis* result in F₂ hybrid males exhibiting up to ~90% lethality during larval development, whereas *N. giraulti* and *N. longicornis* hybrids only exhibit ~8% hybrid lethality (6–10).

In this study, we scored the average number of hybrid and nonhybrid eggs, larvae, pupae, and adults produced by *Nasonia* females ($n = 48$ females, each parasitizing one *S. bullata* host per developmental period) and determined that 78% of hybrid lethality occurs between the first- and the fourth-instar (L4) larval stages (Fig. 1A). There was a slight asymmetry in the number of surviving *N. vitripennis*/*N. giraulti* and *N. giraulti*/*N. vitripennis* hybrids (the F₂ hybrid genotype denotes grandfather or grandmother), but the difference was not statistically significant ($P = 0.36$, Mann-Whitney U test). In contrast, hybrids of the younger sister species *N. giraulti* and *N. longicornis* exhibited little to no F₂ hybrid lethality, as previously reported (6) (fig. S1A). The hybrid lethality between *N. vitripennis* and *N. giraulti* is often diagnosed by larval melanization—a prominent immune response to pathogens in arthropods (Fig. 1B). We postulated that because parental *Nasonia* species assemble phylosymbiotic gut microbiomes (4) (Fig. 2), the melanization and lethality in larval hybrids result in part from altered gut microbiomes.

First, we tested the hypothesis that bacterial community differences occur between larval hybrids and nonhybrids during the L2 larval stage, just before the point of F₂ hybrid male lethality. We focused on the *N. vitripennis*/*N. giraulti* hybrid microbiota, because this genotype elicits elevated lethality as compared to the reciprocal cross; however, this asymmetry was insignificant in our experiments. As hypothesized, the microbiota of *N. vitripennis*/*N. giraulti* hybrids was unlike that of either parental species in both bacterial abundance (Fig. 2B) and diversity (Fig. 2C), whereas the negative control *N. longicornis*/*N. giraulti* hybrids that survived (6) (fig. S1A) had a parental-like microbiota. Both hybridizations

¹Department of Biological Sciences, Vanderbilt University, Nashville, TN 37232, USA. ²Department of Pathology, Microbiology, and Immunology, Vanderbilt University, Nashville, TN 37232, USA.

*Corresponding author. E-mail: bruckerm@gmail.com (R.M.B.); s.bordenstein@vanderbilt.edu (S.R.B.)

had a substantial number of novel and rare operational taxonomic units (OTUs, $P = 0.06$, chi square test with Yates correction, fig. S3). The single major difference in the *N. vitripennis*/*N. giraulti* hybrid microbiota was a shift in the dominant bacterial OTU from *Providencia* sp. IICDBZ10 in pure species controls (81 and 96% of the reads in *N. vitripennis* and *N. giraulti*, respectively) to *Proteus mirabilis* strain SNBS in the *N. vitripennis*/*N. giraulti* hybrid (86% of reads). These two species are natural residents of the *Nasonia* parental species. *P. mirabilis* SNBS is the dominant species in *N. longicornis*, and *Providencia* sp. IICDBZ10 is the dominant species in *N. vitripennis* and *N. giraulti*.

Second, to test whether the *N. vitripennis*/*N. giraulti* F₂ lethality in hybrids is conditional on the microbiome, we reared conventional (on a normal *S. bullata* host), germ-free (without bacteria), and bacteria-inoculated (without bacteria first and subsequently inoculated with specific bacteria) hybrids and nonhybrids. For germ-free rearing of *Nasonia*, we used *Nasonia* rearing medium (NRM), a liquid medium that we recently developed for culturing *Nasonia* without its *S. bullata* fly host (11). If hybrid lethality in larvae is intrinsically based on negative epistasis between host incompatibility genes, then the null hypothesis is that *N. vitripennis*/*N. giraulti* and *N. giraulti*/*N. vitripennis* hybrid lethality occurs regardless of germ-free or conventional rearing conditions. However, if the lethality is conditional on the microbiome, then we expect that germ-free rearing of hybrids will rescue hybrid lethality.

A comparison of results indicates a near-complete rescue of hybrid lethality in germ-free hybrids relative to pure species controls under germ-free conditions (Fig. 1C, $F_{1,46} = 1.207$, $P = 0.277$ for *N. vitripennis* to *N. giraulti*/*N. vitripennis*, and $F_{1,46} = 0.824$, $P = 0.369$ for *N. giraulti* to *N. vitripennis*/*N. giraulti*). Therefore, hybrids that would typically show severe lethality under conventional rearing conditions exhibit a striking increase in survival. In a subsequent experiment, when F₁ female hybrids oviposited their F₂ male hybrid offspring into germ-free (GF) *S. bullata* fly hosts, there was also a marked increase in survival relative to hybrids that were reared on conventional (Cv) *S. bullata* fly hosts (fig. S1B). In contrast, in *N. longicornis*/*N. giraulti* and *N. giraulti*/*N. longicornis* hybrids, survival values of germ-free hybrids and nonhybrid controls were expectedly high and similar to each other (fig. S1A, Mann-Whitney U test, $P > 0.5$).

If the NRM generally increased survival, it should also affect nonhybrid survival as it would that of hybrids. However, average survival rates of controls decreased insignificantly on NRM. Further, germ-free hybrids that were reared on NRM inoculated with bacterial strains once again yielded higher lethality as compared to parental controls (Fig. 1C). The common *Nasonia* bacteria *Providencia rettgeri* strain IITRP2 and *Proteus mirabilis* strain SNBS were isolated from parental *Nasonia* and added to germ-free NRM. Upon con-

suming a 1:1 inoculum of these bacteria, germ-free hybrids exhibited severe lethality in comparison to nonhybrids (Fig. 1C, $F_{1,46} = 23.863$, $P < 0.001$) and at levels similar to those of conventionally reared hybrids (Fig. 1C, Mann-Whitney U test, $P > 0.5$). Furthermore, mono-inoculants of antibiotic-resistant (AR) *P. rettgeri* and *Enterococcus faecalis* strain XJALT-127-2YG1 isolated from *Nasonia*, as well as green fluorescent protein (GFP)-expressing *E. coli*, also recapitulated significant hybrid lethality (fig. S1B, $F_{1,46} = 36.372$, $P < 0.001$, fig. S2A, $F_{1,46} = 7.281$, $P < 0.01$; see the supplementary text).

The requirement of gut bacteria for interspecific hybrid lethality in *Nasonia* is remarkable given that several studies previously mapped quantitative trait loci with hybrid lethality to the wasp

chromosomes and mitochondria (5, 7, 8, 10). Indeed, marker transmission ratio distortion (MTRD) analyses in surviving *Nasonia* F₂ hybrids demonstrate an allelic bias at several loci in the genome toward one parental genome, indicating that an incompatible allele from the other parental species contributes to hybrid lethality (5, 9–11). Based on our observation that germ-free hybrid *Nasonia* exhibit a significant increase in survival, we predicted that MTRD would revert to near-Mendelian inheritance ratios in the germ-free hybrids. We selected four markers—three within genomic regions associated with hybrid lethality and one control locus that is expected to have 50:50 inheritance ratios—and genotyped *N. vitripennis*/*N. giraulti* and *N. giraulti*/*N. vitripennis* hybrid *Nasonia* L4 larvae. Larvae

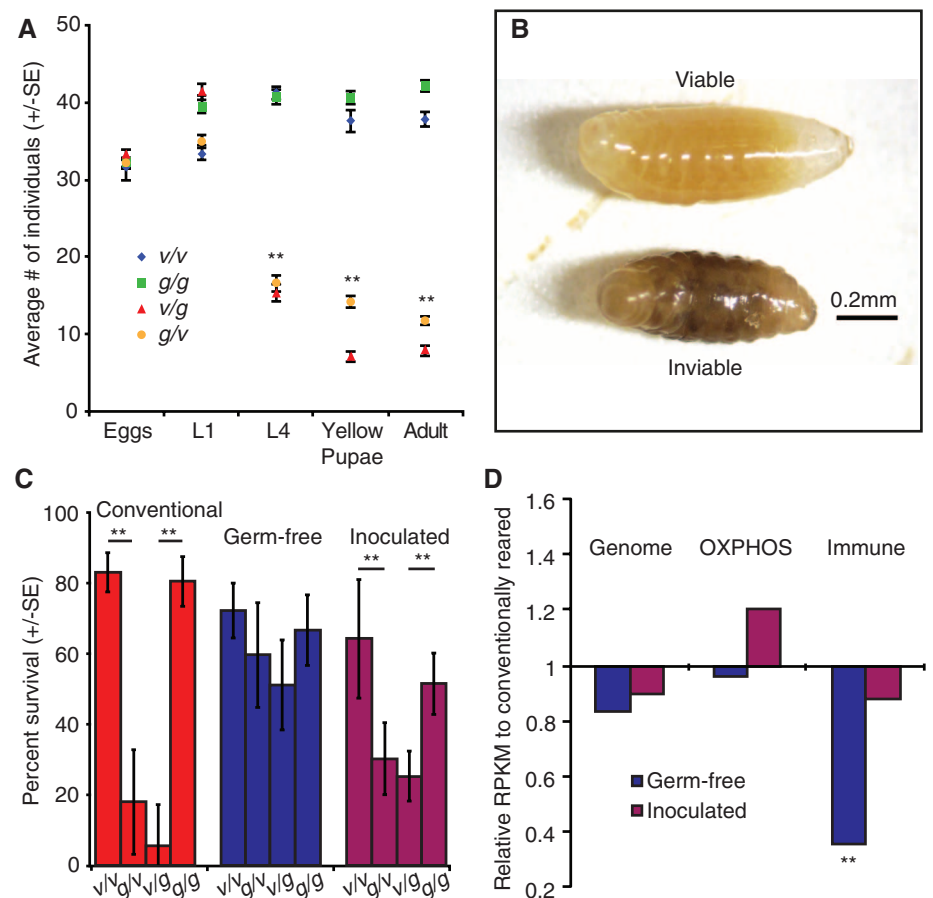


Fig. 1. The symbiotic and genetic basis of hybrid lethality. (A) Average number of F₂ males (±SEM) within the *S. bullata* host during development of the egg, L1 larvae, L4 larvae, yellow red-eye pupae, and eclosed adults conventionally reared on *S. bullata* hosts. The F₂ hybrid genotype is indicated as paternal/maternal where v = *N. vitripennis* and g = *N. giraulti*. Mann-Whitney U test, ** $P < 0.001$. $n = 48$ replicates per developmental stage. (B) (Top) *N. vitripennis* L3 larva that is healthy and alive; (bottom) hybrid v/g L3 larva that is melanized and dead. (C) Percent of survival (±SEM) from egg to pupae of conventionally reared (red), germ-free (blue), and inoculated (purple; germ-free individuals inoculated with *Providencia* and *Proteus* bacteria in the NRM) *N. vitripennis* (v) and *N. giraulti* (g) parental species and hybrids. Mann-Whitney U test, ** $P < 0.001$, $F_{1,46} = 23.863$ and 12.962, *** $P < 0.001$, an average of triplicate experiments with $n = 48$ hosts for egg and pupae counts per conventional cross, and $n = 24$ wells containing 12 to 42 larvae per germ-free and inoculated cross. (D) Average hybrid v/g gene expression relative to conventionally reared hybrids for the total genome, OXPHOS genes, and immunity genes (t test, ** $P < 0.001$). RPKM denotes reads per kilobase per million mapped reads. Conventional $n = 14$, germ-free $n = 20$, and inoculated $n = 20$ individuals were sequenced and averaged.

reared conventionally yielded the expected distorted frequencies for each of the MTRD markers (5), whereas germ-free hybrids exhibited typical Mendelian inheritance at all markers except for MM5.03 (table S1). A large bias against *N. vitripennis* alleles remained (a frequency of 0.08), although the frequency was significantly higher from the MTRD under conventional rearing (*N. vitripennis* frequency of 0.20, *Z* test of proportions, $P < 0.001$).

One explanation for a microbial basis for hybrid lethality is that negative epistasis (mismatched gene-gene interactions) occurs between chromosomal genes and the microbiome. These interactions can accelerate the number of potential hybrid incompatibilities under the Bateson-Dobzhansky-Muller model of genetic incompatibilities (3). To better understand the mechanisms behind host-microbe interactions that underscore hybrid lethality, we compared the transcriptomes of germ-free L2 hybrid larvae with those of con-

ventionally reared and bacteria-inoculated L2 hybrid larvae (just before lethality). The genome-wide expression patterns and the oxidative phosphorylation (OXPHOS) family of genes, a family thought to be causative in hybrid lethality, were similar across all three rearing conditions (Fig. 1D and supplementary text). However, the 489 innate immune genes in *Nasonia* that we previously annotated (12) yielded, on average, a significant decrease in transcript levels in germ-free individuals relative to conventional or inoculated hybrids (Fig. 1D, *t* test, $P < 0.001$). Specifically, 39.7% of the immune genes were underexpressed by twofold or greater in germ-free hybrids relative to conventional and inoculated hybrids, and 4.9% were overexpressed (fig. S4 and table S2). Conventionally reared and inoculated hybrids, in turn, have similar immune gene expression (Fig. 1D, *t* test, $P = 0.104$). However, it is important to note that immune genes may be only one of several possible functional categories that break down

between the host and microbiome during hybrid lethality.

Causes for the postzygotic hybrid lethality in *Nasonia* have traditionally been attributed to host cytonuclear interactions and host gene-by-environment interactions (7–10). However, this study shows that severe hybrid lethality in larvae can also be due to gene-microbe interactions with beneficial members of the phyllosymbiotic gut microbiome. In this light, the phyllosymbiotic microbiome can be understood as an addition to the coadapted genomes of a host organism rather than an arbitrary amalgam. Linking the microbiome and host genome underscores the hologenome as a unit of evolution and blurs the lines between what biologists typically demarcate as the environment (13) and the genotype of a species. Based on the mounting evidence for speciation by symbiosis (3), it is becoming clearer that a unified theory of evolution that considers the nuclear genome, cytoplasmic organelles, and microbiome as interacting components in the origin of new species is an emerging frontier for biology.

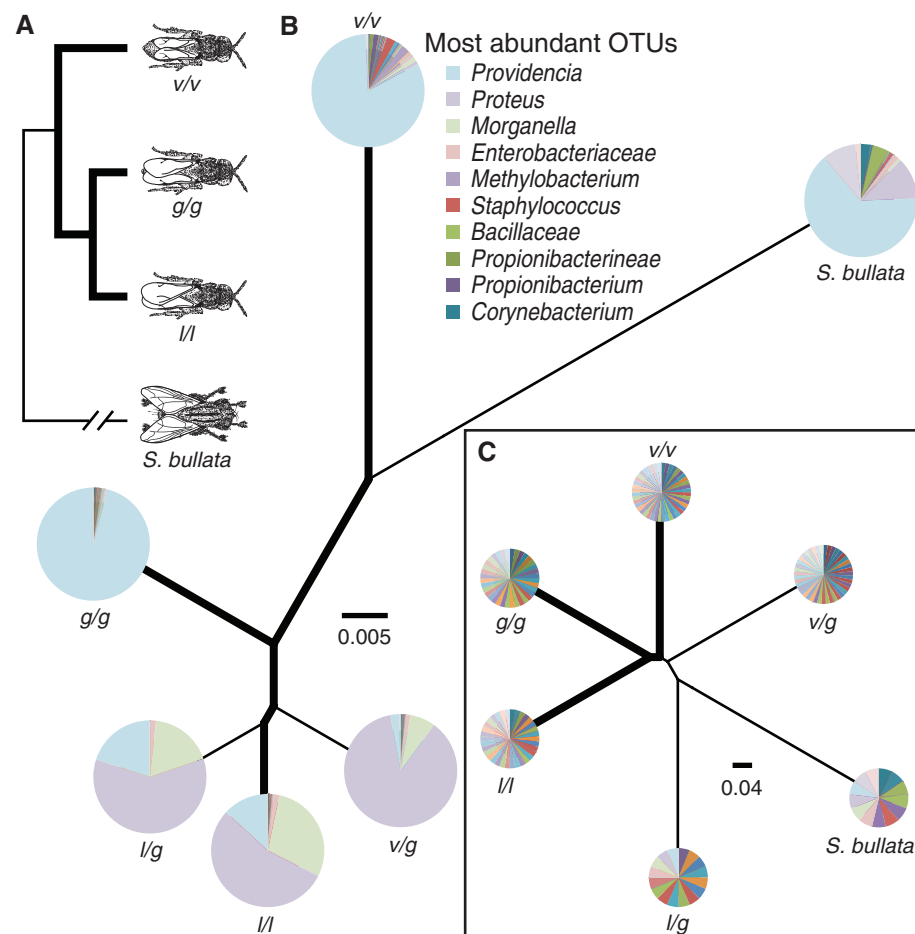


Fig. 2. Phyllosymbiosis and speciation in *Nasonia*. (A) Simplified phylogeny of *Nasonia* (bold lines) and *S. bullata* flies. *N. vitripennis* (v), *N. giraulti* (g), and *N. longicornis* (l). (B) A weighted, to abundance of each OTU, UniFrac cluster analysis depicting the microbial relationships of the three *Nasonia* species (bold lines) and two hybrids for the L2 larval microbiota, as well as the unparasitized *Sarcophaga* host pupa. The tip of each branch is a pie chart depicting the abundance of each genus of bacteria within the host insects. Genera of the top 10 most abundant bacterial genera are listed in the key. (C) An unweighted UniFrac cluster analysis depicting the microbial relationships; pie charts at the tip of each branch represent the genera level, bacteria diversity sampled.

References and Notes

1. E. Mayr, *Animal Species and Evolution* (Harvard Univ. Press, Cambridge, MA, 1963).
2. H. A. Orr, *Genetics* **144**, 1331–1335 (1996).
3. R. M. Brucker, S. R. Bordenstein, *Trends Ecol. Evol.* **27**, 443–451 (2012).
4. R. M. Brucker, S. R. Bordenstein, *Evolution* **66**, 349–362 (2012).
5. J. H. Werren *et al.*, *Science* **327**, 343–348 (2010).
6. S. R. Bordenstein, F. P. O'Hara, J. H. Werren, *Nature* **409**, 707–710 (2001).
7. J. A. J. Breeuwer, J. H. Werren, *Evolution* **49**, 705 (1995).
8. O. Niehuis, A. K. Judson, J. Gadau, *Genetics* **178**, 413–426 (2008).
9. T. Koevoets, O. Niehuis, L. van de Zande, L. W. Beukeboom, *Heredity* **108**, 302–311 (2012).
10. T. Koevoets, L. van de Zande, L. W. Beukeboom, *J. Evol. Biol.* **25**, 304–316 (2012).
11. R. M. Brucker, S. R. Bordenstein, *PLoS ONE* **7**, e51269 (2012).
12. J. H. Werren, D. W. Loehlin, *Cold Spring Harbor Protoc.* **2009**, 10.1101/pdb.emo134 (2009).
13. I. Zilber-Rosenberg, E. Rosenberg, *FEMS Microbiol. Rev.* **32**, 723–735 (2008).

Acknowledgments: Sequences are available at the Dryad Digital Repository, doi:10.5061/dryad.3c190. We thank S. Bordenstein and A. Williams for technical assistance during the development of the in vitro cultivation method; L. Funkhouser, D. Sutherland, and C. Wogland for their assistance in genotyping *Nasonia* hybrids; R. Pauly for bioinformatic assistance; and B. Jovanovic, L. Funkhouser, K. Jernigan, and N. Renner for providing feedback on an earlier version of the manuscript. We apologize in advance to colleagues whose papers we could not cite due to space restrictions. This research was made possible by NSF award DEB 1046149 to S.R.B.

Supplementary Materials

www.sciencemag.org/cgi/content/full/science.1240659/DC1
Materials and Methods
Supplementary Text
Figs. S1 to S4
Tables S1 to S6
References (14–26)

17 May 2013; accepted 8 July 2013
Published online 18 July 2013;
10.1126/science.1240659

Positive Feedback Between PU.1 and the Cell Cycle Controls Myeloid Differentiation

Hao Yuan Kueh,^{1*} Ameya Champhekar,¹ Stephen L. Nutt,² Michael B. Elowitz,^{1,3} Ellen V. Rothenberg^{1*}

Regulatory gene circuits with positive-feedback loops control stem cell differentiation, but several mechanisms can contribute to positive feedback. Here, we dissect feedback mechanisms through which the transcription factor PU.1 controls lymphoid and myeloid differentiation. Quantitative live-cell imaging revealed that developing B cells decrease PU.1 levels by reducing PU.1 transcription, whereas developing macrophages increase PU.1 levels by lengthening their cell cycles, which causes stable PU.1 accumulation. Exogenous PU.1 expression in progenitors increases endogenous PU.1 levels by inducing cell cycle lengthening, implying positive feedback between a regulatory factor and the cell cycle. Mathematical modeling showed that this cell cycle–coupled feedback architecture effectively stabilizes a slow-dividing differentiated state. These results show that cell cycle duration functions as an integral part of a positive autoregulatory circuit to control cell fate.

The transcription factor PU.1 is a central component of the regulatory gene network controlling lymphoid and myeloid development from hematopoietic progenitors (1–4). PU.1 is expressed at intermediate levels in progenitors, and its subsequent levels become a determinant of lymphoid and myeloid fate choices, with down-regulation of PU.1 required for B and T cell development and higher PU.1 levels favoring the development of macrophages or myeloid dendritic cells (5–8).

Differential regulation of PU.1 during lymphoid and myeloid development involves transcriptional positive feedback of PU.1 (9). PU.1 positively regulates its own transcription in myeloid cells and stem cells, but not in lymphoid cells (10–13), and forms additional positive-feedback loops through mutual inhibition with other hematopoietic regulators (7, 14). Positive feedback can, in principle, generate multiple stable states with different levels of regulatory factors, possibly accounting for the observed differences in PU.1 levels. However, it is unclear how PU.1 is regulated during myeloid or lymphoid development, what feedback mechanisms are involved, and why particular feedback architectures may have been selected.

PU.1 promotes growth in several progenitor types (1, 15), but also coordinates cell cycle arrest with differentiation in myeloid progenitors. Reduced PU.1 activity causes acute myeloid leukemia, where progenitors fail to initiate differentiation growth arrest (16–19); conversely, reexpression of PU.1 restores growth arrest (17, 20, 21). However, it is unclear whether PU.1's effect on the cell cycle influences its ability to regulate its own levels and control differentiation.

In this work, we analyzed PU.1 and cell cycle regulation in individual cells during early macrophage and B cell development (Fig. 1A). We isolated fetal liver progenitors (FLPs, Lin[−]Kit⁺CD27⁺) from mice containing a bicistronic PU.1–green fluorescent protein (GFP) knock-in reporter (2), cultured them with cytokines supporting B cell and macrophage differentiation, and analyzed PU.1-GFP levels over time by time-lapse imaging or flow cytometry (Fig. 1 and figs. S1 and S2) (22). PU.1-GFP levels varied linearly with nuclear PU.1 protein levels in this culture system (fig. S3). We found that progenitors initially expressed PU.1-GFP at uniform levels but subsequently up- or down-regulated PU.1-GFP over time (Fig. 1, B to D, and fig. S4). Cells up-regulating PU.1-GFP expressed the macrophage markers CD11b and F4/80, but not the granulocyte marker Gr1, and were also large and adherent, reflecting differentiation into macrophages [Fig. 1, B and C (top right), and fig. S4]. In contrast, cells down-regulating PU.1-GFP expressed the B cell marker CD19 and were also small and round, reflecting differentiation into B cells [Fig. 1, B and C (bottom right), and figs. S2 and S4]. Developing granulocytes and persisting progenitor-like cells maintained PU.1-GFP levels similar to those of starting progenitors (Fig. 1B and fig. S4). Both macrophages and B cells preferentially developed from Fcγ receptor II/III (FcγR2/3)^{low} FLPs, whereas FcγR2/3⁺ FLPs mostly differentiated into granulocytes (fig. S5 and see below). These results validate the use of our system for analyzing PU.1 regulation during B cell or macrophage differentiation.

Changes in PU.1 levels during B cell or macrophage differentiation may result from changes in either the rate of PU.1 synthesis or the rate of PU.1 removal (Fig. 1E), which would occur predominantly through dilution due to cell division (23, 24), as PU.1's protein half-life is substantially longer than the progenitor cell cycle length (fig. S6). To determine how PU.1 levels were

regulated, we measured PU.1 synthesis rates and cell cycle lengths for individual cells within defined progenitor, macrophage (Mac), and B cell populations (Fig. 1D and fig. S7). PU.1 synthesis rates could be measured by the slopes of stable PU.1-GFP increase over time [$(\Delta p/\Delta t)$ for an observed cell cycle; p , GFP or PU.1 protein; t , time], Fig. 1E and fig. S7; fig. S8 shows GFP stability], independent of average PU.1-GFP levels. Although cell movement precluded comprehensive multi-generational tracking (fig. S9), we analyzed time-lapse movies that allowed accurate measurements of average cell cycle lengths and PU.1 synthesis rates for different cell populations. Progenitors comprised two subpopulations with higher and lower rates of PU.1 synthesis (Fig. 1, F and G). Switches between states with high and low PU.1 synthesis rates were infrequent across cell division (Fig. 1G), suggesting that these states are maintained stably in most cells. Macrophages had more PU.1-GFP and PU.1 protein than any of the progenitors (Fig. 1H and fig. S3), as expected. Surprisingly, however, their PU.1 synthesis rates were not higher than that of the progenitor subpopulation with high PU.1 synthesis rates (Fig. 1, F to H, and fig. S9). Instead, macrophages had significantly longer cell cycle lengths (Fig. 1, F to H, and fig. S9) and descended from ancestors with shorter cell cycle lengths but similar PU.1 synthesis rates (Mac early, Fig. 1, F to H). Thus, developing macrophages increase their PU.1 levels by lengthening their cell cycles, which allows PU.1 to accumulate to higher levels. In contrast, emerging B cells had significantly lower PU.1 synthesis rates than progenitors but similar cell cycle lengths (Fig. 1, F to H, and fig. S9). Therefore, unlike macrophages, B cells decrease PU.1 levels by reducing PU.1 transcription.

Increased PU.1 levels caused by cell cycle lengthening may be functionally important for macrophage differentiation or may simply reflect a consequence of differentiation growth arrest (Fig. 2A). To distinguish between these two possibilities, we tested whether artificial cell cycle lengthening promotes myeloid differentiation in a PU.1-dependent manner. We induced cell cycle lengthening in FLPs by two different methods: either by retroviral transduction of cyclin-dependent kinase (CDK)–inhibitors p21^{Cip1} (Cdkn1a) or p27^{Kip1} (Cdkn1b) (Fig. 2B and fig. S10) or by treatment with PD0332991, a CDK4/6 inhibitor (25) (Fig. 2, C and D). Induced cell cycle lengthening in progenitors increased PU.1-GFP and PU.1 protein levels and the percentage of myeloid cells, with these increases being most dramatic in the slowest-dividing cells (Fig. 2, B and C). This differentiation depended on PU.1 activity, because in cells transduced with a competitive inhibitor of PU.1 (PU.1-ets) (fig. S11), PD0332991 treatment still increased PU.1-GFP, but no longer increased the fraction of CD11b-expressing cells as in empty vector (EV)–transduced cells (Fig. 2, C and D). These results suggest that PU.1 accumulation as a result of cell cycle lengthening is functionally important for macrophage differentiation.

¹Division of Biology, California Institute of Technology, Pasadena, CA, USA. ²The Walter and Eliza Hall Institute of Medical Research, Parkville, Victoria, Australia. ³Howard Hughes Medical Institute and Department of Bioengineering, California Institute of Technology, Pasadena, CA, USA.

*Corresponding author. E-mail: kueh@caltech.edu (H.Y.K.); evroth@its.caltech.edu (E.V.R.)

To examine how positive transcriptional feedback regulates PU.1's own expression (10–13), we tested how PU.1 and dominant negative PU.1 transduction affected transcription of the PU.1-GFP reporter. Forced expression of PU.1-ets in FLPs reduced PU.1-GFP levels (fig. S12), implying that a threshold level of PU.1 activity is important for maximal PU.1 expression. Conversely, flow cytometry and imaging showed that exogenous PU.1 up-regulated PU.1-GFP and CD11b while inhibiting PU.1-GFP down-regulation and CD19 up-regulation (Fig. 3, A and B, and fig. S13). However, imaging analysis (Fig. 1E) showed that exogenous PU.1 expression did not increase endogenous PU.1 synthesis rates; instead, it induced cell cycle lengthening in a subpopulation of progenitors, which led to the increase in PU.1-GFP levels (Fig. 3, C and D, and fig. S14). This cell cycle lengthening occurred preferentially in FcγR2/3^{low} FLPs (fig. S5C), which accounted for most of the macrophage potential in the FLP population. Thus, high PU.1 levels

promote cell cycle lengthening in cells capable of generating macrophages, which, in turn, allows high PU.1 levels to be stably maintained. Taken together, our results provide evidence for a regulatory circuit architecture involving positive feedback on a transcription factor through the cell cycle.

Insight into cell cycle lengthening mechanisms emerged from analysis of regulatory gene expression in PU.1-transduced progenitors (Fig. 3E). Consistent with PU.1 autoregulation through cell cycle lengthening rather than transcriptional acceleration, PU.1 transduction did not affect endogenous PU.1 mRNA levels, but it reduced the levels of cell cycle promoting factors cyclin D2 (Cnd2) and Cdc25a. Consistent with other studies (26–28), exogenous PU.1 also reduced the levels of Myb and Myc, growth-promoting proto-oncogenes that are down-regulated during normal differentiation. Exogenous PU.1 also reduced levels of p21 and Gfi1, which can mediate quiescence, although these are up-regulated by PU.1 in stem cells (13). Thus, the mechanisms underlying

PU.1-mediated cell cycle arrest during macrophage differentiation appear distinct from those operating in stem cell quiescence.

How can positive feedback between PU.1 and the cell cycle stabilize a slow-dividing macrophage state with high PU.1 levels? To address this issue, we constructed a stochastic single-cell dynamical model, where PU.1 inhibits the G₁-to-S cell cycle transition above a threshold concentration (Fig. 4A, top). This model exhibits bistability, supporting both a fast-dividing, low-PU.1 state and a slow-dividing, high-PU.1 state (Fig. 4A and figs. S15 and S16). In our simple model, G₁ checkpoint release depends solely on PU.1 levels; during macrophage development, other regulatory factors also promote checkpoint release and, thus, may regulate feedback engagement. Once the high PU.1 state is established, it is relatively stable compared with the corresponding state of a hypothetical pure transcriptional feedback system with similar parameters, which exhibits more frequent spontaneous switches between states due to

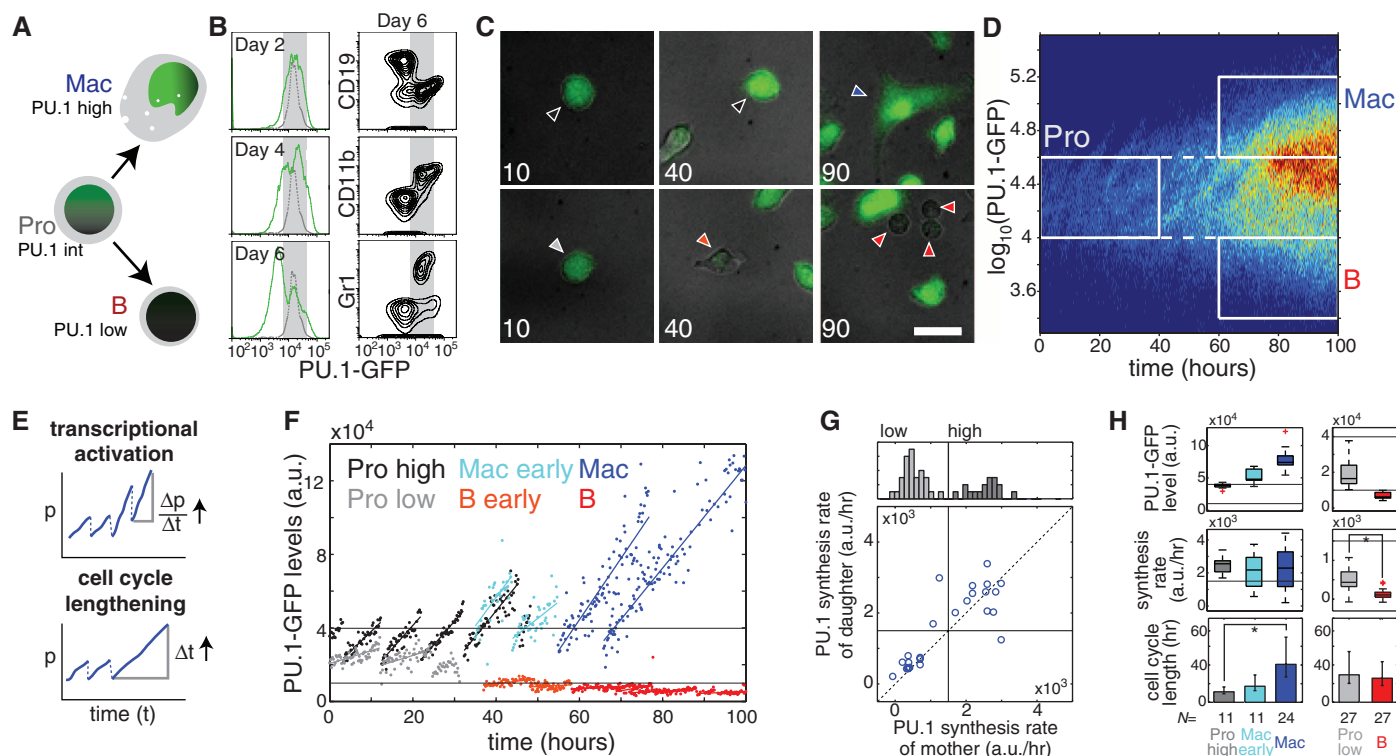


Fig. 1. Cell cycle lengthening drives PU.1 up-regulation during macrophage development. FLPs (Lin-cKit⁺CD27⁺) from embryonic day 13.5 PU.1-GFP mice were cultured with B cell- and macrophage-supporting cytokines [stem cell factor (SCF), interleukin-3 (IL-3), IL-7, Flt3L, macrophage colony-stimulating factor] and analyzed with time-lapse imaging or flow cytometry. (A) Schematic showing myeloid and lymphoid development from hematopoietic progenitor cells. Mac, macrophage; Pro, progenitor; B, B cell. (B) Histograms (left) show PU.1-GFP levels measured after the indicated number of days in culture. Dotted lines give initial PU.1-GFP levels. Flow cytometry plots (right) show CD19, CD11b, and Gr1 levels against PU.1-GFP after 6 days. (C) Merged differential interference contrast (gray) and PU.1-GFP fluorescence (green) images of cultured FLPs, taken after the indicated number of hours. Cells with PU.1-GFP time traces shown in (F) are marked with correspondingly colored arrowheads. Scale bar, 20 μ m. (D) Heat map showing PU.1-GFP levels over time for all imaged cells. Rectangles define progenitor, macrophage, and

B cell populations. (E) Alternative hypotheses for PU.1-GFP up-regulation in macrophages. The PU.1 synthesis rate for a single cell is given by $\Delta p/\Delta t$ over the entire observed cell cycle. (F) Representative single-cell PU.1-GFP time traces for different cell populations. Data are taken from lineages shown in fig. S9. Horizontal lines give PU.1-GFP level thresholds for the defined cell populations. a.u., arbitrary units. (G) Histogram (top) showing distribution of PU.1 synthesis rates in progenitors. Scatter plot showing the relation between PU.1 synthesis rates in mother versus daughter cells. Horizontal and vertical lines indicate the threshold for progenitor subpopulations with higher and lower rates of PU.1 synthesis. (H) Plots comparing mean PU.1-GFP levels (top), PU.1 synthesis rates (middle), and cell cycle lengths (bottom) in different cell populations. Red crosses indicate box-plot outliers. Bottom error bars represent 95% confidence intervals. Asterisks indicate significantly different means ($P < 10^{-7}$, one-tailed t test). Data are representative of three independent experiments. N , number of cells.

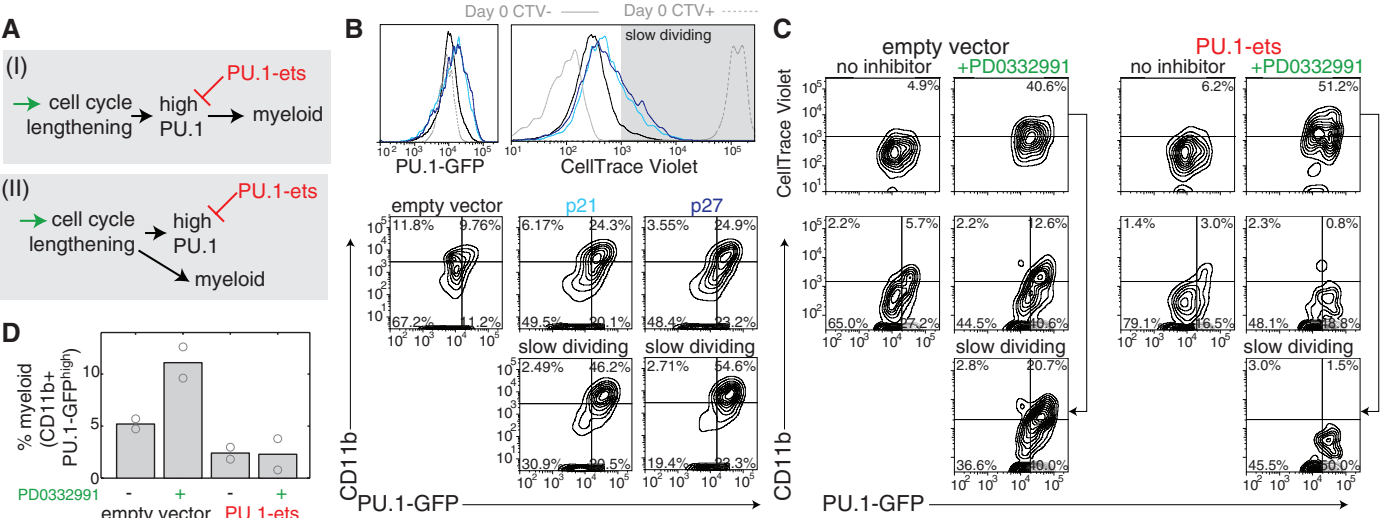


Fig. 2. PU.1 accumulation due to cell cycle lengthening is important for myeloid differentiation. (A) Two hypotheses for the function of high PU.1 levels in differentiating macrophages. (B) FLPs were transduced with EV, p21, or p27; cultured for 4 days; and analyzed by flow cytometry. Histograms (top) show CellTrace Violet (CTV) (Invitrogen, Carlsbad, California) and PU.1-GFP levels for different transduced populations. The gray shaded area indicates a slow-dividing cell gate. Flow plots (bottom) show CD11b versus PU.1-GFP levels

for different transduced cell populations. Percentages of cells in each quadrant are shown. (C) FLPs transduced with EV or PU.1 antagonist (PU.1-ets) were cultured for 3 days with or without 2.1 μM CDK4/6 inhibitor PD0332991 and analyzed by flow cytometry. Flow plots show CellTrace Violet (top) or CD11b (bottom) versus PU.1-GFP for the different conditions. (D) Effects of PD0332991 and PU.1-ets transduction on the percentage of myeloid cells. Bars represent means of two independent experiments, and circles give individual measurements.

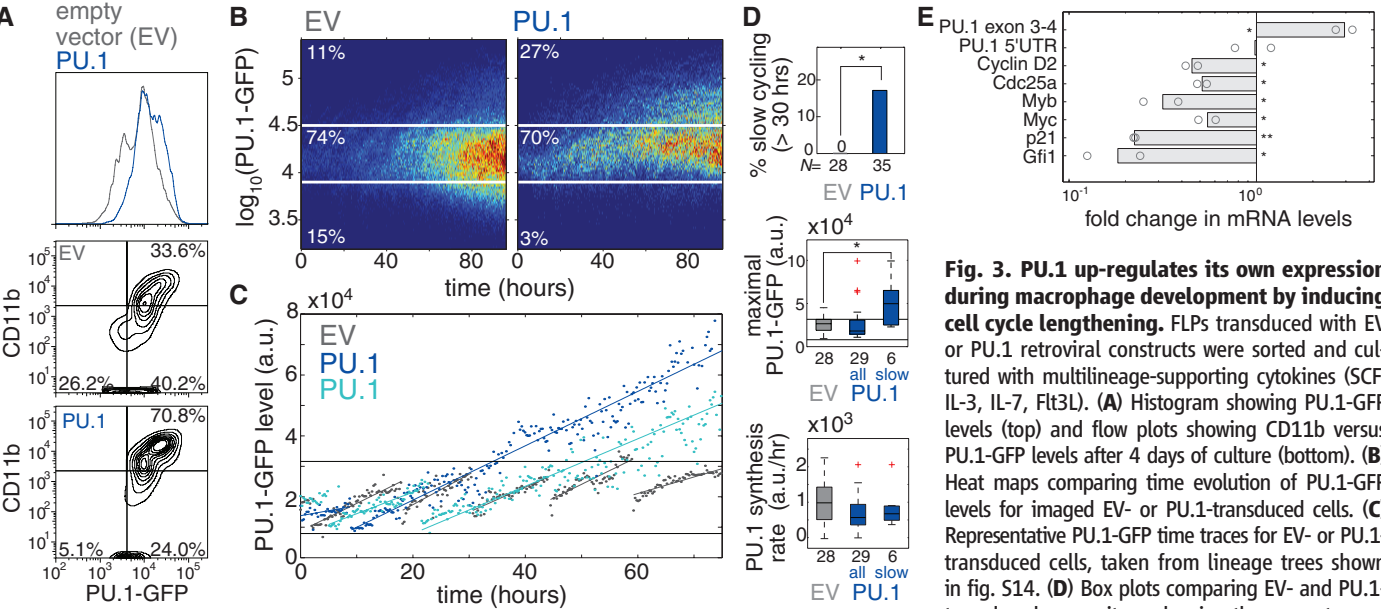


Fig. 3. PU.1 up-regulates its own expression during macrophage development by inducing cell cycle lengthening. FLPs transduced with EV or PU.1 retroviral constructs were sorted and cultured with multilineage-supporting cytokines (SCF, IL-3, IL-7, Flt3L). (A) Histogram showing PU.1-GFP levels (top) and flow plots showing CD11b versus PU.1-GFP levels after 4 days of culture (bottom). (B) Heat maps comparing time evolution of PU.1-GFP levels for imaged EV- or PU.1-transduced cells. (C) Representative PU.1-GFP time traces for EV- or PU.1-transduced cells, taken from lineage trees shown in fig. S14. (D) Box plots comparing EV- and PU.1-transduced progenitors, showing the percentage of slow dividing cells (top), maximal PU.1-GFP levels (middle), and PU.1 synthesis rate (bottom) for both the entire PU.1-transduced progenitor population and slow-dividing progenitors alone. Red crosses indicate outliers. Asterisks indicate significantly different means (percent slow dividing, $P < 0.05$, χ^2 test, $df = 1$; maximal PU.1-GFP, one-tailed t test, $P < 0.005$). Data are representative of two independent experiments. N , number of cells. (E) EV- or PU.1-transduced FcγR2/3^{low} FLPs were cultured for 2 days, harvested for RNA, and analyzed with quantitative real-time polymerase chain reaction. Bar chart shows mRNA level fold change for the indicated genes in PU.1-transduced cells compared with EV-transduced cells. Bars represent the means of two independent experiments, and circles represent individual measurements (* $P < 0.1$; ** $P < 0.01$; two-tailed t test). UTR, untranslated region.

larger, more rapid protein fluctuations (fig. S17) (22). Taken together, these results show how cell cycle-coupled feedback provides a simple mechanism to support multiple stable states that exhibit different rates of cell division. Besides cell cycle-coupled feedback, cells also contain PU.1 transcriptional feedback, which appears to take effect at lower PU.1 levels (fig. S12).

When both feedbacks are incorporated simultaneously, the model can generate three stable steady states with low, medium, and high levels of PU.1 corresponding to the pro-B, progenitor, and macrophage populations, respectively (Fig. 4, B and C). Because of its lower PU.1 threshold, transcriptional feedback allows developing B cells to down-regulate PU.1 while maintaining similar

rates of division, consistent with observations. We propose this dual feedback system as a working model for further study of PU.1 regulation during lymphoid and myeloid development. Could cell cycle-coupled feedback operate in other systems? A similar type of bistability was recently observed in a bacterial synthetic cell cycle-coupled feedback circuit (29). In the

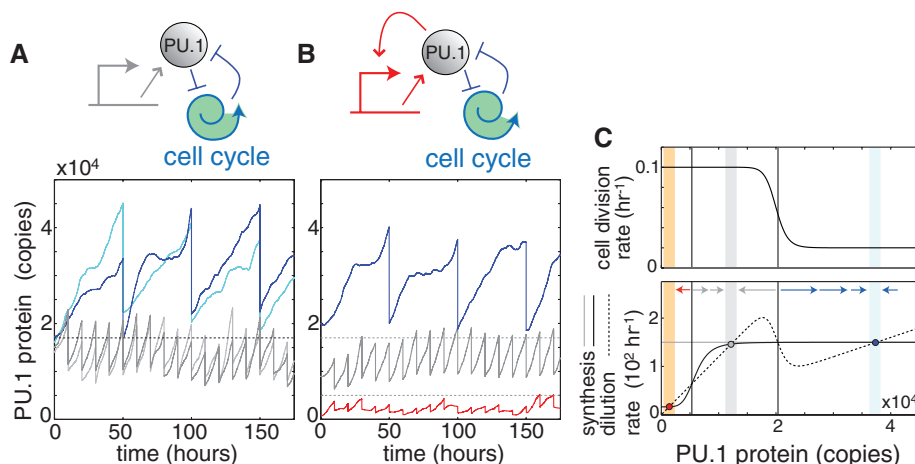


Fig. 4. A cell cycle-coupled feedback loop stably maintains a slow-dividing differentiated state. (A) Schematic of a cell cycle-coupled positive-feedback loop (top) and time traces from stochastic simulations of this circuit architecture (bottom), showing four cells with different initial PU.1 levels but identical rate constants. (B) Schematic of a hybrid cell cycle-coupled transcriptional positive-feedback circuit (top) and stochastic simulations of this architecture (bottom), showing maintenance of three stable, steady states. (C) Phase diagrams for the two circuit architectures, showing PU.1 synthesis rates (black, hybrid; constant thin gray, cell cycle-coupled), as well as dilution rate and cell-division rate (same for both models) against PU.1 levels. Red, gray, and blue circles denote B cell, progenitor, and macrophage steady states, respectively. Arrows indicate the flow of the system. A thorough analysis and discussion of all models is given in the supplementary mathematical appendix (22).

context of cell differentiation, other fate regulators have also been shown to promote cell cycle arrest (30). Although some transcription factors are notoriously short-lived (e.g., Fos), recent studies have found that many mammalian proteins are stable over multiple cell cycles (23, 24), and other regulatory proteins may resemble PU.1 in this respect. Moreover, induced cell cycle lengthening is known to promote differentiation in other systems (31, 32), suggesting that mechanisms based on accumulation of stable fate regulators during cell cycle arrest may be more prevalent. Where cell fate decisions depend on the balance between two factors with different stabilities, such as PU.1 and the unstable C/EBP α (33, 34), cell cycle speed may act as a tiebreaker, with cell cycle slowdown favoring the more stable factor and acceleration favoring the less stable one. In general, our results imply a mutual regulatory relationship between the cell cycle and transcription factor activities in cell differentiation, and similar relationships may affect other processes that involve cell cycle length changes, such as cancer.

References and Notes

1. H. Singh, R. P. DeKoter, J. C. Walsh, *Cold Spring Harb. Symp. Quant. Biol.* **64**, 13–20 (1999).
2. S. L. Nutt, D. Metcalf, A. D'Amico, M. Polli, L. Wu, *J. Exp. Med.* **201**, 221–231 (2005).
3. J. Back, D. Allman, S. Chan, P. Kastner, *Exp. Hematol.* **33**, 395–402 (2005).
4. Y. Arinobu *et al.*, *Cell Stem Cell* **1**, 416–427 (2007).
5. R. P. DeKoter, H. Singh, *Science* **288**, 1439–1441 (2000).
6. M. K. Anderson, A. H. Weiss, G. Hernandez-Hoyos, C. J. Dionne, E. V. Rothenberg, *Immunity* **16**, 285–296 (2002).
7. C. J. Spooner, J. X. Cheng, E. Pujadas, P. Laslo, H. Singh, *Immunity* **31**, 576–586 (2009).
8. S. Carotta *et al.*, *Immunity* **32**, 628–641 (2010).

9. F. Rosenbauer, D. G. Tenen, *Nat. Rev. Immunol.* **7**, 105–117 (2007).
10. Y. Okuno *et al.*, *Mol. Cell. Biol.* **25**, 2832–2845 (2005).
11. M. A. Zarnegar, J. Chen, E. V. Rothenberg, *Mol. Cell. Biol.* **30**, 4922–4939 (2010).
12. M. Leddin *et al.*, *Blood* **117**, 2827–2838 (2011).
13. P. B. Staber *et al.*, *Mol. Cell* **49**, 934–946 (2013).
14. A. B. Cantor, S. H. Orkin, *Oncogene* **21**, 3368–3376 (2002).
15. K. S. Choe, O. Ujhelly, S. N. Wontakal, A. I. Skouttchi, *J. Biol. Chem.* **285**, 3044–3052 (2010).
16. W. D. Cook *et al.*, *Blood* **104**, 3437–3444 (2004).
17. F. Rosenbauer *et al.*, *Nat. Genet.* **36**, 624–630 (2004).
18. M. J. Walter *et al.*, *Proc. Natl. Acad. Sci. U.S.A.* **102**, 12513–12518 (2005).
19. D. Metcalf *et al.*, *Proc. Natl. Acad. Sci. U.S.A.* **103**, 1486–1491 (2006).

20. M. D. Delgado *et al.*, *Biochem. Biophys. Res. Commun.* **252**, 383–391 (1998).
21. R. P. DeKoter, J. C. Walsh, H. Singh, *EMBO J.* **17**, 4456–4468 (1998).
22. Materials and methods are available as supplementary materials on Science Online.
23. E. Eden *et al.*, *Science* **331**, 764–768 (2011).
24. B. Schwanhäusser *et al.*, *Nature* **473**, 337–342 (2011).
25. P. L. Toogood *et al.*, *J. Med. Chem.* **48**, 2388–2406 (2005).
26. F. Kihara-Negishi *et al.*, *Int. J. Cancer* **76**, 523–530 (1998).
27. T. Bellon, D. Perrotti, B. Calabretta, *Blood* **90**, 1828–1839 (1997).
28. C. B. Franco *et al.*, *Proc. Natl. Acad. Sci. U.S.A.* **103**, 11993–11998 (2006).
29. C. Tan, P. Marguet, L. You, *Nat. Chem. Biol.* **5**, 842–848 (2009).
30. L. A. Butti, B. A. Edgar, *Curr. Opin. Cell Biol.* **19**, 697–704 (2007).
31. R. A. Steinman, *Oncogene* **21**, 3403–3413 (2002).
32. P. Salomoni, F. Calegari, *Trends Cell Biol.* **20**, 233–243 (2010).
33. R. Dahl *et al.*, *Nat. Immunol.* **4**, 1029–1036 (2003).
34. A. K. Trivedi *et al.*, *Oncogene* **26**, 1789–1801 (2007).

Acknowledgments: We thank R. Butler and S. Washburn for mouse care and J. Verceles, J. Grimm, and D. Perez of the Caltech Flow Cytometry Facility for cell sorting. We also thank members of the Rothenberg and Elowitz labs and L. Goentoro for insightful discussions. The data presented in this manuscript are tabulated in the main paper and the supplementary materials. This work was supported by a Cancer Research Institute/Irvington Postdoctoral Fellowship to H.Y.K.; an Australian Research Council Future Fellowship and the Victorian State Government Operational Infrastructure Support, National Health and Medical Research Council of Australia Independent Research Institute Infrastructure Scheme to S.L.N.; NIH grants to E.V.R. (RC2 CA148278, R33 HL089123, R01 AI083514, and R01 CA90233); the Albert Billings Ruddock Professorship; the Al Sherman Foundation; and the Louis A. Garfinkle Memorial Laboratory Fund.

Supplementary Materials

www.sciencemag.org/cgi/content/full/science.1240831/DC1
Materials and Methods
Mathematical Appendix
Figs. S1 to S18
Tables S1 to S6
References (35–46)

21 May 2013; accepted 5 July 2013

Published online 18 July 2013;

10.1126/science.1240831

T Follicular Helper Cell Dynamics in Germinal Centers

Ziv Shulman,¹ Alexander D. Gitlin,¹ Sasha Targ,² Mila Jankovic,¹ Giulia Pasqual,² Michel C. Nussenzweig,^{1,3,*} Gabriel D. Victora^{2,*†}

T follicular helper (T_{FH}) cells are a specialized subset of effector T cells that provide help to and thereby select high-affinity B cells in germinal centers (GCs). To examine the dynamic behavior of T_{FH} cells in GCs in mice, we used two-photon microscopy in combination with a photoactivatable fluorescent reporter. Unlike GC B cells, which are clonally restricted, T_{FH} cells distributed among all GCs in lymph nodes and continually emigrated into the follicle and neighboring GCs. Moreover, newly activated T_{FH} cells invaded preexisting GCs, where they contributed to B cell selection and plasmablast differentiation. Our data suggest that the dynamic exchange of T_{FH} cells between GCs ensures maximal diversification of T cell help and that their ability to enter ongoing GCs accommodates antigenic variation during the immune response.

T cells play a pivotal role in affinity maturation by selecting B cells to enter the germinal center (GC), regulating GC positive

selection, and directing B cell differentiation to plasma cells and memory B cells (1–6). These events are orchestrated by a specialized population

of GC-resident T follicular helper (GC- T_{FH}) cells that develop in concert with GC B cells (7–13). T_{FH} cells express the chemokine receptor CXCR5, the CD28 family members ICOS and PD-1, the transcription factor Bcl-6, and the cytokines interleukin-4 (IL-4) and IL-21; many of these are required for GC B cell survival and differentiation (7). Less is known about the dynamic properties of T_{FH} cells and how they might affect GC B cell selection.

To document the kinetics of T cell expansion and localization during the GC reaction, we examined whole-mounted lymph nodes by means of two-photon laser scanning microscopy (TPLSM) (14, 15). In agreement with previous reports (16), large numbers of antigen-specific T cells were found in the T cell zone 3 days after immunization with 4-hydroxy-3-nitrophenylacetyl-ovalbumin

(NP-OVA). T cells then spread throughout the lymph node, including B cell follicles and nascent GCs, by day 5 (Fig. 1A). T cells began to concentrate in GCs only after 8 to 11 days (Fig. 1A), coinciding with the peak of T cell help to GC B cells (5). Thus, unlike B cell clones, which are thought to expand in a confined microanatomical region to produce pauciclonal GCs (17, 18), responding T cells are initially evenly distributed throughout the entire lymph node and accumulate in GCs only after they have coalesced.

T_{FH} and GC- T_{FH} cells are commonly defined on the basis of functional properties and expression of cell surface markers (8, 19) rather than anatomical localization. To verify the correspondence between surface phenotype and microanatomical location, we used photoactivatable green fluorescent protein (PAGFP) to label cells within spatially restricted areas (3). Flow cytometric analysis of photoactivated OT-II T cells (fig. S1, A to C) showed that CXCR5 and PD-1 expression were highest among T cells physically inside the GC and lowest among T cells in the paracortex, whereas T cells in the follicle outside the GC showed intermediate levels of expres-

sion of these molecules (Fig. 1, B and C, and fig. S1D). In contrast, ICOS expression was comparable in all three locations (Fig. 1, B and C, and fig. S1D). Similar results were obtained by photoactivation of endogenous polyclonal T cells (fig. S2). Thus, although CXCR5 and PD-1 expression can be used to distinguish between GC- T_{FH} and paracortical T cells, they cannot be used to definitively distinguish follicular T_{FH} cells from either of these populations.

To determine whether GC- T_{FH} cells, like their B cell counterparts, are clonally restricted within individual GCs (17, 18), we immunized mice that had received a mixture of OT-II T cells expressing one of three fluorescent proteins and visualized GCs 10 days after immunization (Fig. 2A). As suggested by our initial observations, the proportion of T cells of each color within individual GCs was constant across all GCs in the same lymph node, indicating that T cells are not clonally restricted within GCs (Fig. 2, A and B, and fig. S3A).

This pattern of T cell distribution might result from initial colonization by multiple clones and/or from T cell exchange between GCs. To examine the first of these possibilities, we analyzed early

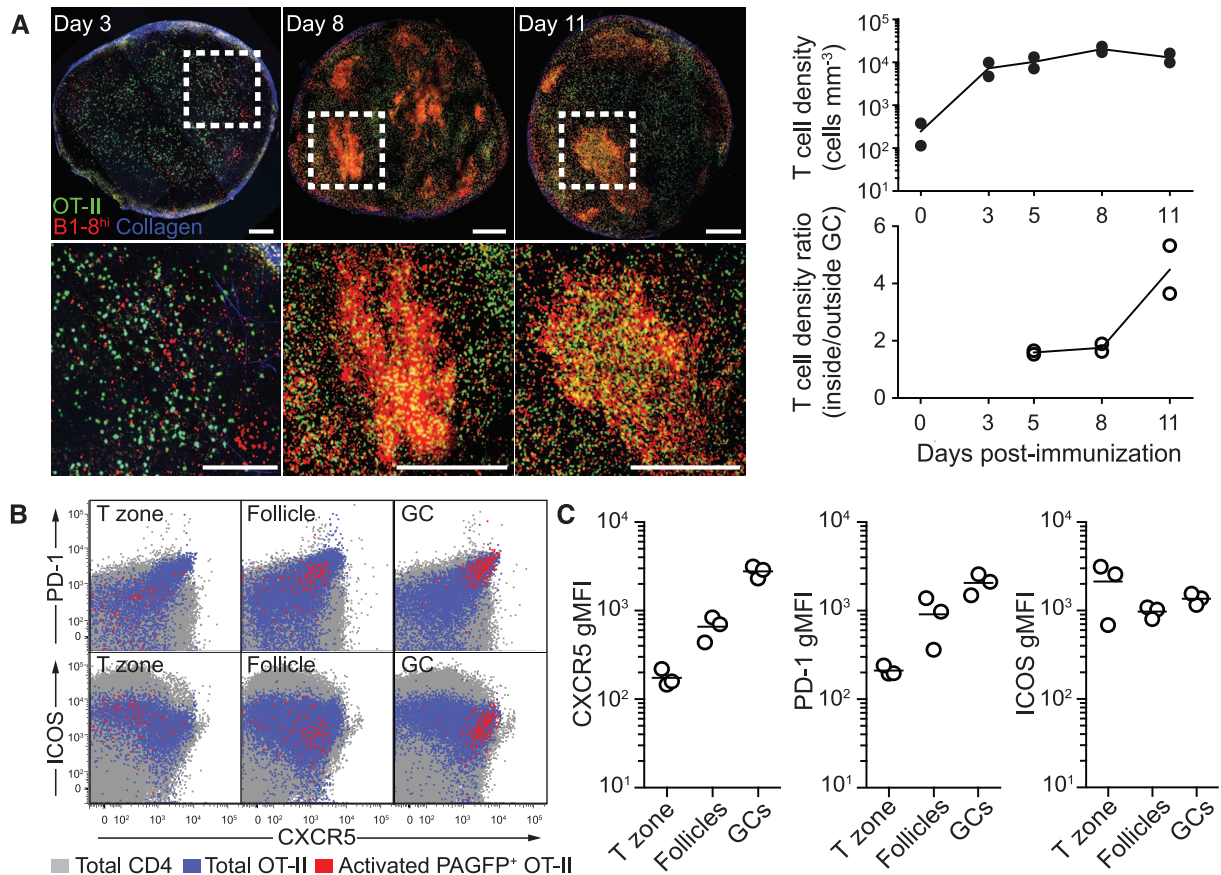


Fig. 1. Expansion kinetics and anatomical distribution of T_{FH} cells during germinal center formation. (A) Left: 3×10^4 GFP⁺ OVA-specific T cells (OT-II) and 1.5×10^6 tdTomato⁺ B1-8^{hi} B cells (corresponding to 1.5×10^5 Igλ⁺, NP-specific B cells) were transferred into wild-type mice 1 day before subcutaneous immunization with NP-OVA in alum. Popliteal lymph nodes were explanted at 0, 3, 5, 8, and 11 days after immunization and subjected to whole-

lymph node scanning by TPLSM. Collapsed Z-stacks (total volume 50 to 100 μm; 5-μm steps) are shown. Scale bars, 300 μm. Right: Quantitation of T cell density and density ratio (proportion of T cells within GC to T cells outside of GC) in two independent experiments. (B and C) Expression of T_{FH} markers on PAGFP⁺ OT-II T cells photoactivated in different lymph node regions, as described in fig. S1. Each symbol represents one experiment. gMFI, geometric mean fluorescence intensity.

GCs. GC- T_{FH} cell distribution was homogeneous across GCs even at the earliest observable time point, which suggests that individual GCs are indeed colonized by several distinct T cell clones (Fig. 2C and fig. S3, B and C). We confirmed this by transferring a much smaller number of T cells (3×10^4 total T cells per mouse) at a 19:1 ratio of GFP:DsRed cells (fig. S4), as well as by reconstituting T cell receptor β -deficient mice with mixtures of genetically labeled polyclonal $CD4^+$ T cells (fig. S5). In both cases, T cells were evenly distributed across GCs after immunization (figs. S4 and S5). Thus, we find no evidence that GC- T_{FH} cells are clonally restricted to individual GCs; instead, GCs appear to be colonized by a heterogeneous population of T cells representing all responding T cell clones.

To determine whether GC- T_{FH} cells can also exchange between GCs by migration, we imaged these cells by TPLSM. Short-term intravital movies showed that GC- T_{FH} cells occasionally migrated out of GCs (movie S1). Whether these emigrants are in fact leaving the GC rather than making a transient foray into the follicle could not be determined because of constraints in the duration of conventional intravital imaging movies (20).

To observe GC- T_{FH} cell migration for longer periods, we photoactivated PAGFP-OT-II T_{FH} cells within single GCs (fig. S6A). Photoactivation did not alter the motility of PAGFP $^+$ OT-II T_{FH} cells relative to controls (movie S2), and, because GC- T_{FH} cells were in G_1 phase (fig. S6B), activated PAGFP was not diluted by cell division, allowing for long-term cell tracking. Immediately after photoactivation, PAGFP $^+$ OT-II T_{FH} cells were restricted to the targeted region (fig. S6C). In contrast, ~ 20 hours after activation, 32% of photoactivated GC- T_{FH} cells were found outside the original GC (Fig. 3, A and B). Emigrating cells were found almost entirely within neighboring follicles and other GCs, and only very rarely (1 cell out of 487 analyzed) in the T cell zone (Fig. 3B, fig. S6D, and movie S3). Consistent with their near-absence from the T cell zone, we could detect only a very small number of photoactivated cells in the blood or pooled distal lymphoid organs of mice examined 36 hours after photoactivation (1 to 4 cells per mouse, seven mice in three independent experiments; fig. S6E). Transfer of PAGFP $^+$ OT-II T cells before priming with OVA did not substantially alter GC size or the ratio of T cells to B cells in the GC (fig. S6, F and G). Thus, GC- T_{FH} cell

emigration to the follicle and neighboring GCs cannot be attributed to a nonphysiological density of T_{FH} cells.

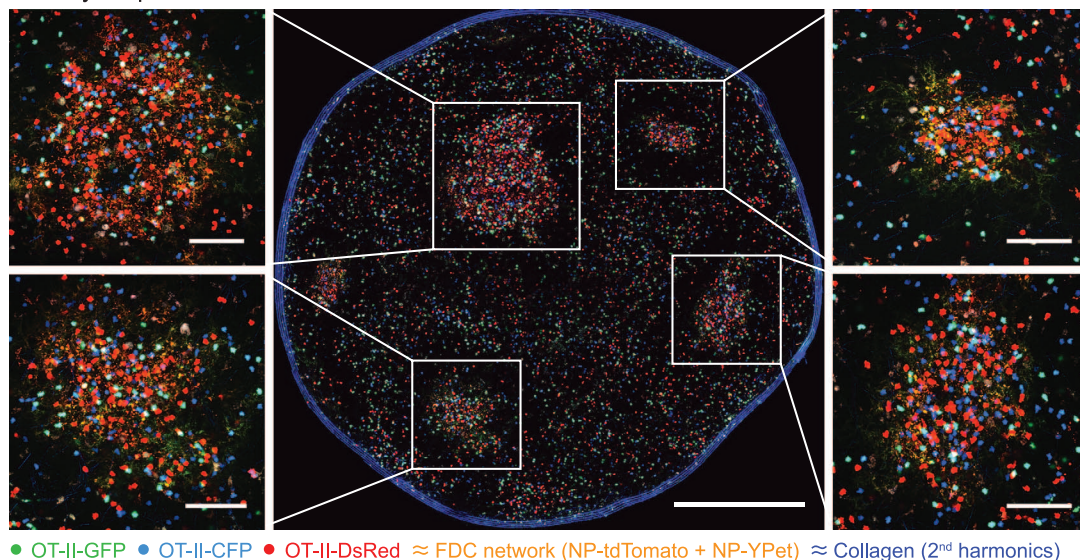
To determine the phenotype of emigrant GC- T_{FH} cells, we microdissected lymph nodes into two fragments, one of which contained the original photoactivated GC (Fig. 3C and fig. S7, A and B). Immediately after activation (0 hours), the lymph node fragment contralateral to the activated GC contained no photoactivated cells (fig. S7C). In contrast, after 24 hours, photoactivated cells corresponding to GC- T_{FH} cells that had emigrated from the original GC could also be found in the nonphotoactivated half of the lymph node (Fig. 3C). In agreement with the lymph node scans (Fig. 3A), emigrant GC- T_{FH} cells remained phenotypically similar to authentic GC- T_{FH} cells, although expression of PD-1 and CXCR5 was slightly decreased (Fig. 3C and fig. S7, D and E). We conclude that GC- T_{FH} cells emigrate and redistribute throughout the follicles and to neighboring GCs, but only rarely leave the follicle to enter circulation in the time frame analyzed.

The exchange of T cells between GCs suggested a hitherto unappreciated dynamic equilibrium between T cells in the follicles and in different GCs. We reasoned that if GCs are in fact

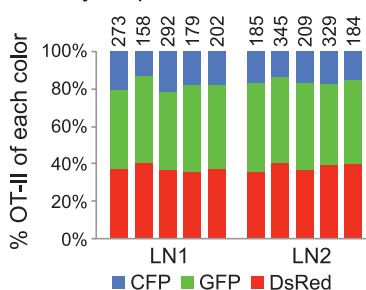
Fig. 2. GC- T_{FH} cells in individual germinal centers are not clonally restricted.

(A) A total of 3×10^5 OT-II T cells expressing CFP, GFP, or DsRed ($\sim 10^5$ of each color) and 3×10^6 to 5×10^6 nonfluorescent B1-8 hi B cells (corresponding to 3×10^5 to 5×10^5 Ig λ^+ , NP-specific cells) were transferred into wild-type recipients 1 day before subcutaneous immunization with NP-OVA in alum. Draining lymph nodes were explanted 10 days later and imaged by TPLSM. Follicular dendritic cell networks were labeled by injection of a mixture of NP-tdTomato and NP-YPet (orange). Central image shows a collapsed Z-stack, 50 μ m deep (10- μ m steps), of a whole lymph node containing multiple GCs, magnified in the outer panels. Scale bars, 300 μ m (large panel), 50 μ m (side panels). **(B)** Quantitation of data as in (A) across multiple lymph nodes from different mice. Each bar represents a single GC. Numbers on top of bars indicate the number of T cells counted in each GC. **(C)** T and B cells as described in (A) were transferred to H-2A β -GFP mice to allow visualization of early GCs, and lymph nodes were imaged 5 days after immunization with NP-OVA in alum. Image of one GC and quantitation of multiple GCs are shown. Scale bar, 100 μ m. Each set of experiments was performed twice (additional images and quantitation in fig. S3).

A Day 10 post immunization



B Day 10 post immunization



C Day 5 post immunization

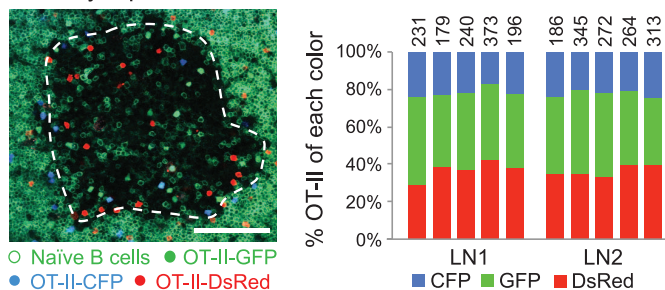
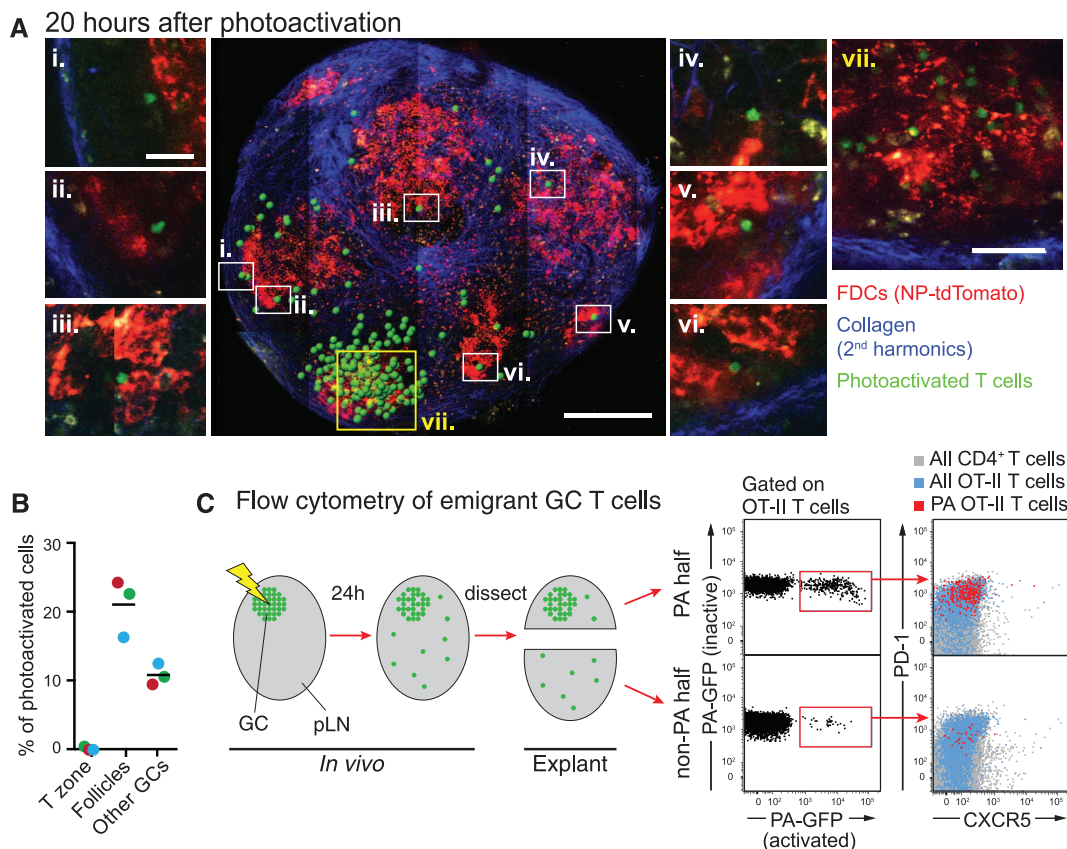


Fig. 3. GC- T_{FH} cells exchange between neighboring germinal centers.

(A) GCs containing OT-II PAGFP $^{+}$ T_{FH} cells were generated as in fig. S6A, and the light zone of a single GC was photoactivated within a living mouse. Central image shows a collapsed Z-stack of the cortical half (depth 250 μ m) of a whole-lymph node scan taken ~20 hours after photoactivation. Outer panels (i-vi) are high-magnification images of the regions indicated in the center panel; panel vii shows the original photoactivated GC. Scale bars, 300 μ m (center panel), 20 μ m (panels i to vi), 30 μ m (panel vii). Green spots are placed over photoactivated OT-II T cells in low-magnification panels to improve visualization. (B) Quantitation of three experiments as in (A) (95, 184, and 208 photoactivated cells analyzed in three independent experiments). Each color represents one experiment. Average distance covered by photoactivated cells was 334 μ m; the farthest 10% of cells traveled on average 790 μ m. (C) Single GCs in popliteal lymph nodes containing PAGFP $^{+}$ OT-II T_{FH} cells were photoactivated in vivo as in (A), then explanted and dissected as shown in fig. S6. Flow cytometry plots show PD-1 and CXCR5 expression in emigrant GC- T_{FH} cells (pooled data from two mice). Data are representative of five mice from three independent experiments.



open to T_{FH} cell exchange, then newly activated T cells may also be able to join an ongoing GC reaction. To examine this possibility, we transferred GFP-expressing OT-II cells into wild-type recipients that were then primed with OVA to induce OT-II expansion. These mice then received B1-8 hi cells expressing cyan fluorescent protein (CFP-B1-8 hi cells) and were immunized with NP-chicken gamma globulin (CGG) in alum to produce GCs in which endogenous CGG-specific T_{FH} cells provide help for CFP-B1-8 hi cells. The immunized mice were then boosted subcutaneously with soluble NP-OVA to trigger invasion of these GCs by OT-II cells (fig. S8A). Before the boost, small numbers of GFP-OT-II cells were found scattered throughout the T cell zone, occasionally entering existing GCs for brief periods (Fig. 4A, fig. S8B, and movie S4). One day after immunization, GFP $^{+}$ cells could be seen proliferating in foci of T and B cells at the follicle-T zone border (Fig. 4A and movie S5). By day 3 after boost, GFP-OT-II T cells were found throughout the lymph node follicles and within preexisting GCs (Fig. 4A and movie S6). All GCs evaluated contained invading GFP-OT-II T cells, indicating that these cells were indeed entering existing GCs rather than producing GCs de novo. Accordingly, control mice boosted with NP-OVA without pre-immunization with NP-CGG had no GCs at this time point (fig. S8C). Over time, GFP-OT-II T

cells began to accumulate progressively within GCs, so that by day 11 after boost, the newly activated T cells were mostly concentrated inside these structures (Fig. 4A, fig. S8B, and movie S6), interacting actively with GC B cells (Fig. 4B and movie S7). Therefore, ongoing GCs are open to invasion by newly activated T_{FH} cells.

To determine whether invading T_{FH} cells contribute to the GC reaction, we measured their ability to provide help to B cells selectively expressing high levels of cognate peptide-major histocompatibility complex (pMHC) by using an antibody to DEC-205 (encoded by *Ly75*) fused to OVA (α DEC205-OVA) to target antigen to GC B cells (3, 4). OVA-specific GC- T_{FH} cells were induced to invade a CGG-specific GC containing a mixture of 85% *Ly75* $^{-/-}$ CD45.1/2 and 15% *Ly75* $^{+/+}$ CD45.1/1 B1-8 hi B cells, and cognate pMHC expression was artificially increased on the *Ly75* $^{+/+}$ B cells by injection of α DEC205-OVA (fig. S8D). Whereas phosphate-buffered saline (PBS) or control antibody had no effect, injection of α DEC205-OVA resulted in selective and marked expansion of the *Ly75* $^{+/+}$ but not *Ly75* $^{-/-}$ GC B cells, and an increase in plasma-blast frequency by nearly an order of magnitude (Fig. 4, C and D). We conclude that T cells that invade ongoing GCs actively participate as helper T cells and positively select B cells expressing high levels of pMHC.

Boosting ongoing NP-CGG-specific GCs with NP-OVA (as detailed in Fig. 4A) resulted in a factor of 5 increase in the proportion of GC B cells 5 days after boost (from 0.9 to 5.1%), whereas the proportion of transferred to endogenous B cells remained constant (Fig. 4E). Thus, GC invasion by newly activated T_{FH} cells can augment ongoing GC reactions.

Physical restriction of responding B cells to a single GC minimizes competition between B cells in different GCs, thereby preventing the immune response from converging on a single dominant clone (21). In contrast, free movement of T_{FH} cells between GCs may be advantageous, in that it ensures diversified and robust support for B cell clonal expansion and affinity maturation (22–24). Thus, diversity in the antibody response appears to be favored by restricting B cell clones to single GCs while exposing them to a multiplicity of different T cell clones that transit between different GCs.

In addition to polyclonal colonization and dynamic exchange between GCs, newly activated T cells can also enter ongoing GCs. This raises the possibility that T cells that are activated late in the immune response can join and potentially prolong the GC reaction. Such a feature may be an important advantage in responding to chronic infections and/or pathogens that diversify their antigenic epitopes during infection, such as HIV.

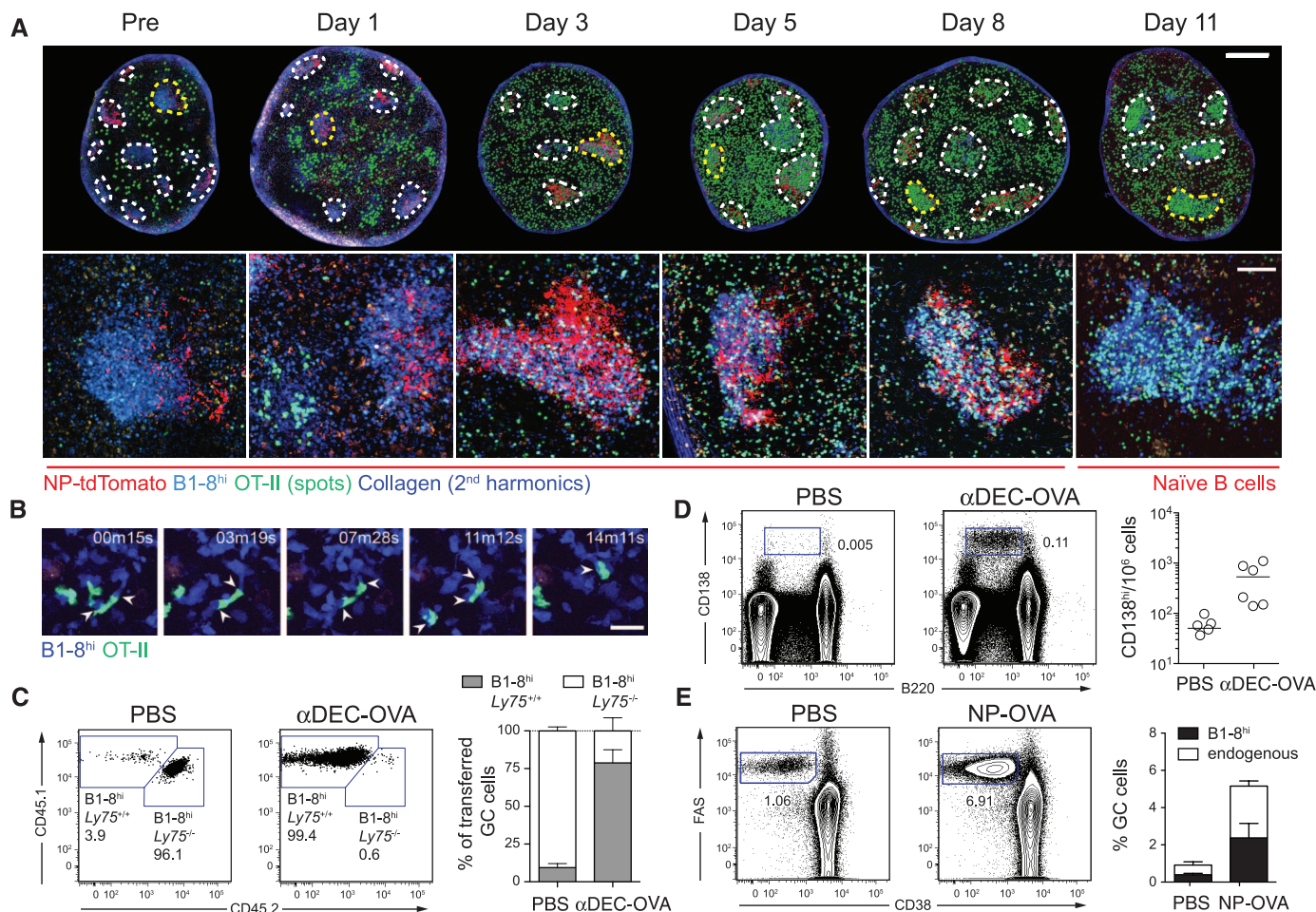


Fig. 4. Newly activated T_H cells can enter ongoing germinal center reactions. (A) Kinetics of invasion of ongoing GCs by newly activated T cells as described in fig. S8A. Top: Montage showing whole-lymph node TPLSM scans. Collapsed Z-stacks are 90 μ m deep (pre and day 1) or 40 μ m deep (days 3 to 11). GCs containing CFP⁺ B1-8^{hi} B cells (blue) and NP-tdTomato-coated follicular dendritic cells (red) are circled with dotted lines. Green spots are placed over GFP⁺ T cells to improve visualization. Background outside lymph nodes was deleted. Bottom: Higher-magnification images of GCs circled in yellow in the top panel. Scale bars, 0.5 mm (top), 100 μ m (bottom).

(B) Time series showing cognate T cell–B cell interactions in an invaded GC on day 11 after boost. Scale bar, 20 μ m. (C and D) Recipient mice were treated with α DEC205-OVA or PBS 6 days after NP-OVA boost as outlined in fig. S8D. Flow cytometry plots show proportion of Ly75^{+/+} and Ly75^{-/-} B1-8^{hi} GC B cells (C) or percentage of plasmablasts among all single cells (D) 3 days after α DEC205-OVA treatment. (E) Flow cytometry plots comparing the proportion of GC cells (B220⁺Fas⁺CD38⁺) in mice treated as outlined in fig. S8E or receiving PBS instead of the NP-OVA boost at day 0. The rightmost panels show means \pm SEM of two or three experiments.

References and Notes

- C. G. Vinuesa *et al.*, *Nature* **435**, 452–458 (2005).
- C. D. Allen, T. Okada, H. L. Tang, J. G. Cyster, *Science* **315**, 528–531 (2007).
- G. D. Victora *et al.*, *Cell* **143**, 592–605 (2010).
- T. A. Schwickert *et al.*, *J. Exp. Med.* **208**, 1243–1252 (2011).
- D. Dominguez-Sola *et al.*, *Nat. Immunol.* **13**, 1083–1091 (2012).
- G. D. Victora, M. C. Nussenzweig, *Annu. Rev. Immunol.* **30**, 429–457 (2012).
- C. G. Vinuesa, J. G. Cyster, *Immunity* **35**, 671–680 (2011).
- S. Crotty, *Annu. Rev. Immunol.* **29**, 621–663 (2011).
- C. King, S. G. Tangye, C. R. Mackay, *Annu. Rev. Immunol.* **26**, 741–766 (2008).
- H. Qi, J. L. Cannons, F. Klauschen, P. L. Schwartzberg, R. N. Germain, *Nature* **455**, 764–769 (2008).
- N. Fazilleau, L. Mark, L. J. McHeyzer-Williams, M. G. McHeyzer-Williams, *Immunity* **30**, 324–335 (2009).
- E. K. Deenick *et al.*, *Immunity* **33**, 241–253 (2010).
- Y. S. Choi *et al.*, *Immunity* **34**, 932–946 (2011).
- See supplementary materials on Science Online.
- K. Liu *et al.*, *Science* **324**, 392–397 (2009).
- P. Garside *et al.*, *Science* **281**, 96–99 (1998).
- F. G. Kroese, A. S. Wubbena, H. G. Seijen, P. Nieuwenhuis, *Eur. J. Immunol.* **17**, 1069–1072 (1987).
- Y. J. Liu, J. Zhang, P. J. Lane, E. Y. Chan, I. C. MacLennan, *Eur. J. Immunol.* **21**, 2951–2962 (1991).
- D. Yu, C. G. Vinuesa, *Trends Immunol.* **31**, 377–383 (2010).
- R. N. Germain, M. J. Miller, M. L. Dustin, M. C. Nussenzweig, *Nat. Rev. Immunol.* **6**, 497–507 (2006).
- R. Küppers, M. Zhao, M. L. Hansmann, K. Rajewsky, *EMBO J.* **12**, 4955–4967 (1993).
- B. Zheng, S. Han, G. Kelsoe, *J. Exp. Med.* **184**, 1083–1091 (1996).
- A. Roers, M. L. Hansmann, K. Rajewsky, R. Küppers, *Am. J. Pathol.* **156**, 1067–1071 (2000).
- S. J. Golby, D. K. Dunn-Walters, J. Spencer, *Eur. J. Immunol.* **29**, 3729–3736 (1999).

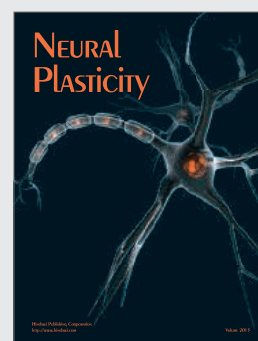
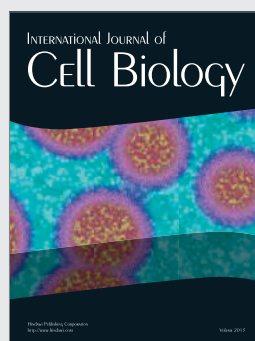
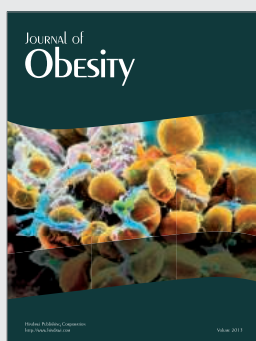
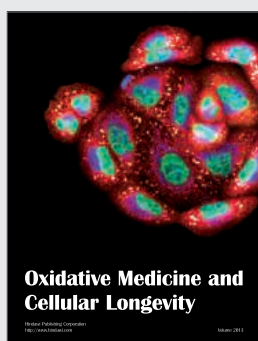
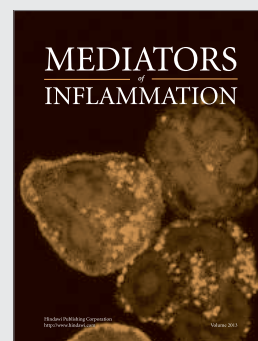
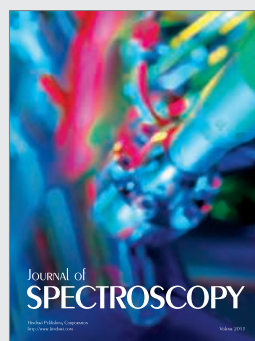
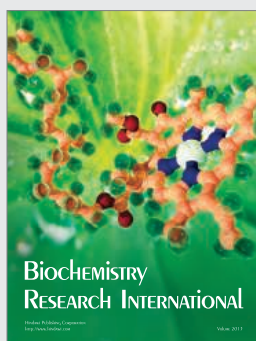
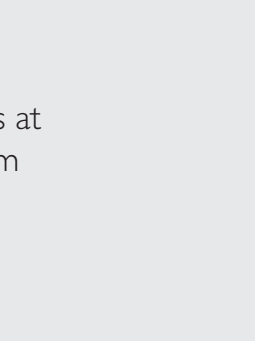
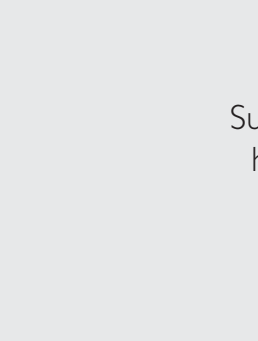
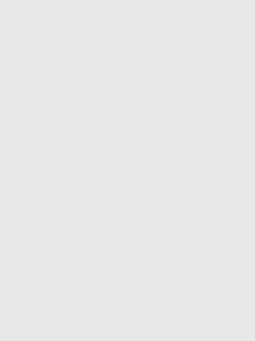
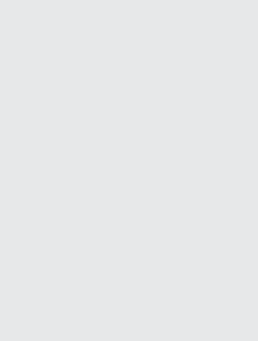
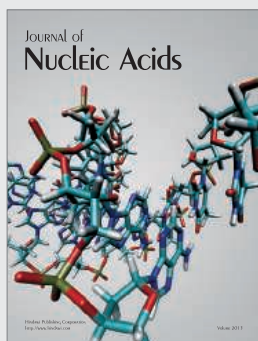
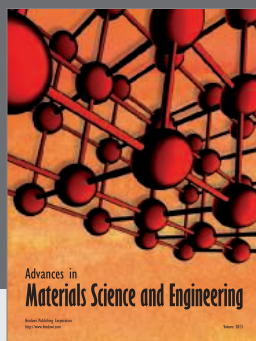
Acknowledgments: We thank H. Ploegh, K. Stribis, and H. Sive for mice and equipment use and E. Browne for helpful discussion. The data presented are tabulated in the main

paper and in the supplementary materials. Support for the Rockefeller University multiphoton microscope was granted by the Empire State Stem Cell Fund through New York State Department of Health contract C023046. Supported by NIH Medical Scientist Training Program grant T32GM07739 to the Weill Cornell/Rockefeller/Sloan-Kettering Tri-Institutional MD-PhD Program (A.D.G.), NIH grant 5DP5OD012146-02 and March of Dimes Foundation Basil O'Connor Award (G.D.V.), and NIH grants AI037526-19, AI075259-06, and AI100663-01 (M.C.N.). Z.S. is a Human Frontiers of Science fellow. G.P. is a Swiss National Science Foundation fellow. M.C.N. is an HHMI investigator.

Supplementary Materials

www.sciencemag.org/cgi/content/full/science.1241680/DC1
Materials and Methods
Figs. S1 to S8
Table S1
Movies S1 to S7
References (25–29)

10 June 2013; accepted 15 July 2013
Published online 25 July 2013;
10.1126/science.1241680



Hindawi

Submit your manuscripts at
<http://www.hindawi.com>

AAAS | 2014 ANNUAL MEETING

13-17 FEBRUARY • CHICAGO

MEETING GLOBAL CHALLENGES:
DISCOVERY AND INNOVATION

The 2014 AAAS Annual Meeting will focus on finding sustainable solutions through inclusive, international, and interdisciplinary efforts that are most useful to society and enhance economic growth.

Advance Registration is Now Open

Advance registration and housing through the AAAS Housing Bureau is available. Register and reserve hotel rooms for discounted rates. AAAS members receive additional special rates.

The scientific program will be online in early October.

www.aaas.org/meetings



WEBINAR

Targeting Noncoding RNAs in Disease: Challenges and Opportunities



Wednesday, September 4, 2013

12 noon Eastern, 9 a.m. Pacific, 5 p.m. UK, 6 p.m. Central Europe

Noncoding RNAs make up the majority of transcribed RNA and have a wide range of functions in cellular and developmental processes. Consequently, they are also implicated in the development and pathophysiology of many diseases and represent potential targets for therapeutic intervention. microRNAs are one class of noncoding RNA that has been intensely studied. Effective inhibition (or silencing) of microRNAs in vivo has enabled scientists to make groundbreaking discoveries about the contribution of these short regulating RNAs to some of the major human diseases, such as cancer, heart disease, and diabetes. Long noncoding RNAs are less well studied, but have recently emerged as another novel class of therapeutic targets in a variety of diseases. Both long and short noncoding RNAs represent new avenues of investigation for drug discovery with several advantages over traditional protein-based targets; however, they come with their own unique set of challenges.

During the webinar the expert panel will:

- Introduce the concept of using noncoding RNAs as therapeutic targets in human disease
- Discuss the unique challenges of targeting functional RNA in vivo
- Describe recent advances enabling effective in vivo inhibition of noncoding RNA
- Answer audience questions during the live webinar.

Speakers



David Corey, Ph.D.

Department of Pharmacology
University of Texas Southwestern
Medical Campus
Dallas, Texas



Stefanie Dimmeler, Ph.D.

Institute of Cardiovascular
Regeneration, Goethe-University
Frankfurt, Germany



Jan-Wilhelm Kornfeld, Ph.D.

Department of Mouse Genetics
and Metabolism
University of Cologne
Cologne, Germany

Register Now!
webinar.sciencemag.org

Webinar sponsored by

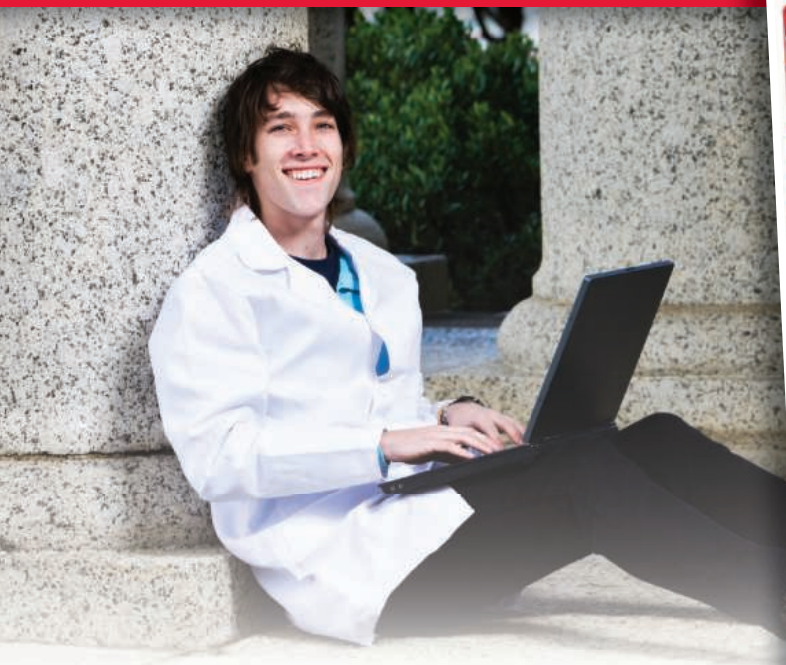
EXIQON
Seek Find Verify

Brought to you by the
**Science/AAAS Custom
Publishing Office**



For your career in science, there's only one **Science**

A career plan customized
for you, by you.



myIDP.sciencecareers.org



Recommended by leading professional societies and endorsed by the National Institutes of Health, an individual development plan will help you prepare for a successful and satisfying scientific career.



In collaboration with FASEB, UCSF, and the Medical College of Wisconsin and with support from the Burroughs Wellcome Fund, AAAS and *Science* Careers present the first and only online app that helps scientists prepare their very own individual development plan.

Visit the website and
start planning today!
myIDP.sciencecareers.org

In partnership with:





AIR CONDENSER

The new Findenser is an innovative and unique air condenser which replaces the need for water-cooled condensers in over 95% of all common chemistry applications. Findenser comprises a glass condenser and an external finned aluminium jacket, between which a small amount of water is permanently sealed. The design of the glass inner and finned jacket mean Findenser has a much greater surface area and heat transfer capacity than a standard air condenser. The result is a 'superair condenser,' that tests have shown performs as well as a traditional water condenser in all popular chemistry applications. Findenser requires no running water to operate, thus eliminating the need to purchase and dispose of water. Findenser can be used in vessels up to 2 L with up to 1 L of solvent. It comes as standard with a B24 ground glass cone and fits all standard tapered glass sockets.

Radleys

For info: +44-(0)-1799-513320 | www.radleys.com

LOW-TEMPERATURE BENCHTOP CHILLERS

Designed to maximize benchspace, LS-Series/LM-Series/MM-Series Chillers provide up to 1,290 watts of cooling at 20°C, making them ideal for use with rotary evaporators, jacketed incubators, small reaction vessels, spectrophotometers, chromatography columns, condensers, and other devices that require robust heat removal. Three different models of compact chillers are available: The LS-Series, which has a working temperature range of -20°C to +40°C and provides 475 watts of cooling at -10°C; the LM-Series, with a working temperature range of -10° to +30°C and a 230 watt cooling capacity at -10°C; and the MM-Series, which has a working temperature range of -5°C to +50°C and provides 129 watts of cooling at -5°C. All three models control temperature with $\pm 0.1^\circ\text{C}$ stability and are equipped with a low-flow-rate alarm, user-adjustable high- and low-temperature alarms, a top-mounted fill port with built-in fluid filter, lighted fluid level indicator, and washable rigid-frame air filter.

PolyScience

For more info: 800-229-7569 | www.polyscience.com

APTAMER PROTEIN PRECIPITATION KITS

A new range of Aptamer Protein Precipitation Kits bind with unmatched high specificity and affinity to target molecules. The new Aptoprecipitation (AP)/Co-Aptoprecipitation (Co-AP) Kits are aptamer-based protein precipitation kits designed to provide easy, quick, and consistent protein precipitation. The new kits offer a range of unique characteristics and provide significant advantages over alternative methods. Based upon a proprietary oligonucleotide, aptamer kits will not contribute to protein/peptide background that can interfere with subsequent mass analysis. Supplied as a complete kit in which aptamer is covalently conjugated to magnetic beads, you can perform successful pull-down experiments with ease, without the traditional troublesome conjugation step. Unlike antibody-based protein precipitation methods, aptamer is highly specific recognizing just the native form of target proteins, not the denatured form. The mild elution conditions used with Aptamer kits enable isolation of intact proteins and protein complexes.

AMS Biotechnology

For info: +44-(0)-1235-828200 | www.amsbio.com/aptamer.aspx

TEMPERATURE CONTROL AND MIXING INSTRUMENT

An exciting new generation of Temperature Control and Mixing Instruments is now set to impress with excellent mixing results, outstanding temperature management, and the ergonomics and simplicity essential for routine use in a busy laboratory. The excellent mixing results of the new Eppendorf ThermoMixer C, F1.5 and FP (two-in one instruments for combined mixing and incubating) are due to the unique ^{2D}Mix-Control technology which ensures fast and efficient mixing in just seconds and now offers reliable mixing solutions in 96- and 384-well plates. Controlled circular movements achieve thorough mixing of liquids in even the smallest volumes, while the anti-spill technology prevents lid wetting and cross-contamination. For dry incubation, the new Eppendorf ThermoMixer C and ThermoStat C are operated together with Eppendorf SmartBlocks which are easily exchangeable in just seconds, thanks to the unique Eppendorf QuickRelease technology. These individually sensor-controlled SmartBlocks are the best solution for maintaining accurate, uniform temperatures.

Eppendorf

For info: 800-645-3050 | www.eppendorf.com/thermomixer-c

REAGENT RESERVOIRS

An extensive range of reagent reservoirs are available for 96-well and 384-well multichannel pipetting systems. Adopting a standard SBS/SLAS footprint—the extended range of reagent reservoirs (100 mL and 300 mL) are fully compatible with all liquid handling systems including Integra's VIAFLO 96 and VIAFLO 384 Handheld Multichannel Electronic Pipettes. Individual pyramidal indentations (96 or 384) in each reagent reservoir allow maximum liquid recovery when using the VIAFLO 96 and VIAFLO 384 electronic pipettes as well as other platforms. VIAFLO multichannel reagent reservoirs are both economically and environmentally friendly because users can reuse the reservoir base and dispose of the reservoir inserts. These reagent reservoirs are also designed to nest within one another without sticking and come in compact, space-saving packages.

Integra Biosciences

For info: +41-(0)-81-286-95-30 | www.integra-biosciences.com

Electronically submit your new product description or product literature information! Go to www.sciencemag.org/products/newproducts.dtl for more information. Newly offered instrumentation, apparatus, and laboratory materials of interest to researchers in all disciplines in academic, industrial, and governmental organizations are featured in this space. Emphasis is given to purpose, chief characteristics, and availability of products and materials. Endorsement by *Science* or AAAS of any products or materials mentioned is not implied. Additional information may be obtained from the manufacturer or supplier.



STAY INFORMED! STAY CONNECTED!

Get more from your AAAS membership

Are you currently registered to receive e-mails from AAAS and *Science*?

E-mail is the primary way that AAAS communicates with our members about AAAS programs, new member benefits, invitations to special events, and, of course, the latest news and research being published in *Science*.

Sign up today to receive e-mails from AAAS and ensure that you are getting the most out of your membership and *Science* subscription.*

To get started visit: promo.aaas.org/stayconnected

You'll need your AAAS Member number. Find it above your name on your *Science* mailing label.

Don't miss a thing. Sign up for e-mail communications from AAAS today!



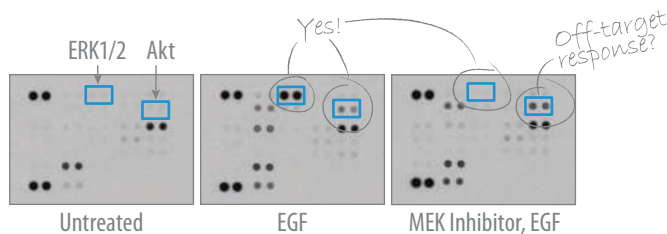
Our cytokines and growth factors are just the tip of the iceberg.

Explore beneath the surface with Signal Transduction reagents from R&D Systems.

Antibody Arrays from R&D Systems shed light on research.

Proteome Profiler™ Antibody Arrays are used in 60% of all published phospho-array studies.

Uncover relationships between multiple signaling pathways. Reveal off-target inhibitor responses. Collect data in the same manner as a traditional immunoblot.



Visit our website for a video protocol and a full EGF phosphorylation profile with inhibitor screens that reveal intriguing results.

RnDSystems.com/Iceberg



Science Careers Advertising

For full advertising details, go to ScienceCareers.org and click For Employers, or call one of our representatives.

Tracy Holmes
Worldwide Associate Director
Science Careers
Phone: +44 (0) 1223 326525

THE AMERICAS

E-mail: advertise@sciencecareers.org
Fax: 202-289-6742

Tina Burks
East Coast/West Coast/South America
Phone: 202-326-6577

Marci Gallun
Midwest/Canada
Phone: 202-326-6582

Candice Nulsen
Corporate
Phone: 202-256-1528

Online Job Posting Questions
Phone: 202-312-6375

EUROPE / INDIA / AUSTRALIA / NEW ZEALAND / REST OF WORLD

E-mail: ads@science-int.co.uk
Fax: +44 (0) 1223 326532

Axel Gesatzki
Phone: +44 (0)1223 326529

Kelly Grace
Phone: +44 (0) 1223 326528

JAPAN

Yuri Kobayashi
Phone: +81-(0)90-9110-1719
E-mail: ykobayas@aaas.org

CHINA / KOREA / SINGAPORE / TAIWAN / THAILAND

Ruolei Wu
Phone: +86-1367-1015-294
E-mail: rwu@aaas.org

All ads submitted for publication must comply with applicable U.S. and non-U.S. laws. Science reserves the right to refuse any advertisement at its sole discretion for any reason, including without limitation for offensive language or inappropriate content, and all advertising is subject to publisher approval. Science encourages our readers to alert us to any ads that they feel may be discriminatory or offensive.



ScienceCareers.org

POSITIONS OPEN



FACULTY RESEARCH POSITIONS in

Pathology

Assistant, Associate, or Full Professor
University of Texas Southwestern Medical Center

The Department of Pathology at UT Southwestern (UTSW), invites applications for two tenure-track faculty positions from scientists (M.D., M.D.-Ph.D., or Ph.D.) with a demonstrated ability to lead an independent, funded research program in cancer, immunology, stem cell biology, or neuroscience. Generous salary, startup packages, and laboratory space will be provided. UTSW offers a highly collaborative environment, outstanding research infrastructure and dynamic translational opportunities.

Applicants should submit a cover letter, curriculum vitae, a statement of research interest, and three letters of reference to e-mail: dorothee.staber@utsouthwestern.edu.

UT Southwestern Medical Center is an Affirmative Action/Equal Opportunity Employer. Women, minorities, veterans, and individuals with disabilities are encouraged to apply.

ASSISTANT PROFESSOR

Bryn Mawr College, Department of Biology

The Department of Biology invites applications for a full-time, beginning tenure-track Assistant Professor position in the area of ecological modeling to begin on August 1, 2014. We are searching for a broadly trained individual who approaches central questions in ecology from a computational or modeling perspective and uses such techniques as key components of an active research program involving undergraduates. The successful candidate is expected to teach at all levels of the curriculum and establish an externally funded research program that provides rigorous collaborative research projects for undergraduates. Teaching responsibilities will include participation in Introductory Biology, a general course in computational modeling in the sciences, and advanced undergraduate courses in ecological modeling. Involvement in the College's minor in Environmental Studies is encouraged. A Ph.D. and at least one year of post-doctoral research experience are required. Submit by October 4, 2013, a cover letter, curriculum vitae, research statement, and teaching philosophy that includes a short description of potential courses to be offered to Ecological Search Committee, c/o Jodi Jacoby, Department of Biology, 101 N. Merion Avenue, Bryn Mawr, PA 19010. In addition, arrange to have three letters of recommendation sent to the same address.

Bryn Mawr College is an Equal Opportunity Employer; minority candidates and women are especially encouraged to apply.

ACADEMIC PROFESSIONAL

The Department of Chemistry at Georgia State University anticipates hiring an Academic Professional beginning in the fall 2013, pending budgetary approval. Duties will include: (1) Coordination of general and organic chemistry labs as well as laboratory manual revisions and updates; (2) maintain chemical inventory and provide oversight of laboratory facilities; (3) serve as instructor of certain lecture and laboratory courses; and (4) provide training and supervision of student and graduate assistants. Instruction of lecture and laboratory courses, not to exceed 50% of total effort. Ph.D. in chemistry or related field required. Strong background in organic chemistry, and college level teaching experience preferred. The salary range is \$50,000 to \$60,000. Applicants should submit curriculum vitae and statement of teaching philosophy, and arrange for three letters of recommendation to be sent to: **Academic Professional Search Committee, Department of Chemistry, Georgia State University, POB 4098, Atlanta, GA 30302-4098**. Open until filled. An offer of employment will be conditional upon background verification. *Georgia State University, a research University of the University System of Georgia, is an Affirmative Action/Equal Employment Opportunity Employer.*

POSITIONS OPEN



Yale University
School of Medicine

RESEARCH ASSOCIATE in Pain Studies

Position available for an experienced pain researcher to join a multidisciplinary research program exploring molecular pathophysiology of painful neuropathies. M.D. and/or Ph.D. degree, and experience in molecular biology, transgenic mouse technology and animal behavior with publications, are required. Experience with analysis of DRG neurons, immunohistochemistry, small animal surgery, and viral platforms for gene transfer are desirable. See **Dib-Hajj et al., *Nature Rev. Neuro.* 14:49-62, 2013** and **Samad et al., *Mol. Therapy* 21:49-56**. Superb opportunity for a skilled scientist to work collaboratively with molecular geneticists, molecular and cell biologists, physiologists, and pharmacologists in a highly collaborative, interactive program. Send letter of interest, curriculum vitae, and three letters of reference to: **Stephen G. Waxman, M.D., Ph.D. (e-mail: stephen.waxman@yale.edu) or Sulayman D. Dib-Hajj, Ph.D. (e-mail: sulayman.dib-hajj@yale.edu).**

TENURE-TRACK FACULTY POSITION

Georgia Institute of Technology
School of Chemistry and Biochemistry
Atlanta, GA 30332-0400

The Georgia Institute of Technology, School of Chemistry and Biochemistry seeks to fill one or more tenure-track faculty positions. The areas of emphasis are Biochemistry, Chemical Biology, and Organic Chemistry, but candidates from all areas will be considered. Georgia Tech is particularly focused on growth in the life sciences, biosciences, and energy and sustainability. Exceptional candidates at all levels are encouraged to apply. Candidates with interdisciplinary research programs may be considered for joint appointments with other campus units. Candidates for appointment at the assistant professor level should submit an application letter, curriculum vitae, and a summary of research plans, and arrange for submission of three letters of reference. Candidates for advanced levels should submit an application letter, curriculum vitae, and the names of three references. All materials and requests for information should be submitted electronically, as per the instructions found at [website: <http://academicjobsonline.org/ajo/jobs/2881>](http://academicjobsonline.org/ajo/jobs/2881).

The application deadline is September 16, 2013 with application review continuing until the positions are filled. *Georgia Tech is an Equal Education/Employment Opportunity Institution.*

ASSISTANT PROFESSOR

The Lymphoma Research Program at the University of Nebraska Medical Center and Eppley Cancer Center is recruiting a faculty member at the rank of assistant professor. The lymphoma program has a large patient population with a comprehensive clinical and pathology database and extensive tissue resources to support basic and translational research. The focus of the program is on lymphoma biology and pathogenesis with the translational goal of biomarkers and therapeutic target discovery. The assistant professor should have a Doctorate degree and postdoctoral experience in lymphoma research. He/she is expected to be a highly creative scientist with a track record of outstanding lymphoma research and a promising line of future investigation. State-of-the-art laboratories and core facilities are available to researchers. Applicants should submit curriculum vitae, summary of research experiences, and three reference contacts to [website: <http://jobs.unmc.edu/postings/16328>](http://jobs.unmc.edu/postings/16328). *Individuals from diverse backgrounds are encouraged to apply.*



Chair for the Department of Human and Molecular Genetics

Florida International University is a comprehensive university offering 340 majors in 188 degree programs in 23 colleges and schools, with innovative bachelor's, master's and doctoral programs across all disciplines including medicine, public health, law, journalism, hospitality, and architecture. FIU is Carnegie-designated as both a research university with high research activity and a community-engaged university. Located in the heart of the dynamic south Florida urban region, our multiple campuses serve over 50,000 students, placing FIU among the ten largest universities in the nation. Our annual research expenditures in excess of \$100 million and our deep commitment to engagement have made FIU the go-to solutions center for issues ranging from local to global. FIU leads the nation in granting bachelor's degrees, including in the STEM fields, to minority students and is first in awarding STEM master's degrees to Hispanics. Our students, faculty, and staff reflect Miami's diverse population, earning FIU the designation of Hispanic-Serving Institution. At FIU, we are proud to be "Worlds Ahead"! For more information about FIU, visit fiu.edu.

The Herbert Wertheim College of Medicine (HWCOC) seeks an internationally-recognized individual with an outstanding record of scientific achievement, grant support, scholarly accomplishments and mentoring as its new Chair of the Department of Human and Molecular Genetics. FIU, which is located in the City of Miami, is the only public urban research university in South Florida and is the gateway to South and Central America. The HWCOC is a new medical school which has just graduated its first medical class and received full LCME accreditation. The college is seeking to expand its base of basic science, translational and clinical research.

Minimum qualifications include an advanced degree (M.D., Ph.D. or equivalent) in the area of genetics and be eligible for full professorship with tenure. The ideal candidate will have a widely recognized international reputation in the area of human and molecular genetics and a record of continuous grant support. Certification by the American Board of Medical Genetics is desired but not obligatory. This is a wonderful opportunity for a new leader to present a vision for the growth of the department. As part of the FIU strategic plan for cluster hires in targeted areas, the new Chair will be responsible for building and maintaining a group of faculty with high-quality funded research programs who would participate in research, graduate and medical education. The successful candidate will be provided with substantial space and funds for her/his research program and associated cluster hires.

Qualified candidates are encouraged to apply to Job Opening ID (506329) at <http://careers.fiu.edu> and attach letter of interest, curriculum vitae and listing of three professional references in a single pdf file.

FIU is a member of the State University System of Florida and is an Equal Opportunity, Equal Access Affirmative Action Employer.



Tufts
UNIVERSITY

TENURE TRACK FACULTY POSITION MICROBIOLOGY

The Department of Biology at Tufts University invites applications for a tenure-track Assistant Professor in Microbiology. We seek a creative scholar with primary expertise in comparative or functional genomics, ecology of microbial populations, or genome evolution of microbial communities. Someone with the ability to work on multiple biological scales, ranging from the molecular to the community, is preferred. The successful candidate will use modern research techniques of computational genomics to address fundamental questions in evolution and ecology. We seek a scientist who will complement and add to our strengths, allowing new collaborations and synergistic research to occur within our department as well as across departments. The Biology department has expertise in genome structure and function, genome evolution, and the physiology and ecology of host organisms (see <http://ase.tufts.edu/biology/>).

The candidate will develop an active externally funded research program involving graduate and undergraduate students. Instructional duties will include an undergraduate microbiology course and an associated microbiology laboratory course, as well as contributions to other undergraduate or graduate courses based on the expertise and interests of the new faculty member. A clear commitment to teaching excellence at the undergraduate and graduate levels is essential. Doctoral degree, post-doctoral experience and a record of research productivity are required.

To Apply: Applicants should use the link <https://secure.interfolio.com/apply/21916> to submit a cover letter, curriculum vitae, and separate statements of (1) research interests and plans and (2) teaching experience and philosophy. Submission of 1-3 selected reprints in PDF format is encouraged. Applicants should also ensure that three confidential letters of reference are submitted to this link. Review of applications begins **October 1, 2013**, and continues until the position is filled.

Tufts University is an Affirmative Action/Equal Opportunity Employer. We are committed to increasing the diversity of our faculty. Members of underrepresented groups are strongly encouraged to apply.



The Department "Development and Regeneration" at the KU Leuven combines academicians involved in embryology and stem cell biology, human reproduction and sexuality, pre- and postnatal development and regenerative medicine. (<https://gbiomed.kuleuven.be/dep/devreg>).

We currently have **2 full-time academic vacancies**:

Assistant or associate professor in pluripotent stem cell biology.
(Ref. ZAP-2013-225)

To expand our basic research program, we aim to recruit an excellent basic scientist with focus on signals and their molecular mechanisms of action that govern pluripotency versus differentiation, with preference for studying the ground state of pluripotent stem cells as well as their derivatives, such as epiblast stem cells or extraembryonic cells. Ideally, the candidate also co-develops systems biology approaches that rely on transcriptomics, epigenetics and/or proteomics in a cell system of choice (<https://icts.kuleuven.be/apps/jobsite/vacatures/52485861>).

Assistant or associate professor with focus on endogenous tissue responses (Ref. ZAP-2013-224)

Within regenerative medicine, interactions between grafts and host are increasingly important. The endogenous tissue responses towards cell therapy, in particular with stem cells, or transplantation, determine the structural and functional outcome of the intervention. The department wishes to develop specific expertise unifying immunology and stem cell biology to further expand knowledge of development and regeneration. (<https://icts.kuleuven.be/apps/jobsite/vacatures/52485852>)

You can apply for these positions no later than **February 28, 2014** via the KU Leuven online application tool: <http://www.kuleuven.be/personnel/jobsite/en/senior>.

Full selection procedure: <http://www.kuleuven.be/personnel/jobsite/en/senior-info#selection>



UNIVERSITÉ
DE GENÈVE

The Faculty of Science of the University of Geneva invites applications for the position of

PROFESSOR In Plant Biology (Full, Associate or Assistant with Tenure Track)

JOB DESCRIPTION : We seek applicants with a record of excellence in research, who have proven their ability to develop and apply novel concepts in the general area of plant molecular and cellular biology. The successful candidate is expected to lead a strong, independent research program and attract external funding.

The position is full time and includes 4 to 6 hours per week of teaching spread across different courses and seminars at the Bachelor and Master level, as well as overseeing and directing the research of undergraduate and graduate students.

He/she will also take care, if necessary, of administrative duties linked with the Department of Botany and Plant Biology and the Faculty of Science.

ACADEMIC TITLE AND EXPERIENCE REQUIRED :

PhD degree or a title judged equivalent;
Experience in leading a research team and teaching;
Publications in international journals.

STARTING DATE : April 2014 or a date to be agreed.

Applications must be posted online by **September 30th 2013**, on the Geneva University website: <https://jobs.icams.unige.ch> where this advert and the job description can be viewed.

No hard copies will be accepted.

The University of Geneva is an equal opportunity employer and encourages applications from female candidates.

The NIH Intramural Research Program is Recruiting Tenure-Track “Earl Stadtman Investigators”

The National Institutes of Health, the U.S. government’s premier biomedical and behavioral research enterprise, is pleased to announce its fifth annual call for “NIH Earl Stadtman Investigators,” a broad recruitment of tenure-track investigators for all NIH intramural programs. Scientific discoveries from our intramural laboratories, with their extensive infrastructure and critical mass of expertise, have a crucial role in both maintaining America’s research excellence and advancing medical treatments and cures.

Come join the team whose hallmarks are stable funding, intellectual freedom, shared resources, and access to a wide range of scientific expertise. We seek creative, independent thinkers eager to take on high-risk, high-impact research. A fantastic array of early-career scientists already have been hired through the “Stadtman” recruitment in the last four years.

A variety of basic and translational/clinical positions are available, with areas of active recruitment including (but not limited to): Biochemistry, Biomedical Engineering, Biophysics, Biostatistics, Cancer Biology, Cell Biology, Cell Metabolism, Chemical Biology, Chromosome Biology, Circadian Biology, Computational Biology, Developmental Biology, Epidemiology, Genetics, Genomics, Health Disparities, Hearing & Balance, Immunology, Infectious Diseases, Microbiology, Molecular Pharmacology, Neurodevelopment, Neurosciences, Sensory Biology, Structural Biology, Systems Biology, Toxicology, Translational Research, and Virology.

Who we are: Among our approximately 1,100 principal investigators and 5,000 trainees are world-renowned experts in basic, translational, and clinical research. Our strength is our diversity in pursuit of a common goal, to alleviate human suffering from disease. Similar to academia, we offer our scientists the opportunity to mentor outstanding trainees at all levels (e.g., graduate students and postdoctoral fellows) in a research setting.

Whom we seek: For this broad, trans-NIH recruitment effort, we seek talented, early-career scientists with a clear and creative research vision who wish to contribute to the nation’s health.

Qualifications/eligibility: Candidates must have an M.D., Ph.D., D.D.S./D.M.D., D.V.M, D.O., R.N./Ph.D., or equivalent doctoral degree and have an outstanding record of research accomplishments as evidenced by publications in major peer-reviewed journals. Applicants may be in early stages of their research careers or non-tenured early-to-mid career scientists. Appointees may be U.S. citizens, resident aliens, or non-resident aliens with, or eligible to obtain, a valid employment-authorization visa.

How to apply: Applicants must submit four items: (1) a CV; (2) a three-page proposal titled Research Goals, i.e., the research you hope to perform at the NIH; (3) a one-page statement titled Long-term Research Vision and Impact, i.e., what you hope to achieve for yourself, your field, and society; and (4) contact information for three professional references. Submit these through our online application system at <http://tenuretrack.nih.gov/apply> between August 1 and 11:59 p.m. EDT October 1, 2013. You will be asked to designate a primary and secondary scientific area of expertise to aid in assigning your application to the appropriate review committee. Requests for letters of recommendation will be sent to your references when you submit your application. Reference letters will be accepted via upload to the website until 11:59 p.m. EDT October 15, 2013. We cannot accept paper applications.

What to expect: Search committees of subject-matter experts will review and evaluate applicants based on publication record, scientific vision and potential scientific impact of current and proposed research, demonstrated independence, awards, and references. The committees will identify the most highly qualified candidates to invite to the NIH for a lecture in November or December 2013, open to the NIH scientific staff, and for subsequent interviews with the search committees. Search committee chairs and NIH Scientific Directors, who lead our intramural programs, will identify finalists for possible recruitment as Earl Stadtman Investigators. Candidates not selected as finalists can be considered for other open NIH research positions. The entire process from application review to job offer may take several months, depending on the volume of applications.

We call upon individuals who will open our eyes to possibilities we haven’t yet envisioned, to complement our scientific mission and enhance our research efforts. More information about our program is at <http://irp.nih.gov>. The inspiring story of Earl and Thressa Stadtman’s research at the NIH is at <http://history.nih.gov/exhibits/stadtman>. Specific questions regarding this recruitment effort may be directed to Dr. Roland Owens, Assistant Director, NIH Office of Intramural Research, at owensrol@mail.nih.gov. DHHS and NIH are Equal Opportunity Employers.

STAY INFORMED! STAY CONNECTED!

Get more from your
AAAS membership



Are you currently registered to receive e-mails from AAAS and *Science*?

E-mail is the primary way that AAAS communicates with our members about AAAS programs, new member benefits, invitations to special events, and, of course, the latest news and research being published in *Science*.

Sign up today to receive e-mails from AAAS and ensure that you are getting the most out of your membership and *Science* subscription.*

To get started visit: promo.aaas.org/stayconnected You'll need your AAAS Member number. Find it above your name on your *Science* mailing label.

Don't miss a thing. Sign up for e-mail communications from AAAS today!



*AAAS follows CAN-SPAM and European Safe Harbor guidelines for protecting your privacy. We will never sell your e-mail address and you can opt-out of receiving e-mails at any time.



Research Fellow T Cell Receptor Biology

Seeking a postdoc to participate in an exciting new area of T cell receptor (TCR) biology involving mechanotransduction. The ideal candidate should have excellent skills in biochemistry, molecular biology and T cell functional studies including transfection of T cells, cell growth and functional analysis as well as flow cytometry.

Research Fellow HIV-1 Development

A postdoc position is available in the area of HIV vaccine immunology with the goal to modulate B cell selection and ultimately elicit high affinity, broadly neutralizing antibodies. A strong scientific background with emphasis on B cell and molecular immunology is required.

Please send your CV, a brief summary of research experience and names of three referees to: Ellis Reinherz, MD, Professor of Medicine, Harvard Medical School and the Department of Medical Oncology, Dana-Farber Cancer Institute, 77 Avenue Louis Pasteur, HIM 419, Boston, MA 02215; Email: ellis_reinherz@dfci.harvard.edu.

Dana-Farber Cancer Institute is an Affirmative Action/Equal Opportunity Employer – committed to diversity and inclusion in our workforce.



Georgia Research Alliance Eminent Scholar in Emerging and Zoonotic Pathogen Research

The University of Georgia, College of Veterinary Medicine, Department of Infectious Diseases is seeking applications for a Georgia Research Alliance Eminent Scholar in Emerging and Zoonotic Pathogen Research. A renowned scientist will be recruited to lead an infectious diseases research and development program with organisms of high public health impact potential. This Eminent Scholar position will be supported by annual income from an endowment exceeding \$1.5 million, 9-months of salary supported annually, and features a start up package commensurate with the prestige of this pre-eminent position. Available to support this program are newly renovated facilities including ACL3 space, and state-of-the-art BSL3, ABSL3 and BSL3-Ag animal and human health research laboratories at the Animal Health Research Center (<http://www.vet.uga.edu/AHRC>). The successful candidate will be an outstanding scholar with an established externally funded research program. In addition, candidates with demonstrated leadership in developing inter- or multi-disciplinary programs are especially encouraged to apply. Successful applicants are anticipated to possess a PhD in fields including virology, bacteriology, parasitology and immunology, and greater than six years of research experience. A DVM or MD, while desirable, is not required for this position.

Applications will be accepted until **October 1, 2013**. Interested applicants should submit cover letter, curriculum vitae and the names of three professional references by email (elafon10@uga.edu) to **Dr. Eric Lafontaine, Chair, GRA Scholar Search Committee, Department of Infectious Diseases, 501 DW Brooks Drive, University of Georgia, Athens, GA 30602**. All materials will be handled with strict confidentiality. Georgia is well known for its quality of life both outdoors and urban activities (www.exploregeorgia.org).

The University of Georgia (www.uga.edu) is a land grant/sea institution located 75 miles northeast of Atlanta, and is an Affirmative Action and Equal Opportunity Employer.

Science Careers is the forum that answers questions.



Science Careers is dedicated to opening new doors and providing timely answers to the career questions that matter to you.

Science Careers Forum:

- » Relevant Career Topics
- » Timely Advice and Answers
- » Community, Connections, and More!

Your Future Awaits.



Visit the forum and join the conversation today!

ScienceCareers.org

ISTFELLOW: Call for Postdoctoral Fellows

Are you a talented, dynamic, and motivated scientist looking for an opportunity to conduct research in the fields of **BIOLOGY**, **COMPUTER SCIENCE**, **MATHEMATICS**, **PHYSICS**, or **NEUROSCIENCE** at a young, thriving institution that fosters scientific excellence and interdisciplinary collaboration?

Apply to the ISTFellow program. Deadlines March 15 and September 15

www.ist.ac.at/istfellow



ISTFELLOW is partially funded by the European Union



ANNOUNCEMENTS



Biodiversity & Ecosystem Services Call for Synthesis Research Proposals Application Deadline: September 30, 2013

The U.S. National Socio-Environmental Synthesis Center (SESYNCC, www.sesync.org) and two German national research centers—the Helmholtz Centre for Environmental Research (UFZ, www.ufz.de) and the Synthesis Centre for Biodiversity Sciences (sDiv, www.idiv-biodiversity.de) within the German Centre for Integrative Biodiversity Research—are pleased to announce a joint trans-Atlantic socio-environmental synthesis activity on “Biodiversity and Ecosystem Services.”

Collaborative funding is available for synthesis projects that bring together data, ideas, theories, or models to address a critical socio-environmental question at the interface of biodiversity and ecosystem services. Proposals are welcome from investigators whose home institutions are anywhere in the world.

All three centers are dedicated to investigating pressing environmental issues involving complex human-nature interactions and global change and to developing sustainable solutions to these issues. Funded projects will receive support in: travel/logistic, group facilitation, cyberinfrastructure, geospatial analysis, and outreach/communications.

Details and submission instructions:
www.sesync.org/bio-ess



Presidential Endowed Chair in Health and Biomedicine Lehigh University

The Department of Biological Sciences at Lehigh University invites applications and nominations for a Presidential Endowed Chair in Health and Biomedicine. Applicants must hold a Ph.D. or M.D. degree and should be qualified for faculty appointment at the rank of Full Professor with tenure. The successful candidate will have a distinguished record in biomedical research, including significant external support, demonstrated leadership skills, and a strong commitment to graduate and undergraduate education. The position carries an expectation of scholarly and administrative leadership. As part of these responsibilities, the successful applicant will be expected to assume the Department Chair's position within two years of their appointment.

Lehigh's Biological Sciences Department includes 19 faculty with additional growth anticipated. Current faculty research interests span molecular, cellular and developmental biology, neuroscience, evolution and animal behavior. The department has Ph.D. programs in Integrative Biology, Biochemistry and Cell/Molecular Biology, a Distance Education M.S. program in Molecular Biology and the largest undergraduate major constituency within the college of Arts and Sciences.

Applications, including a C.V., letter of intent, description of administrative experience and philosophy, and the names of three potential references should be submitted to <https://academicjobsonline.org/ajo/jobs/2641>. For additional information contact **Dr. Lynne Cassimeris, Search Committee Chair, Biological Sciences, 111 Research Dr., Bethlehem, PA 18015, inbios@lehigh.edu**. For more information about the department: www.lehigh.edu/~inbios. The deadline for submission is **October 7, 2013**.

Lehigh University is an Equal Opportunity Affirmative Action Employer. Lehigh University provides comprehensive benefits including partner benefits. Lehigh University is a recipient of an NSF ADVANCE Institutional Transformation award for promoting the careers of women in academic sciences and engineering.

The College of Arts and Sciences at Lehigh is especially interested in qualified candidates who can contribute, through their research, teaching, and/or service, to the diversity and excellence of the academic community.



AAAS is here – helping scientists achieve career success.

Every month, over 400,000 students and scientists visit ScienceCareers.org in search of the information, advice, and opportunities they need to take the next step in their careers.

A complete career resource, free to the public, *Science* Careers offers a suite of tools and services developed specifically for scientists. With hundreds of career development articles, webinars and downloadable booklets filled with practical advice, a community forum providing answers to career questions, and thousands of job listings in academia, government, and industry, *Science* Careers has helped countless individuals prepare themselves for successful careers.

As a AAAS member, your dues help AAAS make this service freely available to the scientific community. If you're not a member, join us. Together we can make a difference.

To learn more, visit aaas.org/plusyou/sciencecareers





AAAS is here – promoting universal science literacy.

In 1985, AAAS founded Project 2061 with the goal of helping all Americans become literate in science, mathematics, and technology. With its landmark publications *Science for All Americans* and *Benchmarks for Science Literacy*, Project 2061 set out recommendations for what all students should know and be able to do in science, mathematics, and technology by the time they graduate from high school. Today, many of the state standards in the United States have drawn their content from Project 2061.

Every day Project 2061 staff use their expertise as teachers, researchers, and scientists to evaluate textbooks and assessments, create conceptual strand maps for educators, produce groundbreaking research and innovative books, CD-ROMs, and professional development workshops for educators, all in the service of achieving our goal of universal science literacy.

As a AAAS member, your dues help support Project 2061 as it works to improve science education. If you are not yet a AAAS member, join us. Together we can make a difference.

To learn more, visit aaas.org/plusyou/project2061



Women in Science Booklet

Science and the L'Oréal Foundation present



Read inspiring profiles of women
making a difference in biology.

Free download at
ScienceCareers.org/LorealWIS